

**FAILURE OF THICK, LOW DENSITY AIR PLASMA SPRAYED THERMAL  
BARRIER COATINGS**

by

**Michael Aaron Helminiak**

BS, University of Pittsburgh, 2008

MS, University of Pittsburgh, 2010

Submitted to the Graduate Faculty of  
Swanson School of Engineering in partial fulfillment  
of the requirements for the degree of  
Doctorate of Philosophy

University of Pittsburgh

2013

UNIVERSITY OF PITTSBURGH  
SWANSON SCHOOL OF ENGINEERING

This dissertation was presented

by

Michael A. Helminiak

It was defended on

February 28<sup>th</sup>, 2013

and approved by

Fredrick S. Pettit, PhD, Professor Emeritus, Department of Mechanical Engineering and  
Materials Science

Ian Nettleship, PhD, Professor, Department of Mechanical Engineering and Materials Science

Nazik M. Yanar, PhD, Research Professor, Department of Mechanical Engineering and  
Materials Science

Thomas A. Taylor, PhD, Praxair Surface Technologies – Retired

Jack L. Beuth Jr., PhD, Professor, Department of Mechanical Engineering – Carnegie Mellon  
University

Dissertation Director: Gerald H. Meier, PhD, Professor, Department of Mechanical  
Engineering and Materials Science

Copyright © by Michael A. Helminiak

2013

# **FAILURE OF THICK, LOW DENSITY AIR PLASMA SPRAYED THERMAL BARRIER COATINGS**

Michael A. Helminiak, PhD

University of Pittsburgh, 2013

This research was directed at developing fundamental understandings of the variables that influence the performance of air plasma sprayed (APS) yttria-stabilized zirconia (YSZ) thermal barrier coatings (TBC). Focus was placed on understanding how and why each variable influenced the performance of the TBC system along with how the individual variables interacted with one another.

It includes research on the effect of surface roughness of NiCoCrAlY bond coats deposited by argon-shrouded plasma spraying, the interdiffusion behavior of bond coats coupled to commercial superalloys, and the microstructural and compositional control of APS topcoats to maximize the coating thicknesses that can be applied without spallation. The specimens used for this research were prepared by Praxair Surface Technologies and have been evaluated using cyclic oxidation and thermal shock tests.

TBC performance was sensitive to bond coat roughness with the rougher bond coats having improved cyclic performance than the smoother bond coats. The explanation being the rough bond coat surface hindered the propagation of the delamination cracks.

The failure mechanisms of the APS coatings were found to depend on a combination of the topcoat thickness, topcoat microstructure and the coefficient of thermal expansion (CTE) mismatch between the superalloy and topcoat. Thinner topcoats tended to fail at the topcoat/TGO

interface due to bond coat oxidation whereas thicker topcoats failed within the topcoat due to the strain energy release rate of the thicker coating exceeding the fracture strength of the topcoat.

Properties of free-standing high and conventional purity YSZ topcoats of both a low-density (LD) and dense-vertically fissure (DVF) microstructures were evaluated. The densification rate and phase evolution were sensitive to the YSZ purity and the starting microstructure. Increasing the impurity content resulted in enhanced sintering and phase decomposition rates, with the exception of the conventional-purity DVF which exhibited a density decrease during sintering. A combination of the DVF and LD topcoat microstructures (dual TBC) resulted in significant increase in cyclic durability. A 1275  $\mu\text{m}$  thick dual TBC coating was found to have a comparable furnace cyclic life to that of a 100  $\mu\text{m}$  LD TBC.

## TABLE OF CONTENTS

LIST OF TABLES .....	x
LIST OF FIGURES .....	xi
PREFACE .....	xxiv
1.0 INTRODUCTION .....	1
2.0 BACKGROUND .....	5
2.1 TBC SYSTEM OVERVIEW .....	5
2.2 TOPCOAT PARAMETERS: INFLUENCE ON TBC LIFETIME.....	10
2.2.1 Influence of Topcoat Microstructure.....	10
2.2.2 Influence of YSZ Purity .....	16
2.2.3 Influence of Topcoat Thickness .....	21
2.3 BOND COAT INFLUENCE ON LIFETIME .....	30
2.3.1 Surface Roughness .....	30
2.3.2 Bond Coat Open Porosity .....	34
2.4 SUBSTRATE INFLUENCE ON LIFETIME .....	35
2.4.1 Compositional Effect.....	35
2.4.2 Mechanical Effect.....	37
3.0 EXPERIMENTAL.....	39
3.1 THERMAL EXPOSURE TYPES .....	40

3.2	SPECIMEN BREAKDOWN.....	43
3.2.1	Topcoat Modifications .....	44
3.2.1.1	YSZ Purity .....	44
3.2.1.2	Topcoat Thickness .....	45
3.2.1.3	Topcoat Microstructure.....	45
3.2.2	Bond Coat Modifications .....	46
3.2.3	Substrate Influences .....	47
3.3	CHARACTERIZATION TECHNIQUES .....	48
4.0	RESULTS AND DISCUSSION.....	49
4.1	TOPCOAT VARIABLES.....	49
4.1.1	Topcoat YSZ Purity.....	49
4.1.1.1	Overview.....	49
4.1.1.2	Experimental Design.....	49
4.1.1.3	Results: Free-Standing Topcoats .....	51
4.1.1.4	Discussion.....	94
4.1.1.5	Conclusions.....	99
4.1.2	Topcoat Thickness.....	100
4.1.2.1	Overview.....	100
4.1.2.2	Experimental Overview .....	102
4.1.2.3	Experimental Results .....	108
4.1.2.4	Discussion.....	117

4.1.2.5	Conclusions.....	126
4.1.3	Topcoat Microstructure .....	128
4.1.3.1	Overview.....	128
4.1.3.2	Design Approach .....	129
4.1.3.3	Observational Approach .....	152
4.1.3.4	Conclusions.....	159
4.2	BOND COAT VARIABLES .....	160
4.2.1	Chapter Overview.....	160
4.2.2	Experimental Overview.....	161
4.2.3	Experimental Results.....	165
4.2.3.1	Surface Characterization.....	165
4.2.3.2	FCT Results .....	176
4.2.3.3	Percent Lifetime.....	188
4.2.3.4	JETS Results .....	202
4.2.4	Discussion .....	204
4.2.5	Conclusions Summary.....	210
4.3	SUBSTRATE INFLUENCES .....	211
4.3.1	Overview .....	211
4.3.2	Mechanical Effects .....	212
4.3.2.1	Experimental Overview .....	212
4.3.2.2	Mechanical Results and Discussion.....	213
4.3.3	Compositional Effects .....	217

4.3.3.1	Experimental Overview .....	217
4.3.3.2	Compositional Results and Discussion: Aluminum Depletion...	221
4.3.3.3	Compositional Results and Discussion: Oxide Formation .....	225
4.3.4	Substrate Effect Summary.....	234
5.0	CONCLUDING REMARKS.....	236
6.0	SUGGESTED FUTURE WORK .....	242
	BIBLIOGRAPHY.....	244

## LIST OF TABLES

Table 1 - Parameters for temperature calculations [19].....	24
Table 2 - Parameters for strain energy calculation [33].....	28
Table 3 - Ra and Rz values of the bond coat interface, bond coat temperature (during testing) and cycles to failure of TBC specimens [3].....	31
Table 4 - Composition of materials in weight percent.....	40
Table 5 - Composition of powders used for the free-standing topcoat specimens. ....	50
Table 6 - XRD Scan Settings .....	51
Table 7 - Calculated Sintering Rates of Topcoats .....	53
Table 8 - Difference in mass between pre-sintered and post-sintered specimens. ....	55
Table 9 - Percent Monoclinic Content of Aged Topcoats .....	90
Table 10 - Percent Monoclinic Before and After 150°C Aging .....	92
Table 11 - Data Type and Fit Parameter.....	118
Table 12 - Number of TBCs tested for each type of thermal exposure. ....	164
Table 13 - Percent Lifetime Testing Summary.....	188
Table 14 - Characterization summary of Percent Lifetime Tests .....	202
Table 15 - Number of cycles the bond coat only specimens were cycled to and examined.....	219
Table 16 - Diffusion coefficients for ternary Ni-Cr-Al and Co-Cr-Al alloys. ....	223

## LIST OF FIGURES

Figure 1 - Standard free energy of formation of a number of oxides as a function of temperature [6].....	7
Figure 2 - APS TBC containing large globular pores (black arrows) and horizontal delaminations (gray arrows) [14]. .....	12
Figure 3 - Fracture section of an APS topcoat. White arrows indicate horizontal microcracks, the gray arrows point out pores from gas being trapped and the black arrows indicate vertical microcracks. ....	13
Figure 4 - APS TBC that contains vertical segmentation cracks.....	14
Figure 5 - Burner rig life versus percent silica [27].....	17
Figure 6 - Influence of: a.) silica; b.) alumina; c.) titania; and d.) silica & alumina content on the mean shrinkage at 1200°C within the first 60hr [30].....	18
Figure 7 - The effect of time, temperature, and impurity level on shrinkage [25]. ....	19
Figure 8 - Through thickness thermal conductivity as a function of time spent at 1400°C [28]..	20
Figure 9 - Temperature distribution in a TBC system exposed to hot combustion gases on one side and cooling air on the other. ....	22
Figure 10 - Temperature profiles as a function of topcoat thickness.....	24
Figure 11 - a.) Surface temperature as a function of TBC thickness and b.) the front and back face temperature drop as a function of TC thickness.....	25

Figure 12 – The stored elastic strain energy per unit area as a function of topcoat thickness.....	27
Figure 13 - Cross-sectional micrographs of failures of a) 1.1mm and b) 0.75mm TBC failures. The TBC in a) failed after 20 thermal cycles and b) failed after 140 thermal cycles in a bottom-loading furnace. Note the location of the failure in both micrographs: a) failure occurs within the TBC and b) at the TBC/TGO interface. ....	29
Figure 14 - Effect of segment size and test temperature on buckling life for segmented TBCs in interrupted and cyclic exposures (Points labeled “E” refer to edge delaminations of non- segmented backside or control samples; arrows indicate no failure at end of test [39]....	33
Figure 15 - Schematic diagram of a thermally sprayed bond coat that oxidized during deposition. Note the interconnected network of alumina that surround the bond coat particles.....	35
Figure 16 - Weight change of Pt aluminate/EB-PVD TBC coated René N5 during 1 hr cycles at 1150°C. Both desulfurization and the addition of Y to the underlying substrate improved coating lifetime [48].....	37
Figure 17 - Photograph of a bottom loading furnace used for the furnace cycling tests (FCT)..	41
Figure 18 - Praxair JETS testing rig. ....	42
Figure 19 - Percent theoretical density of as-processed and sintered topcoats. Measured according to ASTM-B328.....	52
Figure 20 - HP-LD in the as-processed condition. White arrows indicate small micro-cracks, black – globular pores and grey – horizontal delmainations. ....	56
Figure 21 - HP-LD after 10 hours at 1300°C.....	57
Figure 22 - HP-LD after 100 hours at 1300°C.....	58
Figure 23 - HP-LD after 100 hours at 1200°C.....	59

Figure 24 - CP-LD in the as-processed condition. White arrows indicate regions of SiO <sub>2</sub> and Al <sub>2</sub> O <sub>3</sub> impurities.....	60
Figure 25 - CP-LD in the as-processed condition. White arrows indicate regions of SiO <sub>2</sub> and Al <sub>2</sub> O <sub>3</sub> impurities.....	61
Figure 26 - CP-LD after 10 hours at 1300°C. White arrows indicate regions of SiO <sub>2</sub> and Al <sub>2</sub> O <sub>3</sub> impurities. ....	62
Figure 27 - CP-LD in the as-processed condition. White arrows indicate regions of SiO <sub>2</sub> and Al <sub>2</sub> O <sub>3</sub> impurities.....	63
Figure 28 - CP-LD after 10 hours at 1300°C. White arrows and red box indicate regions of SiO <sub>2</sub> and Al <sub>2</sub> O <sub>3</sub> impurities. ....	64
Figure 29 - CP-LD after 100 hours at 1300°C. White box highlights small pores. Red box indicates a region of SiO <sub>2</sub> and Al <sub>2</sub> O <sub>3</sub> impurities.....	65
Figure 30 - CP-LD after 100 hours at 1300°C. White arrows indicate regions of SiO <sub>2</sub> and Al <sub>2</sub> O <sub>3</sub> impurities. ....	66
Figure 31 - CP-LD after 100 hours at 1200°C. White arrows indicate regions of SiO <sub>2</sub> and Al <sub>2</sub> O <sub>3</sub> impurities. ....	67
Figure 32 - HP-DVF in the as-processed condition. White arrows indicate vertical fissures, black – globular pores and grey – horizontal delmainations.....	68
Figure 33 - HP-DVF after 10 hours at 1300°C.....	69
Figure 34 - HP-DVF after 100 hours at 1300°C.....	70
Figure 35 - HP-DVF after 100 hours at 1200°C.....	71
Figure 36 - CP-DVF in the as-processed condition. White arrows indicate vertical fissures, black – globular pores and grey – horizontal delmainations.....	72

Figure 37 - CP-DVF in the as-processed condition. White arrows indicates a splat rich in magnesium and zirconium. ....	73
Figure 38 – CP-DVF in the as-processed condition. Large black particle was a silica-alumina rich phase. ....	74
Figure 39 - CP-DVF after 10 hours at 1300°C .....	75
Figure 40 - CP-DVF after 10 hours at 1300°C. The dark structure is a silica-alumina impurity particle.....	76
Figure 41 - CP-DVF after 100 hours at 1300°C .....	77
Figure 42 - CP-DVF after 100 hours at 1300°C. High-magnification image of pores in the coating.....	78
Figure 43 - CP-DVF after 100 hours at 1200°C. ....	79
Figure 44 - ZrO <sub>2</sub> -YO <sub>1.5</sub> phase diagram [54]. ....	81
Figure 45 - XRD patterns for the as-processed structure of the four topcoats. ....	82
Figure 46 – 72°-75° 2θ region of the XRD pattern for the HP-LD topcoat before and after the thermal exposures. ....	84
Figure 47 - 72°-75° 2θ region of the XRD pattern for the HP-DVF topcoat before and after the thermal exposures. ....	86
Figure 48 – 72°-75° 2θ region of the XRD pattern for the CP-LD topcoat before and after the thermal exposures. ....	87
Figure 49 - 72°-75° 2θ region of the XRD pattern for the CP-DVF topcoat before and after the thermal exposures. ....	89
Figure 50 - Enhanced portion of the ZrO <sub>2</sub> -YO <sub>1.5</sub> phase diagram [54]......	91

Figure 51 - XRD pattern of the CP-LD and HP-LD topcoats aged for 100 hours at 1300°C rapidly quenched, and then again exposed at 150°C for 24 hours.....	93
Figure 52 - Sintering rate of plasma sprayed topcoats at 1200°C for 60 hours [30]. .....	97
Figure 53 - Cycles to failure of three groups of TBCs with different topcoat thicknesses. All TBCs have IN 718 substrates with dual layer NiCoCrAlY bond coats and YSZ topcoats [2].....	101
Figure 54 - 100 μm topcoat in the as-processed condition. ....	104
Figure 55 - 225 μm TBC in the as-processed condition. ....	105
Figure 56 - 425 μm TBC in the as-processed condition. ....	105
Figure 57 - 750 μm TBC in the as-processed condition. ....	106
Figure 58 - 1150 μm TBC in the as-processed condition. Red arrow indicates pull-out in the topcoat as a result of metallographic preparation. ....	106
Figure 59 - 1425 μm TBC in the as-processed condition. Red arrows indicate pull-out in the topcoat as a result of metallographic preparation. ....	107
Figure 60 - FCT results for TBCs with varying topcoat thicknesses. All specimens had the same substrate (PWA 1484) and bond coat type (dual layer NiCoCrAlY). ....	108
Figure 61 - High resolution images of the fracture surfaces of each of the 6 different thickness coatings. The upper circles are the substrate-bond coat portion of the TBC and the lower circles are the undersides of the corresponding topcoats that spalled off.....	109
Figure 62 - 100μm TBC with 830 cycles to failure. The topcoat is still intact however at least 30% had become delaminated which was termed to be a technical failure.....	110
Figure 63 - 225 μm TBC with 810 cycles at failure. The topcoat is still intact however at least 30% had become delaminated which was determined to qualify as a technical failure. ....	110

Figure 64 - 425  $\mu\text{m}$  TBC with 560 cycles at failure. Note, the topcoat and the substrate were cross-sectioned at different positions which accounts for their apparent differences in length..... 110

Figure 65 - 750  $\mu\text{m}$  TBC with 440 cycles at failure. The topcoat is still intact however at least 30% had become delaminated which was determined to qualify as a technical failure. 111

Figure 66 - 1150  $\mu\text{m}$  TBC with 280 cycles at failure. .... 111

Figure 67 - 1425  $\mu\text{m}$  TBC with 160 cycles at failure. The spalled topcoat is not present however there is a significant amount of YSZ present at the surface. .... 111

Figure 68 - 1425 $\mu\text{m}$  coating which failed at 160 cycles. Note both the horizontal and diagonal cracking within the topcoat. The red arrows point out diagonal cracks which have formed but not propagated to the extent of the other diagonal cracks. .... 112

Figure 69 - 1150 $\mu\text{m}$  topcoat after spalling off with 280 cycles. The red arrows highlight diagonal cracking that occurred near the topcoat-TGO interface..... 113

Figure 70 - Enlarged composited micrograph of 750 $\mu\text{m}$  coating with 440 cycles at failure previously shown in Figure 65. Red arrows highlight diagonal cracks which formed in the topcoat..... 113

Figure 71 - 750  $\mu\text{m}$  coating with 440 cycles until a technical failure occurred. This micrograph was taken in the interior of the specimen as indicated by the black box in Figure 65. .. 114

Figure 72 - 225  $\mu\text{m}$  coating with 810 cycles until technical failure. .... 115

Figure 73 - 100  $\mu\text{m}$  topcoat after 830 cycles at 1100°C. The white arrow points out areas in the outer portion of the dual layer bond coat that experienced chemical failure..... 116

Figure 74 - Plot of topcoat thickness vs. cycles to failure. .... 117

Figure 75 - 750 $\mu$ m TBC after 440 cycles. This portion of the topcoat was still intact and far ahead of an edge crack.....	121
Figure 76 - The edge of a 425 $\mu$ m topcoat after 510 cycles (91% lifetime).....	123
Figure 77 - The interior of a 425 $\mu$ m topcoat after 510 cycles (91% lifetime).....	123
Figure 78 - Critical delamination radius needed for topcoat buckling. ....	125
Figure 79 - As-processed LD topcoat on DL bond coat on PWA 1484 substrate.....	131
Figure 80 - As-processed DVF topcoat on DL bond coat on PWA 1484 substrate. Black arrows indicate large vertical fissures.....	132
Figure 81 - As-processed dual TBC on DL bond coat on PWA 1484 substrate. ....	132
Figure 82 - High magnification micrograph of interface between LD and DVF layers showing good adherence and no large delamination cracks between the layers.....	133
Figure 83 - FCT results for the topcoat microstructure specimens.....	134
Figure 84 - High resolution image of failed LD, DVF and dual TBC specimens. ....	135
Figure 85 - Failed LD specimen with 280 cycles at failure. Topcoat completely spalled off. ...	137
Figure 86 - Failed DVF specimen with 440 cycles at failure. ....	137
Figure 87 - Failed dual TBC specimen with 1020 cycles at failure.....	138
Figure 88 - Failed DVF specimen with 440 cycles at failure. ....	139
Figure 89 - Failed dual TBC specimen after 860 cycles. This is only a micrograph of the spalled topcoat. Arrows indicate horizontal cracks present at the interface between the LD and DVF layers. ....	140
Figure 90 - Dual TBC specimen which experienced a technical failure after 1020 cycles. Arrows indicate horizontal micro-cracks at the interface between the LD and DVF layers. ....	141
Figure 91 - Failed dual TBC with 1020 cycles at failure.....	142

Figure 92 - 225 $\mu\text{m}$ topcoat after 810 cycles at 1100°C. ....	142
Figure 93 - Percent edge cracking after 2000 cycles in the JETS apparatus. ....	144
Figure 94 - 1.1mm LD topcoat on PWA 1484 after 2000 JETS cycles.....	145
Figure 95 - 1.1mm LD topcoat on PWA 1484 after 2000 JETS cycles. Micrograph was taken far from the edge of the specimen. ....	145
Figure 96 - Dual TBC on PWA 1484 after 2000 JETS cycles. ....	146
Figure 97 - Dual TBC on PWA 1484 after 2000 JETS cycles. Micrograph was within the interior of the specimen away from the free edge. ....	147
Figure 98 - 1.1mm DVF topcoat on PWA 1484 after 2000 JETS cycles. ....	148
Figure 99 - 1.1mm DVF topcoat on PWA 1484 after 2000 JETS cycles. Micrograph was taken far from the edge of the specimen.....	149
Figure 100 - FCT lifetimes of TBCs from 3 different batches of specimens. All specimens had N5 substrates and dual layer bond coats with the exception of the red bar which had a PWA 1484 substrate. ....	154
Figure 101 - Generation II 85% dense 1100 $\mu\text{m}$ topcoat on a dual layer bond coat and N5 substrate with 560 cycles at failure. ....	155
Figure 102 - Generation III 89% dense 1100 $\mu\text{m}$ topcoat on a dual layer bond coat and N5 substrate with 120 cycles at failure. ....	155
Figure 103 - Generation IV 82% dense 1100 $\mu\text{m}$ topcoat on a dual layer bond coat and PWA 1484 substrate with 280 cycles at failure. ....	156
Figure 104 - Dual layer bond coat in the as-processed state. Original micrograph (a), surface of bond coat outlined in white (b) and converted binary image with remaining white bond coat surface trace (c). ....	163

Figure 105 - Average roughness of the 4 bond coat types.....	165
Figure 106 - Schematic of $R_z$ measurement.....	167
Figure 107 - Average maximum height of the bond coat surface profiles. ....	168
Figure 108 - A secondary electron image of the surface of a DL bond coat. ....	169
Figure 109 - A secondary electron image of the surface of a 50:50 bond coat. ....	170
Figure 110 - A secondary electron image of the surface of a 75:25 bond coat. ....	170
Figure 111 - A secondary electron image of the surface of a SL bond coat.....	171
Figure 112 - Cross sectional micrograph of a DL bond coat in the as-processed condition. A white outline has been added to enhance the visibility of the bond coat/topcoat interface. White arrows point to large round particles which are likely individual LN14 particles and the red arrows point out the large peaks which correspond to the highlighted peaks in Figure 108. ....	173
Figure 113 - Cross sectional micrograph of a 50:50 bond coat in the as-processed condition. A white outline has been added to enhance the visibility of the bond coat/topcoat interface. White arrows point to large round particles which are likely individual LN14 particles and the red arrows point out the large peaks which correspond to the highlighted peaks in Figure 109. ....	173
Figure 114 - Cross sectional micrograph of a 75:25 bond coat in the as-processed condition. A white outline has been added to enhance the visibility of the bond coat/topcoat interface. White arrows point to large round particles which are likely individual LN14 particles and the red arrows point out the large peaks which correspond to the highlighted peaks in Figure 110. ....	174

Figure 115 - Cross sectional micrograph of a SL bond coat in the as-processed condition. A white outline has been added to enhance the visibility of the bond coat/topcoat interface .  
..... 174

Figure 116 - FCT results for the bond coat modification specimens tested at 1100°C. .... 176

Figure 117 - High resolution images of fracture surfaces. Top specimen is the bond coat surface and the bottom specimen is the spalled topcoat surface. The white material is YSZ and the blue is the TGO. .... 177

Figure 118 - Failed SL bond coat TBC on N5 after 320 cycles. .... 179

Figure 119 - Failed 75:25 bond coat TBC on N5 after 320 cycles. .... 179

Figure 120 - Failed 50:50 bond coat TBC on N5 after 720 cycles. .... 180

Figure 121 - Failed DL bond coat TBC on N5 after 600 cycles. .... 180

Figure 122 - Failed 75:25 bond coat TBC on N5 after 320 cycles. The red line connects the peaks along the bond coat surface. .... 181

Figure 123 - Failed DL bond coat TBC on N5 after 600 cycles. The red line connects the peaks along the bond coat surface. .... 182

Figure 124 - SL bond coat after 320 cycles. Note 80%+ of the aluminum rich  $\beta$ -phase is still remains. .... 183

Figure 125 - 75:25 bond coat after 320 cycles. Note the limited amount of aluminum-rich  $\beta$ -phase remaining and the presence of a  $\beta$ -phase depletion zone adjacent to the bond coat / superalloy interface ..... 184

Figure 126 - Failed 50:50 bond coat TBC on N5 after 720 cycles. Note the oxide layer at both the bond coat surface (white arrow) and at the superalloy-bond coat interface (black arrow).  
..... 185

Figure 127 - Failed DL bond coat TBC on N5 after 620 cycles. Note the surface connected pores which have oxidized (white arrows). .....	186
Figure 128 - SL bond coat on PWA 1484 with 140 cycles (~50% Lifetime). .....	189
Figure 129 - SL bond coat on PWA 1484 with 140 cycles. White arrows point out cracks at interface between TGO and YSZ.....	190
Figure 130 - SL bond coat on PWA 1484 with 200 cycles. ....	191
Figure 131 - SL bond coat on PWA 1484 with 200 cycles. ....	192
Figure 132 - 75:25 bond coat on PWA 1484 with 140 cycles (50% lifetime).....	193
Figure 133 - 75:25 bond coat with 200 cycles (71% lifetime). ....	194
Figure 134 - 75:25 bond coat with 140 cycles (50% lifetime). ....	194
Figure 135 - 75:25 bond coat with 200 cycles (71% lifetime). ....	195
Figure 136 - 50:50 bond coat with 200 cycles (33% lifetime). ....	196
Figure 137 - 50:50 bond coat with 200 cycles (33% lifetime). ....	196
Figure 138 - 50:50 bond coat with 200 cycles (33% lifetime). ....	197
Figure 139 - 50:50 bond coat with 510 cycles (85% lifetime). ....	198
Figure 140 - 50:50 bond coat with 510 cycles (85% lifetime). ....	198
Figure 141 - 50:50 bond coat with 510 cycles (85% lifetime). ....	199
Figure 142 - DL bond coat with 200 cycles (35% lifetime). ....	200
Figure 143 - DL bond coat with 200 cycles (35% lifetime). ....	200
Figure 144 - DL bond coat with 510 cycles (91% lifetime). ....	201
Figure 145 - DL bond coat with 510 cycles (91% lifetime). ....	201
Figure 146 - 75:25 bond coat on PWA 1484 with 2000 JETS cycles. ....	203
Figure 147 - 50:50 bond coat on PWA 1484 with 2000 JETS cycles. ....	204

Figure 148 - DL bond coat on PWA 1484 with 2000 JETS cycles. ....	204
Figure 149 - Bond coat and accompanying stresses before and after thermal exposure. Figure was taken from [65]. ....	208
Figure 150 - The number of cycles to failure for low density, high purity APS TBCs of two topcoat thicknesses on Inconel 718, Haynes 188 and René N5 substrates. All substrates had dual layer NiCoCrAlY bond coats. Each bar is the average of three specimens with the error bars showing the standard deviations [2]. ....	214
Figure 151 - Mean CTE of the alloys used in this study. ....	215
Figure 152 - Failed 375 $\mu\text{m}$ TBC on N5 after 920 cycles. ....	216
Figure 153 - Starting microstructure of $\beta$ - $\gamma$ NiCoCrAlY bond coat. Dark grey phase is the $\beta$ -phase and the lighter regions are $\gamma$ -phase. The black regions are pores within the bond coat. ....	218
Figure 154 - Depth of $\beta$ -phase depletion zone as a function of thermal cycles. Solid lines represent depletion due to interdiffusion and the dashed lines represent depletion due to TGO formation. ....	221
Figure 155 - High resolution images of the surfaces of the specimens for various number of cycles. Red arrows point out some of the marks left by the ceramic trays the specimens are placed in during thermal cycling. ....	226
Figure 156 - Cross-section of IN718 specimen after 500 cycles. White arrows indicate oxides rich in Ni, Co, Cr, Nb, and Fe and the black arrows point out $\text{Al}_2\text{O}_3$ . ....	228
Figure 157 - High resolution scanned images of HA188 and N5 specimens after a set number of cycles. ....	230

Figure 158 - HA188 specimen with 1000 cycles. White arrows indicate non-aluminum oxides and the black arrows point to the aluminum oxides. .... 231

Figure 159 - N5 specimen after 1000 cycles. White arrows indicate non-aluminum oxides and the black arrows indicate aluminum oxide. .... 232

## **PREFACE**

This work at University of Pittsburgh was performed in support of the National Energy Technology Laboratory's ongoing research under RES contract DE-FE0004000. The author is grateful to GE Aircraft Engines (B. Nagaraj) and Pratt and Whitney (M. Maloney) for providing superalloy substrates and Praxair Surface Technologies for preparing the specimens used in this body of work.

As a disclaimer, this report was prepared as an account of work sponsored by an agency of the United States Government. Neither the United States Government nor any agency thereof, nor any of their employees, makes any warranty, express or implied, or assumes any legal liability or responsibility for the accuracy, completeness, or usefulness of any information, apparatus, product, or process disclosed, or represents that its use would not infringe privately owned rights. Reference herein to any specific commercial product, process, or service by trade name, trademark, manufacturer, or otherwise does not necessarily constitute or imply its endorsement, recommendation, or favoring by the United States Government or any agency thereof. The views and opinions of authors expressed herein do not necessarily state or reflect those of the United States Government or any agency thereof.

Finally, special thanks go out to Dr. Li Li, Dr. Mike Task and Al Stewart for all of their advice and expertise which was called upon during the time of this research.

## 1.0 INTRODUCTION

In the electric power generation industry, hydrogen fuel technologies are leading to FutureGen-type (i.e. near-zero emissions which utilize carbon capture and sequestration (CCS)) power plants that involve a transition from standard gas turbines operating with coal or natural-gas combustion to very high hydrogen fuels derived from syngas and syngas burned in nearly pure oxygen using steam to control temperatures (oxy-fuel systems). The transition will require materials technologies to accommodate expansion gases that are not only increasingly hotter but also contain higher concentrations of water vapor. Likewise, in aircraft and marine gas turbines (as well as land based gas turbines), there is a continual demand for higher fuel efficiencies and increased thrust and/or power, both of which can be answered by increasing the turbine inlet temperatures (among other engine design configurations). Additionally, the efficiency of these engines can be increased by using less cooling air for the structural components of the turbines which again raises the operating temperature of these components. In all cases, the higher temperatures will require improved thermal barrier coatings (TBCs) for the structural materials in the hot sections of the engines (i.e. combustor, initial rotor blades, and nozzle guide vanes of the high pressure turbine)[1].

The effectiveness of a thermal barrier coating can be scaled by examining its effective thermal resistance, which is a ratio of the TBC thickness to the TBC thermal conductivity which is shown in Equation 1.

$$R_{\text{Therm}} = \frac{h_{\text{topcoat}}}{\kappa_{\text{topcoat}}}$$

While there has been some progress in identifying oxides with lower thermal conductivities than conventionally-used yttria-stabilized zirconia (YSZ), these oxides do not have the balance of properties necessary for advanced systems. An alternative approach is use TBCs at larger thicknesses or to modify their microstructures as to reduce the thermal conductivity of the YSZ coating.

The two types of TBCs used in service are electron beam physical vapor deposited (EBPVD) TBCs and air plasma sprayed (APS) TBCs. The columnar structure of the EBPVD TBCs allows them to accommodate large thermo-mechanical strains and their smooth surface finish makes them ideal for rotating blades and some high-pressure turbine sections. APS TBCs are not well suited for these applications because of their rough finishes and comparatively poor strain tolerance. However, EBPVD TBCs have a higher thermal conductivity than APS TBCs and they cannot be deposited in the wide range of thicknesses APS coatings can be sprayed (100-1500 $\mu\text{m}$ ). These two limitations put an upper limit on the maximum thermal resistance of EBPVD coatings. APS TBCs are comparatively more versatile, as they can be sprayed in a variety of thicknesses and microstructures permitting their thermal resistance to be tailored for a specific application. For these reasons APS TBCs may be the potential solution to the higher operating temperatures in future gas turbines.

Before moving forward with thicker or lower thermal conductivity APS TBCs, a better understanding of how these variables influence the durability and lifetime of these coatings is required. Likewise, a broader understanding of why APS TBCs fail would also provide

information as how to extend the lifetime of current TBC systems. The latter would involve investigating variables associated with all three layers of the TBC system: topcoat, bond coat and superalloy.

Previous work [2] identified the thickness of the ceramic topcoat (i.e. TBC thickness) impacts the lifetime of the TBCs, where thinner TBCs have extended lifetimes, and the failure characteristics, where thin TBCs fail due to bond coat oxidation but thick TBCs fail within the topcoat (above the interface). It was unclear though whether TBC lifetime would continue to increase as thickness decreased or whether some other limiting factor would cut short the lifetime and even change the failure characteristics.

Likewise, the role impurities in the YSZ play on the phase stability and the sintering behavior of the coatings needs more investigation. Previous work [2] demonstrated that free standing high-purity coatings are resistance to high temperature sintering and phase transformations, however, a direct comparison of the phase stability and sintering behavior of a high purity and a conventional purity coating is lacking. A complementary microstructural investigate is also absent from the literature.

Dual TBCs consisting of two topcoat layers, a dense vertically-fissured (DVF) YSZ layer adjacent to the bond coat and a porous low-density outer layer on top of the DVF layer, were also tested in previous work [2]. This layering improved the lifetime of the thick (1.1mm) TBCs to that of the thin low-density (0.3mm) TBCs. However, a direct comparison of the dual TBC to a similar thickness low-density TBC or to a fully DVF TBC was not completed. A comparison of their performances could provide insight on why such a dual TBC performs so well. Furthermore, while the performance of the dual TBC was exceptional in furnace cycle testing, it

remains unknown whether such a TBC would perform as well in when exposed to a thermal gradient.

The substrate superalloy was identified as having an influence on the cyclic lifetime of a TBCs [2]. For the thick APS TBCs ( $>1100 \mu\text{m}$ ), this was linked to the coefficient of thermal expansion (CTE) mismatch between the substrate and the topcoat layer. With the thinner ( $375\mu\text{m}$ ) TBCs that had longer lifetimes than the thick TBCs ( $1100\mu\text{m}$ ), the effect of the substrate selection was still apparent, however, it was unclear whether the effect was a result of the CTE mismatch, the compositional differences, a combination of the two, or some other unidentified variable like substrate oxidation.

Finally, while it is generally accepted a rough bond coat surface finish is ideal for APS topcoat adherence it is unclear what the ideal roughness is and why exactly a high roughness is beneficial. Likewise, it is unknown how sensitive TBC lifetime is to this parameter. What is known is that the oxidation of the bond coat layer is sensitive to the topography of the bond coat [3, 4] where bond coats which are too rough have worse oxidation performance than smoother ones. An understanding of why and how roughness is important could justify the rough surfaces despite their inferior oxidation performance.

These deficiencies identified in the literature and a continuation of previous research will be the focus of this current body of work.

## **2.0 BACKGROUND**

### **2.1 TBC SYSTEM OVERVIEW**

Thermal barrier coatings (TBCs) are primarily used in turbine applications where high temperatures are encountered (900°C-1400°C). More specifically, they are most often used in the hot sections of turbine engines (blades and vanes) and combustor liners[5].

A thermal barrier coating system is comprised of three layers, the superalloy, the bond coat, and the ceramic TBC. The superalloy is the engine component which requires thermal protection from the hot combustion gases. The superalloy used for these engine components are required to have excellent high temperature strength and creep resistance since parts such as engine blades experience large centrifugal forces and high temperatures during operation [6]. However, the superalloy compositions required to achieve high creep strength offer very poor oxidation and corrosion protection primarily because they utilize high refractory metal and platinum-group metal contents [6-8]. As a result several methods of protection against this high temperature corrosion have been introduced. Coatings have been used to provide oxidation and corrosion resistance and they operate on the principle of selective oxidation which will be discussed later. However, as the combustion gas temperatures approach the melting points of the superalloys, their mechanical strength begins to rapidly decrease, despite the corrosion protection from the coatings. To accommodate this, cooling channels were designed into the engine

components which lower the surface temperature by thin film cooling. With still the push for higher combustion temperatures, TBCs were introduced which utilize a low thermal conductivity ceramic layer to provide a thermal break between the hot combustion gases and the underlying alloys [5, 6].

The next part of the TBC system is the bond coat which is a metallic coating that is directly applied over the superalloy. As mentioned in the previous paragraph, it provides the superalloys with oxidation and corrosion protection from the combustion gases. It also helps bonds the ceramic TBC to the alloy substrate, hence the name “bond coat.” In general, the bond coat has a similar coefficient of thermal expansion (CTE) to that of the substrate and will also be of similar chemical composition (not the same). The oxidation resistance they provide to the superalloy is a result of selective oxidation. Selective oxidation is the process by which one element in the bond coat is selectively oxidized leaving the other elements (parent elements) otherwise unaffected. For the sake of oxidation protection, the selectively oxidized element should form a continuous slow growing oxide at the surface of the alloy which then prevents the other elements in the coating from oxidizing. There are both thermodynamic and kinetic stipulations that must be fulfilled in order to form a continuous external oxide scale.

The first thermodynamic requirement for a particular element to be selectively oxidized is the standard free energy of formation of its oxide counterpart must be negative, meaning the reaction will occur spontaneously towards the direction of the products (oxide). The second requirement is the standard free energy of formation of the solute element oxide must be more negative than the standard free energy of formation of the parent or base oxide. Thermodynamically speaking, this ensures the solute element will oxidize instead of the parent element. Ellingham diagrams are a useful tool in this matter as they graphically show the

standard free energy of formation of an oxide (per mole O<sub>2</sub>) as a function of temperature for several different elements. Figure 1 shows one such diagram.

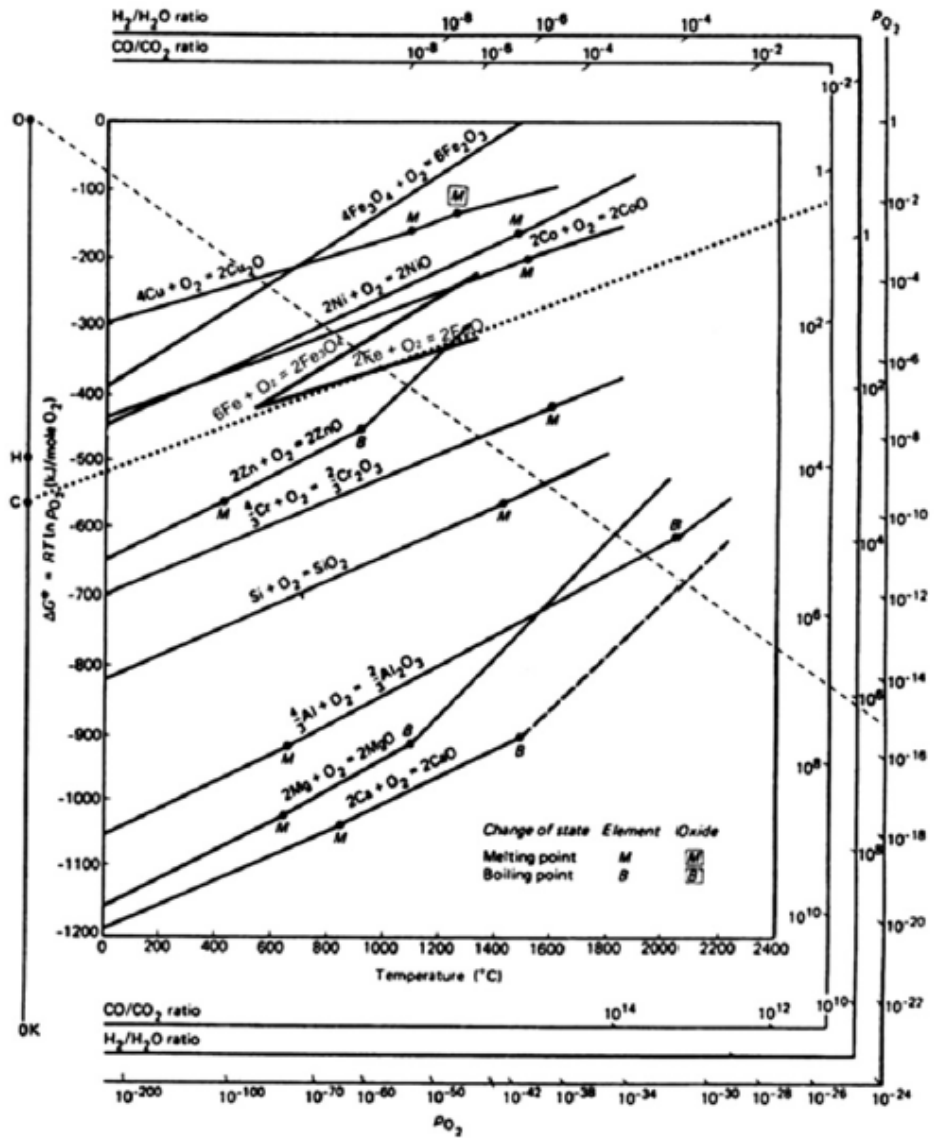


Figure 1 - Standard free energy of formation of a number of oxides as a function of temperature [6].

The position of an oxide on this graph indicates its relative stability as compared to other oxides, where the lower the oxide on the graph, the more negative the free energy of formation and the more stable the oxide. So if the solute element's oxide is below the parent element(s)'s oxide, the second thermodynamic stipulation is fulfilled [5].

The kinetic requirements for successful selective oxidation, which is defined as the formation of a slow growing protective continuous outer scale, center on the ability of the alloy to supply the oxide/alloy interface with enough solute element to: 1) sustain the exclusive growth of the solute oxide and 2) form a continuous external solute oxide (i.e. prevent internal oxidation of the solute element) [5]. Kinetic analysis performed by Wagner yielded two equations that detail the alloy parameters needed to fulfill these requirements [9, 10]. To sustain the exclusive growth of the solute oxide, Equation 2 must be satisfied:

**Equation 2**

$$N_{B(\min)}^{(o)} \geq \frac{2V_m}{V_{ox}} \left( \frac{k_p}{D_B} \right)^{\frac{1}{2}}$$

Where  $N_{B(\min)}$  is the minimum critical concentration of solute element (given the subscript 'B'),  $V_m$  is the molar volume of the metal alloy,  $V_{ox}$  is the molar volume of the oxide,  $D_B$  is the diffusivity of B in the alloy and  $k_p$  is the reaction product for the formation of the solute oxide. The parameters for the second kinetic requirement of ensuring a continuous external oxide scale are detailed in Equation 3:

$$N_B^{(o)} > \left[ \frac{\pi g^*}{2v} N_O^{(s)} \frac{D_O V_m}{D_B V_{ox}} \right]^{\frac{1}{2}}$$

$N_B$  is again the critical concentration needed to form an external oxide,  $g^*$  is the critical volume fraction of oxide needed to transition from internal oxidation to external oxidation ( $g^* \approx 0.3$ ),  $v$  is the stoichiometric coefficient of the oxide,  $D_O$  and  $D_B$  are the diffusivities of oxygen and solute element B in the alloy (respectively), and  $N_O$  is the oxygen solubility in the metal alloy. These two equations lay the framework for the theory of selective oxidation and were used in the design of the protective coatings used in industry today.

Protective coatings used today either utilize aluminum, chromium or silicon to form a protective oxide on the surface. These elements are chosen because they form relatively adherent, slow growing protective scales. At the temperatures TBCs are used at, alumina is the preferred oxide as its growth rate is much less than chromia and it has better thermal shock resistance than silica scales [5]. For this reason, most all bond coats utilize aluminum to form the external scale. The formation of the alumina scale is a major step during the operation of the TBC system. This layer is known as the thermally grown oxide (TGO) and its thickness will increase with increased exposure time [11].

The final layer of the TBC system is the ceramic topcoat. There has been, and still is, a search for new ceramic materials for this layer. However yttria stabilized zirconia (YSZ) remains the dominant choice for this application. This material has high temperature phase stability, high toughness, low thermal conductivity, and an acceptable CTE that is similar to the other layers thereby reducing thermal strain mismatch. Air plasma spraying (APS) and electron beam physical vapor deposition (EBPVD) are the two main topcoat deposition techniques. The

main role of the topcoat is to insulate the underlying layers from high temperatures by effectively producing a thermal gradient between the exposed top surface and the bond coat/topcoat interface. While the topcoat acts as a thermal barrier it does not provide any oxidation resistance (other than by lowering the bond coat temperature) because TBCs are highly porous and, in the case of YSZ, completely transparent to oxygen and other gas permeation [12].

## **2.2 TOPCOAT PARAMETERS: INFLUENCE ON TBC LIFETIME**

### **2.2.1 Influence of Topcoat Microstructure**

Air plasma spraying is a very versatile coating deposition method for TBC topcoats, which are the focus of this research. By carefully controlling the temperature and velocity distribution of the plasma particles during deposition along with the substrate deposition conditions, a wide variety of topcoat microstructures can be produced. However, controlling all of these parameters is a complex process, especially in an industrial setting. Parameters such as torch power, torch transverse speed, stand-off distance, powder feed rate, powder type (fused and crushed versus plasma-densified hollow sphered versus agglomerated and sintered), powder size distribution, carrier gas flow rate and primary and secondary gas flow rate [13-15] all control the plasma characteristics which ultimately control the resultant microstructure. Similarly substrate deposition conditions such as spray angle, substrate temperature and torch dwell time also dictate the resultant topcoat [13-15]. The exact influence of each parameter on the microstructure is beyond the scope of this study and instead focus will be directed towards the variety of microstructures and microstructural features which can be produced.

As the YSZ powder is injected into the plasma flame it is melted and accelerated towards the substrate. Upon impact, the molten (sometimes partially molten) particles flatten out and rapidly solidify and cool to form splats which are the building elements of a plasma sprayed coating [14]. The shape and thickness of each splat along with the interactions between successive splats (adherence, build-up rate) and between the substrate and the splats (i.e. cooling rate, angle of impact and temperature drop) all influence the microstructure.

Besides the layered splat structure, the first microstructural feature indicative of plasma sprayed TBCs are globular pores which form as a result of incomplete filling/coverage during the spraying process. These pores are quite large and on the order of 15  $\mu\text{m}$  [14] or larger and because of their size, can account for a majority of the overall porosity of the coating. These pores are shown in Figure 2 and pointed out by the black arrows.

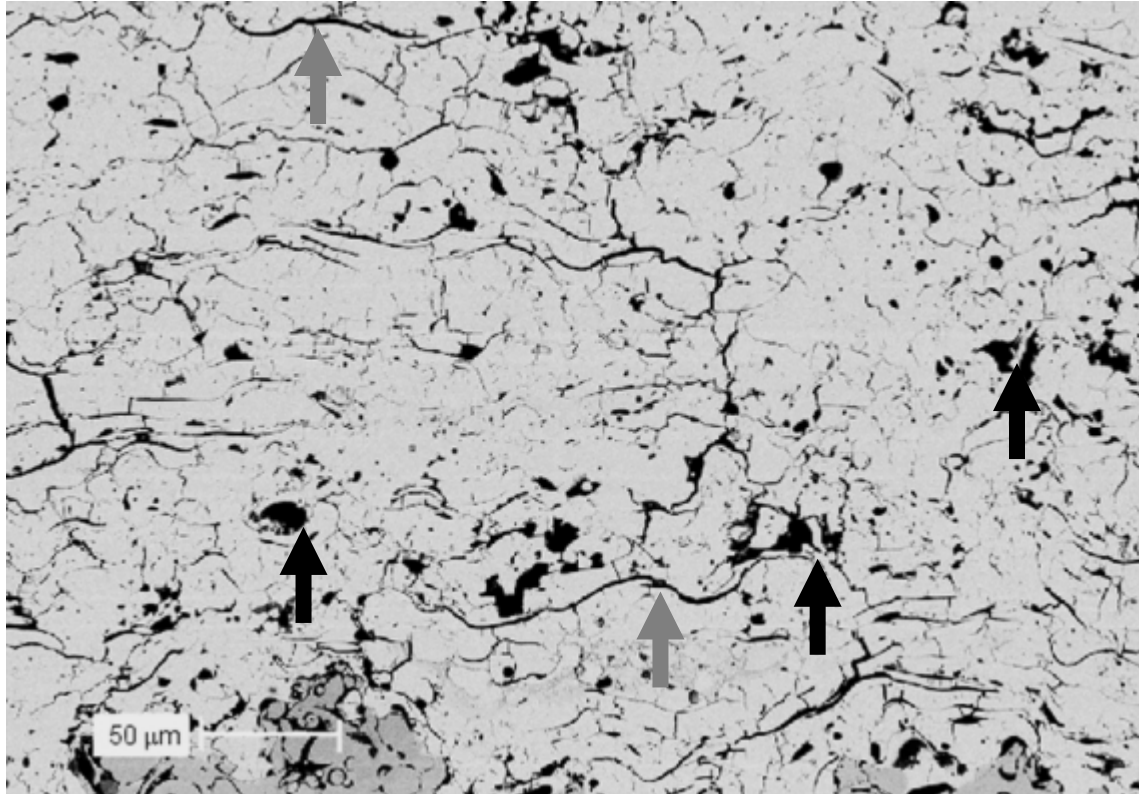


**Figure 2 - APS TBC containing large globular pores (black arrows) and horizontal delaminations (gray arrows) [14].**

Moving down in scale are microcracks which come in both the vertical and the horizontal types. Horizontal microcracks, defined as cracks parallel to the substrate surface, are defined to range in size from  $0.02\ \mu\text{m}$  to  $15\ \mu\text{m}$  [14]. The very fine pores form as a result of small gas pockets being entrapped in the coating during spraying (Figure 3 gray arrows) while the larger horizontal microcracks are formed when the splats solidify, contract, then buckle up/pull away from the underlying layers (Figure 3 white arrows) [14-17]. Larger horizontal cracks, which span numerous splats, are referred to as delaminations (Figure 2 gray arrows) [14].

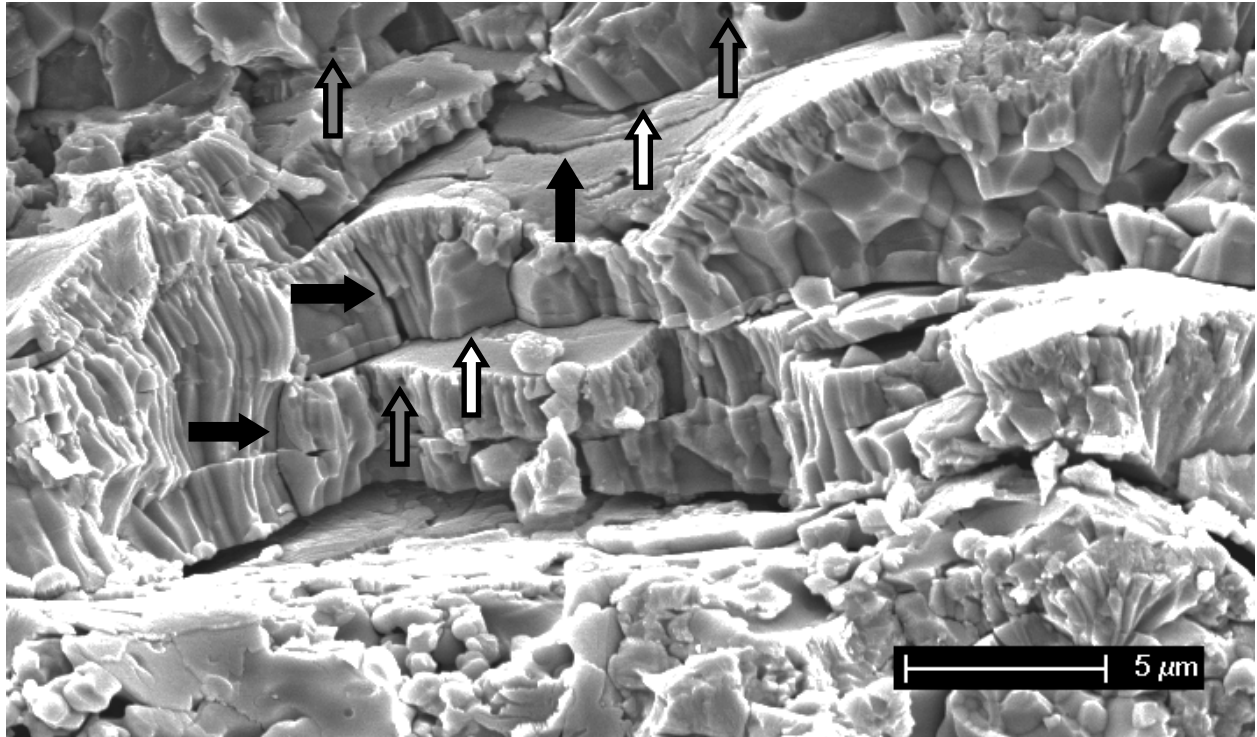


**Figure 3 - Fracture section of an APS topcoat. White arrows indicate horizontal microcracks, the gray arrows point out pores from gas being trapped and the black arrows indicate vertical microcracks.**

The vertical microcracks (Figure 3 black arrows) are perpendicular to the substrate surface and they form when a splat bonds to the substrate, solidifies and begins to cool down to the temperature of the substrate. As the splat cools it will try to contract in the lateral direction, however since a bond has already been established to the underlying layer, it is not free to move which, if the stresses are high enough, results in the formation of vertical stress relief cracks [14, 17]. Furthermore, this vertical cracking behavior can be controlled and enhanced to produce coatings which have large cracks that span multiple splats or span 10%-100% of the entire coating thickness. These large cracks are often referred to as segmentation cracks [18] and are depicted in Figure 4.

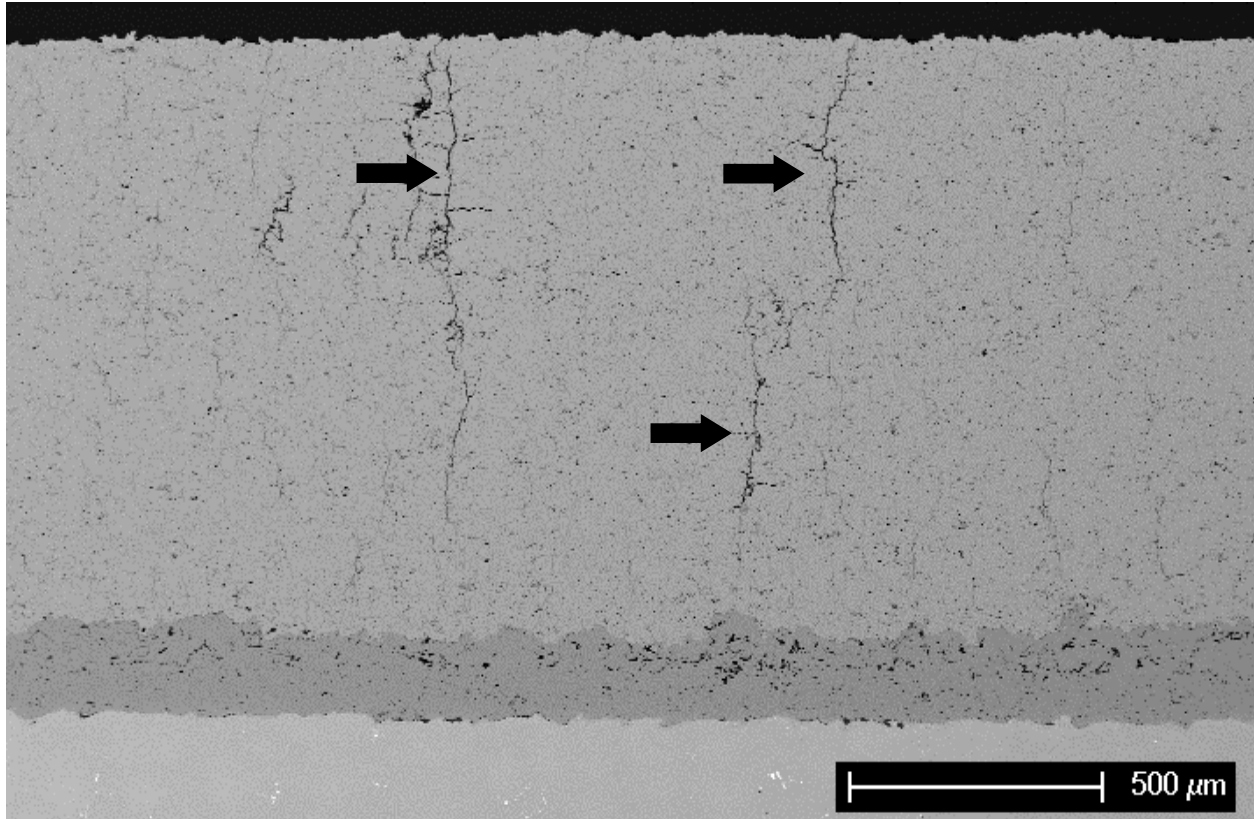


**Figure 4 - APS TBC that contains vertical segmentation cracks.**

As with all materials, the physical and thermal properties (thermophysical) of the bulk material are controlled by the material's microstructure. The same relationship is found in these plasma sprayed topcoats where all of the features described above control critical thermophysical properties such as thermal conductivity and elastic modulus and also influence the thermal cycling performance of the TBC.

As the name indicates, the primary role of the thermal barrier coating is to provide thermal insulation to the metallic bond coat and substrate. Fully dense yttria stabilized zirconia (YSZ), which is the dominate choice of materials for TBC topcoats, has a thermal conductivity of 2.5 W-m-1K-1 at room temperature and 2.0 W-m-1K-1 at high temperature [16]. Compared to the bond coat and the substrate alloys, which have thermal conductivities around 10 W-m-1K-1

[19], this is quite low, but further reductions are achieved through the incorporation of the above mentioned microstructural features. In particular, globular pores, horizontal microcracks and horizontal delaminations, which are both oriented perpendicular to the heat flow direction, can reduce the thermal conductivity well below the bulk value. This is accomplished through a combination of radiative heat scattering by the high volume density of pore and crack interfaces, gas-phase conduction through the larger pores (which is orders of magnitude lower than through solids) and Knudsen heat transfer through the submicron pores [16]. The other features like the vertical cracks and the grain boundaries within the splats also aid in scattering the radiative heat, further reducing the conductivity, but to a much lesser degree. All combined, the thermal conductivity of a plasma sprayed 7-8wt% YSZ topcoat can reach as low as  $\sim 0.9 - 1.0 \text{ W}\cdot\text{m}^{-1}\text{K}^{-1}$  [13, 16, 20, 21] at room temperature for an as-sprayed, porous, defect-filled coatings. For denser coatings, similar to the coating in Figure 4, which have vertical segmentation cracks but fewer horizontal microcracks (which is a consequence of the spraying process), the thermal conductivity is higher and closer to that of an EBPVD coating which is around  $\sim 1.4 - 1.6 \text{ W}\cdot\text{m}^{-1}\text{K}^{-1}$  [13, 16, 21, 22].

Since this property is dependent on the microstructure, if any changes occur to the structure so too will the thermal conductivity change. In particular, experimental observations have shown when these coatings are exposed to high temperatures ( $>1000^\circ\text{C}$ ) the thermal conductivity rapidly increases. This is a result of sintering where the fine pores and horizontal micro-pores in the coating begin to heal and form bridges /necks over the individual splat boundaries. The magnitude of this increase depends on the extent of the sintering process which in turn is heavily dependent on the starting microstructure, coating purity and pore size

distribution, not just the overall amount of porosity, which can be a misleading indicator of thermal conductivity and other thermophysical properties [16].

Likewise, the elastic modulus is heavily depended on the microstructure. Ideally the topcoat should be compliant, to accommodate the thermal strain mismatch between the three layers of the TBC, and it should also be tough, to avoid excessive erosion during service caused by foreign object damage (FOD). The microcracks within the coatings and the splat boundaries aid in the compliance, allowing for splat sliding and microcrack opening [23, 24]. Again though, after high temperature exposure, as the small cracks heal and the splats bridge, this compliance will decrease and the coating will become stiffer. Here, vertical segmentation cracks are beneficial because they can maintain this compliance during exposure since these cracks are much larger and less susceptible to permanent closure. The tradeoff being, at least in APS topcoats that the deposition parameters used to produce these large segmentation cracks also produce a denser structure which has a larger thermal conductivity. Ultimately, there is a trade-off between high thermal conductivity, tough, compliant coatings and low thermal conductivity stiff coatings which are susceptible to high erosion rates. Thus future coating design must find a balance between the two.

### **2.2.2 Influence of YSZ Purity**

The powder used for YSZ TBC always contains some level of impurities. Typical impurities in zirconia and yttria powders are titania, silica, and alumina. The effects of these impurities on microstructural behavior and TBC lifetime behavior have been studied in previous works [25-30]. Miller *et al* examined the effect of varying the silica content of a 7wt% YSZ plasma sprayed coating in a burner rig test [27]. The results are shown in Figure 5.

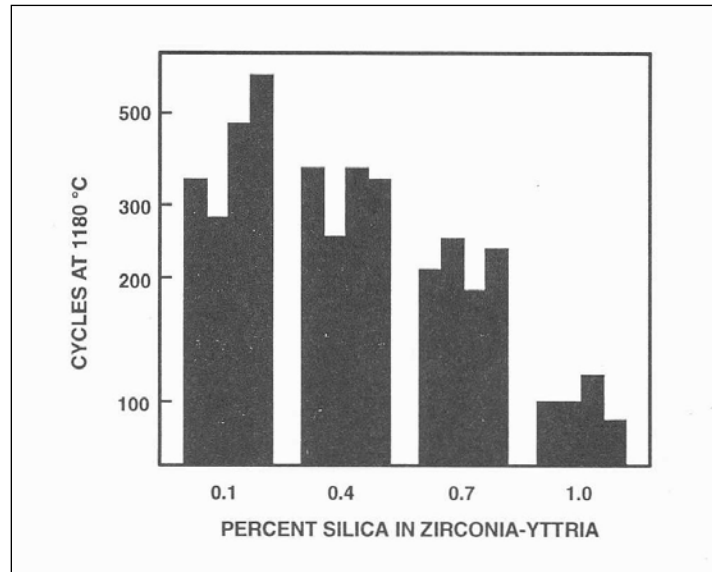


**Figure 5 - Burner rig life versus percent silica [27].**

This plot indicates as the silica content in the coating increases, the lifetime of the TBC system decreases. The difference in the coating lifetime was simply attributed to the increased silica contents without any direct speculation as to the physical reason behind this finding [26]. Another study by Vaßen et al examined the sintering behavior of plasma sprayed TBCs with varying impurity contents of alumina, silica, and titania [30]. They performed high temperature anneals of free standing coatings at 1200°C and measured the changes in length as a function of time and calculated the mean shrinkage rates. A plot of the mean shrinkage rate as a function of impurity content is shown in Figure 6.

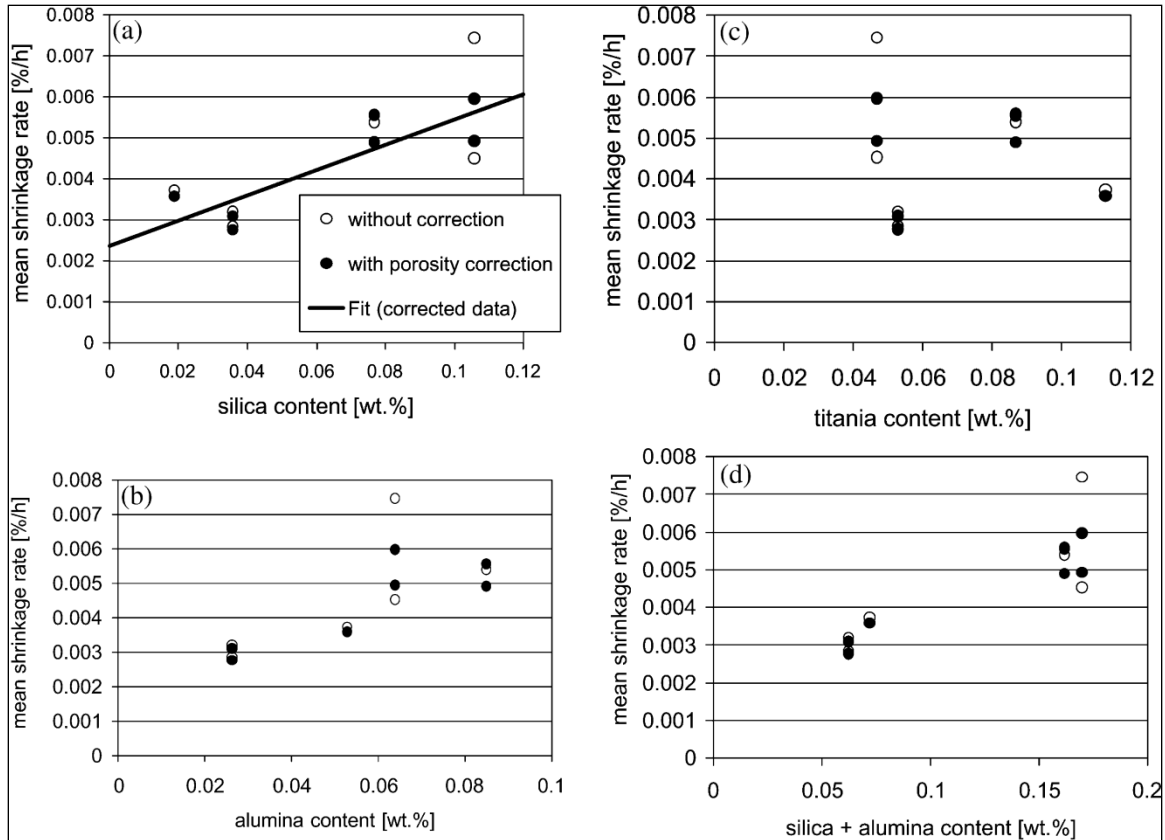


**Figure 6 - Influence of: a.) silica; b.) alumina; c.) titania; and d.) silica & alumina content on the mean shrinkage at 1200°C within the first 60hr [30].**

From their experiments they concluded alumina and silica both contributed to the shrinkage of the coatings as shown by Figure 6a, c, and d. They also concluded, through extrapolation, that reducing the impurity content to the zero-impurity point will still result in a significant sintering rate. Therefore, further efforts to decrease the impurity content below a certain level, say 0.02wt%, would have no more significant effect on the properties of these coatings than keeping the impurity content at a modest level [30]. Paul *et al* [28] found similar results in their work and they hypothesize the sintering of these coatings was a result of splats chemically bonding and small pores healing which combined cause the stiffness and elastic modulus of the coatings to increase. Eaton and Novak [25] also reported that an increase in  $\text{SiO}_2$

content of plasma sprayed TBCs from 0.2wt% to 4.0wt% caused a five fold increase in the percent shrinkage after 24hrs at 2600°F (1427°C) as seen in the right hand plot in Figure 7.

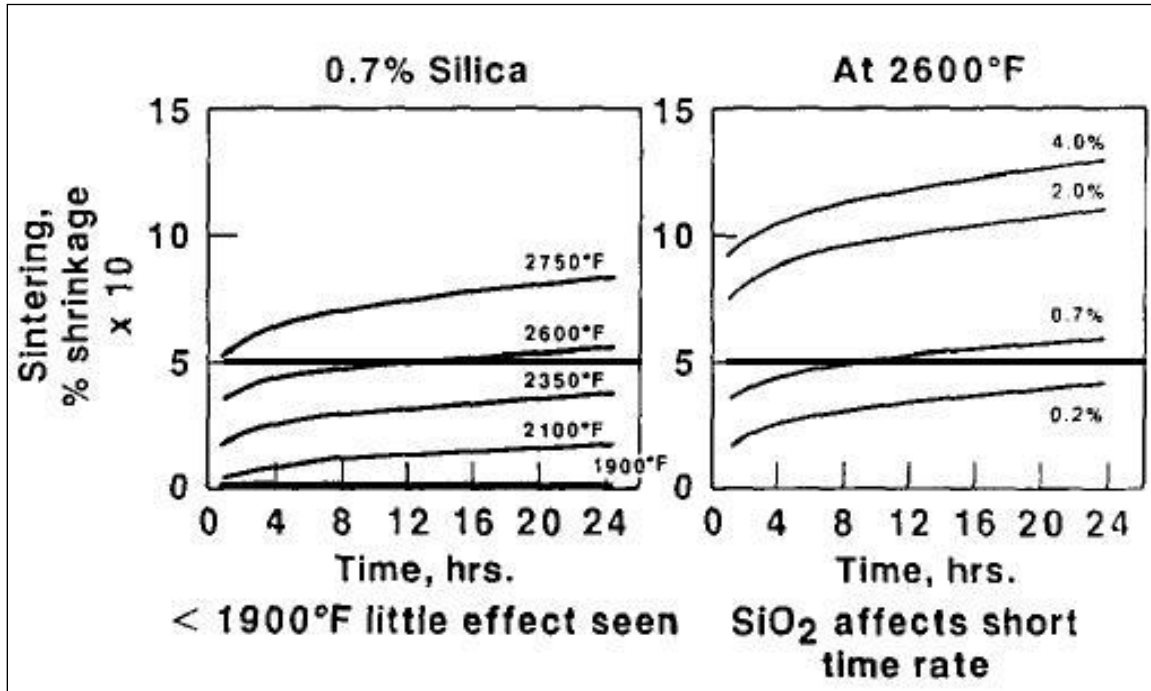


Figure 7 - The effect of time, temperature, and impurity level on shrinkage [25].

This plot also indicates that SiO<sub>2</sub> content affects the short term sintering behavior of the plasma sprayed coatings, where the 4.0wt% coatings show rapid shrinkage after this short amount of time. They too propose the SiO<sub>2</sub> impurities (and other impurities like Na<sub>2</sub>O, CaO, and Al<sub>2</sub>O<sub>3</sub>) cause rapid bridging between splats, which then stiffens the entire coating [25]. As the elastic modulus of the topcoat increases, the strain tolerance decreases and the coating becomes much more susceptible to spallation.

Along with a decrease in toughness, the accelerated healing of microcracks and splat pores in the coatings caused by these impurities also causes the through thickness thermal

conductivity to increase. This is undesired as the function of the TBC is to provide thermal protection which is negated by increasing the thermal conductivity. Paul *et al* observed this rise in conductivity as the level of alumina and silica increased, which can be observed in Figure 8 [28]. Note the almost identical values of thermal conductivity at the start of the test for all three specimens.

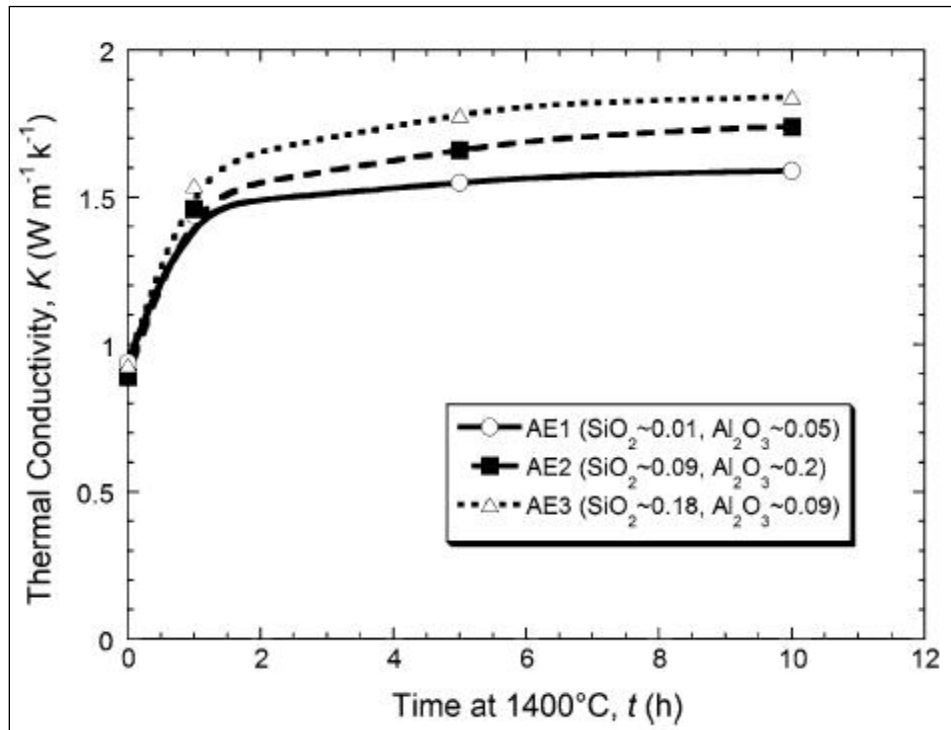


Figure 8 - Through thickness thermal conductivity as a function of time spent at 1400°C [28].

A study of the phase stability of plasma sprayed TBCs with different levels of SiO<sub>2</sub> and Al<sub>2</sub>O<sub>3</sub> content was performed by Tsipas [31]. Plasma sprayed TBCs were prepared using different purity powders and then heat treated at temperatures between 1200°C and 1400°C. Slow scan XRD was then performed in the regions of the 27-32° 2θ-angle to detect any monoclinic phase and then also at 72-75° 2θ-angle to resolve the amount of cubic and tetragonal

phases present. She found as the impurity content increased, the rate of decomposition of the metastable tetragonal phase, which is the primary phase present after spraying of the coatings, to the equilibrium tetragonal and cubic phases was reduced. Generally, the decomposition reaction is undesired because there is a volume increase (4%) associated with the tetragonal to monoclinic phase change which occurs upon cooling from elevated temperatures to room temperature. From Tsipas' findings, it would seem beneficial to have silica and alumina present to slow the rate of the decomposition reaction.

As indicated above, there has been an extensive amount of work identifying the differences in the sintering rate, the thermal conductivity, and the elastic modulus of TBCs with varying purity levels, however, the microstructural evidence and backing often is missing from these published studies. Characterization of the starting microstructures and identifying the location(s) of the impurities is not well documented yet there is significant speculation as to where these impurities are and the role they are playing in the sintering process.

### **2.2.3 Influence of Topcoat Thickness**

One way to accommodate higher operating temperatures is to make the YSZ topcoats thicker, providing the bond coat and substrate with more thermal protection. However, this simple relationship between thermal protection and thickness is not so straight forward. There are several complicating factors that accompany changes in the thickness of the TBC.

The first of these complicating factors is the change in surface temperature caused by the increase in the thickness of the TBC. A free-body temperature diagram for a simplified TBC system is shown in Figure 9.

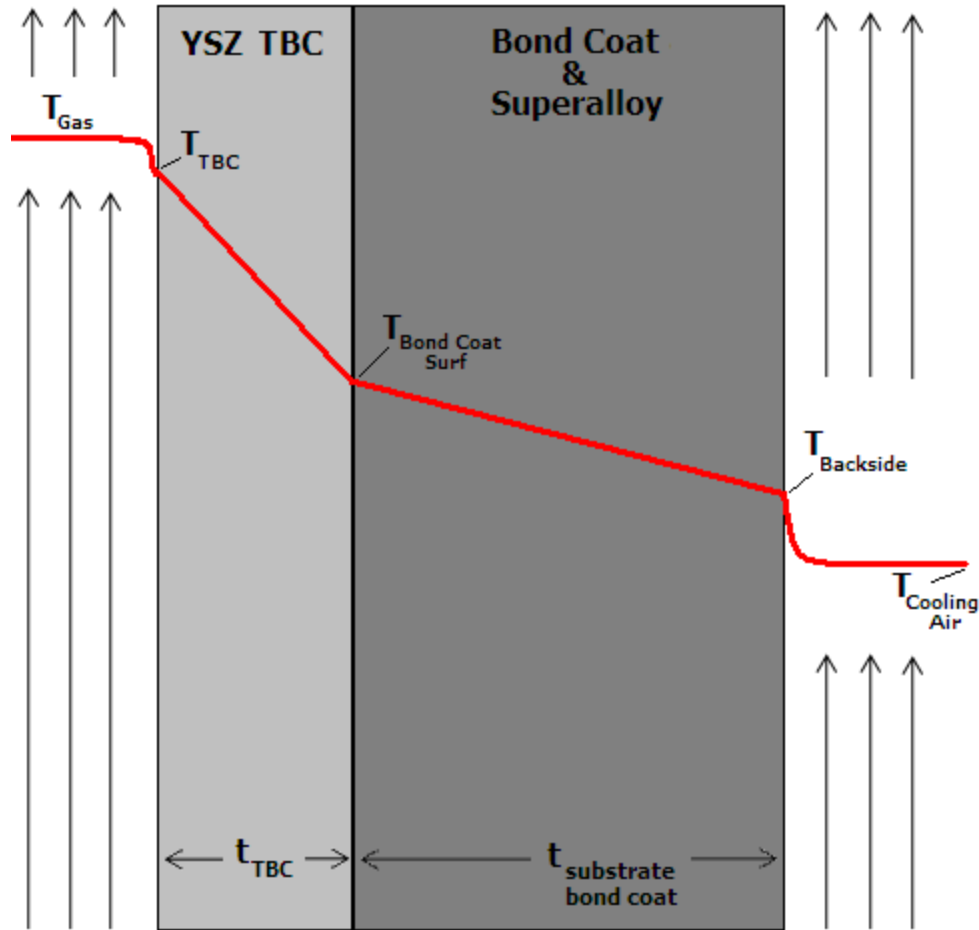


**Figure 9 - Temperature distribution in a TBC system exposed to hot combustion gases on one side and cooling air on the other.**

For the sake of simplifying the analysis, the TBC system is treated as a plane wall and radiation heat transfer from the gases is neglected. It is assumed that the combustion gas temperature and convective heat transfer coefficient are constant, regardless of TBC thickness. Likewise, as with modern turbine engines, cooling air is provided to the back of the superalloy substrate which will also be assumed to have a constant gas temperature and heat convection transfer coefficient. In this diagram the bond coat and superalloy are treated as one layer, as their thermal conductivities are almost identical. Finally, the interfacial thermal resistance between the TBC and the bond coat is assumed to be zero. Given these assumptions, a steady-state

temperature profile can be calculated for TBC systems with varying TBC thickness. The overall heat flux per unit area through the TBC system can be calculated using Equation 4:

**Equation 4**

$$\frac{q_x}{A} = \frac{T_{gas} - T_{cooling\ air}}{\left[ \frac{1}{h_{gas}} + \frac{t_{TBC}}{\kappa_{TBC}} + \frac{t_{sub/bc}}{\kappa_{sub/bc}} + \frac{1}{h_{cooling\ air}} \right]}$$

Where  $h_{gas}$ ,  $h_{cooling\ air}$ ,  $T_{gas}$  and  $T_{cooling\ air}$  are the convective heat transfer coefficients and temperatures of the combustion gases and cooling air respectively,  $\kappa_{TBC}$ ,  $\kappa_{sub/bc}$ ,  $t_{TBC}$  and  $t_{sub/bc}$  are the thermal conductivities and thicknesses of the TBC and substrate/bond coat respectively, and  $q_x/A$  is the heat flux per unit area. This heat flux can then be equated with each of heat fluxes through the surfaces of interest which are the TBC surface temperature ( $T_{TBC}$ ), bond coat surface temperature ( $T_{BC\_Surf}$ ) and backside superalloy temperature ( $T_{backside}$ ). The equation for  $T_{TBC}$  is given in Equation 5:

**Equation 5**

$$T_{TBC} = T_{gas} - h_{gas} \left( \frac{T_{gas} - T_{cooling\ air}}{\frac{1}{h_{gas}} + \frac{t_{TBC}}{\kappa_{TBC}} + \frac{t_{sub/bc}}{\kappa_{sub/bc}} + \frac{1}{h_{cooling\ air}}} \right)$$

Equations similar to the one above can be used to calculate  $T_{BC/Surf}$  and  $T_{backside}$ . Values for the variables in this equation are listed in Table 1 and the resultant temperature profiles are shown in Figure 10.

**Table 1 - Parameters for temperature calculations [19].**

$h_{\text{gas}}$ (W/m <sup>2</sup> -K)	$h_{\text{cooling air}}$ (W/m <sup>2</sup> -K)	$T_{\text{gas}}$ (°C)	$T_{\text{cooling air}}$ (°C)	$t_{\text{TBC}}$ (mm)	$t_{\text{sub/bc}}$ (mm)	$\kappa_{\text{TBC}}$ (W/m-K)	$\kappa_{\text{sub/bc}}$ (W/m-K)
1000	500	1600	227	variable	5	1.75	24

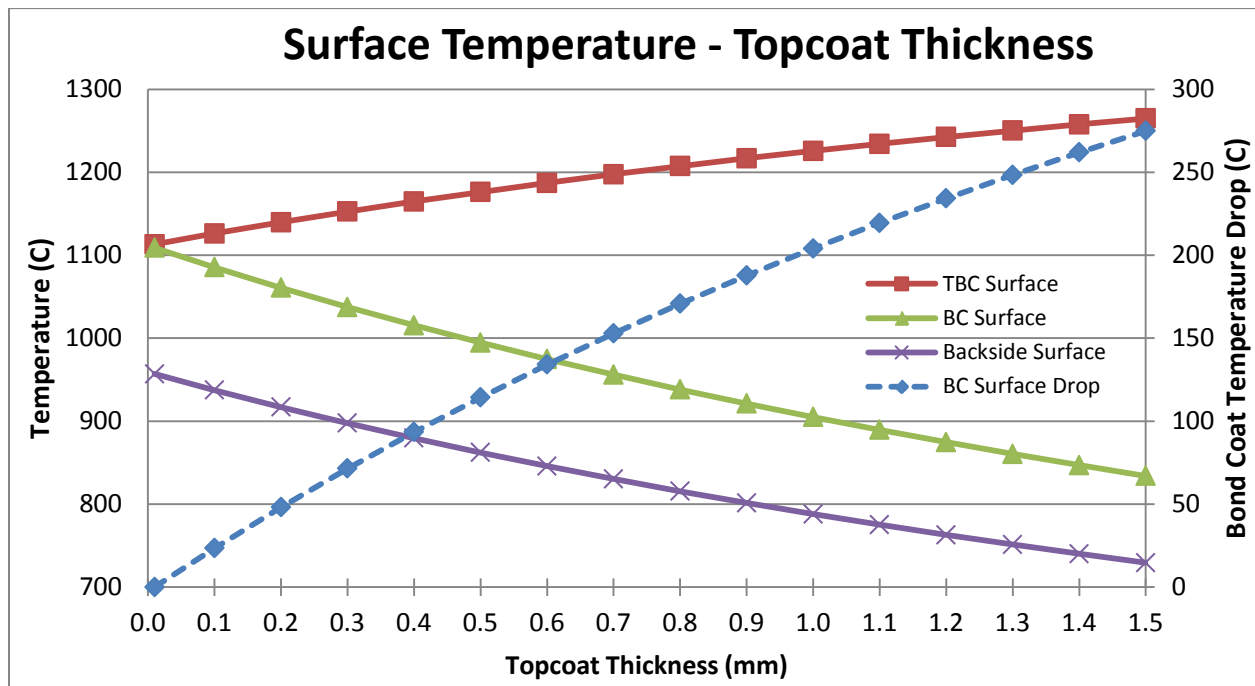


**Figure 10 - Temperature profiles as a function of topcoat thickness.**

Based on these calculations, the surface temperature of the TBC increases with increasing TBC thickness as shown by the red line in the plot above. This is a result of the heat buildup at the surface due to the increasing quantity of the low thermal conductivity YSZ. At the same time though, the bond coat surface temperature drops so the extra thickness is reducing the surface temperature, but at the expense of the TBC surface temperature. This was confirmed experimentally in previous work where TBC disc specimens with different thickness topcoats

were prepared and exposed to an oxy-propylene torch [2]. The front TBC surface temperature and the back substrate temperature were recorded and are shown in Figure 11.

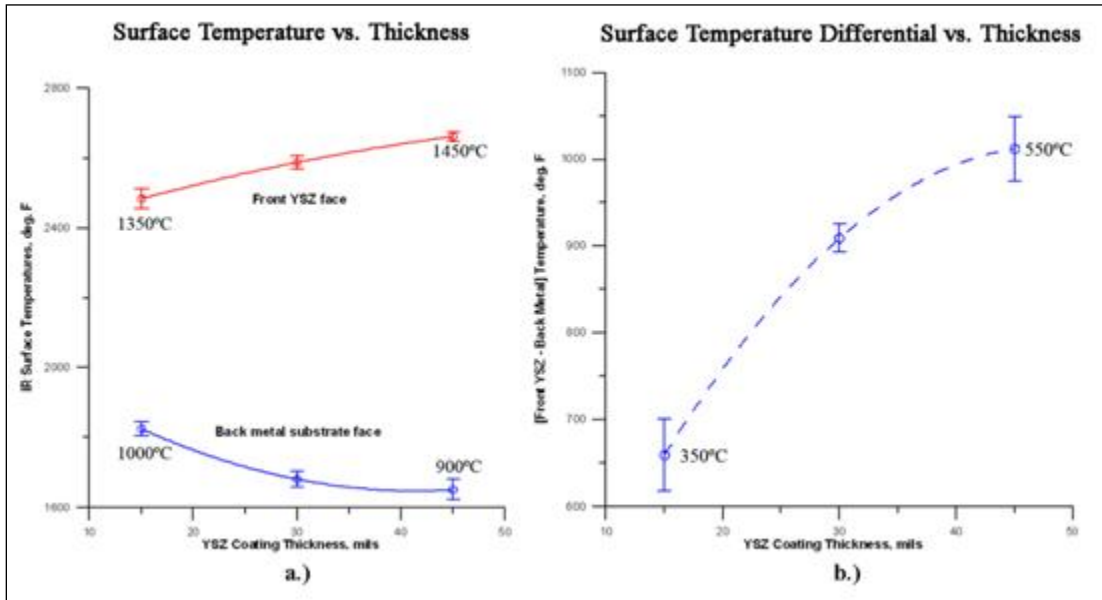


**Figure 11 - a.) Surface temperature as a function of TBC thickness and b.) the front and back face temperature drop as a function of TC thickness.**

Again the thicker topcoats provide more insulation as shown by the lower substrate temperature (blue line in Figure 11a) but they also drove up the surface temperature (red line in Figure 11a) creating larger thermal gradients between the TBC free surface and the underlying substrate alloy (Figure 11b). Larger thermal gradients translate into larger thermal stresses within the TBC and higher TBC surface temperatures lead to faster sintering rates which affect physical properties such as elastic modulus and thermal conductivity.

The second complicating factor is the TBC thickness influences the thermal stress in the TBC, which arise due to coefficient of thermal expansion mismatch between the layers of a TBC system. This in turn also influences the strain energy release rate of the TBC.

Thermal stresses develop in the TBC during heating and cooling of the TBC system from the operating temperatures down to ambient temperatures. Analysis of the thermal stresses in a bimaterial strip subjected to a temperature change was first performed by Timoshenko which was then modified to analyze the stresses that develop in an oxide layer, which grew on a metallic substrate, upon cooling by Birks et al [5, 32]. Since the TBC is similar to an oxide layer on a metallic substrate, Equation 6 will be used to describe the thermal stress that forms in the TBC as a result of cooling from elevated temperatures, where the TBC was assumed to be stress-free.

**Equation 6**

$$\sigma_{thermal} = \frac{(\alpha_{metal} - \alpha_{tbc})(T_{RT} - T_{HT})}{\frac{t_{tbc}(1 - \nu_{metal})}{t_{metal}E_{metal}} + \frac{(1 - \nu_{tbc})}{E_{tbc}}}$$

Here  $\alpha_{metal}$ ,  $\alpha_{tbc}$ ,  $\nu_{metal}$ ,  $\nu_{tbc}$ ,  $t_{metal}$ ,  $t_{tbc}$ ,  $E_{metal}$  and  $E_{tbc}$  are the coefficients of thermal expansion, Poisson's ratios, thicknesses and elastic moduli of the metal and TBC layers respectively,  $T_{RT}$  and  $T_{HT}$  are the room temperature and high temperature temperatures the system is being cooled between, and  $\sigma_{thermal}$  is the resulting residual stress in the TBC. For thin TBCs the first term in the denominator can be neglected as the thickness of the TBC compared to the thickness of the metal is much less than unity so its contribution in the denominator is minimal. However, as the thickness of the TBC increases, this will not hold and the TBC thickness can no longer be neglected. When the TBC thickness is taken into consideration the thermal stress decreases slightly depending on the ratio of the thicknesses and of the elastic moduli of the two layers. Continuing on, the stored elastic strain energy in the TBC is a function

of the residual stress in the coating and the volume of the TBC. Furthermore, the stored elastic energy per unit area of TBC/bond coat interface is given by Equation 7.

Equation 7

$$U_e = \frac{(1 - \nu_{tbc})}{E_{tbc}} \sigma_{thermal}^2 t_{tbc}$$

Here,  $U_e$  is the stored elastic strain energy per unit area. Combining Equation 6 and Equation 7, the stored elastic energy can be computed to see how it varies as a function of TBC thickness, which is plotted in Figure 12. Values for the coefficients in the two equations are listed in Table 2.

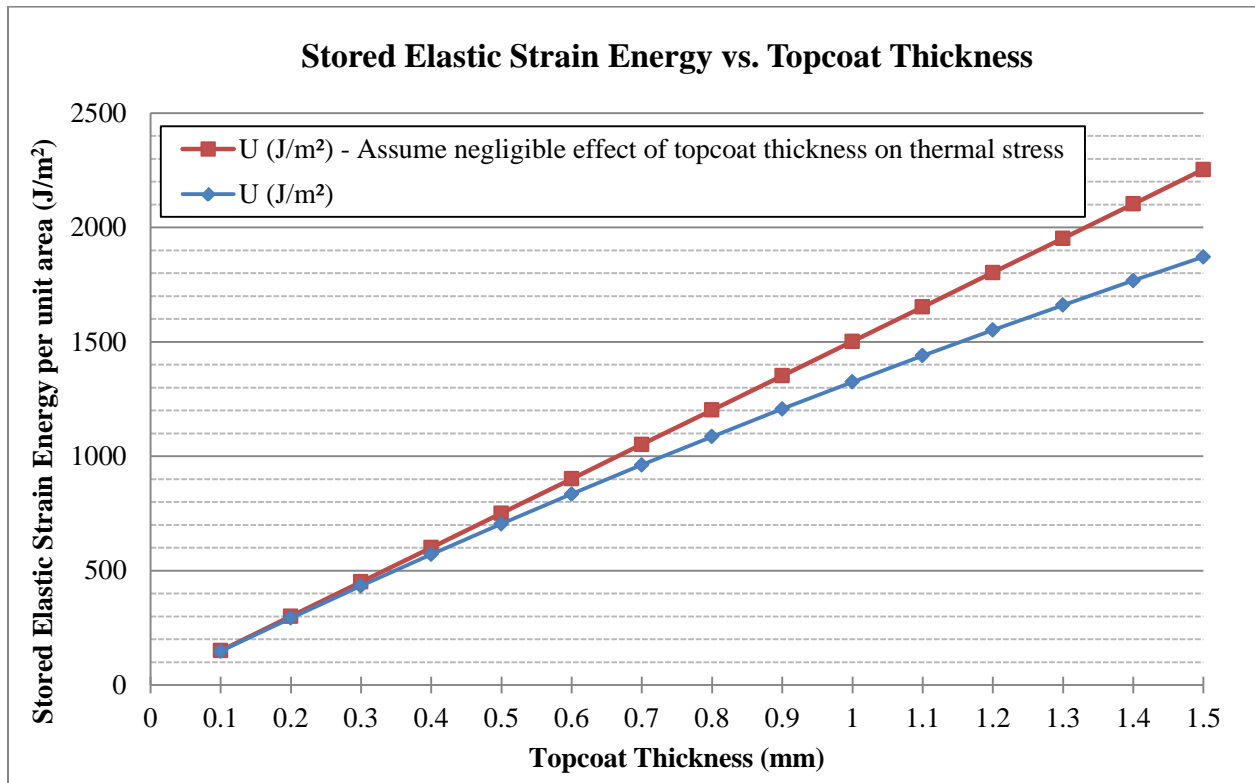


Figure 12 – The stored elastic strain energy per unit area as a function of topcoat thickness.

**Table 2 - Parameters for strain energy calculation [33].**

$v_{tbc}$	$v_{metal}$	$E_{tbc}$ (GPa)	$E_{metal}$ (GPa)	$\alpha_{tbc}$ ( $10^{-6}/K$ )	$\alpha_{metal}$ ( $10^{-6}/K$ )	$T_{rt}-T_{ht}$
0.1	0.3	50	200	11.1	17.1	-1075

The stored elastic strain energy in the TBC increases as the thickness increases as shown by the red and blue lines in Figure 12. The blue line shows the variation of the stored energy when the thickness of the TBC is taken into consideration when calculating the thermal stresses and the red line shows the variation when the thermal stresses in the TBC are assumed to be independent of TBC thickness. The difference between the two cases increases with increasing thickness, but the general relationship between stored strain energy and TBC thickness is the same for both cases.

Since the stress intensity factor at a crack tip ( $K$ ) is proportional to the square root of the stored elastic strain energy, as the TBC thickness increases so does the stress intensity factor, which is the driving force for crack propagation. For a topcoat with a given critical toughness,  $K_c$ , which is material property assumed to be independent of TBC thickness, once the stress intensity factor induced by the thermal stresses surpasses the critical toughness, crack propagation can occur. For these reasons, thick topcoats have failed due to spalling, cracking, and chipping within the TBC layer, whereas thinner TBCs, exposed to the same conditions, have failed after a significantly longer amount of time and due to bond coat oxidation related reasons. Previous work supports the trend that failure within the TBC layer occurs well before failure due to bond coat oxidation [2, 34]. Cross-sectional images of these two types of failure are shown in Figure 13.

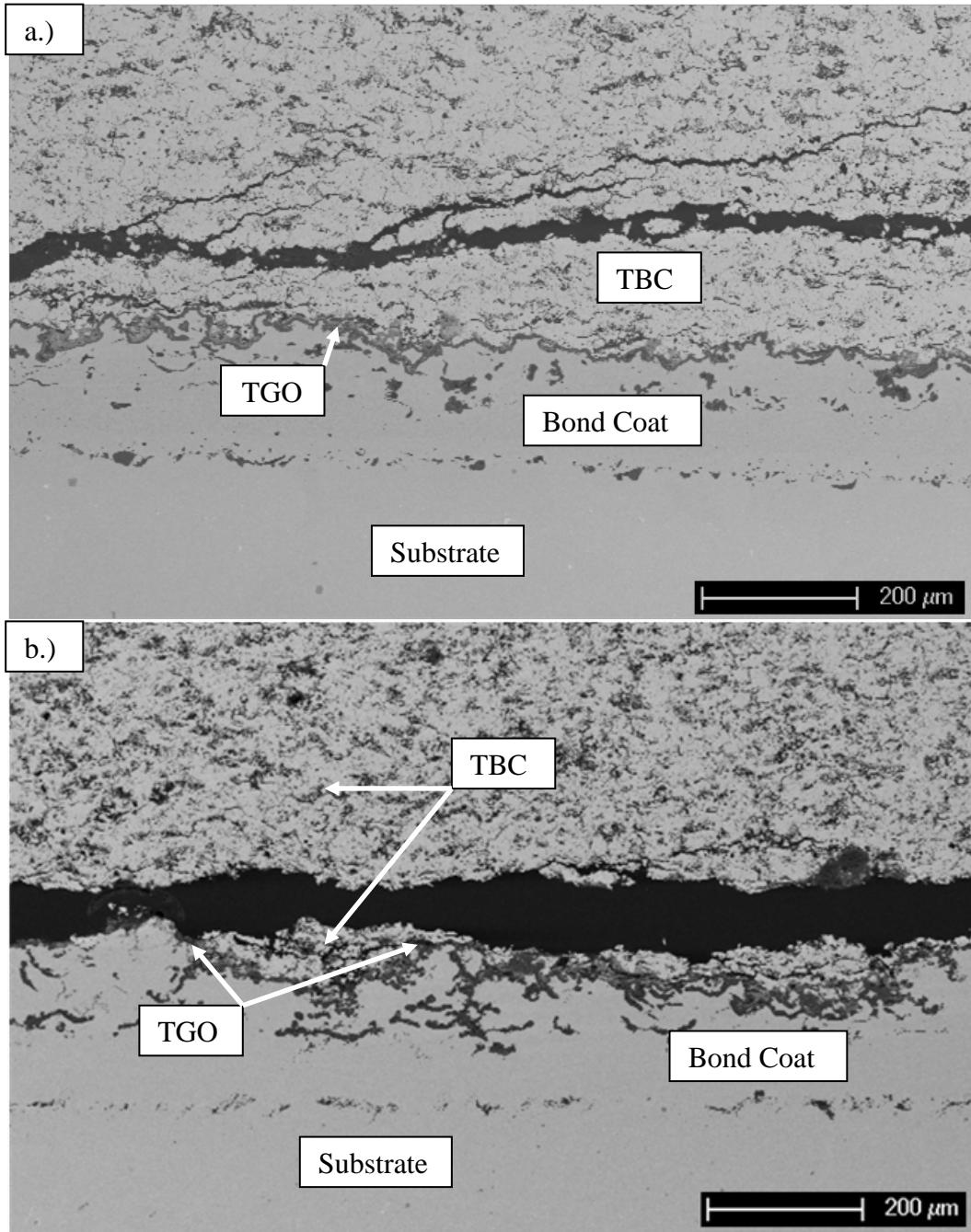


**Figure 13 - Cross-sectional micrographs of failures of a) 1.1mm and b) 0.75mm TBC failures. The TBC in a) failed after 20 thermal cycles and b) failed after 140 thermal cycles in a bottom-loading furnace. Note the location of the failure in both micrographs: a) failure occurs within the TBC and b) at the TBC/TGO interface.**

Based on these two factors, it seems reasonable to suggest there is an optimum topcoat thickness between extremely thick ( $>1.5\text{mm}$ ) and thin ( $<0.1\text{mm}$ ) [35]. This optimal thickness would need to balance the thermal gradient, thermal insulating capabilities and the strain tolerance.

Two methods to accommodate the internal stresses are to either introduce vertical segmentation cracks within the topcoat or to grade the porosity of the topcoats. The vertical segmentation cracks provide strain relief within the topcoat and temporarily relieve the stress buildup during cooling and heating. These types of controlled cracks are common in EBPVD topcoats due to the columnar growth mechanisms during deposition [36]. Praxair Surface Technologies (PST) has developed a dense, thermally-sprayed topcoat with controlled vertical segmentation cracks that provides very high thermal shock resistance [18]. The second mechanism utilizes a gradient in porosity which reflects a gradient in elastic properties that can accommodate the high temperatures at the top surface and the mismatch stresses at the bond coat/topcoat interface. These types of coatings are relatively new and are in the experimental phase [35].

## **2.3 BOND COAT INFLUENCE ON LIFETIME**

### **2.3.1 Surface Roughness**

In general, surfaces with high roughness are preferred with plasma-sprayed YSZ TBCs. The rough surface provides a stronger mechanical bond of the TBC to the bond coat[37]. However,

this increased roughness can cause inhomogeneous TGO formation during oxidation. In particular, local areas where the bond coat protrudes into the topcoat tend to form thicker TGO layers. In these regions, because of their curvature, the aluminum can diffuse to the topcoat interface and deplete the bond coat at a faster rate than in the smooth areas, therefore allowing the TGO to grow faster causing inhomogeneous scale thickening [35]. As the TGO thickens, the thermal expansion mismatch between the three layers (TGO-BC-TC) becomes more significant and cracks can nucleate. As a result, the regions where the TGO is relatively thick can serve as failure nucleation regions [38]. In these regions, the rapid depletion of aluminum can also lead to the formation of other oxides involving chromium, nickel, or cobalt that can weaken the interface between the TGO and the topcoat. It seems as though a smooth bond coat surface will not provide adequate mechanical attachment while an extremely rough interface can lead to the formation of an abnormally thick TGO layer with numerous non-alumina oxides present which can later serve as failure initiation sites. Likewise, if the bond coat surface is too rough, voids can form during the spraying of the topcoat which limit the amount of surface contact area and weakens the interface.

Traegar et al [3] performed a study where, by changing the bond coat powder particle size, the roughness of the bond coat was varied between  $R_a=5.5\mu\text{m}$  and  $R_a=9.8\mu\text{m}$ . They cycled these specimens in a burner rig and their results are shown in Table 3.

**Table 3 -  $R_a$  and  $R_z$  values of the bond coat interface, bond coat temperature (during testing) and cycles to failure of TBC specimens [3].**

Sample #	$R_a$ ( $\mu\text{m}$ )	$R_z$ ( $\mu\text{m}$ )	$T_{\text{bond coat}}$ (K)	$1000/T_{\text{bond coat}}$ ( $\text{K}^{-1}$ )	Cycles to Failure
1	5.6	34.8	1035	0.7645	1033
2	5.8	34.0	1036	0.7639	1672
3	9.9	54.9	1030	0.7675	2704

The rougher bond coats had the longer lifetimes. From these results and from FEA simulations, they proposed by increasing the roughness of the bond coat, the compressive stress state in the TBC above the hills in the bond coat morphology and the tensile states above the valleys are both initially larger than if the bond coat was smoother. As a result, when the stress state in these regions is reversed, which naturally occurs by the growth of TGO layer, it will take more cycles (a thicker TGO) to reverse the larger stress fields, which is necessary before crack propagation can occur [3].

Smialek compared the cyclic lifetime behavior of TBCs with different bond coat finishes [39]. In his work, Smialek intentionally introduced groove patterns and rib patterns to the surface of disc PWA 1484 substrates and then sprayed them with 8YSZ coatings and cycled them both in 1 hour cycles and 100 hour cycles. Results are shown in Figure 14.

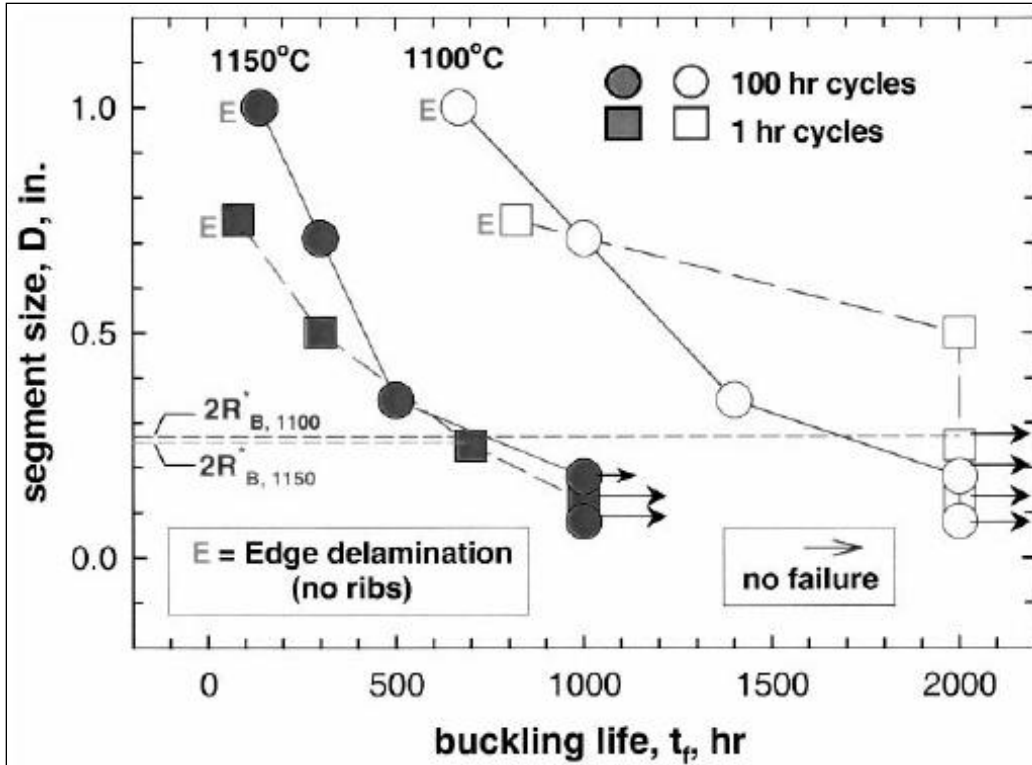


Figure 14 - Effect of segment size and test temperature on buckling life for segmented TBCs in interrupted and cyclic exposures (Points labeled “E” refer to edge delaminations of non-segmented backside or control samples; arrows indicate no failure at end of test [39]).

The ribs, or grooves, provide a mechanical barrier to delamination and from the plot above, the closer the ribs are together, the longer the lifetime of the coatings. The explanation was that the critical stress needed for delamination of the YSZ between these ribs is inversely proportional to the spacing between the ribs, thus smaller spacings require a larger stress for delamination [39]. This idea of precisely tailoring the surface of the bond coat is a unique approach to increasing TBC lifetime and has accompanied with it some major questions (i.e. how will this ribbing affect the aerodynamics or oxidation resistance of the engine component) however, it indicates the importance of bond coat topography on TBC lifetime.

### 2.3.2 Bond Coat Open Porosity

Open porosity, or pores open to the atmosphere, in the bond coats is undesired since the open pores provide paths for oxygen to infiltrate the bond coat surface. This, in combination with high temperatures leads to oxidation of the internal pores and faster depletion of the aluminum content in the bond coat. Once the aluminum content in the bond coat drops below a critical level, alumina is no longer the stable oxide and other less protective nickel and chromium rich oxides form [40]. The formation of these non-protective oxides have been associated with the failure of APS TBCs [33, 38, 40-47].

Pores can be incorporated into the thermal sprayed bond coat several ways during deposition process. The first method is related to the surface roughness. As discussed in the previous section, bond coats with rough surface finishes provide a strong mechanical attachment of the TBC to the metallic coating. To achieve the required roughness, in some spraying processes, a larger sized powder feedstock is used. The larger bond coat particles yield an undulating surface profile ideal for TBC adherence; however they also form a network of interconnected pores that are also connected to the surface.

The second method introduces surface connected pores by the oxidation of bond coat particles during the deposition process. During the thermal spraying process, depending on the composition of the gases atmosphere, the melted bond coat particles can oxidize in situ. The resulting bond coat microstructure is a network of metallic bond coat particles outlined with an oxide layer, as shown in Figure 15. These oxides are all interconnected which provides a path for oxygen to penetrate into the bond coat.

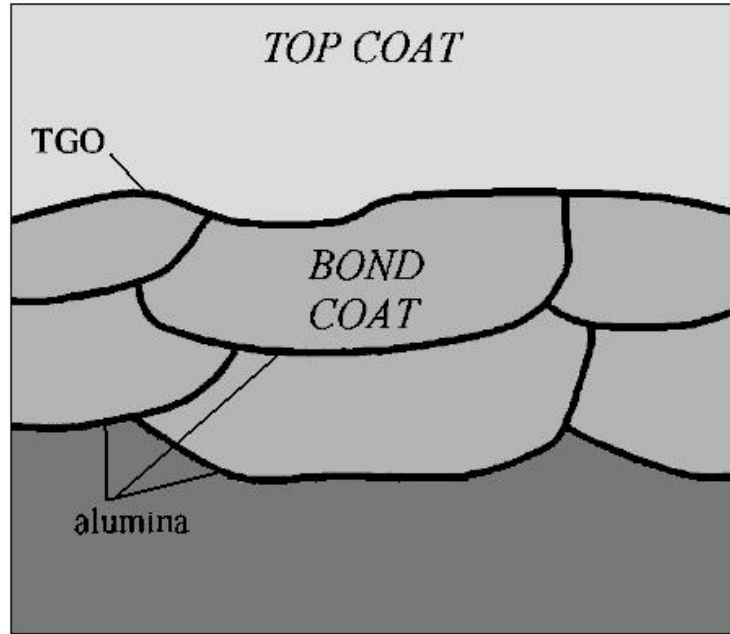


**Figure 15 - Schematic diagram of a thermally sprayed bond coat that oxidized during deposition. Note the interconnected network of alumina that surround the bond coat particles.**

## **2.4 SUBSTRATE INFLUENCE ON LIFETIME**

The superalloy substrate has been shown to affect the lifetime behavior of TBCs in two direct ways: through compositional effects and the through thermal expansion misfit effects.

### **2.4.1 Compositional Effect**

Compositional effects arise from interdiffusion between the bond coat and the substrate material. In this study, the bond coatings used are NiCoCrAlY bond coats which are alumina formers. As the alumina scale forms during high temperature exposure, the aluminum in the bulk of the coatings diffuses up to the surface where it is incorporated in the scale. Likewise, when at high

temperatures, the aluminum can also diffuse down into the substrate given the appropriate thermodynamic conditions. Such conditions require a chemical potential gradient to exist which, in this case, is established by the composition difference between the bond coat and superalloy. In the case where a gradient does exist with the underlying alloy, the aluminum will be depleted faster than in the case with just the scale formation because of the second “sink” the aluminum is “consumed” by. Once the aluminum content drops below a critical level, alumina is no longer the stable oxide and so nickel and chromium oxides can begin to grow. These oxides are not as adherent as the alumina and can spall off more easily [48, 49].

Similar to the aluminum depletion by diffusion into the substrate alloy, elements in the substrate material can diffuse up into the bond coat. Elements such as tantalum (Ta), niobium (Nb), sulfur (S), and yttrium (Y) can diffuse through the bond coat and affect the growth rate and adherence of the oxide and thus affect the overall TBC lifetime [5, 50]. Pint et al. showed this by coating two different René N5 substrates, one with and the other without yttrium, with a PtAl bond coat and a YSZ TBC and thermally cycling the specimens until failure. The specimens with yttrium in the substrate had longer lifetimes as shown in Figure 16 [48].

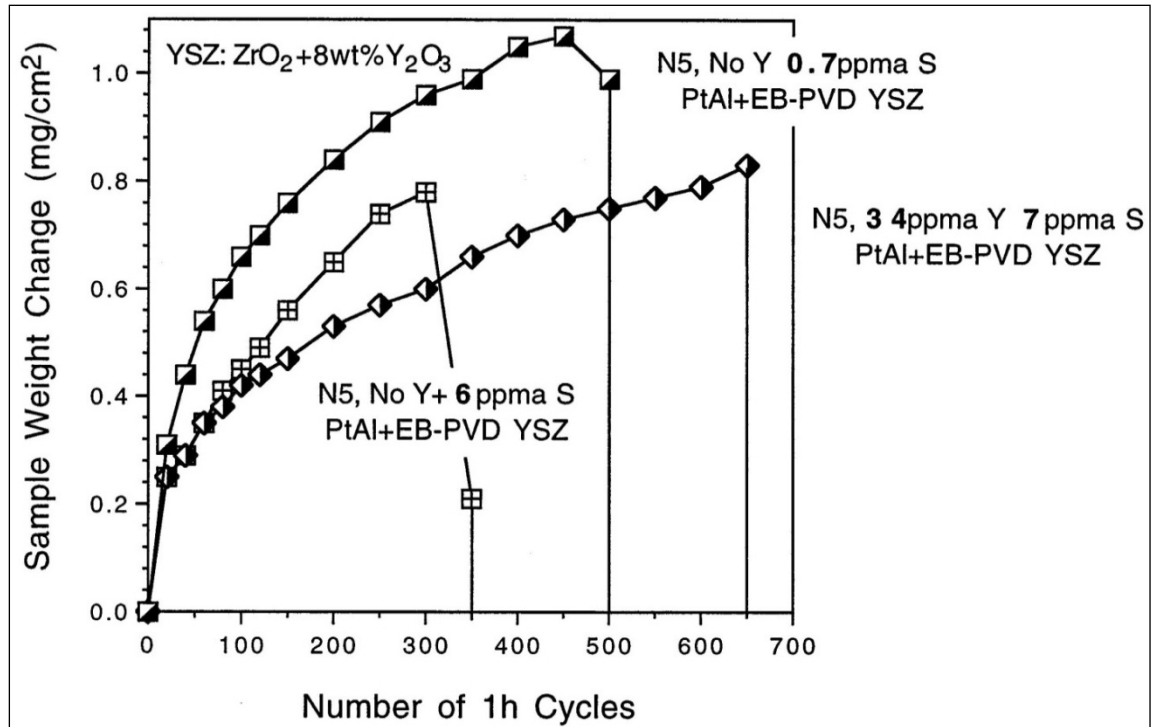


**Figure 16 - Weight change of Pt alumide/EB-PVD TBC coated René N5 during 1 hr cycles at 1150°C. Both desulfurization and the addition of Y to the underlying substrate improved coating lifetime [48].**

The yttrium from the Rene N5 was believed to induce the reactive element effect. Lifetime was also improved through desulfurization of the substrate. At high enough levels, sulfur can weaken the cohesive strength of the scale metal interface causing spallation [5, 48].

### 2.4.2 Mechanical Effect

The differences in the coefficient of thermal expansion (CTE) between the layers in a TBC system will give rise to thermal stress buildup in these layers. The thermal stresses within the topcoat are proportional to the CTE mismatch between the topcoat and the superalloy as indicated by Equation 6. Furthermore, the stored elastic strain energy, Equation 7, in the topcoat

is proportional to the square of the thermal stresses and it is this stored energy that drives cracks to form and to propagate.

Given this behavior, an ideal TBC system design would be one that minimizes the CTE mismatch between the layers which should increase TBC lifetime [51]. Previously, the effect of substrate selection on TBC performance reported by Stecura showed, in furnace and burner rig testing, that by changing the base substrate metal to alloys with lower thermal expansion coefficients, that the lifetime of the coatings could be increased [52]. Wu et al. argued however, that coating lifetime is not directly proportional to CTE mismatch but instead more solely dependent on bond coat oxidation with the CTE mismatch acting as a conjugate part of the failure mechanism [53]. Regardless of whether the CTE mismatch is a dominant or conjugate part of the failure mechanism though, a review of the literature indicates that it is nonetheless detrimental to the coating lifetime but there does exist a gap in understanding of exactly how detrimental it is.

### 3.0 EXPERIMENTAL

All of the specimens used in this study were prepared at Praxair Surface Technologies (PST) in Indianapolis, Indiana. A list of the specimens prepared will be given at the beginning of each chapter of the results and discussion section for the reader's convenience. A general explanation of the specimen production, testing and characterization will be given in this section.

All of the TBC specimens had the similar dimensions and the same general makeup. They consisted of a disk shaped superalloy substrate, with a bond coat deposited on only one of the surfaces on which a ceramic topcoat was then deposited. The superalloy substrate disks had an approximate diameter of 2.5cm and a thickness of 3 millimeters. The bond coats, which all were two phase  $\beta/\gamma$ -NiCoCrAlY bond coats, were deposited by argon-shrouded plasma spraying. Unless stated otherwise, all of the bond coats used in this study were dual layer bond coats. Dual layer bond coats are prepared in two steps using two powders of different sizes but with identical compositions. The first layer in the bond coat (directly deposited on the substrate superalloy) is sprayed with a fine sized powder which produces a smooth dense coating. Afterwards, a second layer is sprayed on top of the first with the coarse powder which leaves a rough surface finish containing numerous surface connected pores. The purpose of this two-step deposition process is to first seal the superalloy with a dense bond coat layer and then to roughen the surface with the second step which gives the necessary roughness needed for a strong bond between the topcoat and bond coat.

After deposition, the bond coat/superalloys were heat treated in a vacuum furnace at 1080°C for 4 hours to establish the two-phase microstructure in the bond coat. The YSZ topcoats were then deposited via air-plasma spraying. The details of the spraying process are proprietary to PST and will not be discussed. The nominal compositions of the bond coat, topcoat and the various substrates are detailed in Table 4.

**Table 4 - Composition of materials in weight percent.**

Nominal Composition of Materials (wt%)																
Layer	Material	Ni	Co	Cr	Al	W	Mo	Fe	Ta	Nb	Ti	C	Hf	La	Zr	Re
Superalloy	IN-718	Bal	-	19	0.5	-	3	18	-	5	1	-	-	-	-	-
	IN-738	Bal	9	16	3.3	2.8	1.8	-	1.8	1	4	0.1	-	-	-	-
	René N5	Bal	7.5	7.5	6.3	6.4	1.4	-	7.1	-	-	0.1	0.2	-	-	3
	PWA-1484	Bal	10	5	5.6	6	2	-	8.7	-	-	-	0.1	-	-	3
	HA-188	22	Bal	22	-	14.5	-	-	-	-	-	-	-	0.1	-	-
	MarM-509	10	Bal	23	-	7	-	-	3.5	-	0.2	0.6	-	-	0.4	-
Bond Coat	NiCoCrAlY	Ni	Co	Cr	Al	Y										
		Base	22	16	13	0.5	-	-	-	-	-	-	-	-	-	-
YSZ Topcoat		ZrO <sub>2</sub>	Y <sub>2</sub> O <sub>3</sub>	Al <sub>2</sub> O <sub>3</sub>	CaO	Fe <sub>2</sub> O <sub>3</sub>	HfO <sub>2</sub>	MgO	SiO <sub>2</sub>	All Other						
	High Purity	Base	7.74	0.011	0.003	0.007	1.69	<0.001	0.01	0.157						

### 3.1 THERMAL EXPOSURE TYPES

The durability of the TBCs was evaluated using several types of thermal exposures. The three types of exposures were furnace cyclic testing (FCT), jet engine thermal shock testing (JETS) and isothermal sintering exposures. While these tests do not exactly mimic the operating conditions in a jet or land based turbine engine, they do accurately represent the industry standard for testing the durability of TBC specimens.

For FCT testing, bottom loading furnaces from CM Furnaces were used. An image and a schematic are shown in Figure 17.



**Figure 17 - Photograph of a bottom loading furnace used for the furnace cycling tests (FCT).**

In these tests the specimens were placed in a ceramic holder which was raised into the hot zone of the furnace and then heated to 1100°C in ten minutes. They are isothermally held at this temperature for 45 minutes then dropped out of the hot zone and forced-air cooled for an additional ten minutes.

The JETS test was performed at PST in Indianapolis by trained technicians. This test is more simulative of the operating conditions in a turbine because it induces a temperature gradient across the thickness of the TBC (whereas the FCT test does not).

In this test, the TBC specimens are fastened onto a large rotating ring shown in Figure 18 (white dots).

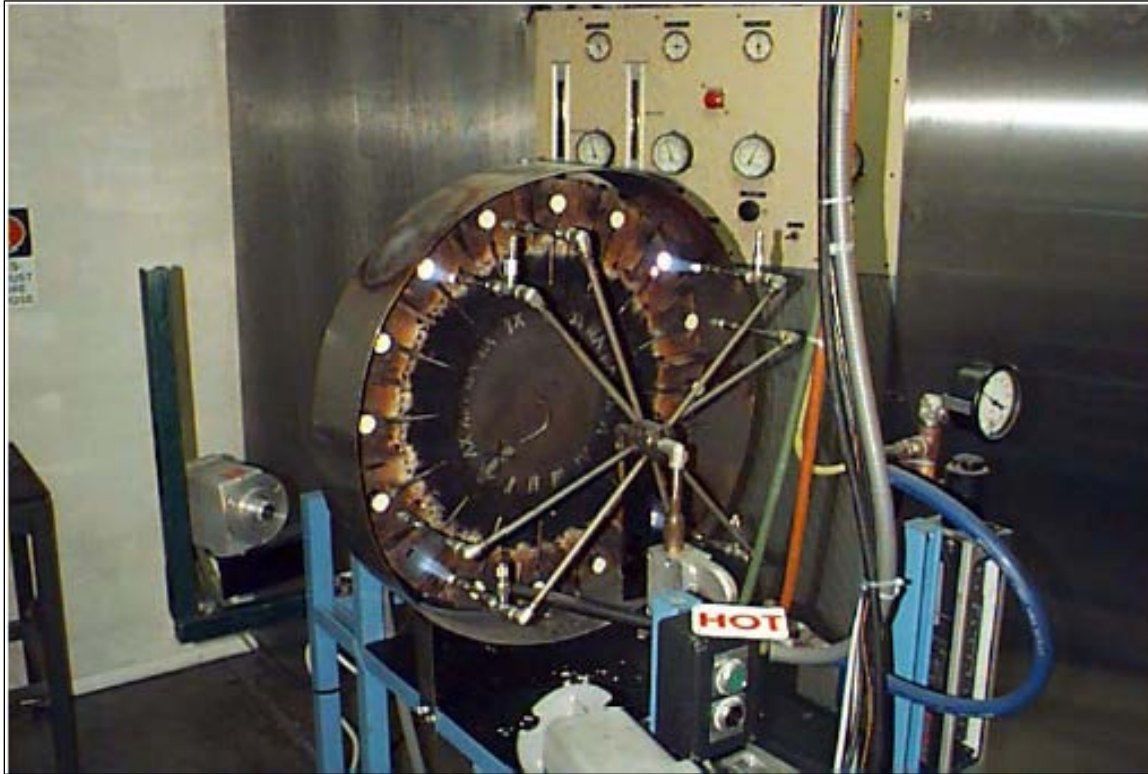


Figure 18 - Praxair JETS testing rig.

Once loaded, the test begins and the specimens are rotated through a series of different exposure conditions. In the first condition, the sample is rotated under an oxy-propylene flame for 20 seconds which heats the surface to approximately 1400°C. The specimen is next rotated under a nozzle that cools the YSZ surface for 20 seconds with compressed nitrogen. After this, the specimen is rotated to a position where it experiences two 20 second ambient cooling periods. This procedure is repeated for a set number of cycles, usually 2000. The damage, which is usually cracking, is monitored by an optical pyrometer that measures and records the front and back face temperatures of the TBCs. In the event a crack forms or some of the YSZ spalls off,

the temperature of the back face will either drop or spike up, respectively, so an accurate number of cycles to cracking or spallation can be determined. Upon completing a set number of cycles, the specimens are removed from the rig and using a traveling microscope, the amount of edge separation between the bond coat and the topcoat is measured and compared to the pre-test cracking value.

High temperature anneals were also performed on free-standing YSZ topcoats. These were also carried out in the bottom loading furnaces. In this test, the specimens were heated to the desired temperature (1300°C or 1200°C) over a period of 20 minutes, held at this temperature for a specific length of time and then dropped from the hot zone and force-air cooled to room temperature within 60 seconds.

### **3.2 SPECIMEN BREAKDOWN**

The specimens tested in this study can be broken down into three categories:

1. Topcoat Modifications
2. Bond Coat Modifications
3. Substrate Influences

### 3.2.1 Topcoat Modifications

**3.2.1.1 YSZ Purity** As previously stated in the background section, impurities in YSZ such as silica and alumina have been observed to increase the sintering rate of topcoats.

Topcoat sintering and phase transformation tests were performed on free standing YSZ topcoats which were prepared by plasma spraying YSZ on aluminum panels and then leaching away the aluminum in a 25% NaOH aqueous solution leaving free-standing YSZ panels. Two YSZ purity levels were used, high and conventional purity, where there was an order of magnitude difference in SiO<sub>2</sub> and Al<sub>2</sub>O<sub>3</sub> content between the two coatings. Low density (90% dense) and high density coatings (92% dense) were prepared at these two purity levels yielding a total of 4 different coatings that were tested.

The free standing coatings were exposed for various time lengths at 1300 °C and 1200°C. Density measurements were performed on the specimens using Archimedes's Principles to determine the extent of the sintering process by measuring the change in density. In particular, ASTM B-328-94 was followed for these measurements. First, the specimens were weighed using a microbalance (0.01mg resolution) and then submerged in Alcatel-100 vacuum pump oil which met the viscosity requirements outlined in the ASTM standard. The density of the oil was measured to be 0.869g/cm<sup>3</sup>. Once submerged, the specimens were placed in a vacuum chamber where a vacuum of 0.0691atm was established and held for 30 minutes. Afterwards they were removed from the vacuum, let sit for 10 minutes at ambient pressure and then removed from the oil. An absorbent tissue was used to remove the excess oil from the surface being careful not to draw out the oil which had impregnated the specimens and then the mass was again recorded. The submerged mass of the specimen was measured using a specially designed Mettler-Toldeo apparatus which suspended the specimen under water. A wetting agent was added to the water to

ensure air bubbles did not attach to the specimen during the measurement. Likewise, at the time of the measurement, the temperature of the water was recorded with a precision of 0.1°C. The density of the water was established using a temperature-density look-up table provided by Mettler-Toldeo. Using all of this data, the density of the specimens was computed using Equation 8.

**Equation 8**

$$\text{Density} = \left( \frac{(m_{\text{dry-air}})}{(m_{\text{oil-air}}) - (m_{\text{oil-water}})} \right) \times \rho_{\text{water}}$$

X-ray diffraction (XRD) was performed in order to determine the extent of the phase transformations that occurred at temperature. Finally, the specimens were examined in the SEM to observe the microstructural changes.

**3.2.1.2 Topcoat Thickness** To investigate the influence of topcoat thickness on TBC performance, TBCs with dual layer NiCoCrAlY bond coats on PWA 1484 substrates were prepared with topcoats of the following thicknesses: 100, 225, 425, 750, 1150 and 1425  $\mu\text{m}$ . Three specimens were tested for each thickness in the FCT. The density of the topcoats was determined (via ASTM B 328-94) to be  $82 \pm 0.6\%$  the theoretical density (TD) of YSZ at this composition (6.050g/cm<sup>3</sup>).

**3.2.1.3 Topcoat Microstructure** Strain relief topcoats were prepared on dual layer NiCoCrAlY bond coats on PWA 1484 substrates. These strain relief topcoats were prepared by adjusting the plasma spraying deposition parameters such that the resultant topcoat was dense

but contained vertical fissures (termed a dense vertically fissured (DVF) TBC) which can then provide strain relief much like the vertical fissures do in EBPVD TBCs.

Two types of strain relief topcoats were prepared using the DVF microstructures. The first, termed a Dual TBC, had a 1250  $\mu\text{m}$  topcoat comprised of a 125 $\mu\text{m}$  inner-layer of DVF microstructure (adjacent to the bond coat) and a 1125  $\mu\text{m}$  outer-layer of the low-density topcoat (82% T.D.). The second type of strain relief topcoat, referred to as a DVF TBC, was solely comprised of 1150  $\mu\text{m}$  of the DVF coating. TBCs were prepared on PWA 1484 substrates and all types of TBCs were FCT and JETS tested, three per test type.

### **3.2.2 Bond Coat Modifications**

The influence of bond coat roughness on TBC lifetime (in both JETS and FCT testing) was examined as well as the influence of roughness on the oxidation performance of the bond coat by preparing four bond coats with different surface finishes. This was done by blending two bond coat powders, a fine sized powder (LN11) and a large sized powder (LN14) both of which have identical compositions, in different ratios and then depositing them via argon-shrouded plasma spraying. The four ratios (by weight) were: 100% LN11, 75%LN11-25%LN14, 50%LN11-50%LN14 and the fourth was a dual layer bond coat which had a thin 100% LN11 layer with a thin 100% LN14 layer on top. The target thickness of the bond coat was 7-8mils. After the bond coats were deposited on PWA 1484 and René N5 substrates, they were heat treated at 1080°C for 4 hours. Lastly, a 425  $\mu\text{m}$  high-purity low-density APS TBC was deposited which was also 82 $\pm$ 0.6% dense.

The surface roughness was measured with a Talysurf Surtronic 3+ contact profilometer (prior to topcoat deposition) with a 5  $\mu\text{m}$ -tip radius and also using a cross-sectional microscopy

technique (which was performed after the topcoat was deposited). For the surface profilometer, a traverse distance on 4mm was used with a cut-off length of 0.8mm. Multiple passes were performed on one specimen of each bond coat type and then an average and standard deviation were calculated. For the cross-sectional technique, 24 high resolution back-scattered SEM images were collected of each specimen, converted into binary images and then loaded into Matlab where, simple calculations were performed to compute an average roughness, Ra.

These specimens were FCT and JETS tested. A group of them was also tested to a percentage of their overall lifetime with the purpose of examining how the failure progresses over the lifetime of the TBC.

### **3.2.3 Substrate Influences**

Two approaches to establish the influence of the substrate superalloy on TBC lifetime were investigated; the first was the mechanical influence and the second was the compositional influence.

The mechanical approach focused on identifying the influences of the physical properties (CTE, elastic modulus) on the mismatch stresses in the coatings and how this contributes to TBC failure. This was carried out experimentally by thermally cycling TBC systems with multiple superalloy substrates (IN 718, HA 188 and René N5) comparing their performance.

The compositional approach focused on identifying the significance of the interdiffusion between the bond coat and the superalloy and what influence this may have had on the oxidation performance of the bond coat. This was accomplished by argon-shrouded plasma spraying one composition bond coat onto five separate superalloy materials (no YSZ was deposited). These bond coat-superalloy couples were then thermally cycled and periodically imaged and

characterized to track the compositional changes of the TGO and within the bond coat. Five superalloys were used, IN 718, IN 738, MarM 509, HA 188 and René N5.

### **3.3 CHARACTERIZATION TECHNIQUES**

The fracture surfaces and cross-sections of specimens from these tests were analyzed using a SEM equipped with energy dispersive spectroscopy (EDS). Cross-sections of the specimens were prepared by vacuum mounting them in warm epoxy followed by cross-sectioning in a high speed precision saw and then polishing to a 0.04  $\mu\text{m}$  finish. X-ray diffraction was used to identify oxide species on the bond coat only specimens as well as to identify the phases present in the sintered free-standing YSZ topcoat specimens.

## **4.0 RESULTS AND DISCUSSION**

### **4.1 TOPCOAT VARIABLES**

#### **4.1.1 Topcoat YSZ Purity**

**4.1.1.1 Overview** As in all material processing, compositional control is vital in TBC fabrication. By minimizing certain impurities, a material's performance can be enhanced. However, impurity control can be a drain on resources, time and money. Insight and knowledge on how certain impurities influence a material's performance could be used to justify or not justify these resources needed to remove these impurities. Herein lies the focus of this research.

The influence of YSZ impurity content on the properties of TBCs topcoats was investigated by preparing free-standing YSZ topcoats and sintering them at typical engine combustion gas temperatures to gain understanding of how and if the impurities in the YSZ influence the sintering rate, phase stability and microstructural evolution of the coatings.

**4.1.1.2 Experimental Design** Free-standing YSZ topcoats (i.e. no superalloy or bond coat, just YSZ) were prepared by plasma spraying  $\sim 750 \mu\text{m}$  of YSZ on aluminum panels and then leaching away the aluminum in a warm 25% NaOH aqueous solution. Afterwards, the coatings were rinsed in isopropanol several times and again in deionized water. Finally they were given a

light polish to remove any residual aluminum and aluminum oxide that still remained attached to the backside of the coating.

Four topcoats were prepared from four powder lots, two of which were high purity (HP) YSZ powders and two were conventional purity (CP) YSZ powders. Furthermore, two microstructures were prepared, a low density (LD) microstructure and a dense vertically fissured (DVF) microstructure. The four coatings were: High-purity low-density (HP-LD), conventional-purity low-density (CP-LD), high-purity dense vertically-fissured (HP-DVF) and conventional-purity dense vertically-fissured (CP-DVF). The compositions of the powders used for these coatings are given in Table 5. The major differences in the powder compositions were the SiO<sub>2</sub> and Al<sub>2</sub>O<sub>3</sub> contents.

**Table 5 - Composition of powders used for the free-standing topcoat specimens.**

	Powder Lot Compositions (wt%)									
	ZrO <sub>2</sub>	Y <sub>2</sub> O <sub>3</sub>	HfO <sub>2</sub>	Al <sub>2</sub> O <sub>3</sub>	SiO <sub>2</sub>	TiO <sub>2</sub>	CaO	Fe <sub>2</sub> O <sub>3</sub>	MgO	Other
HP-LD	Bal	7.90	1.7	0.010	0.007	0.004	0.004	0.010	0.004	0.078
CP-LD	Bal	7.40	1.6	0.100	0.500	0.027	0.004	0.033	0.002	0.350
HP-DVF	Bal	7.35	1.7	0.004	0.014	0.006	0.002	0.003	0.002	0.700
CP-DVF	Bal	7.46	2.1	0.100	0.100	0.100	0.240	0.350	0.025	0.100

Separate groups of the four specimens were sintered for 100 hours at 1200°C, 10 hours at 1300°C and 100 hours at 1300°C. The high temperature exposures was performed in a CM bottom loading furnace where they were heated to the target temperature over a period of 20 minutes, held for the set amount of time and then dropped out of the furnace and force air cooled to room temperature at a rate of about 30°C per second. Afterwards, density measurements were

performed according to ASTM B-328 which utilizes Archimedes' principle. The difference between the starting density and the after-heat treatment density divided by the time at temperature was taken to be the sintering rate (%/hr). X-ray diffraction was also performed on the sintered specimens to measure the change in the phase content during the high temperature exposure. A Philips PW3710 Diffractometer with a CuK $\alpha$  radiation ( $\lambda= 1.54056$ ) was used for this and three different equipment settings were used in order to gather detailed diffraction patterns of certain peaks, the details of which are listed in Table 6.

**Table 6 - XRD Scan Settings**

Scan Name	2 $\theta$ Range	Step Size	Dwell Time
Full	20°-90°	0.05°	0.25 sec
Monoclinic	27°-32°	0.01°	5 sec
Tetragonal/Cubic	72.5°-75.5°	0.005°	5 sec

Finally, the as-processed and sintered specimens were mounted in warm epoxy, sectioned with a high-speed precision saw and polished to a 0.04 $\mu$ m finish and examined in an SEM equipped with standardless EDS.

#### **4.1.1.3 Results: Free-Standing Topcoats**

**4.1.1.3.1 Density Measurements** One set each of free-standing topcoats were sintered for 100 hours at 1200°C, 10 hours at 1300°C and 100 hours at 1300°C. The density of these coatings was measured after exposure and the results are given in Figure 19.

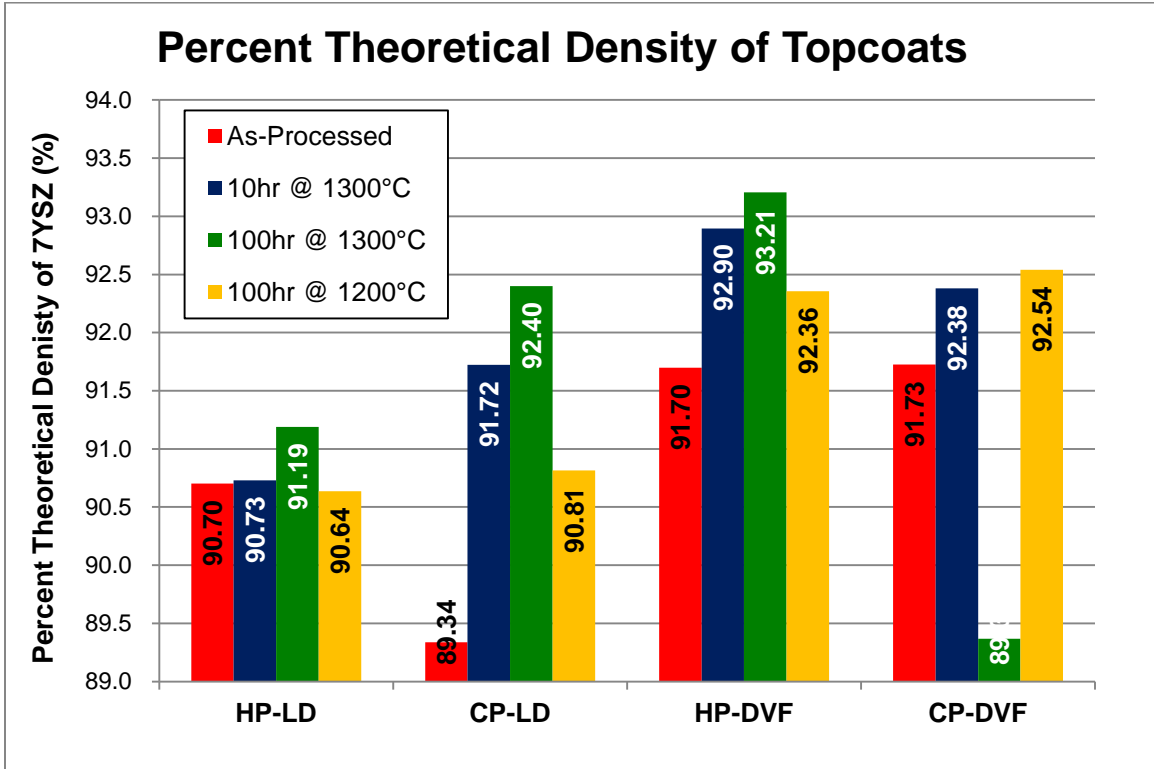


**Figure 19 - Percent theoretical density of as-processed and sintered topcoats. Measured according to ASTM-B328.**

Furthermore, sintering rates, defined as the percent density change (difference between the as-processed density and the sintered density, divided by as-processed density) divided by the time, are given in Table 7.

**Table 7 - Calculated Sintering Rates of Topcoats**

Sintering Rate ( % Density Change / hour)					
Temp	Time	HP-LD	CP-LD	HP-DVF	CP-DVF
1300	10	0.0031	0.2670	0.1308	0.0712
1300	100	0.0054	0.0343	0.0165	-0.0257
1200	100	-0.0007	0.0165	0.0072	0.0089

The HP-LD topcoats were very resistant to sintering indicated by their comparatively small sintering rates. The small negative sintering rate of the 100 hour 1200°C HP-LD coating (gold bar Figure 19) is attributed to the experimental error associated with the resolution of the microbalance used to measure the mass of the specimens. The differences in the various mass measurements used to compute the densities were on the order of ~9mg which is just above the resolution of the microbalance which is 10<sup>-4</sup> grams (0.1mg). This resulted in the as-processed and the 100 hour at 1200°C specimens roughly having the same density, at least according to the resolution of the microbalance used.

The CP-LD coating had much larger sintering rates compared to the HP-LD specimens. After 10 hours at 1300°C there was a sharp increase in the density (blue bar) followed only by a modest increase in the density when the heat treatment time was extended to 100 hours (green bar). This suggests, at least at this temperature, there is a rapid shrinkage period within the first 10 hours followed by a much slower densification process. When the temperature was reduced to 1200°C the sintering rate dropped, as compared to the 1300°C rates, but still remained much higher than the HP-LD coating. According to a literature survey [30], plasma sprayed coatings with lower densities (i.e. higher levels of porosity) should sinter faster than denser coatings.

Since the CP-LD specimens had a lower starting density than the HP-LD specimens, 89.3% and 90.7% respectively, they would be expected to sinter faster. However, differences in coating porosity will only account for so much of the difference between the observed sintering rates. Vassen et al [30] estimated a difference in porosity of 1.4% could account for roughly a 25% difference in the sintering rates. Since there is an order of magnitude difference in the sintering rates (i.e. 100% difference) of these two coatings it seems other variables besides coating porosity are having an influence on the sintering rates.

The HP-DVF specimens, despite the high purity powder, had significantly larger sintering rates than the HP-LD coatings. Again, as with the CP-LD coatings, there was an initial period of rapid shrinkage within the first 10 hours (blue bar) at 1300°C followed by a much slower densification rate for the remaining 90 hours (green bar). Unlike the HP-LD coating, even at 1200°C there was an increase in density, well above the resolution of the measurement process.

The CP-DVF coating exhibited behavior different from the other three coatings. After 10 hours at 1300°C there was an increase in the density, however, after an additional 90 hours (green bar) the density decreased. Measurement error cannot account for the large density decrease as it did with the HP-LD 100hr at 1200°C coating. A decrease in density could only be achieved via two pathways. First, the mass of the specimen could decrease during the course of the high temperature exposure. The differences in the mass of the specimens before and after the sintering experiments are given in Table 8.

**Table 8 - Difference in mass between pre-sintered and post-sintered specimens.**

Difference in the Pre-Sintering Mass and After-Sintering Mass (milligrams)					
Temp	Time	HP-LD	CP-LD	HP-DVF	CP-DVF
10hr @ 1300°C	10	0.01	0.72	-0.40	-1.15
100hr @ 1300°C	100	0.24	0.76	-0.38	-0.77
100hr @ 1200°C	100	0.11	0.77	-0.63	-1.04

The LD coatings experienced slight weight increases during the heat treatment whereas the DVF specimens experienced small mass losses. Possible explanation of the weight changes could involve evaporation of YSZ material, evaporation of the residual water droplets left over from the leaching process or the filling of empty oxygen vacancies which could have existed prior to heat-treatment leading to a mass increase. Regardless of reason for these mass changes, they alone cannot account for the magnitude of the decrease in the density of the 100 hour 1300°C coating. At best, the slight mass loss in this specimen could account for a 0.01% decrease in the density. Thus the only other explanation must be the volume of the CP-DVF specimen increased during exposure at 1300°C. The source/cause of the volume increase will be discussed later.

In summary, the HP-LD coating experienced little densification during the thermal treatments whereas the CP-LD and HP-DVF coatings experienced significant densification in all three exposures. Furthermore, the CP-LD and HP-DVF coatings experienced a rapid increase in the density after 10 hours at 1300°C but then saw little additional shrinkage upon extending the aging time to 100 hours. The CP-DVF coating exhibited unique behavior as its density decreased during the 100 hour heat treatment at 1300°C. The decrease was attributed to an increase in the volume of the specimen, not due to a decrease in mass.

**4.1.1.3.2 Microstructural Results** Cross-sectional micrographs were taken of each specimen. The as-processed HP-LD specimen is shown in Figure 20.

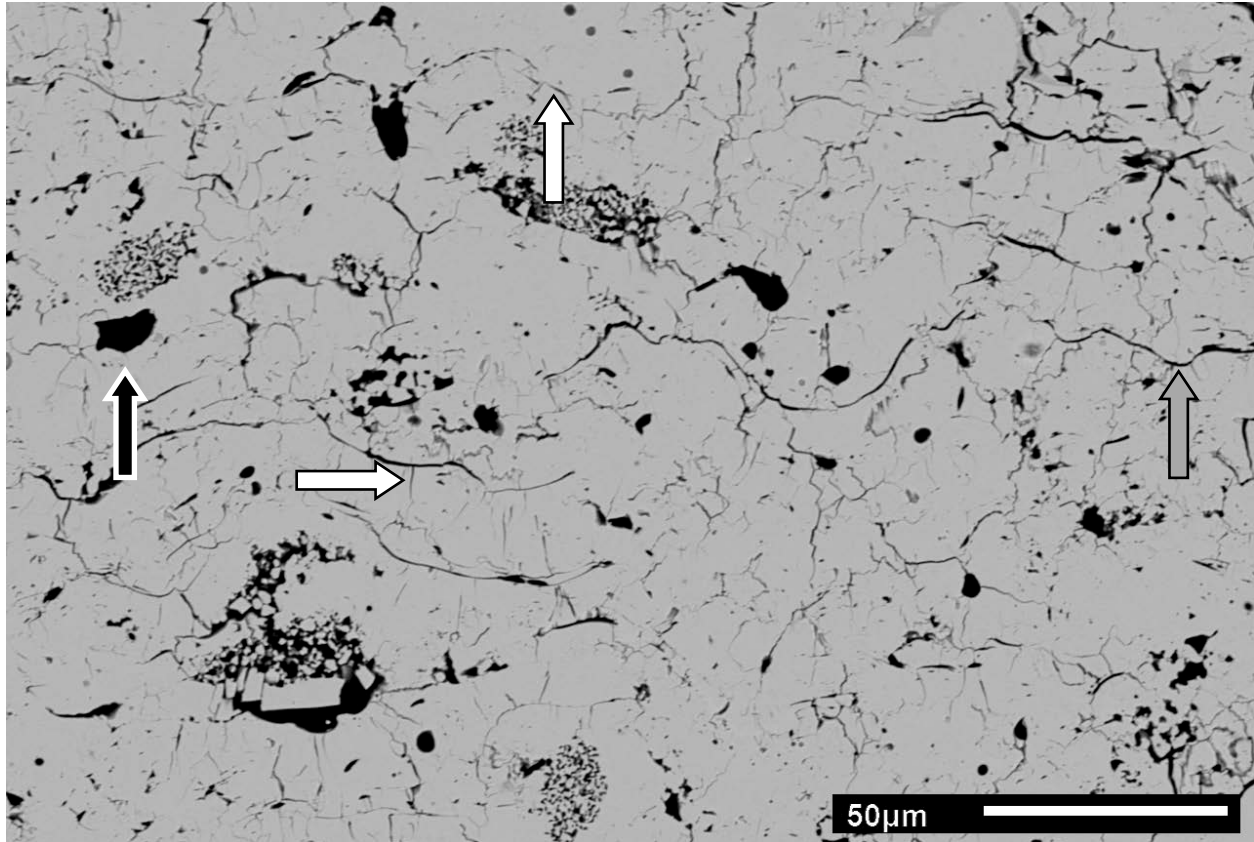


**Figure 20 - HP-LD in the as-processed condition. White arrows indicate small micro-cracks, black – globular pores and grey – horizontal delaminations.**

In the as-processed state, the coating contained small horizontal and vertical microcracks (white arrows), larger globular pores (black arrows) and large horizontal splat boundaries (gray arrow). After 10 hours at 1300°C, Figure 21, many of the small micro-cracks had partially healed/bridged and some had completely disappeared. This is depicted in Figure 21 by the lack of small black cracks.

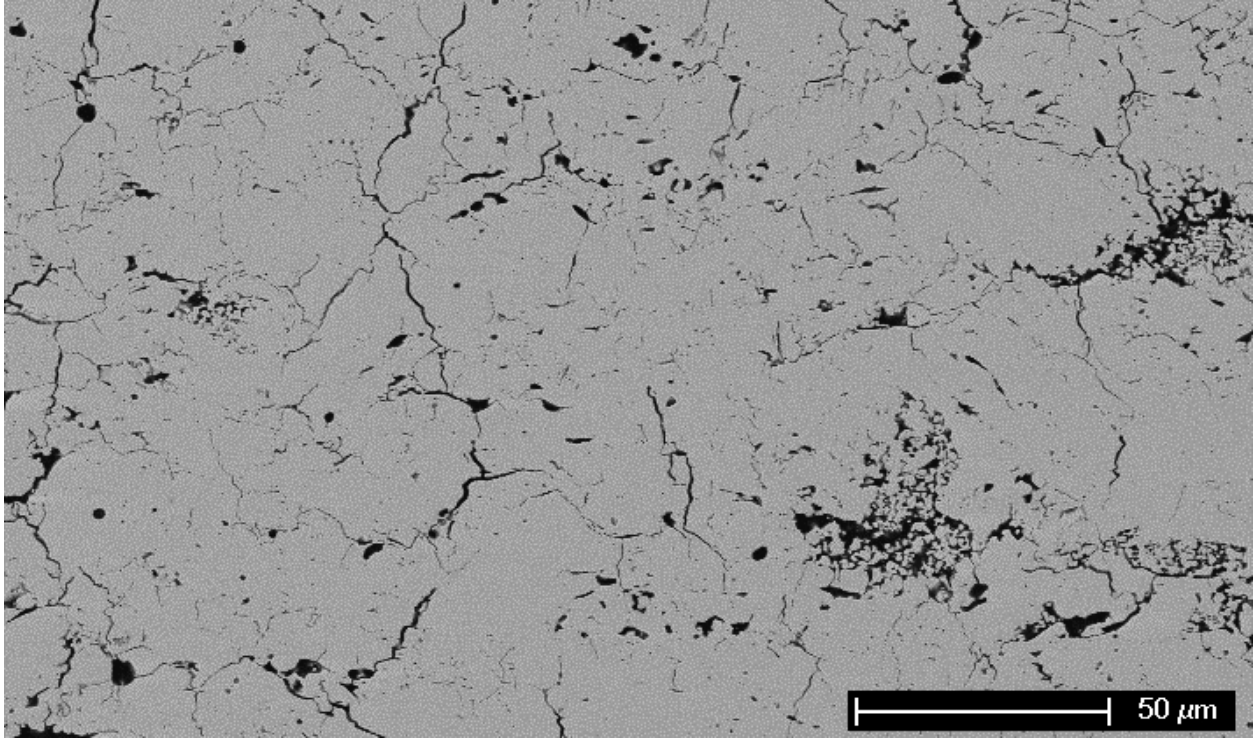


**Figure 21 - HP-LD after 10 hours at 1300°C.**

After 100 hours at 1300°C, Figure 22, few changes beyond those discussed in the 10 hour specimen had occurred. The small micro-cracks, the large horizontal delaminations and the vertical cracks have begun to heal/bridge. As an example, a bridged horizontal micro-crack is highlighted in red in Figure 22. The pore was broken-up by several YSZ bridges (white arrow) that extended over the crack. The large globular pores are still present.

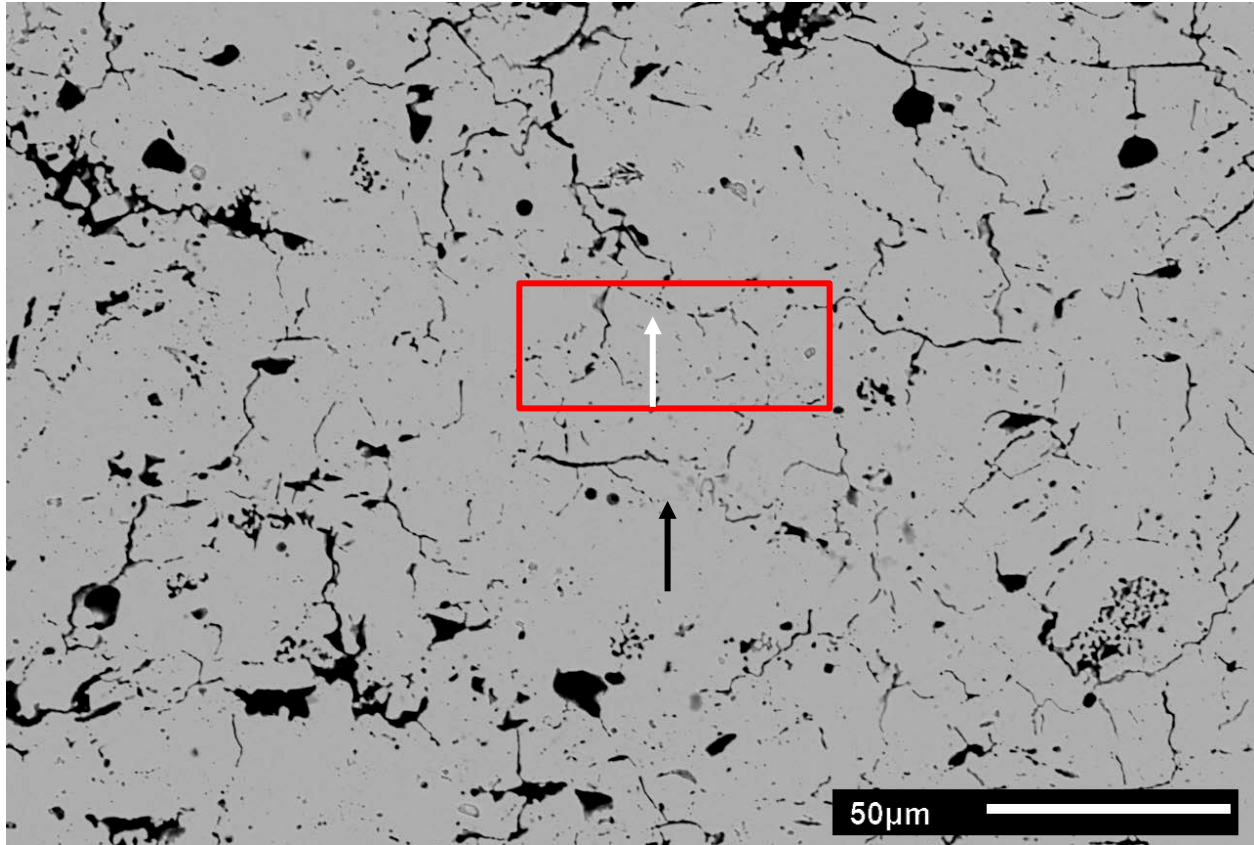


**Figure 22 - HP-LD after 100 hours at 1300°C.**

Comparing the as-processed and the 100 hour at 1300°C specimens, it is clear some densification has occurred, at least visually confirming the measured increase in density. After 100 hours at 1200°C there again was bridging of micro-cracks in isolated areas, red box in Figure 23. However, many of the microstructural features in the as-processed coating still exist in the 100 hour 1200°C coating. Impurities such as  $\text{SiO}_2$  and  $\text{Al}_2\text{O}_3$  were not found in this coating during any of the observation sessions.

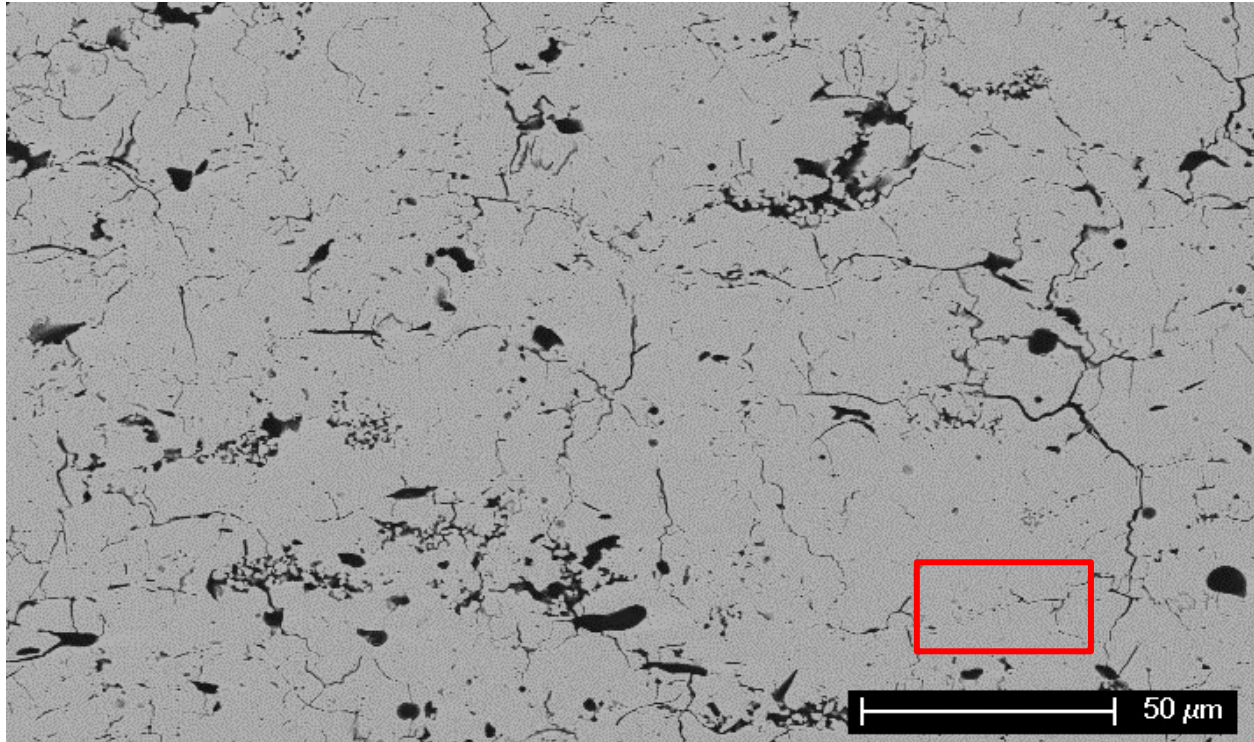


**Figure 23 - HP-LD after 100 hours at 1200°C.**

The starting microstructure of the CP-LD coating is shown in Figure 24. As with the HP-LD specimen, this coating also contained small horizontal and vertical microcracks, larger globular pores and large horizontal splat boundaries. In addition, this coating also contained isolated regions of high  $\text{SiO}_2$  and  $\text{Al}_2\text{O}_3$  content, Figure 25, indicated by white arrows. The impurity regions appear dark because of the atomic number difference between silicon/aluminum and zirconium/yttrium.

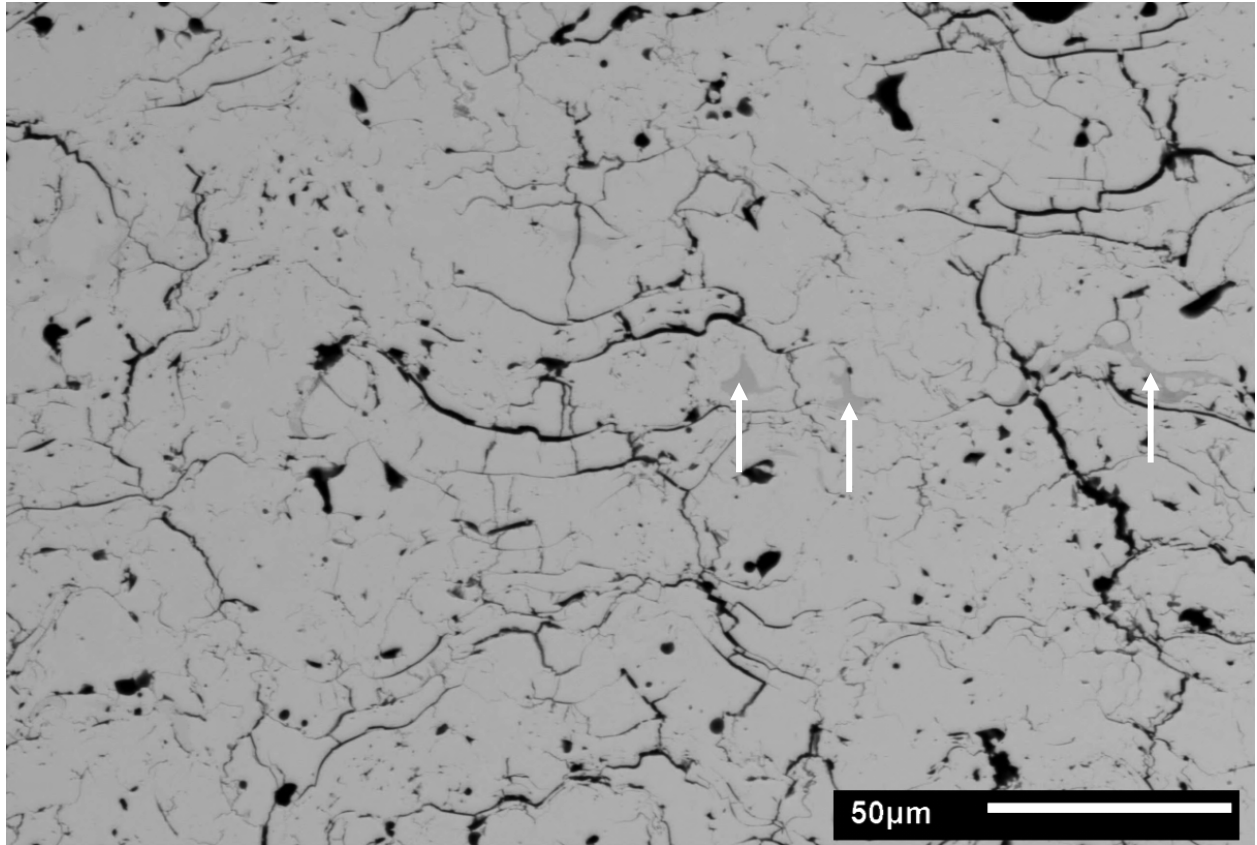
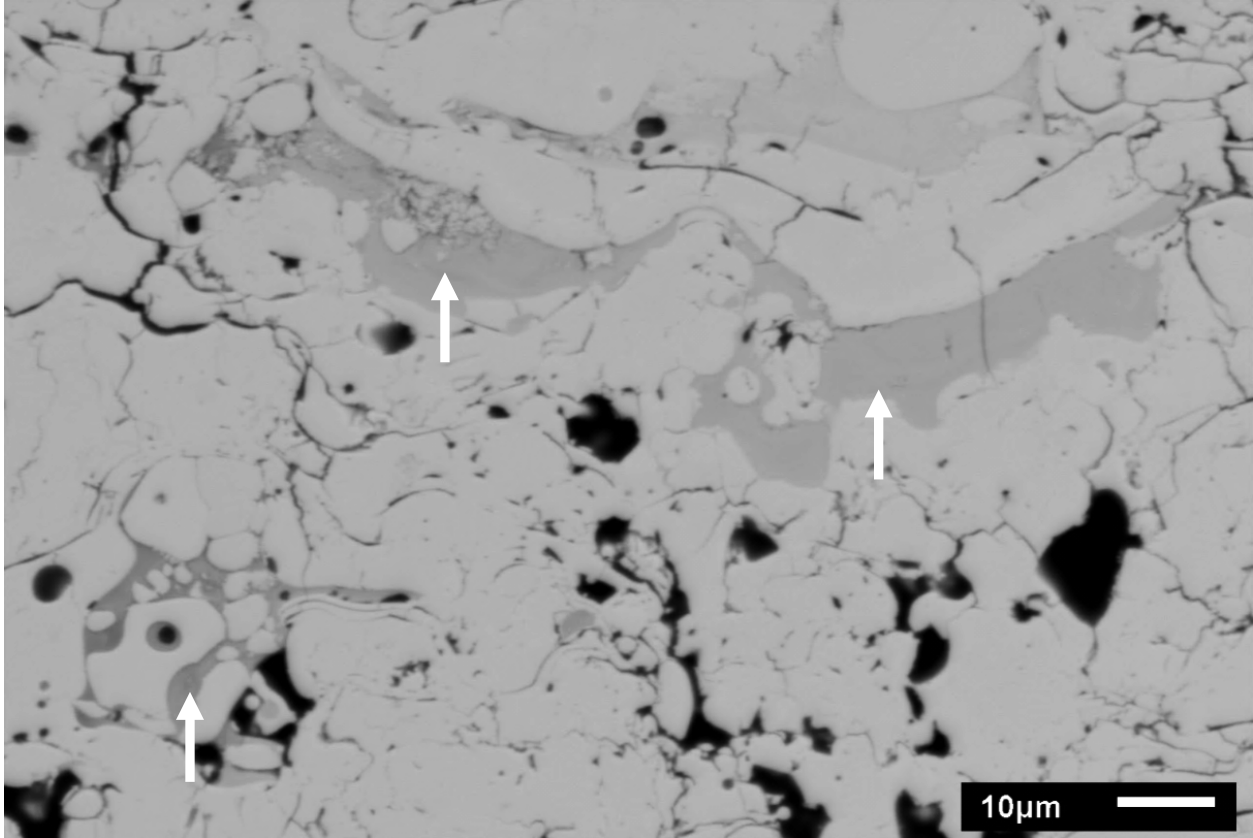


Figure 24 - CP-LD in the as-processed condition. White arrows indicate regions of SiO<sub>2</sub> and Al<sub>2</sub>O<sub>3</sub> impurities.



**Figure 25 - CP-LD in the as-processed condition. White arrows indicate regions of SiO<sub>2</sub> and Al<sub>2</sub>O<sub>3</sub> impurities.**

Some of the impurity regions appear to be individual splats (Figure 25 - far right arrow) whereas others seem to be unmelted particles (Figure 25 - lower left arrow). This observation suggests the impurity elements are discrete powder particles that are randomly incorporated into the coating during the spraying process.

After 10 hours at 1300°C, Figure 26, many of the micro-cracks have disappeared while the larger horizontal delaminations remain present.

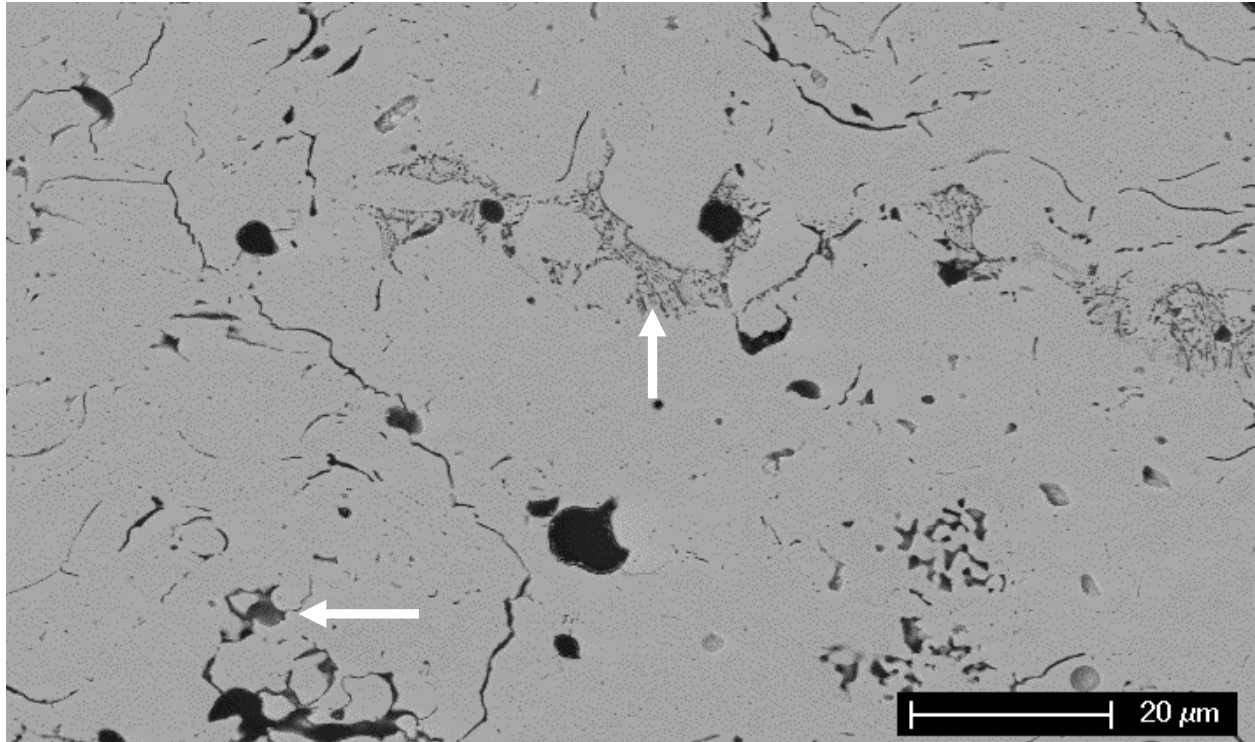


**Figure 26 - CP-LD after 10 hours at 1300°C. White arrows indicate regions of SiO<sub>2</sub> and Al<sub>2</sub>O<sub>3</sub> impurities.**

The impurity regions have changed in appearance from splat-like structures (Figure 27) to a more segregated structure (Figure 28 – red box). Thus the silica-alumina rich regions appeared to have redistributed and/or coarsened.

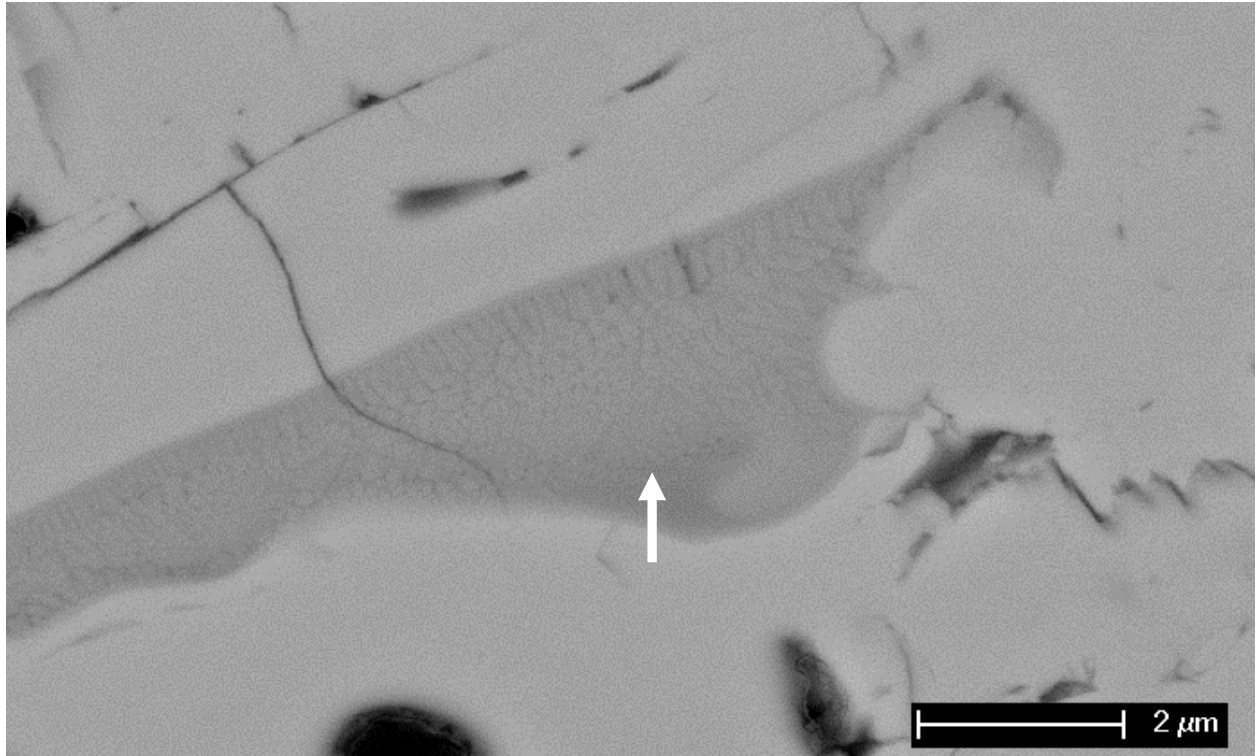


**Figure 27 - CP-LD in the as-processed condition. White arrows indicate regions of SiO<sub>2</sub> and Al<sub>2</sub>O<sub>3</sub> impurities.**

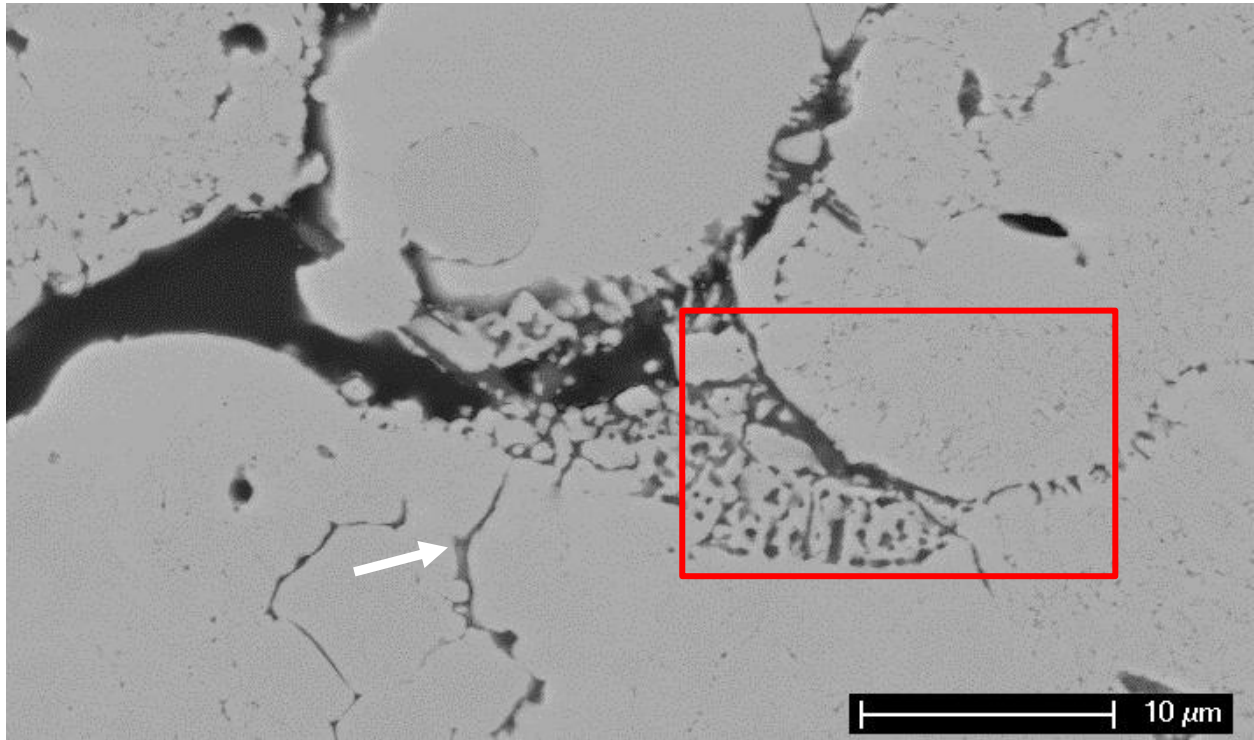


**Figure 28 - CP-LD after 10 hours at 1300°C. White arrows and red box indicate regions of  $\text{SiO}_2$  and  $\text{Al}_2\text{O}_3$  impurities.**

After 100 hours at 1300°C, Figure 29, the splat-like structure of the as-sprayed coating was no longer distinguishable.

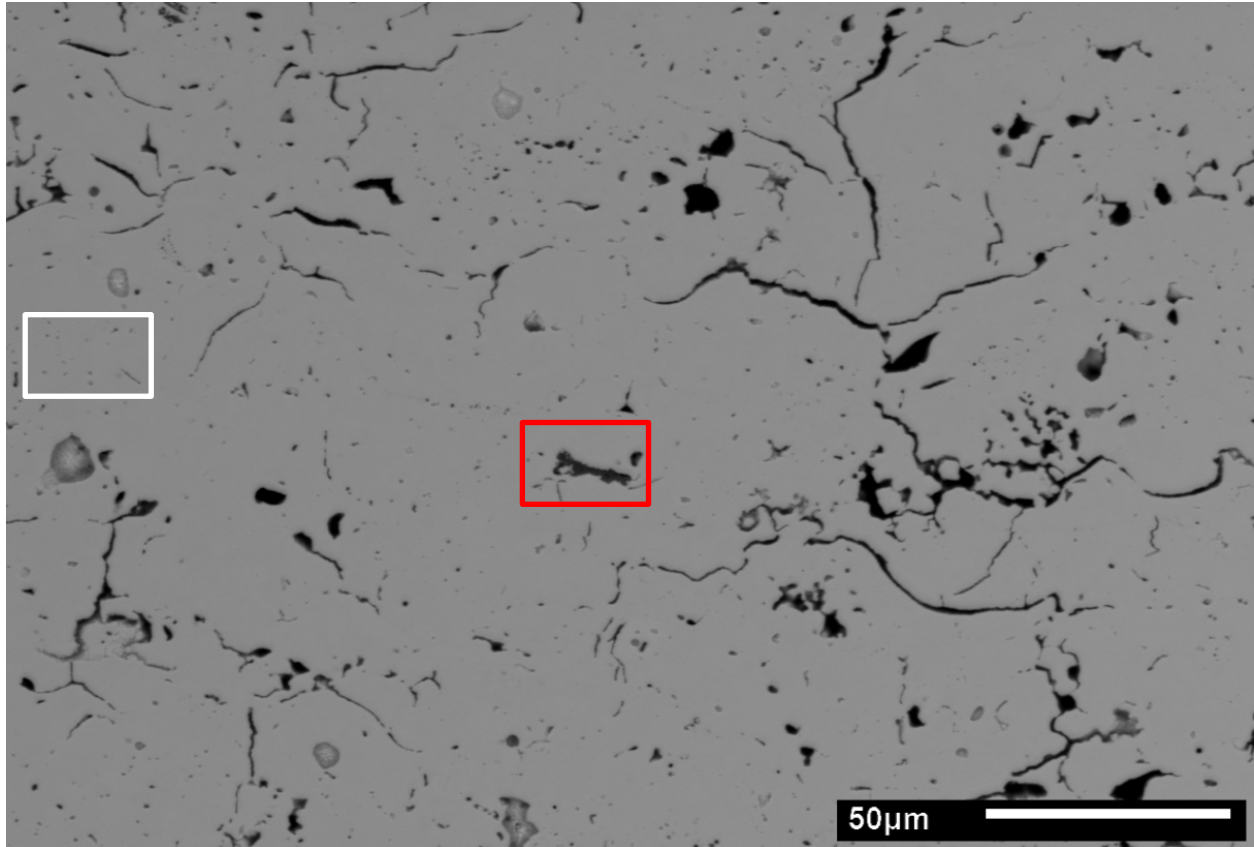


**Figure 29 - CP-LD after 100 hours at 1300°C. White box highlights small pores. Red box indicates a region of  $\text{SiO}_2$  and  $\text{Al}_2\text{O}_3$  impurities.**

Vertical and horizontal micro-cracks had almost completely healed, leaving small isolated pores behind (white box). The larger horizontal delaminations had also begun to bridge and heal, although some of the larger delaminations still exist.

Small pools of the impurity elements appeared all over the coating (Figure 29 - red box). A higher magnification micrograph of the highlighted region is shown in Figure 30.

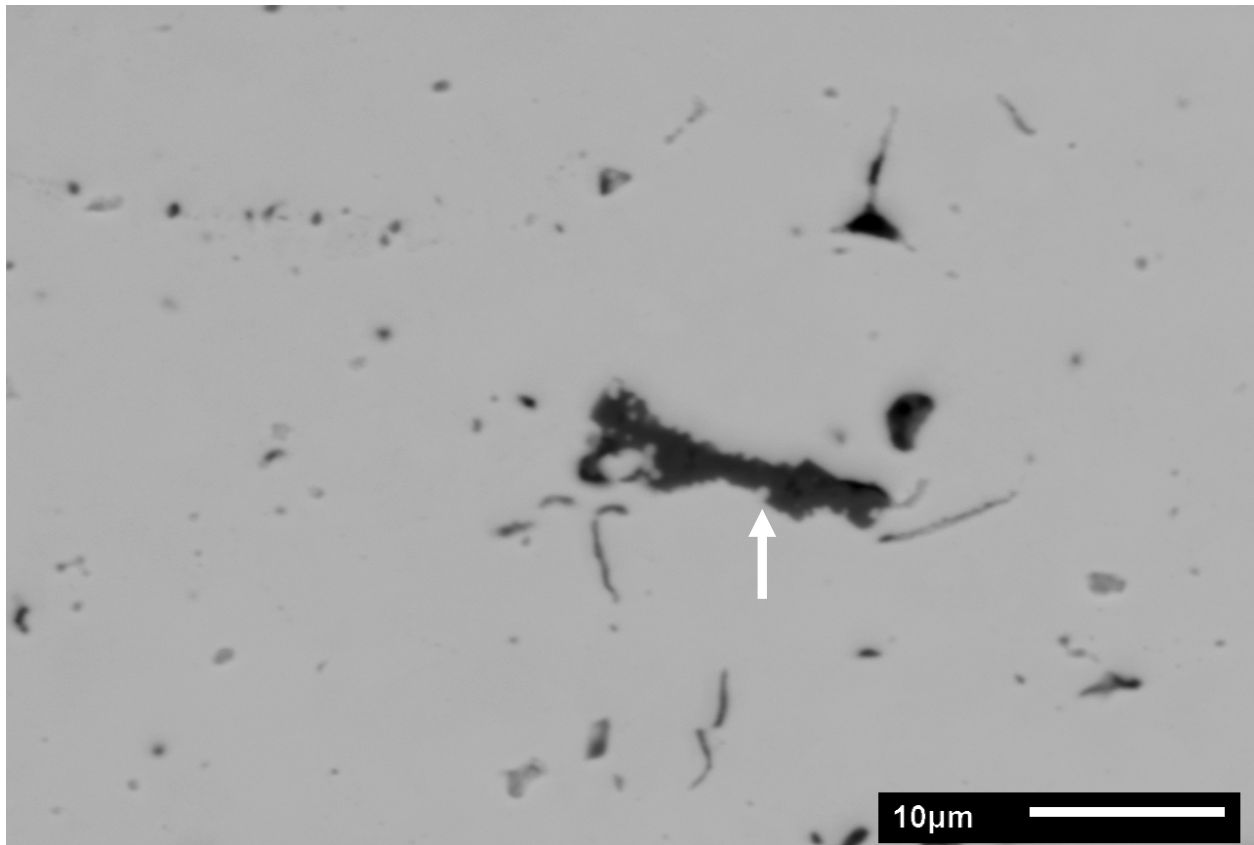


**Figure 30 - CP-LD after 100 hours at 1300°C. White arrows indicate regions of SiO<sub>2</sub> and Al<sub>2</sub>O<sub>3</sub> impurities.**

Composition of these pooled regions were difficult to measure as they were very small (<1µm) and pickup from the surrounding regions during EDS analysis was a problem. Regardless, the primary constituents were silicon, aluminum with traces levels of magnesium and sodium.

After 100 hours at 1200°C, Figure 31, many of the small microcracks had healed. The morphology of the impurity regions did not seem to change to the extent they did after 100 hours at 1300°C. Many of these regions, such as that indicated by the white arrows in Figure 31, still appeared to have a splat-like shape whereas the impurity regions in the 100 hour 1300°C coatings appeared more like pools.

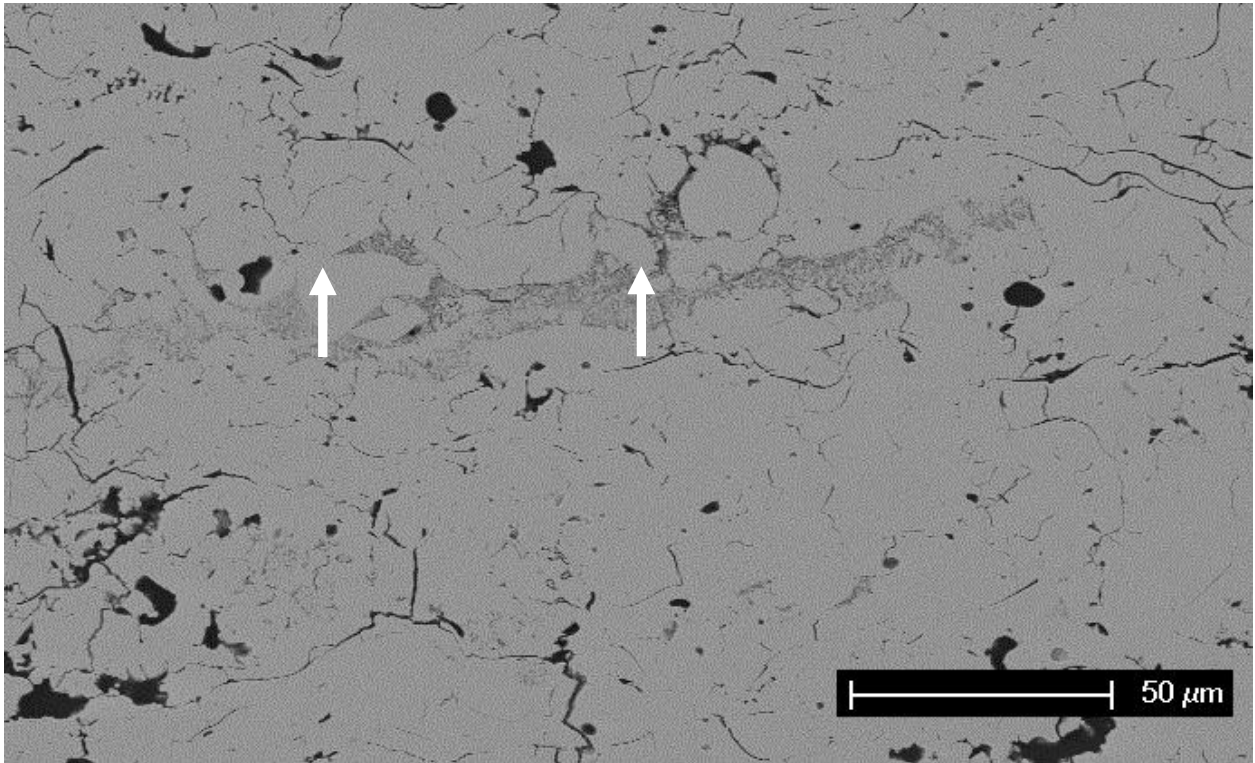


**Figure 31 - CP-LD after 100 hours at 1200°C. White arrows indicate regions of SiO<sub>2</sub> and Al<sub>2</sub>O<sub>3</sub> impurities.**

The as-processed HP-DVF coating is shown in Figure 32.

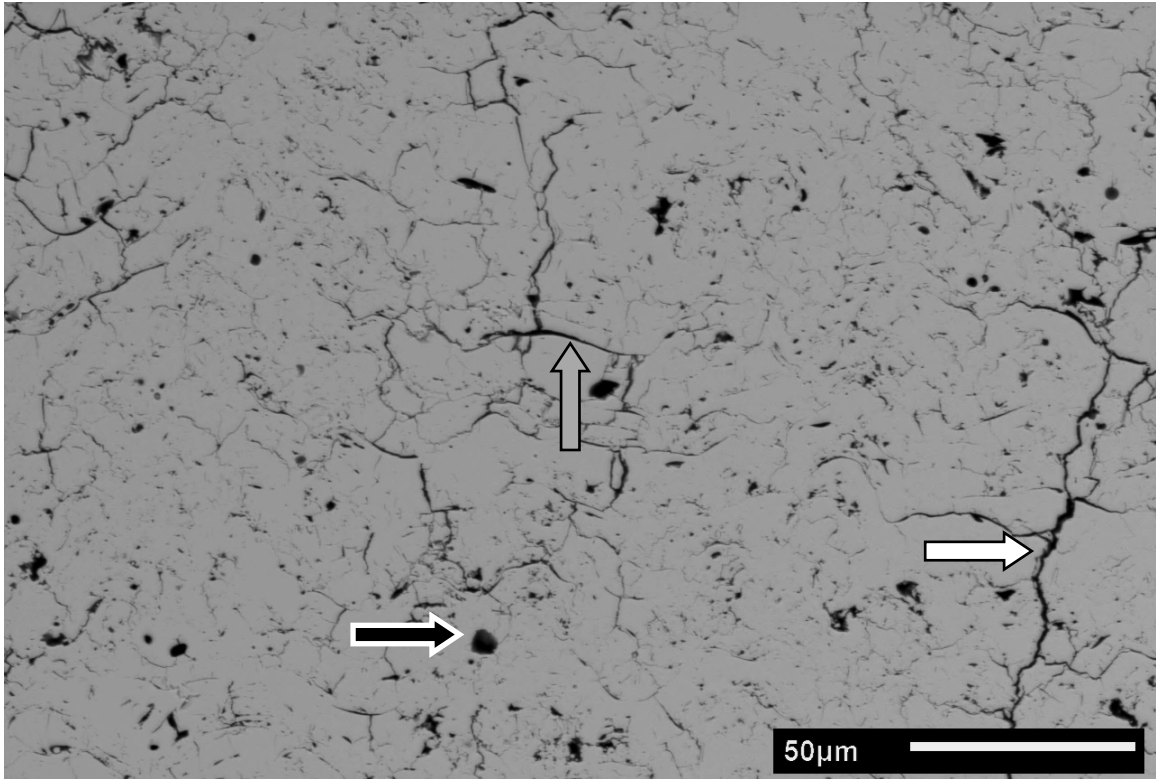


**Figure 32 - HP-DVF in the as-processed condition. White arrows indicate vertical fissures, black – globular pores and grey – horizontal delaminations.**

The large vertical fissures, which are characteristic of this coating, are indicated by the white arrow, horizontal delaminations by the gray arrow and globular pores by the black arrow. This coating also contained a high density of fine micro-cracks which are scattered all over the coating.

With 10 hours at 1300°C, Figure 33, many of the small micro-cracks had begun to heal/bridge as indicated by the white box. The larger vertical fissures and horizontal delaminations remained open though.

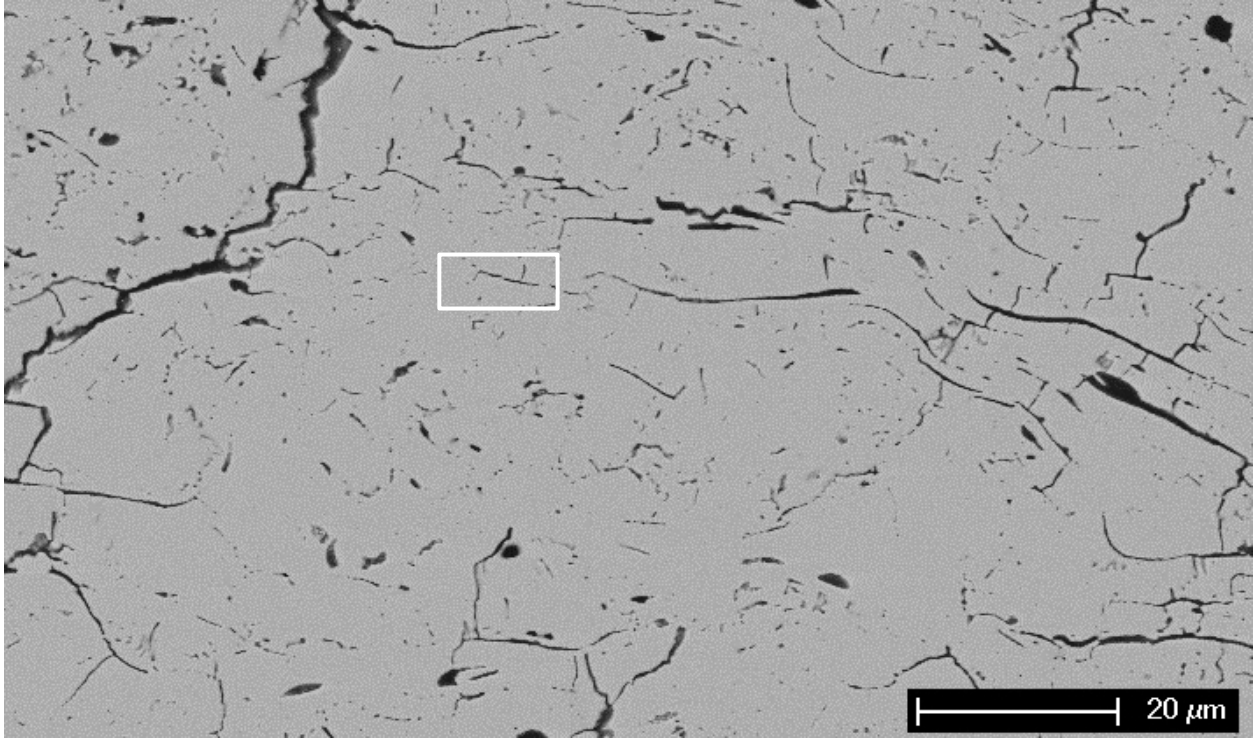


**Figure 33 - HP-DVF after 10 hours at 1300°C.**

With an additional 90 hours, the micro-cracks in the 100 hour specimen at 1300°C, Figure 34, healed even further leaving small round pores throughout the coating (red box).

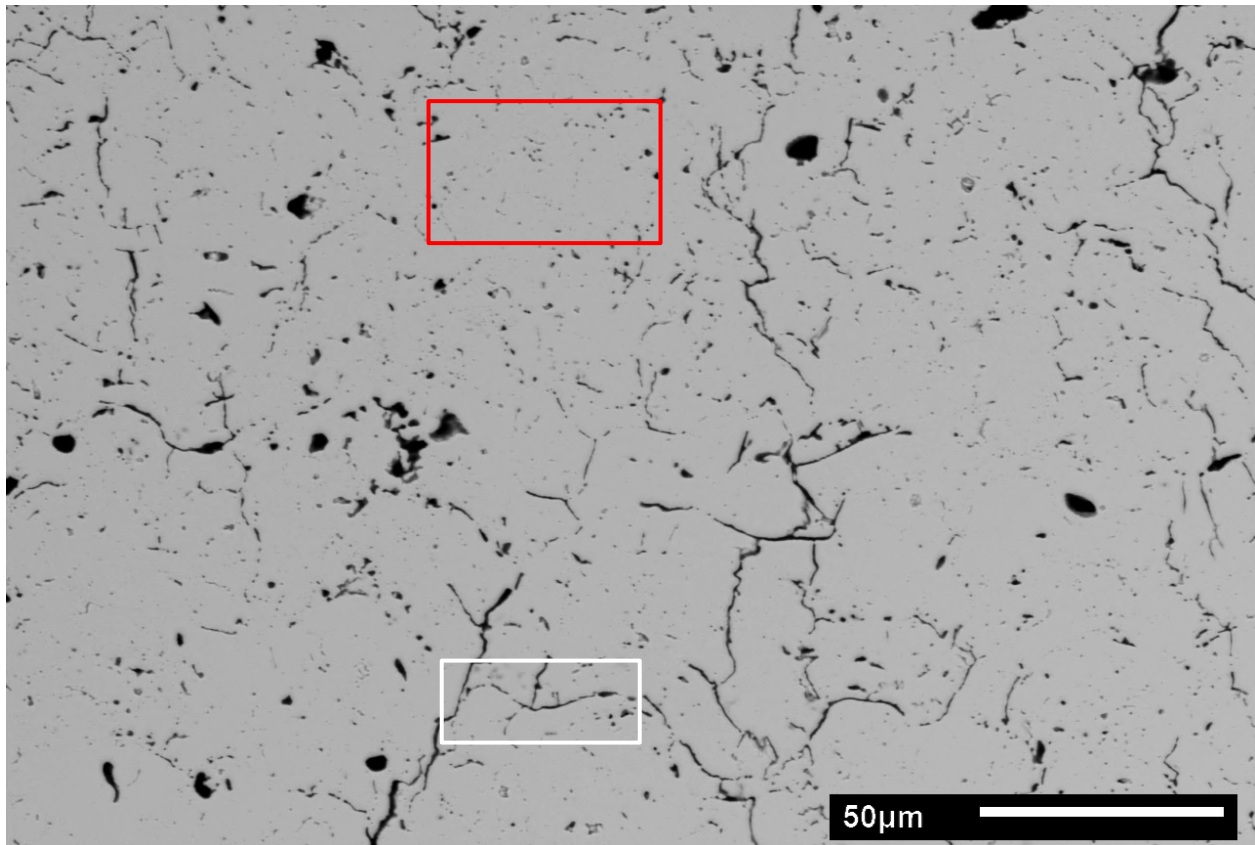


**Figure 34 - HP-DVF after 100 hours at 1300°C.**

Furthermore, some of the larger horizontal delaminations (white box) had begun to make contact/heal. The large vertical fissures still remained open though.

The 100 hour 1200°C specimen, shown in Figure 35, again exhibited significant closure of the micro-cracks. Larger delaminations and pores remained open.

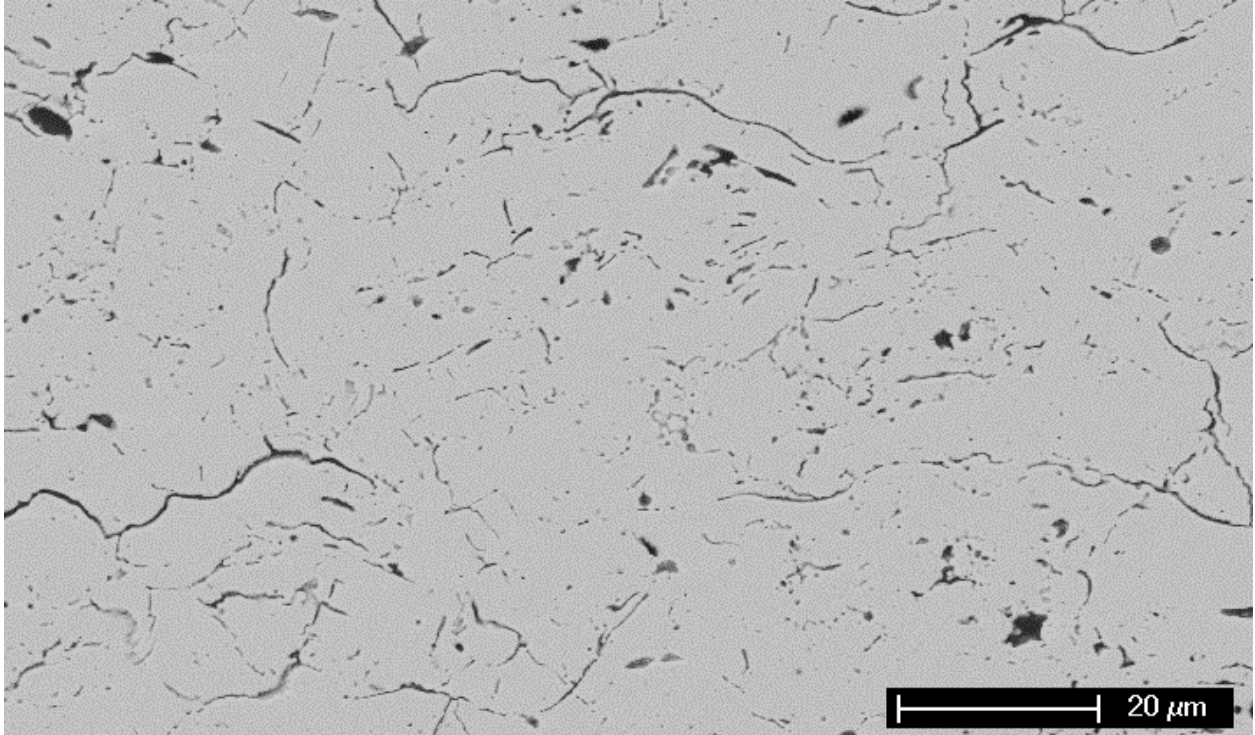


**Figure 35 - HP-DVF after 100 hours at 1200°C.**

The last specimen is the CP-DVF topcoat, which is shown in Figure 36.

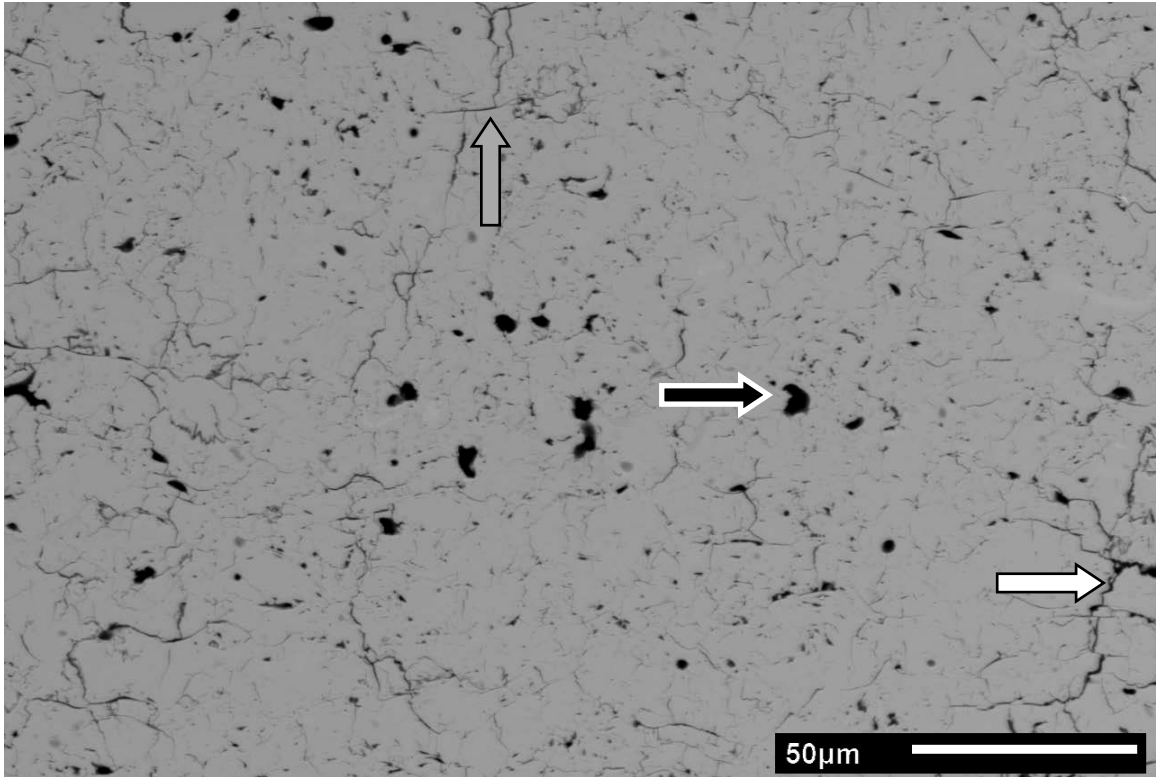


**Figure 36 - CP-DVF in the as-processed condition. White arrows indicate vertical fissures, black – globular pores and grey – horizontal delaminations.**

At first glance, the microstructure of the CP-DVF coating appeared similar to that of the HP-DVF coating. There were large vertical fissures, horizontal delaminations, globular pores and a high-density of the micro-cracks. However, closer examination revealed impurity splats and particles. The splat highlighted in Figure 37 was composed of zirconium, magnesium and oxygen.

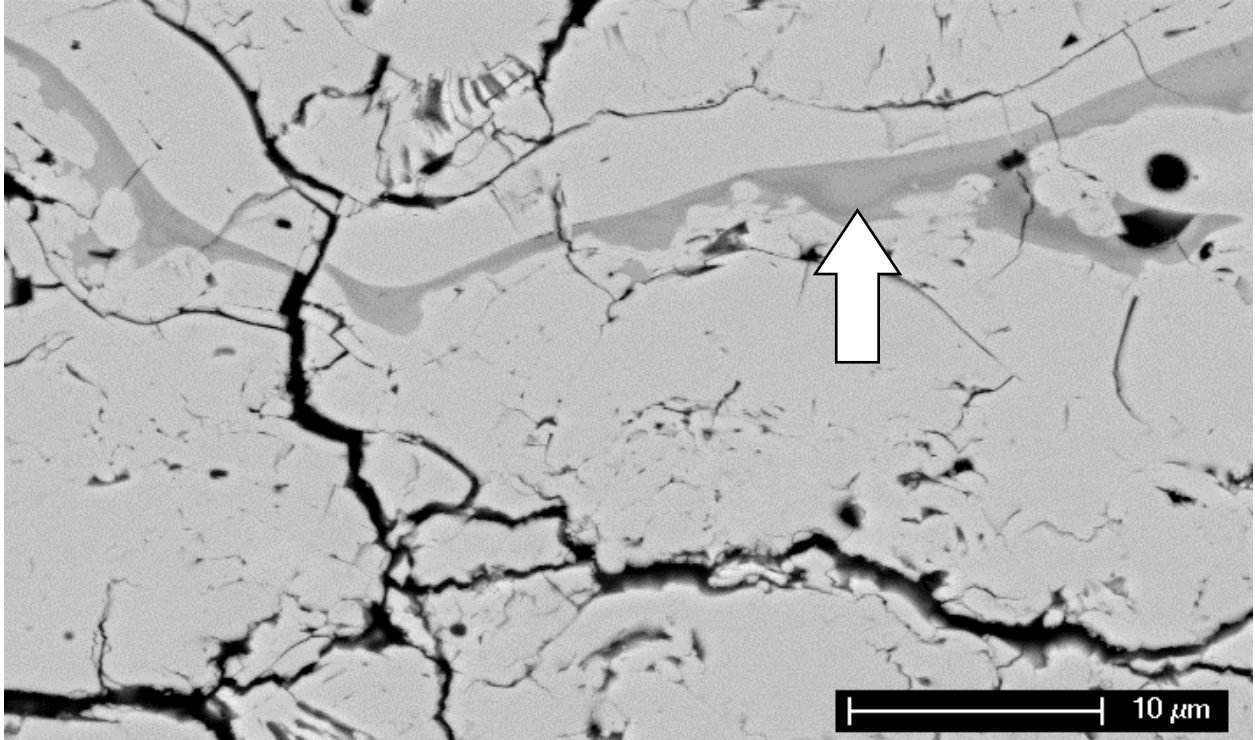


**Figure 37 - CP-DVF in the as-processed condition. White arrows indicates a splat rich in magnesium and zirconium.**

Figure 38 shows another impurity particle.

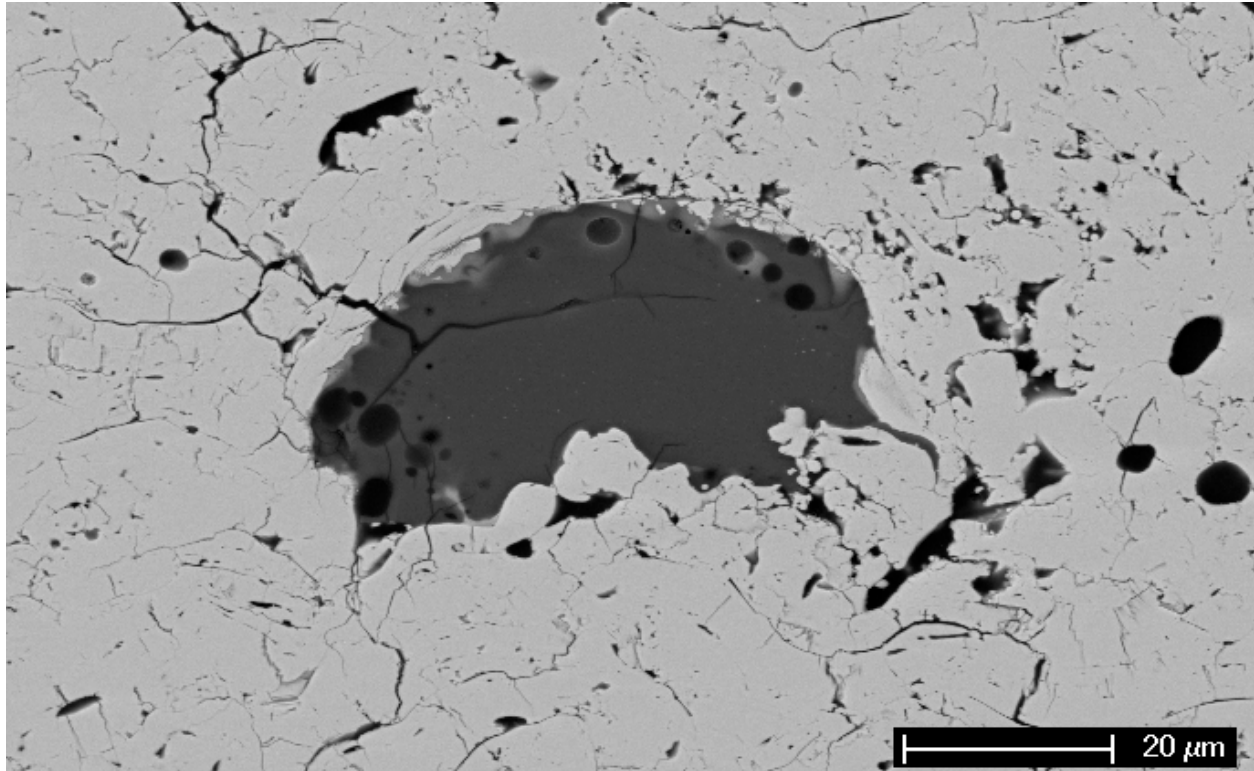


**Figure 38 – CP-DVF in the as-processed condition. Large black particle was a silica-alumina rich phase.**

This particle's composition, determined by standardless EDS, was approximately: 42 at% Si, 5 at% Al, 1 at% Hf and 51 at% oxygen. This composition does not seem to correspond to any  $\text{SiO}_2\text{-Al}_2\text{O}_3\text{-HfO}_2$  combination, as the oxygen content is not high enough to permit the appropriate molar ratios to be satisfied, thus either the EDS is not measuring the composition accurately or this particle is oxygen deficient. Most likely the EDS measurement is inaccurate and the particle is silica with minor alumina contents.

Upon exposure for 10 hours at  $1300^\circ\text{C}$ , Figure 39, the micro-cracks in the coating healed.

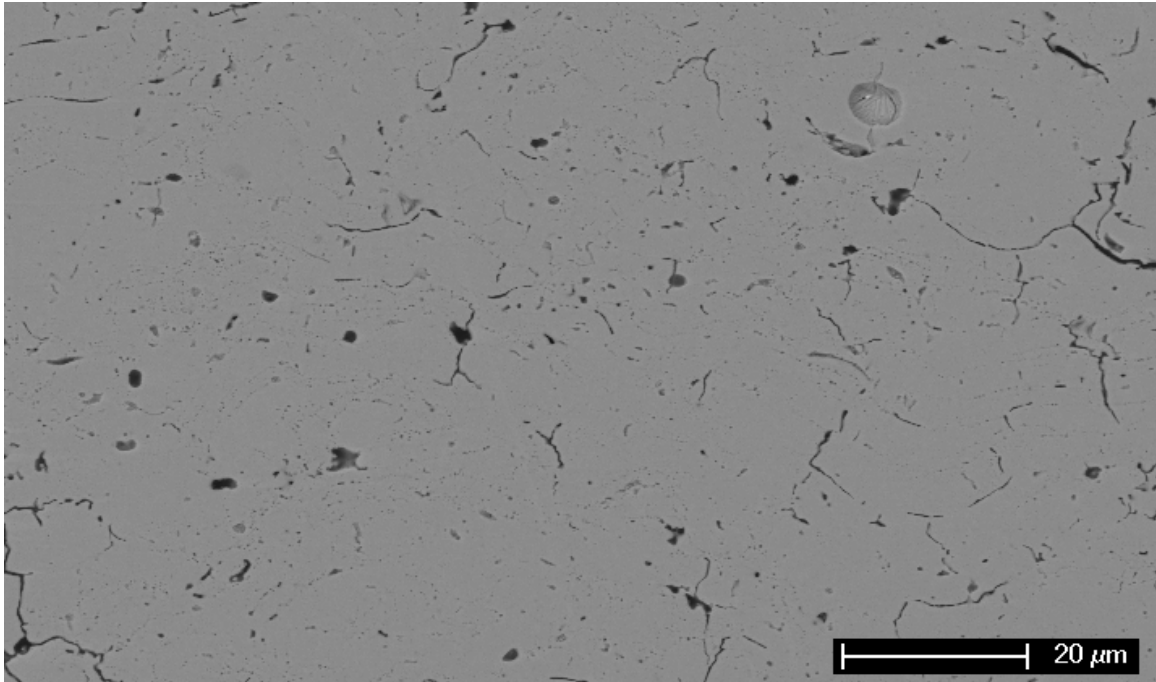


**Figure 39 - CP-DVF after 10 hours at 1300°C**

Furthermore, small pores appeared all over the coating, which are visible in Figure 40.

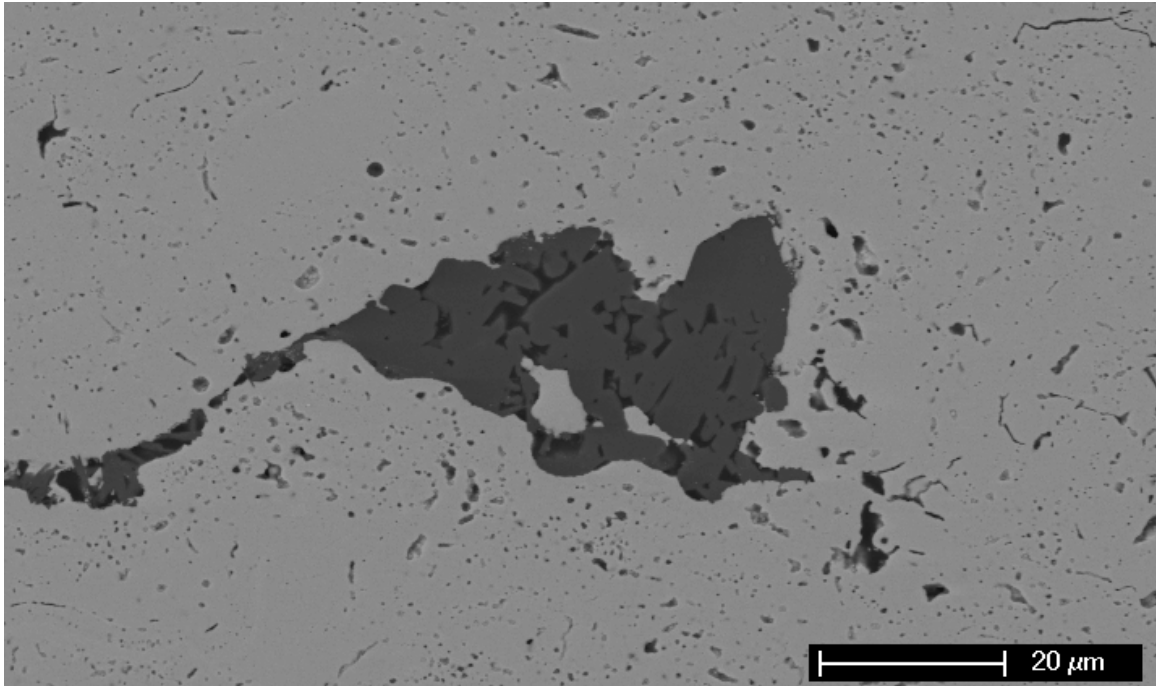


**Figure 40 - CP-DVF after 10 hours at 1300°C. The dark structure is a silica-alumina impurity particle.**

These pores were scattered all over the coating. As shown in Figure 40, the pores were scattered around an impurity particle rich in silicon and aluminum, however, they were also located all over the coating.

After 100 hours at 1300°C, the quantity and size of the small pores increased, Figure 41.

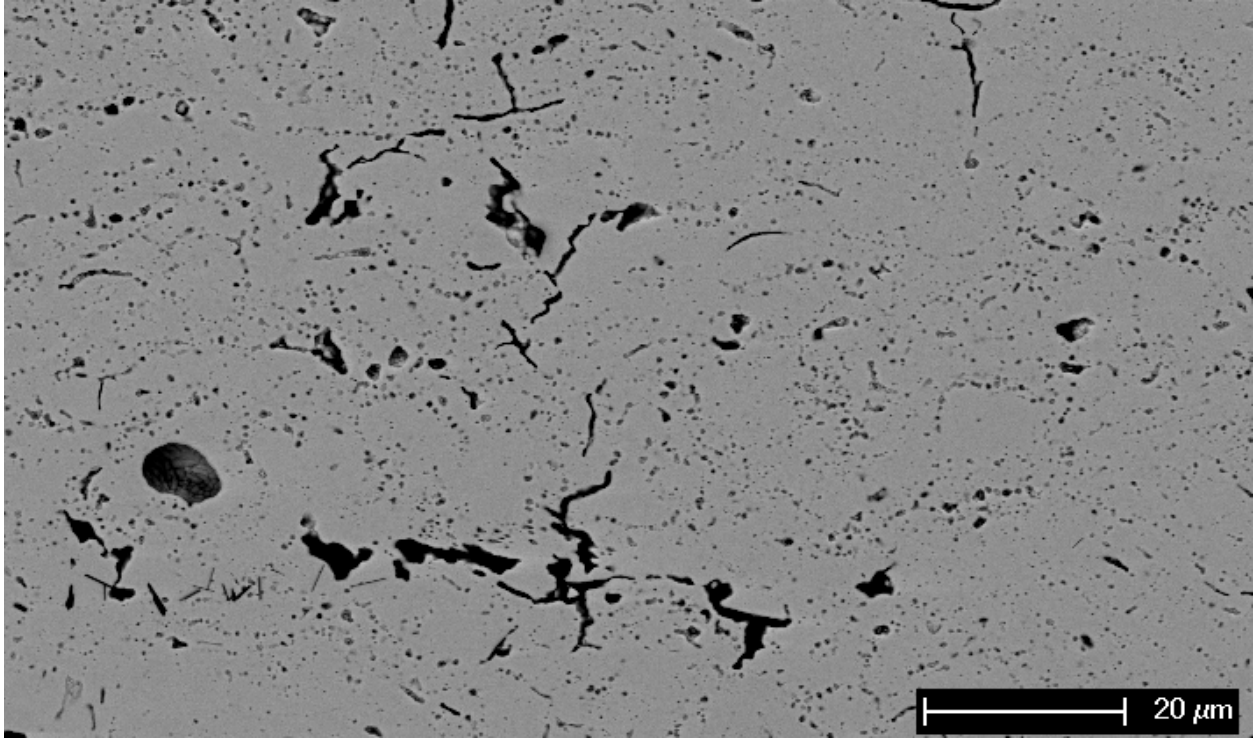


**Figure 41 - CP-DVF after 100 hours at 1300°C**

Likewise, the splat-structure present in the as-processed coating no longer existed in this specimen and many of the large fissures and horizontal delaminations closed. A high magnification image of the small pores is shown in Figure 42.

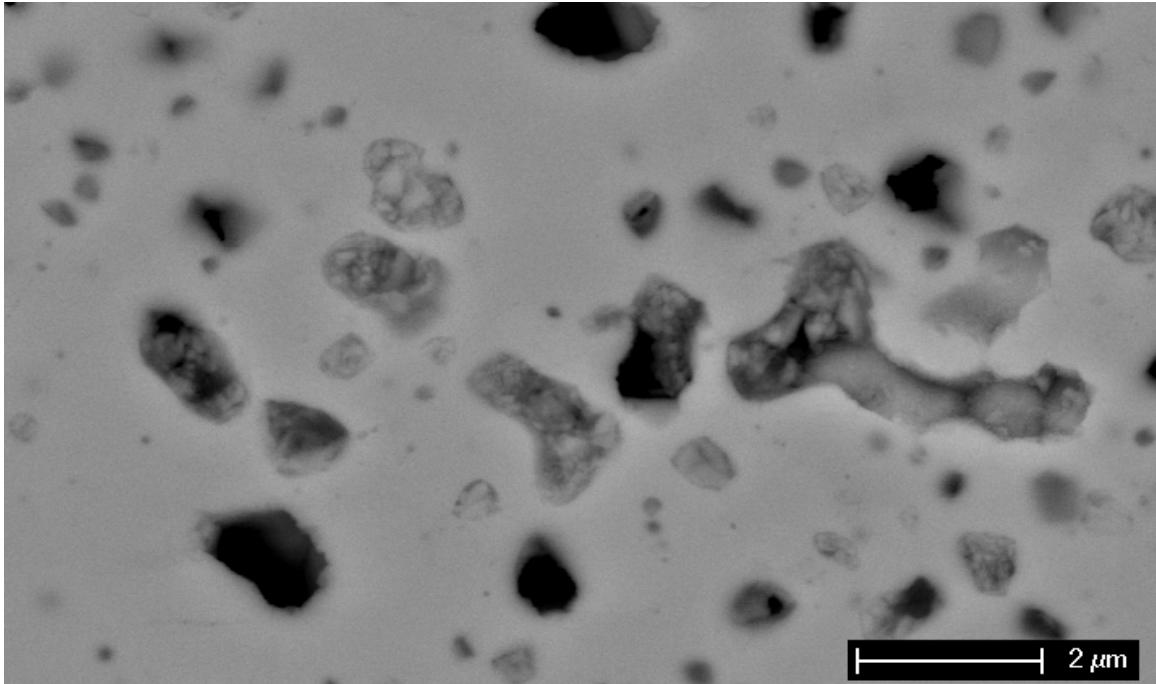


**Figure 42 - CP-DVF after 100 hours at 1300°C. High-magnification image of pores in the coating.**

The pores did not appear to contain any secondary impurity phase, at least to the detectable limit of the EDS equipment. The formation and growth of these pores during the 100 hour sintering period could account for the additional volume needed to cause the decrease in the density which was observed in the previous section. However, the source and driving force for their formation is unclear.

The 100 hour 1200°C coating, Figure 43, also contained these pores, though they were much smaller than those in the 1300°C specimen.

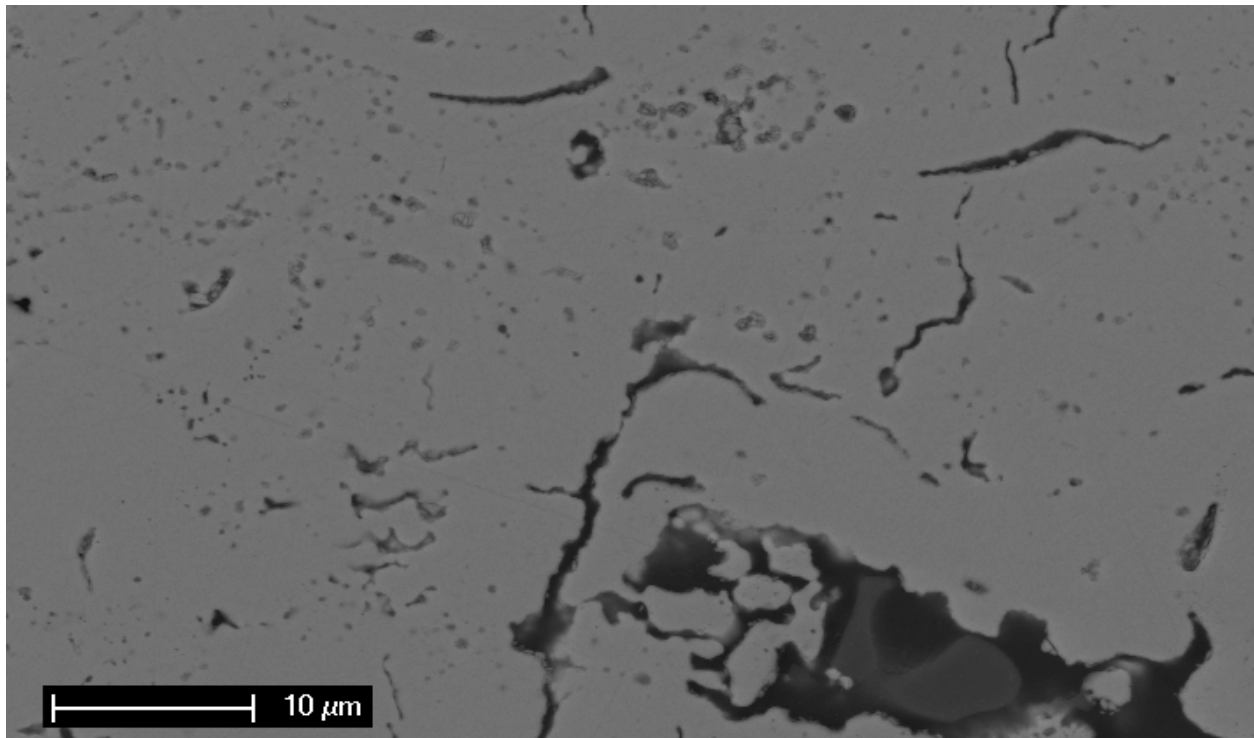


**Figure 43 - CP-DVF after 100 hours at 1200°C.**

To recap, the microstructure of the HP-LD coating was quite stable in all of the heat treatments. Many of the micro-cracks, delaminations and globular pores were still present after the 100 hour 1300°C heat treatment. At 1200°C only minor bridging of micro-cracks and inter-splat pores occurred. The lack of changes to the microstructure at 1200°C supports the previous result that the density of the coating did not change during this exposure.

The micro-crack density in the HP-DVF coating decreased when it was exposed to the elevated temperatures, however, the vertical fissures and larger horizontal delaminations remained largely unchanged even after 100 hours at 1300°C.

The CP-LD specimens behaved much differently from the HP-LD specimens. In all three heat treatments micro-cracks closed, inter-splat pores vanished and densification appeared to occur. Impurity elements of aluminum, silicon and magnesium were found throughout the

coatings. In the 1300°C exposures, these impurities appeared to have redistributed throughout the coating, and in some cases, appeared to be pooling. This same behavior was also observed in the CP-DVF specimens exposed at 1300°C. Furthermore, the closure of micro-cracks and pores in the 1200°C specimen also confirmed the previously observed increase in the density of the CP-LD coating.

The CP-DVF topcoat exhibited pore formation and pore growth during the 1200°C and 1300°C exposures. These pores could potentially account for the decrease in the density observed in the 1300°C 100 hour specimen. The source and driving force for these pores remains unclear.

**4.1.1.3.3 Phase Analysis** The zirconia rich portion of the  $ZrO_2$ - $Y_2O_3$  phase diagram is presented in Figure 44.

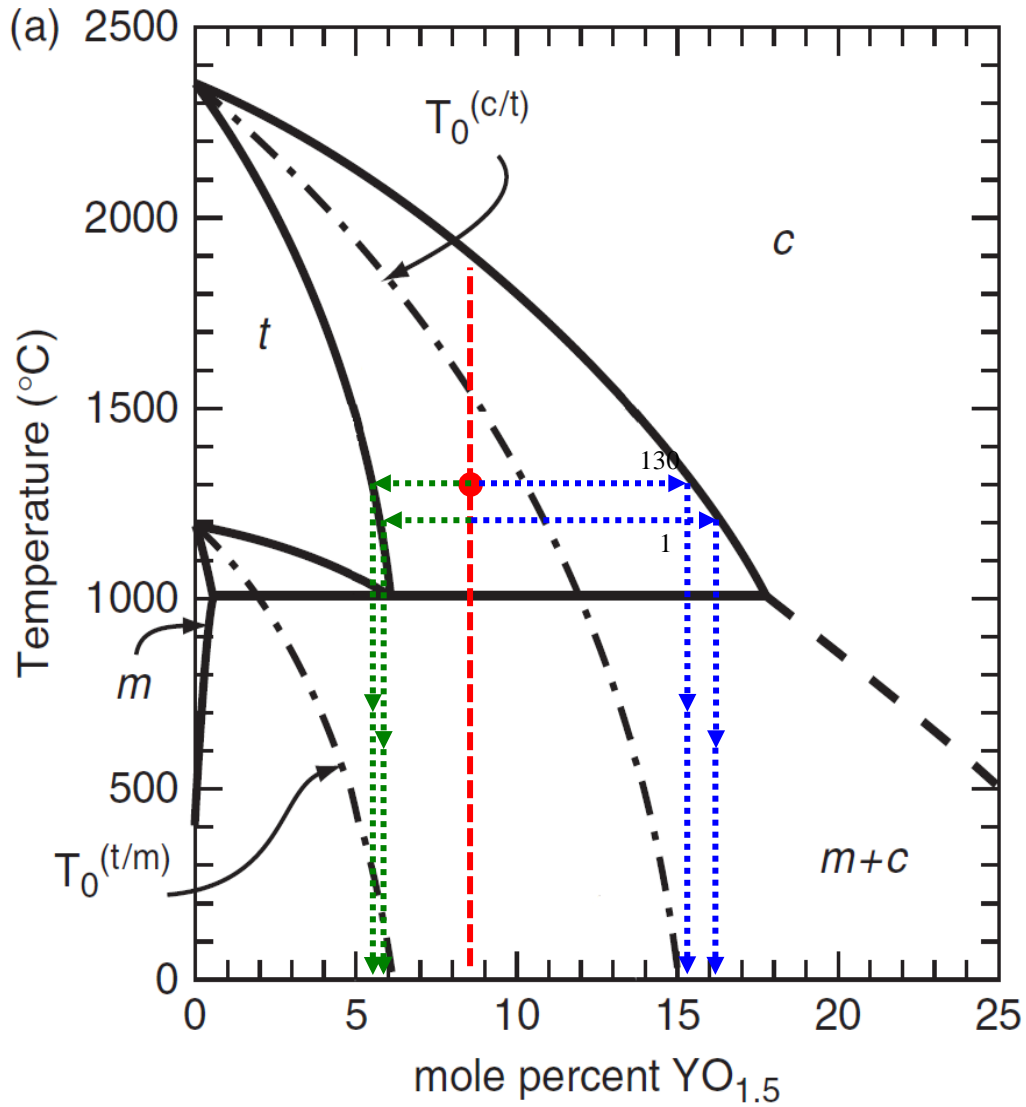


Figure 44 -  $\text{ZrO}_2\text{-YO}_{1.5}$  phase diagram [54].

In the as-sprayed condition, all of the free-standing topcoats used in this study had the metastable tetragonal-primed ( $t'$ ) phase with a yttria content of  $\sim 7.5\text{wt}\%$   $\text{Y}_2\text{O}_3$  (equivalent to  $\sim 8.5\text{mol}\%$   $\text{YO}_{1.5}$ ). A small amount of the monoclinic phase was observed in the CP-LD coating which is believed to be caused by the incorporation of unmelted YSZ powder, of the monoclinic structure, into the coating. The amount of monoclinic phase present was determined using the

one peak powder diffraction method described in [37]. In short, a detailed powder diffraction pattern of the coating is gathered and then the peak height of the (111) cubic /tetragonal phase, which occurs around  $\sim 30^\circ 2\theta$ , is compared to the peak height of the (111-) monoclinic peak. The ratio of these peak heights yields the approximate phase fractions. An example of these peaks is shown in Figure 45. Note the previously mentioned monoclinic peak for the CP-LD coatings.

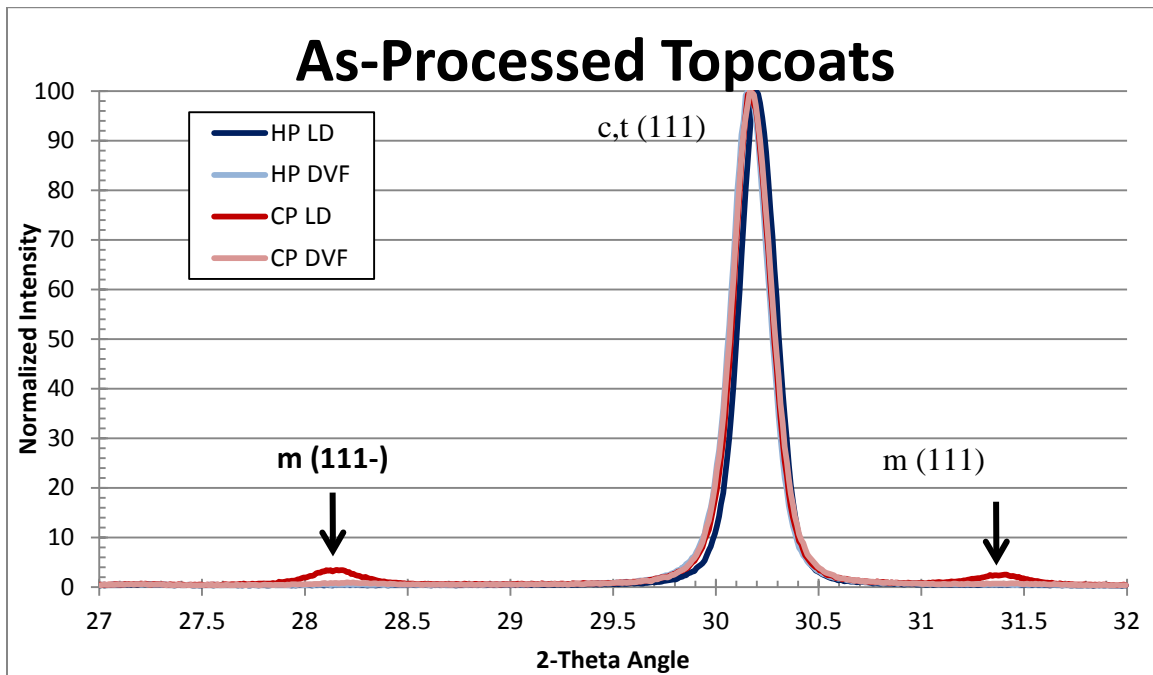


Figure 45 - XRD patterns for the as-processed structure of the four topcoats.

The yttria-rich  $t'$  phase present in these coatings forms directly from the high temperature cubic phase via a displacive transformation as the structure is rapidly quenched during the plasma spraying process and passes below the  $T_0(c/t)$  curve in Figure 44. The metastable  $t'$  is beneficial because it does not change crystal structure as it is heated and cooled (assuming it is not reheated over the  $T_0(c/t)$ ), whereas pure zirconia does (i.e. monoclinic  $\rightarrow$  tetragonal  $\rightarrow$  cubic). However, the  $t'$  structure is only metastable and when heated into the two phase field, red

dot in Figure 44, decomposition into the equilibrium yttria-deficient tetragonal phase (t) (green dotted line) and the yttria-rich cubic phase (c) (blue dotted line) can occur. The new tetragonal phase which forms is susceptible to the ‘tetragonal to monoclinic’ martensitic phase transformation at lower temperatures if the composition crosses the  $T_0(t/m)$  curve [54, 55]. The 4% volume increase associated with this phase transformation can be detrimental to the structural integrity of the TBC system and is therefore undesired. The extent of the t’ phase decomposition could be monitored by measuring the amount of monoclinic phase that forms at the expense of the newly formed tetragonal phase, however, this transformation does not always occur. It is sensitive to grain size, mechanical restraint, and tetragonality (i.e. yttria content) among other factors [54, 55]. Furthermore, it is suppressible if the coating is rapidly quenched to room temperature, which was the case in this set of experiments.

Instead, the decomposition can also be monitored by examining another region of the XRD pattern around  $72-75^\circ 2\theta$  where the (400) cubic, (400) and (004) tetragonal peaks can be differentiated. While it is difficult to differentiate the metastable tetragonal phase from the newly formed tetragonal phase, as their lattice parameters are similar, the cubic phase which forms is more easily distinguished. Thus, for this set of experiments the evolution of the cubic phase was used to compare the rates of the decomposition of the t’-phases.

The XRD patterns for the HP-LD specimens in the  $72-75^\circ 2\theta$  region are given in Figure 46.

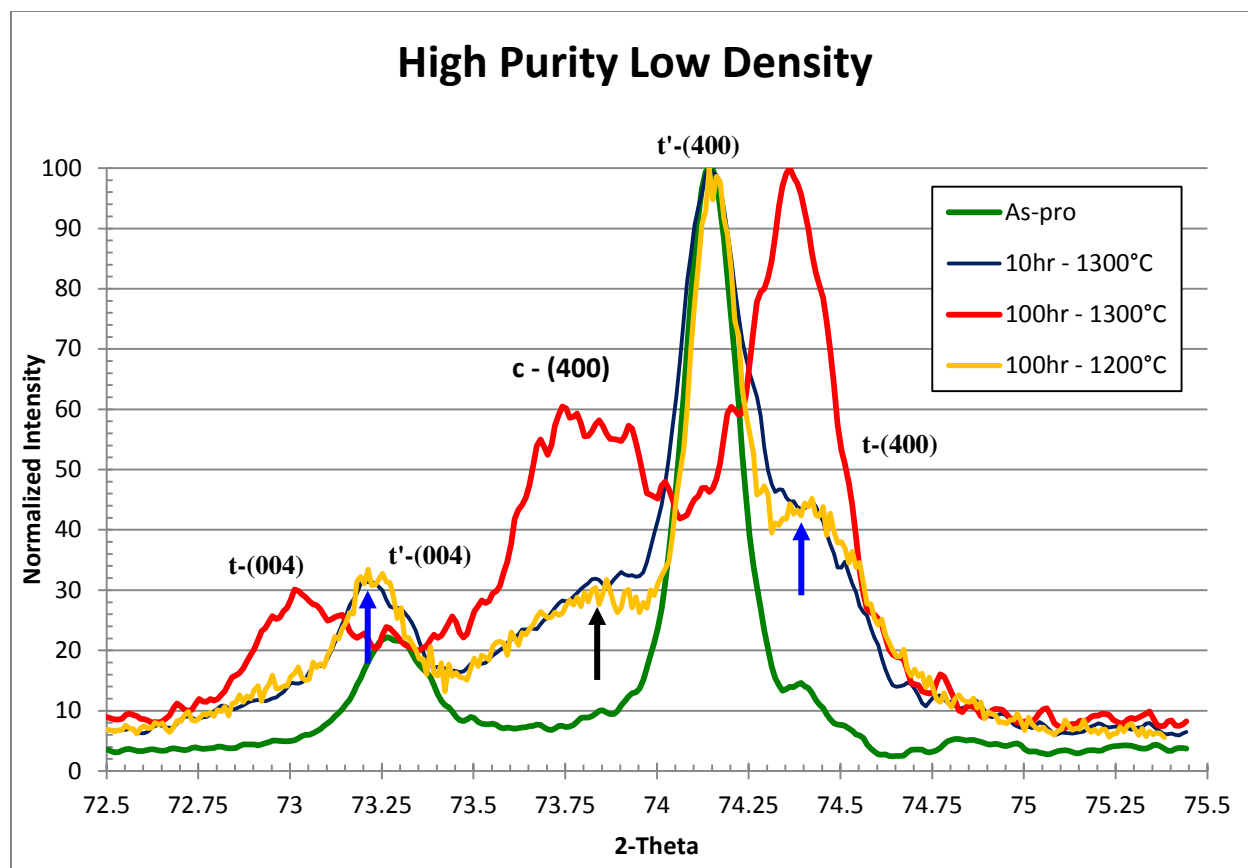


**Figure 46 – 72°-75° 2θ region of the XRD pattern for the HP-LD topcoat before and after the thermal exposures.**

In the as-processed condition (green curve) the coating was 100% t' where only the (004) and (400) peaks were present. After 10 hours at 1300°C (blue curve), both the t'-(400) and t'-(004) peaks formed shoulders (blue arrows) indicating the formation of the new low-yttria tetragonal phase. A faint cubic peak (black arrow) also formed. The 100 hour 1200°C pattern, gold curve, appeared to be identical to the 10 hour 1300°C pattern. While these XRD patterns indicated the structure was still dominated by the t'-phase because this peak has not shifted, this may not be accurate. Transmission electron microscopy (TEM) analysis of aged t'-YSZ performed by Krogstad et al [54] revealed that while XRD patterns suggest the t'-phase is present after short aging times, in actuality, this is only a pseudo-t' phase. They discovered that

at high temperatures and after short times the  $t'$ -phase rapidly dissociated into coherent, compositionally-modulated domains which were distinctly different from the starting  $t'$ -phase structure. Assuming their findings are applicable to this study, the  $t'$ -phase depicted in Figure 46 is likely to actually be the pseudo- $t'$  phase, not the true, as-processed  $t'$  phase. Regardless of this possibility, the newly formed cubic and tetragonal peaks on the XRD patterns should accurately represent true cubic and true tetragonal structures, unlike the  $t'$  peaks do. Thus, the phase evolution of these coatings still can be monitored by comparing the extent to which the cubic and tetragonal phases appear on the XRD patterns.

After 100 hours at 1300°C, the cubic and tetragonal peaks increased in intensity and the pseudo- $t'$  peak almost completely disappeared. Deconvolution of the cubic and two tetragonal peaks was not attempted as precise lattice parameters (i.e. compositions) and calibrated XRD equipment were unavailable. However, it remains clear the pseudo- $t'$  phase was almost completely gone.

The XRD patterns of the four heat treated HP-DVF coatings are given in Figure 47.

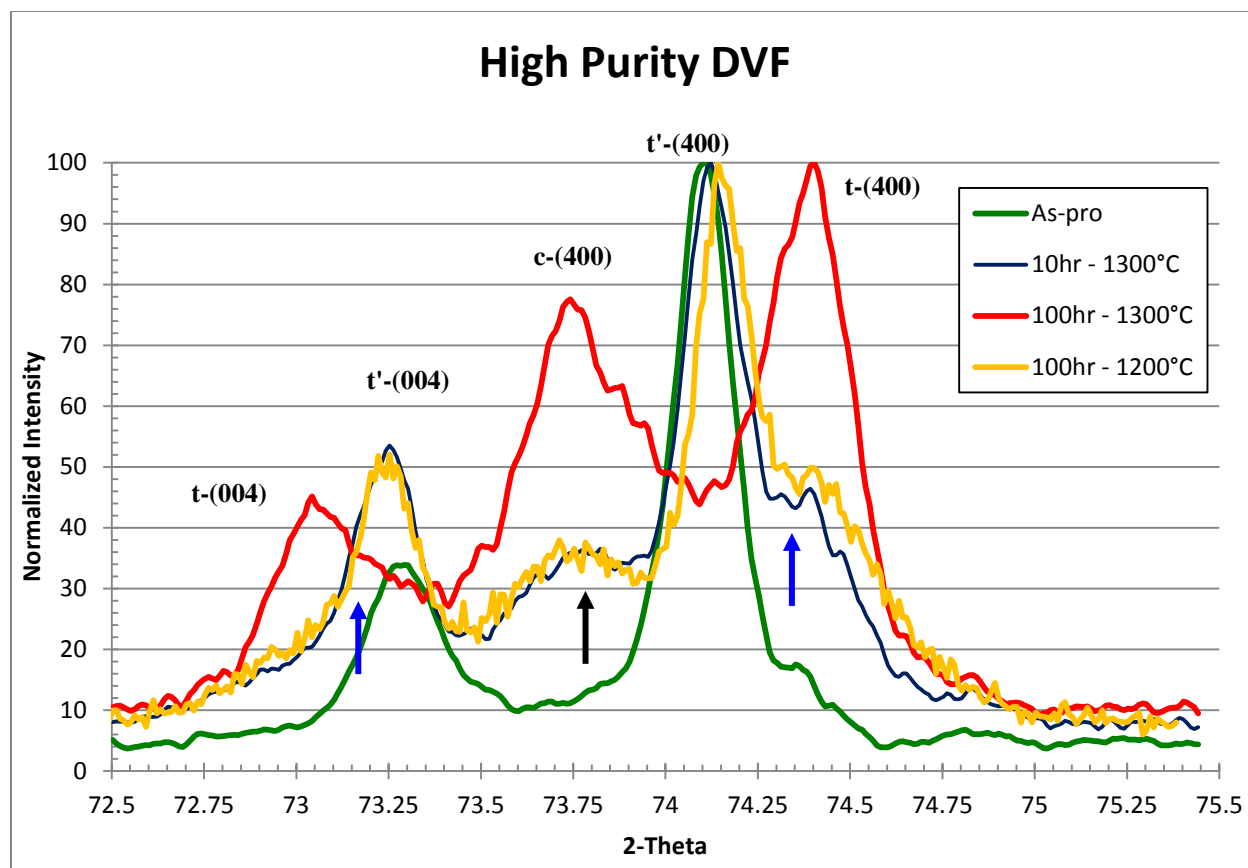


Figure 47 - 72°-75° 2θ region of the XRD pattern for the HP-DVF topcoat before and after the thermal exposures.

The HP-DVF and the HP-LD patterns appeared very similar if not identical. In the as-processed condition (green curve) the coating was 100%  $t'$  where only the (004) and (400) peaks were present. After 10 hours at 1300°C (blue curve), both the  $t'$ -(400) and  $t'$ -(004) peaks formed shoulders (blue arrows) indicating the formation of the new low-ytria tetragonal phase. A faint cubic peak (black arrow) also formed. The 100 hour 1200°C pattern, gold curve, appeared to be identical to the 10 hour 1300°C pattern. Finally, with the 100 hours at 1300°C specimen, the cubic and tetragonal peaks increased in intensity and the pseudo- $t'$  peak almost completely disappeared.

The XRD patterns for the CP-LD specimens are shown in Figure 48.

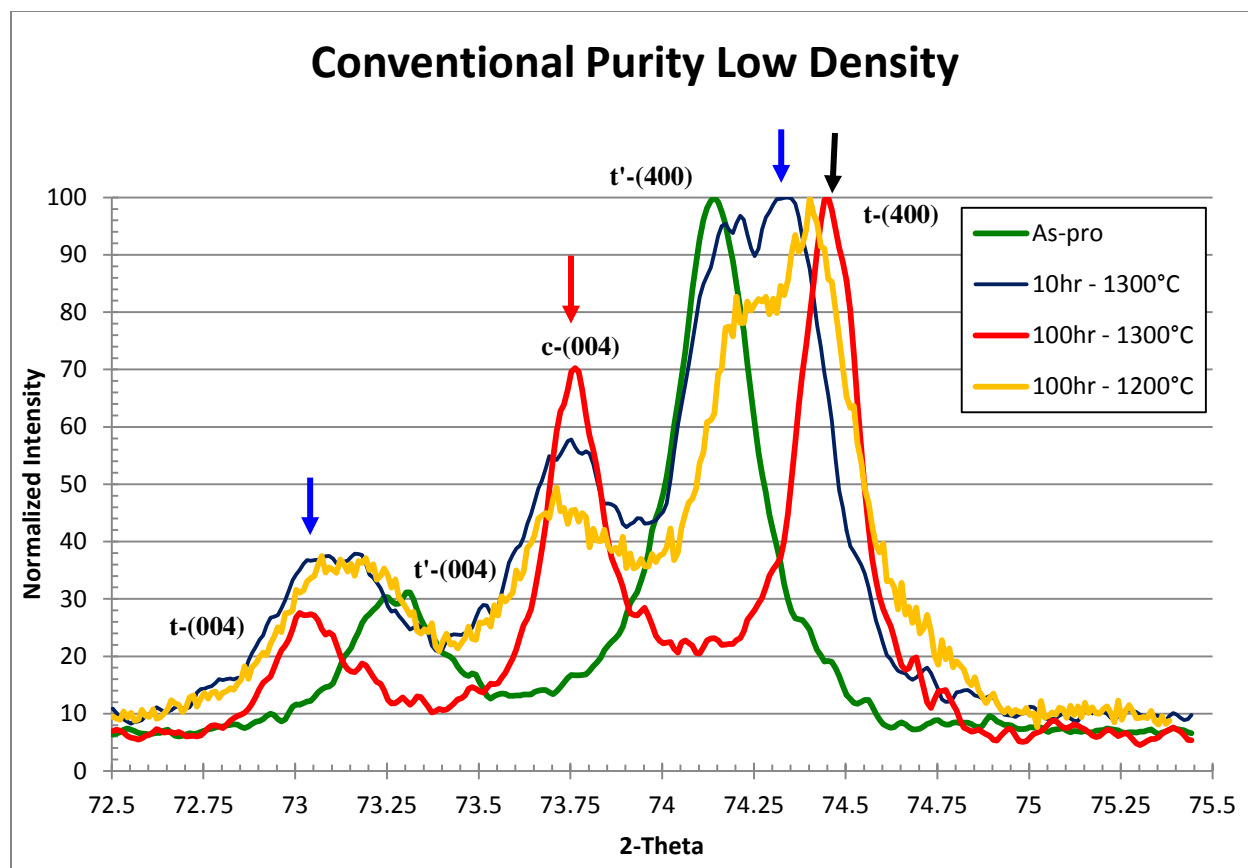


Figure 48 – 72°-75° 2θ region of the XRD pattern for the CP-LD topcoat before and after the thermal exposures.

The CP-LD topcoat behaved differently than the previous two topcoats. In the as-processed condition (green curve) the coating was 100%  $t'$  where only the (004) and (400) peaks were present as they were with the other coatings. After 10 hours at 1300°C (blue curve), two peaks, presumably the  $t$ -(400) and  $t$ -(004) peaks (blue arrows), formed next to the two pseudo- $t'$  peaks. Comparing this curve to the HP-LD curve, the intensity of the newly formed tetragonal phase was much stronger in the CP-LD specimen. Furthermore, a strong cubic peak appeared in this pattern. The 100 hour 1200°C pattern (gold curve) was similar to the 10 hour 1300°C pattern with the exception of the positions and relative intensities of the pseudo- $t'$ (400) and  $t$ -(400) peaks. After 100 hours at 1300°C, the pseudo- $t'$  phase peaks were gone and the XRD pattern

only had peaks from the cubic and tetragonal phases, thus the decomposition seemed to have completed.

An interesting observation with this particular specimen was that the evolution of the low-yttria tetragonal phase appeared to evolve over the course of the thermal exposure meaning the (400) tetragonal peak which formed after 10 hours (top blue arrow) shifted to smaller d-spacing (i.e. higher  $2\theta$ ) after 100 hours (black arrow). A shift of this magnitude could suggest the composition of this phase was constantly changing during the course of the heat treatment. In contrast, the cubic phase which formed did not exhibit this evolving composition, but instead appeared to maintain a constant composition (i.e. peak position) (red arrow) throughout the exposure. Similar behavior was observed by Brandon et al [56] in plasma sprayed coatings they aged at 1300°C and 1200°C.

The XRD patterns of the final CP-DVF specimens are shown in Figure 49.

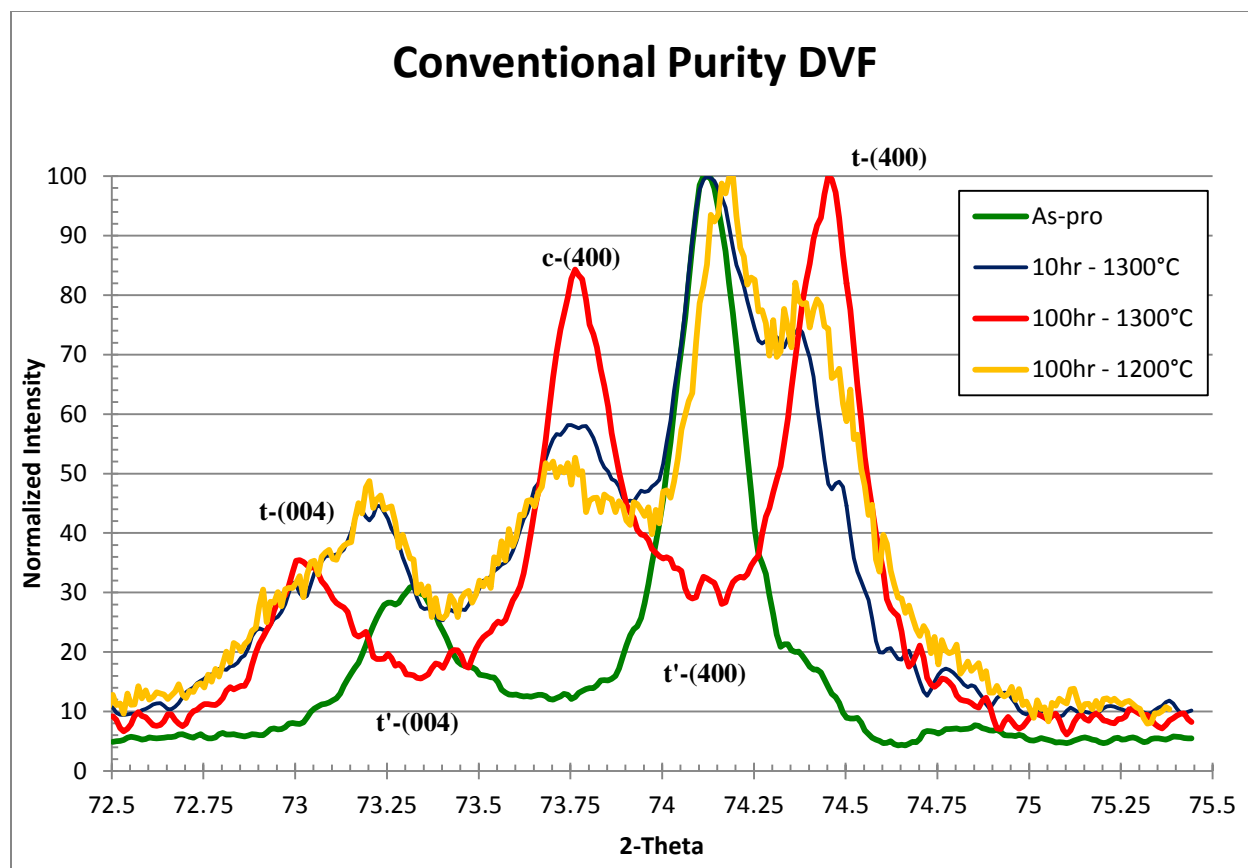


**Figure 49 - 72°-75° 2 $\theta$  region of the XRD pattern for the CP-DVF topcoat before and after the thermal exposures.**

The as-processed topcoat (green curve) was composed of the t' phase. After 10 hours at 1300°C (blue curve) cubic and tetragonal peaks appeared. Unlike the CP-LD coating, the pattern of the 1200°C 100 hour specimen (gold curve) was very similar to the 10 hour 1300°C pattern. At 100 hours at 1300°C (red curve) the coating contained cubic and tetragonal phases. Overall, this coating exhibited the same pattern of phase evolution as the HP-LD and HP-DVF coatings with the exception that more cubic phase formed in this coating after 10 hours than did in the two high purity coatings.

As mentioned previously, the tetragonal phase which forms at high temperature can transform into monoclinic when it is cooled down to room temperature thus all of the coatings

were also analyzed for monoclinic phase content using the one-peak method described earlier in this chapter. The results are listed in Table 9.

**Table 9 - Percent Monoclinic Content of Aged Topcoats**

Percent Monoclinic Content - One Peak Method				
	HP-LD	HP-DVF	CP-LD	CP-DVF
0hr @ 1300C	ND	ND	3.02%	0.64%
10hr @ 1300C	ND	ND	0.51%	0.52%
100hr @ 1300C	ND	ND	0.58%	0.74%
100hr @ 1200C	ND	ND	0.38%	0.53%
*ND = Not Detected				

Neither of the HP coatings contained any detectable monoclinic phase whereas both of the CP coatings contained small, yet detectable, amounts of the monoclinic phase. Overall, little monoclinic was detected indicating the quenching from the aging temperature was sufficiently fast to suppress the transformation of the tetragonal phase to the monoclinic phase.

In attempts to examine the stability of the tetragonal phase, a group of the topcoats, which had previously been aged at 1200°C and 1300°C, were heat treated at a much lower temperature and then furnace cooled in attempts to induce the phase transformation. Experimentally, the aged HP-LD and CP-LD topcoats were all placed in a furnace set at 150°C for 24 hours. This temperature was chosen because the composition of the tetragonal phase which forms at 1300°C, if cooled, intersects the  $T_0(t/m)$  curve at 300°C (see Figure 50).

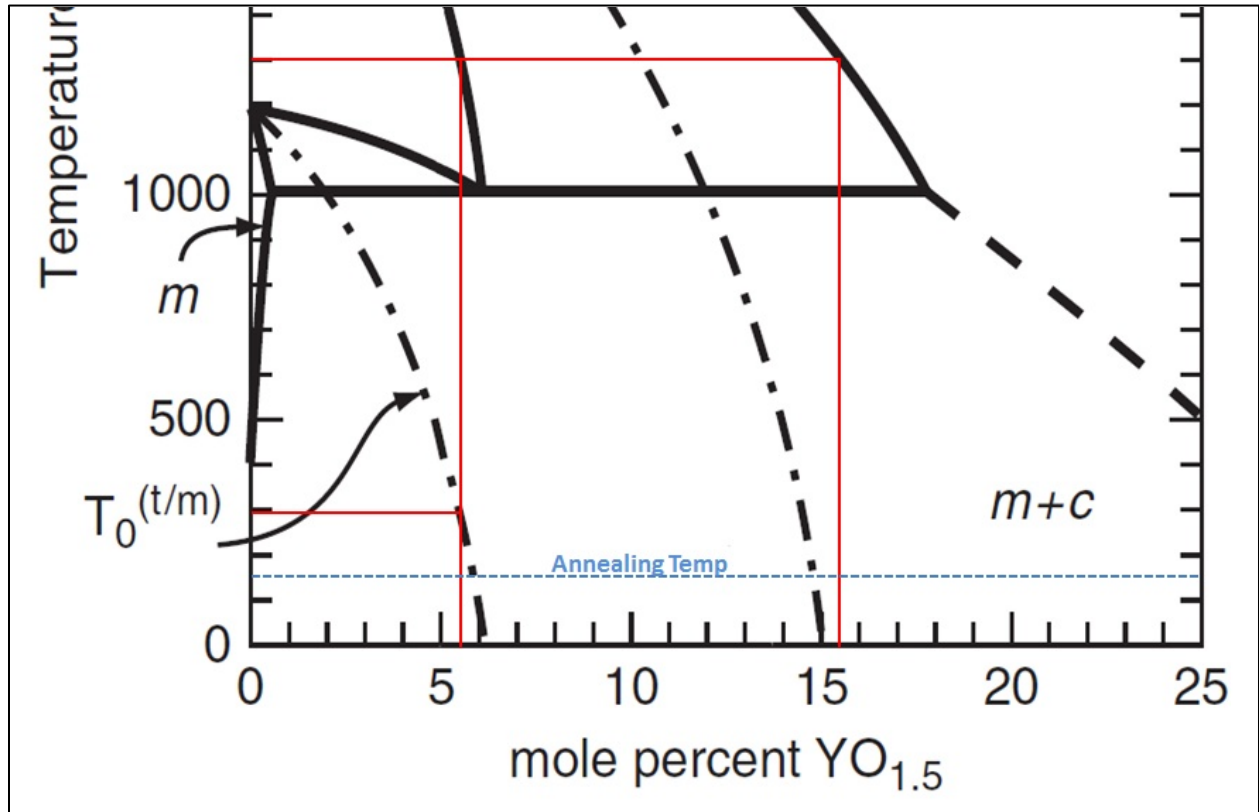


Figure 50 - Enhanced portion of the ZrO<sub>2</sub>-YO<sub>1.5</sub> phase diagram [54].

Furthermore, if the diffusionless martensitic transformation is to occur, the coating must be held below this temperature for it to be thermodynamically possible. If aged above 300°C, the transformation would have to take place via an alternative mechanism (i.e. diffusion). XRD patterns were collected before and after the heat treatment and the percent monoclinic phase content was again estimated using the one-peak method described earlier. The results of the monoclinic phase measurements are listed in Table 10.

**Table 10 - Percent Monoclinic Before and After 150°C Aging**

	HP-LD Before HT	HP-LD After HT	CP-LD Before HT	CP-LD After HT
10hr @ 1300°C	ND	0.40%	0.51%	3.23%
100hr @ 1300°C	ND	0.99%	0.58%	18.82%
100hr @ 1200°C	ND	1.62%	0.38%	3.35%

After the low temperature aging, the HP-LD coatings contained detectable, although not large, amounts of the monoclinic phase whereas the CP-LD topcoats, especially the 100 hour at 1300°C specimen, contained upwards of 18.8%.

To ensure such a large fraction of monoclinic was forming at the expense of the tetragonal phase, the 72°-75° 2θ region of the XRD scan was analyzed and is presented in Figure 51.

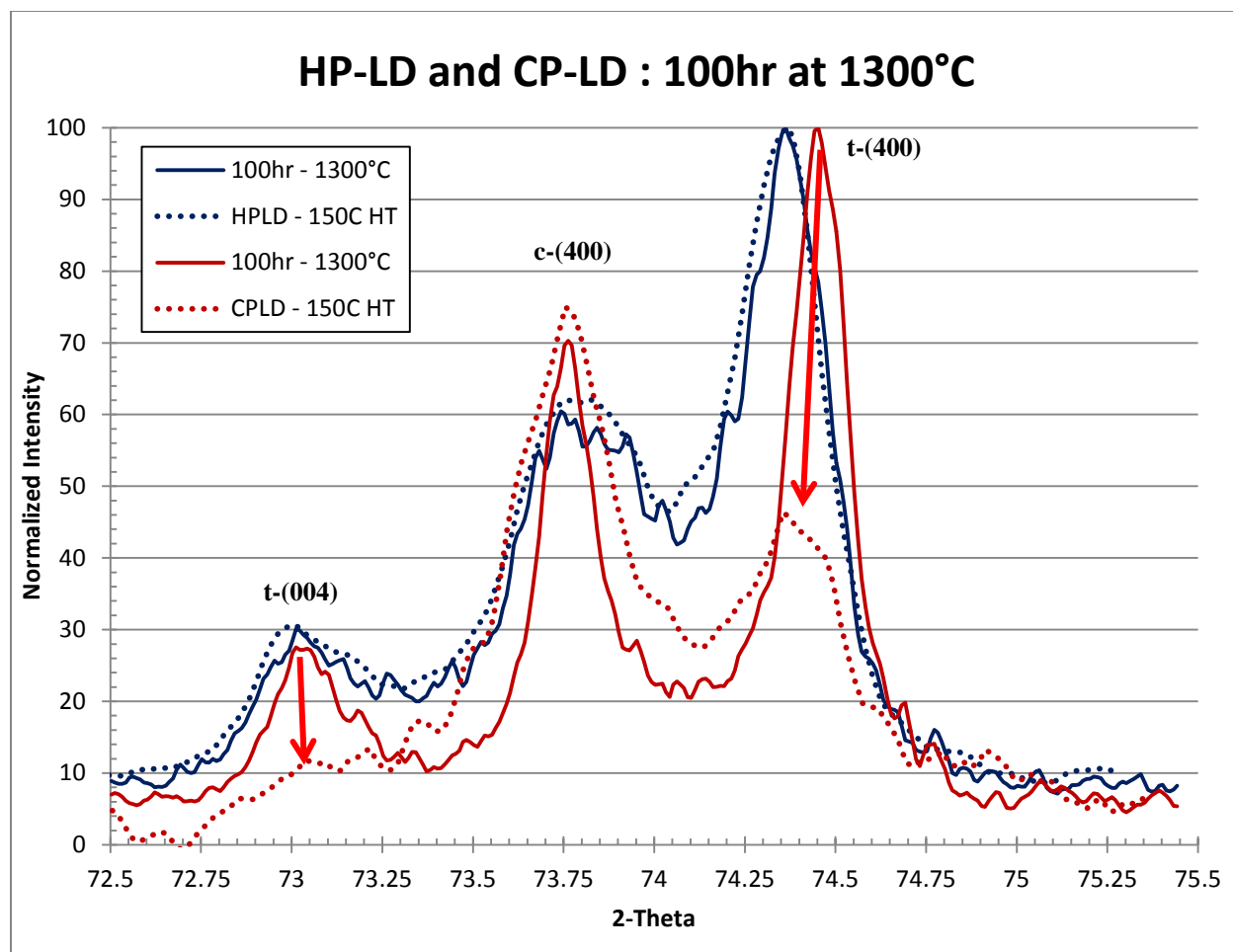


Figure 51 - XRD pattern of the CP-LD and HP-LD topcoats aged for 100 hours at 1300°C rapidly quenched, and then again exposed at 150°C for 24 hours.

After 100 hours at 1300°C both the HP-LD topcoat (solid blue curve) and the CP-LD topcoat (solid red curve) appeared to both have cubic and tetragonal phases present. After the 150°C heat treatment, the XRD pattern of the HP-LD specimen (blue dotted curve) appeared almost identical to pre-aging curve. This suggests that very little, if any, monoclinic phase formed which is consistent with the monoclinic phase content measurements (only ~1% was detected). In contrast, after the 150°C heat treatment, the XRD pattern of the CP-LD specimen (red dotted curve) had very weak tetragonal peaks (red arrows) indicating the phase fraction

decreased as a result of the second aging step. This significant decrease in the tetragonal content confirms the large increase in monoclinic phase content discovered earlier in the CP-LD specimen.

In summary, the phase evolution was found to be sensitive to the composition of the topcoat. The CP coatings experienced a slightly faster decomposition of the  $t'$ -structure into the equilibrium tetragonal and cubic structures than the HP coatings experienced. However, after 100 hours at 1300°C all four of the coating types had almost completely decomposed. The tetragonal phase which formed at high temperature in the HP-LD coating was also shown to be more stable than that formed in the CP-LD coating, at least at the temperatures tested.

**4.1.1.4 Discussion** The HP-LD specimens experienced little densification at 1300°C and an almost negligible amount at 1200°C. However, in all three thermal exposures visible changes had occurred throughout the microstructure. Micro-cracks closed and larger cracks and delaminations partially healed during the heat treatments, yet little densification occurred. This observation suggests bulk and, even to a certain degree, grain boundary diffusion were severely limited at these temperatures since densification was minimal. This is of no surprise since it is known lattice cation diffusion in YSZ is sluggish [57, 58] at these temperatures. Surface diffusion, however, was not limited which was responsible for the microstructural changes.

In contrast, the CP-LD coatings densified much faster than the HP-LD coatings, with densification even occurring at 1200°C. Since lattice and/or grain boundary diffusion in pure YSZ are limited at these temperatures, yet are required for densification [59], some other mechanism must be aiding the transport of the cation species. Likewise, the decomposition of the metastable  $t'$ -phase would also require bulk diffusion or grain boundary diffusion in order to create the new cubic and tetragonal phases which were observed in the XRD studies. The likely

explanation is that impurity phases, present along grain boundaries or even within the bulk lattice, aided in the transport of the cations. Silica and alumina impurities were observed throughout the microstructure of the CP-LD and CP-DVF coating. In cross-sectional micrographs, these impurity elements appeared to be clustered and were not homogeneously spread throughout the coating, however, it is possible thin films of these impurities, beyond the resolution of the characterization techniques used, were present throughout the coating. This could potentially give rise to liquid phase transport or these glassy phases, even if solid, could act as fast diffusivity pathways for cation transport [25, 28, 30]. Further high resolution TEM analysis would be required to confirm this, however, the evidence gathered in this study suggests silica and alumina enhanced the transport of zirconium and yttrium. This enhanced mobility then led to faster densification and to significant changes in the microstructural features of the coating. Although not measured, these changes would subsequently cause an increase in the thermal conductivity because inter-splat and intra-splat pores along with the horizontal delaminations are no longer present which all reduce the thermal conductivity of the topcoat to levels below that of bulk YSZ. Since the primary purpose of the topcoat is to reduce temperatures, an increase in thermal conductivity is undesired.

The HP-DVF coating had a faster sintering rate than the HP-LD coating which could be partially attributed to the HP-DVF coating having a silica content double of that of the HP-LD coating. Another explanation could stem from the difference in the type of porosity of the two coatings. Referring back to Figure 20 (HP-LD) and Figure 32 (HP-DVF), the HP-LD coating visually contained a wider size range of pores meaning it contained globular pores, micro-cracks and large horizontal delamination cracks. After the aging at 1300°C the small micro-cracks were the first to disappear, however, since these small pores only constituted a fraction of the overall

porosity, the density did not change much. In the HP-DVF coating, Figure 32, the porosity was split between small micro-cracks/pores and large vertical fissures. After thermal exposure at 1300°C, the large fissures remained open but the micro-cracks healed (Figure 34). Since the micro-cracks/pores visually appeared to account for a larger fraction of the overall porosity, the density would have increased more. This is a qualitative analysis based on visual comparisons of the coatings. An accurate pores size distribution could quantitatively verify this observation, however, measurement methods such as mercury porosimetry do not always accurately resolve the larger pores/cracks and therefore tend to over misrepresent the pore-size distribution. Thus a qualitative analysis may be sufficient.

The CP-DVF coating exhibited atypical behavior during the thermal exposures because its density decreased instead of increased. The weight change measurements indicated there was little to no mass loss during the test so evaporation of volatile species can be ruled out and so the only other explanation is the volume increased. An increase in volume could result from a phase transformation. The tetragonal to monoclinic phase transformation discussed earlier is accompanied with a 3-4% volume increase [60], thus if enough monoclinic were to have formed this could mathematically account for the decrease in density. However, XRD analysis indicated there was only 0.7% monoclinic in the coating which cannot account for such a large density decrease. The likely explanation then is the small pores which formed in the coating increased the total volume. The source of these pores and the reason for their coarsening remains unclear though. For pores to form within a grain there must be a source of vacancies and for the pore to grow there must be a vacancy gradient continually driving them into the pore from a source. Possible explanations for such gradients are unknown; however the pores do seem to be the cause of the volume increase and subsequent density decrease.



impurity content below 0.02wt% would not reduce the sintering rate of the coating and that even a completely pure YSZ topcoat would still have a significant sintering rate. Our results, however, indicates, a very pure YSZ coating, beyond their purest coating, would have a sintering rate well below their fit line. This drop-off in the sintering rate at very low silica contents could indicate a solubility limit has been reached, where below a critical level, say 0.02wt%, the silica in the coating is soluble in the YSZ matrix but above it, the silica must be present as a separate phase. If the silica is in fact aiding in the transport at the grain boundaries then dropping below such a solubility limit would be beneficial from the perspective of transport.

The CP-DVF coating falls close to this line, however, this coating exhibited atypical sintering behavior where small pores were formed and grew during the thermal exposure. Thus it must be put into a category of its own and not compared with the others. Similarly, the HP-DVF coating had a very different microstructure from the low density coatings Vassen et al used in their study. So a direct comparison between the two is not applicable since coating microstructure alone (i.e. porosity and pore size distribution) can influence how a coating will sinter [15, 30].

In another study by Tsipas [31] YSZ topcoats with silica and alumina dopants were sintered at 1300°C for 50 to 100 hours. XRD patterns were collected and analyzed to determine the extent of the decomposition of the  $t'$ -phase to the equilibrium tetragonal and cubic phase. The conclusion of this work suggested that the presence of silica and alumina slowed the decomposition of  $t'$ -phase which is counter to what was observed for the HP-LD and CP-LD coatings in the current study. The XRD pattern of the CP-LD coating after 100 hours at 1300°C (Figure 48) indicated the decomposition had almost completed (no pseudo- $t'$  peak was present) whereas the HP-LD pattern (Figure 46) indicated there was still some of the pseudo- $t'$  phase

present. While this is only a semi-quantitative comparison of the CP and HD coatings, in principle, it is valid since the phase quantification performed by Tsipas uses peak heights/intensities to estimate the phase fractions. Furthermore, the tetragonal phase that formed in the HP-LD coating was more stable (with respect to the monoclinic phase transformation) than that formed in the CP-LD coating which almost entirely transformed to monoclinic during the second thermal aging at 150°C. This observation does not support the claim that the CP-LD decomposed faster than the HP-LD specimen, however it does indicate there are differences in the phase decomposition behavior of the two coatings. Additionally, a coating with 20% monoclinic phase content, such as in the CP-LD coating, from a mechanics standpoint, is undesired because of the transformation induced cracking which could occur during heating and cooling. So from this perspective the HP-LD coating was more stable than the CP-LD coating.

**4.1.1.5 Conclusions** Four topcoats, two made with high purity YSZ powder and two with conventional purity powder were sintered at both 1300°C and 1200°C for 10 to 100 hours. The densification rate was slowest in the HP-LD coating to the extent that little to no densification occurred at 1200°C. This was attributed to the lack of impurity phases which could aid in the transport of cations. The CP-LD coatings had a comparatively larger sintering rate than the HP-LD topcoat which was attributed to the presence of an impurity phase. Furthermore, the metastable t'-phase decomposed at a faster rate in the CP-LD specimens than in the HP-LD specimens and the tetragonal phase which formed was less stable in the CP-LD coatings.

The HP-DVF topcoat had a higher densification rate than the HP-LD coating which was attributed to the difference in the microstructure. The HP-DVF topcoats contained higher fractions of micro-cracks which are the first microstructural features to vanish during the

sintering process resulting in increased densification. Beyond this, the phase decomposition behavior of the two high purity coatings was similar.

The CP-DVF coating exhibited a decrease in density over the course of the thermal exposure. This was attributed to the formation and growth of small pores which increased the volume of the coating and decreased the density. The source and growth mechanism of these pores is still unclear.

The microstructural stability of the HP-LD coating along with its slow densification rate makes a strong case in justifying the usage of the high purity powder as compared to the conventional purity powder. While the HP-DVF coating experienced higher densification rates than the HP-LD, in a head-to-head comparison with the CP-DVF, it performed much better at retaining the starting microstructure which is vital to the performance of the TBC.

## **4.1.2 Topcoat Thickness**

**4.1.2.1 Overview** The motivation for investigating the influence of topcoat thickness on lifetime stems from a multitude of reasons. First, when considering the effective thermal resistance (Equation 1) of the topcoat, the insulating capacity of the topcoat scales with the thickness. Therefore, the temperature drop across the TBC system is increased as the coating thickness increases which is graphically shown in Figure 10. From this relationship, it would seem appropriate to use the maximum coating thickness to gain the most thermal protection, however, the additional strain energy contributions (driving force for spallation) from having a thicker coating contradicts this reasoning (Figure 12). Furthermore, previous work [2, 34] with furnace cyclic testing of TBC specimens of three thickness topcoats, 375, 750 and 1125 $\mu\text{m}$ ,

demonstrated TBC lifetime is influenced by TBC thickness where thicker TBCs had shorter lifetimes than thinner TBCs, Figure 53.

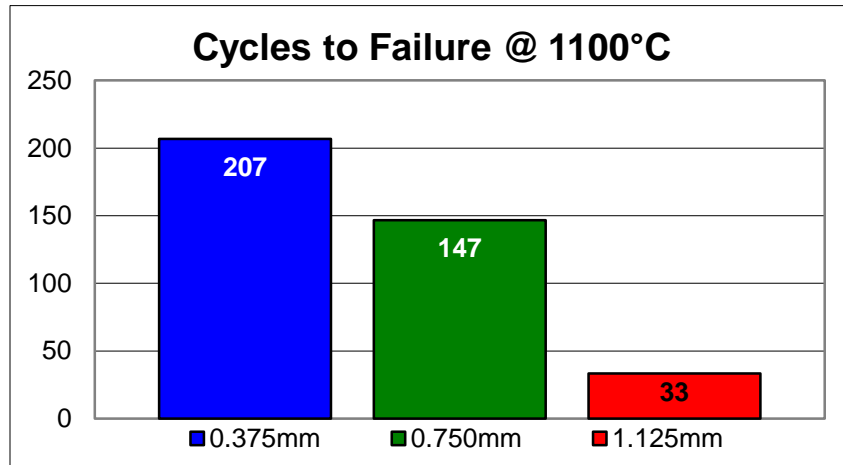


**Figure 53 - Cycles to failure of three groups of TBCs with different topcoat thicknesses. All TBCs have IN 718 substrates with dual layer NiCoCrAlY bond coats and YSZ topcoats [2].**

Additionally, the location of the failure in the thick TBCs was within the YSZ topcoat layer whereas the thinner TBCs failed at the bond coat – TGO interface suggesting bond coat oxidation played a more significant role in the failure events of the thin TBCs. The failure location in the thick TBCs indicates bond coat oxidation is not the primary contributor to failure and that other mechanical influences from the thicker topcoat are the likely causes for these failures. Given this behavior, bond coat oxidation and the additional strain energy from thicker coatings both contribute to the failure of TBCs, but to unknown degrees. In the case of the thicker TBCs, which provide greater thermal protection, the bond coats have less oxidation at failure (because they failed after fewer cycles) but more stored strain energy in their thicker topcoats whereas, in the case of the thinner TBCs, which provide less thermal protection, they

have more severe bond coat oxidation at failure but with less stored strain energy in their topcoats.

Despite these mathematical relationships and the experimental findings, questions remain unanswered. The TBCs tested in the previous work [2] are very thick especially when considered in the context of a typical EBPVD TBC which is usually around 150 $\mu$ m thick. So the question remains of whether the previously established relationship between topcoat thickness and TBC lifetime continues out to the extremes. More specifically, at very thin topcoat thicknesses (similar to EBPVD thicknesses), it is unclear whether the lifetime will continue to steadily increase, or, whether an upper limit to the lifetime exists beyond which further reductions in the thickness of the topcoat will not yield longer lifetimes. Knowledge of such an upper limit would be beneficial in TBC design as it would represent the optimum topcoat thickness which provides the most thermal protection without reducing the TBC lifetime through the addition of more insulation (topcoat material). The suggestion of such an upper lifetime limit is grounded in the oxidation theory, wherein the bond coat will only be able to sustain a continuous adherent TGO for a limited amount of time before breakaway oxidation occurs, causing the TBC system to fail [5, 6] and therefore supporting the idea of an upper limit. The existence of an optimum topcoat thickness was investigated in this study.

**4.1.2.2 Experimental Overview** All the TBCs tested had the same substrate, PWA 1484, and bond coat, dual layer NiCoCrAlY bond coat the compositions of which are given in Table 4. The bond coats were argon-shrouded plasma sprayed onto the substrate discs (2.5cm in diameter and 3mm thick) and then the entire batch of specimens was vacuum heat treated at 1080°C for four hours. After heat treatment, the topcoats were deposited by air plasma spraying. Four specimens of each of the following topcoat thicknesses were prepared: 100, 225, 425, 750, 1150

and 1425 $\mu\text{m}$ . Each thickness group was sprayed in separate runs meaning four of the bond coat – substrate heat treated specimens were placed in the coating chamber, passed under the torch for a predetermined number of cycles until the appropriate coating thickness had been obtained and then removed so the next group could be sprayed. This technique was used instead of a technique where all the specimens (all 24 coupons) are loaded into the chamber, coated with 100 $\mu\text{m}$ , stopped, three are removed (100 $\mu\text{m}$  thickness group), then the remaining are coated with an additional 125 $\mu\text{m}$ , stopped again, three more are removed (225 $\mu\text{m}$  thickness group) and this starting and stopping process is continued until all specimens are coated with the appropriate thickness topcoat. Despite being more time consuming, the first method was used in order to eliminate any coating variations which may be introduced during the repetitive starting and stopping (heating and cooling, respectively) processes present in the second method. Afterwards, the density was measured according to ASTM-B328-94 and was determined to be  $82.0\pm 0.6\%$  the theoretical density of 7YSZ.

After deposition, the edges of the 750, 1150 and 1425 $\mu\text{m}$  coatings were gently brushed to remove over-spray, which is YSZ that was inadvertently deposited on the sides of the disk coupons due to the geometry of the spray process. If not removed, this artifact can induce complex stresses at the free edge of the coating causing premature failure.

Three of the four TBC specimens were furnace cycle tested (FCT) in a CM bottom loading furnace where one furnace cycle consisted of a 10 minute heating period to 1100 $^{\circ}\text{C}$ , a 45 minute isothermal hold and a 10 minute forced-air cooling period down to  $\sim 60^{\circ}\text{C}$ . Every 20 cycles, specimens were examined and visually checked for spallation, cracking and delamination. Most of the TBCs failed by complete topcoat spallation however some experienced cracking, chipping and buckling without complete topcoat spallation. To account for

this, failure was defined as at least 30% delamination/spallation of the topcoat. Furthermore, the term ‘technical failure’ was used to classify TBCs which did not fail by complete topcoat spallation but still met the failure criteria. After failure, the fracture surfaces were imaged with a high resolution flatbed scanner and a SEM. Following, the specimens were mounted in warm epoxy, sectioned with a high-speed precision saw and polished to a 0.04 $\mu$ m finish and examined in an SEM equipped with standardless EDS.

The fourth specimen of each group was set aside for the purpose of characterizing the starting microstructure. The six different topcoat thicknesses are shown in Figure 54 through Figure 59.

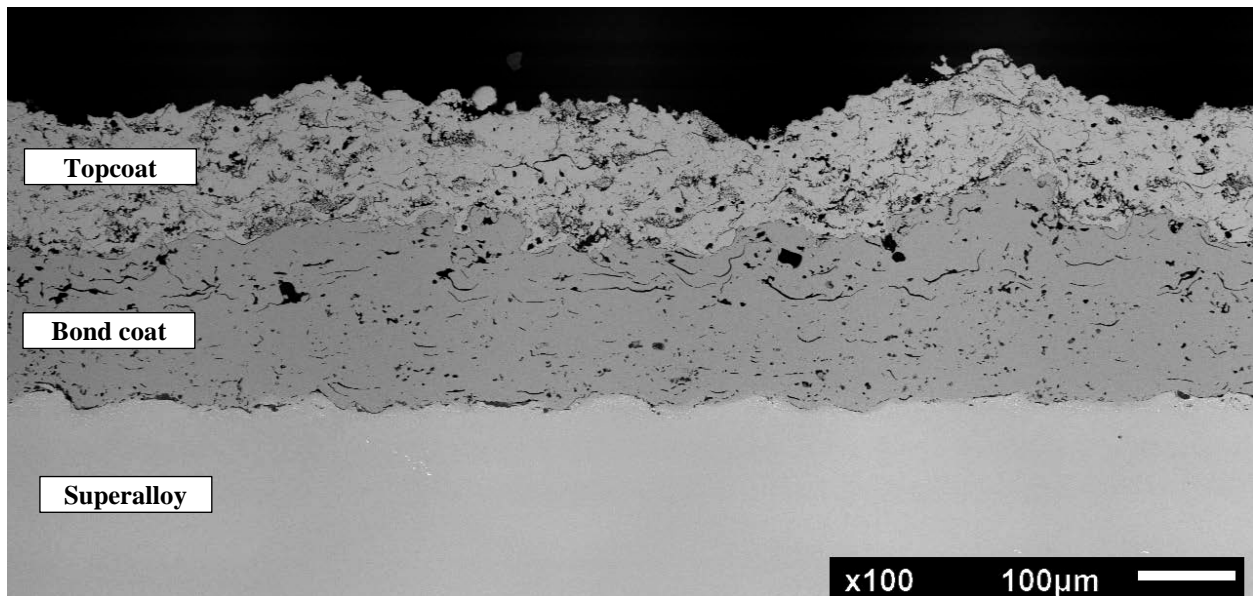
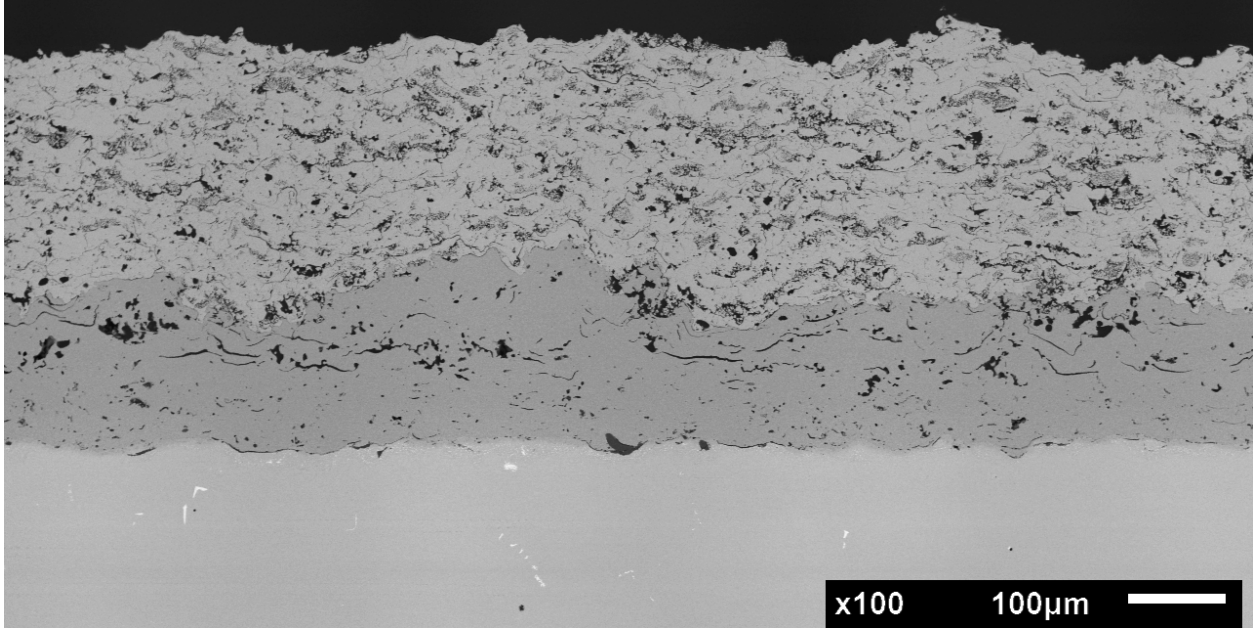
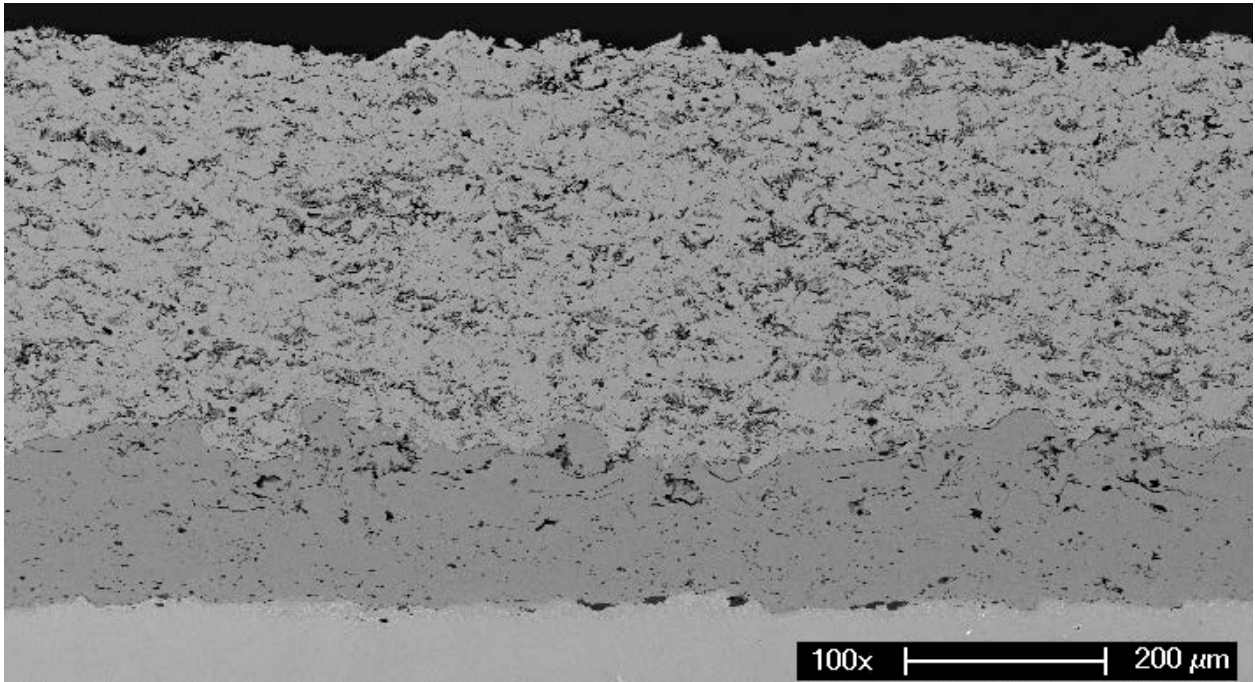


Figure 54 - 100  $\mu$ m topcoat in the as-processed condition.



**Figure 55 - 225 μm TBC in the as-processed condition.**



**Figure 56 - 425 μm TBC in the as-processed condition.**

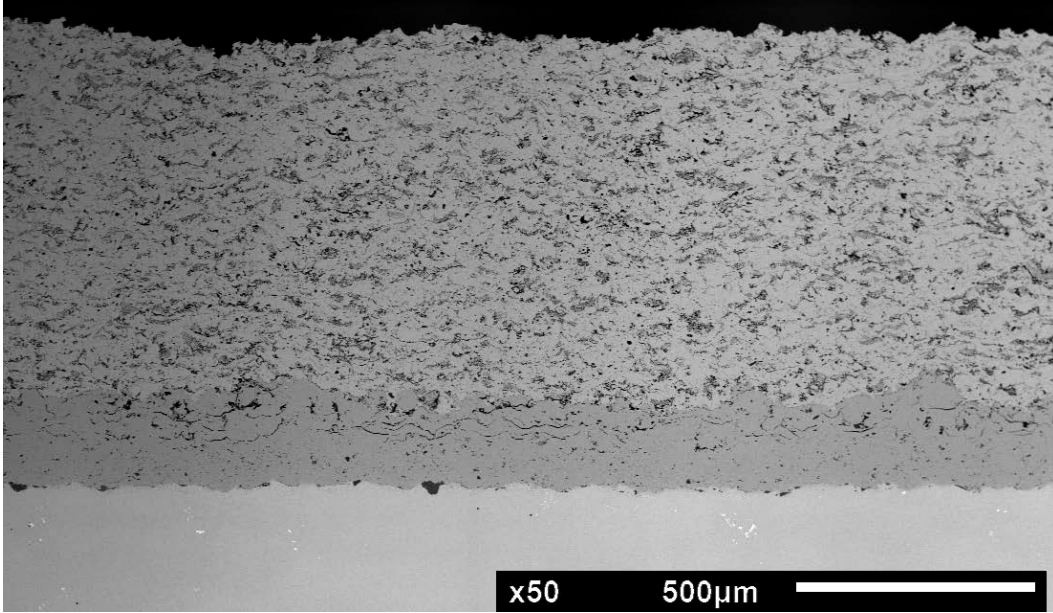


**Figure 57 – 750 μm TBC in the as-processed condition.**

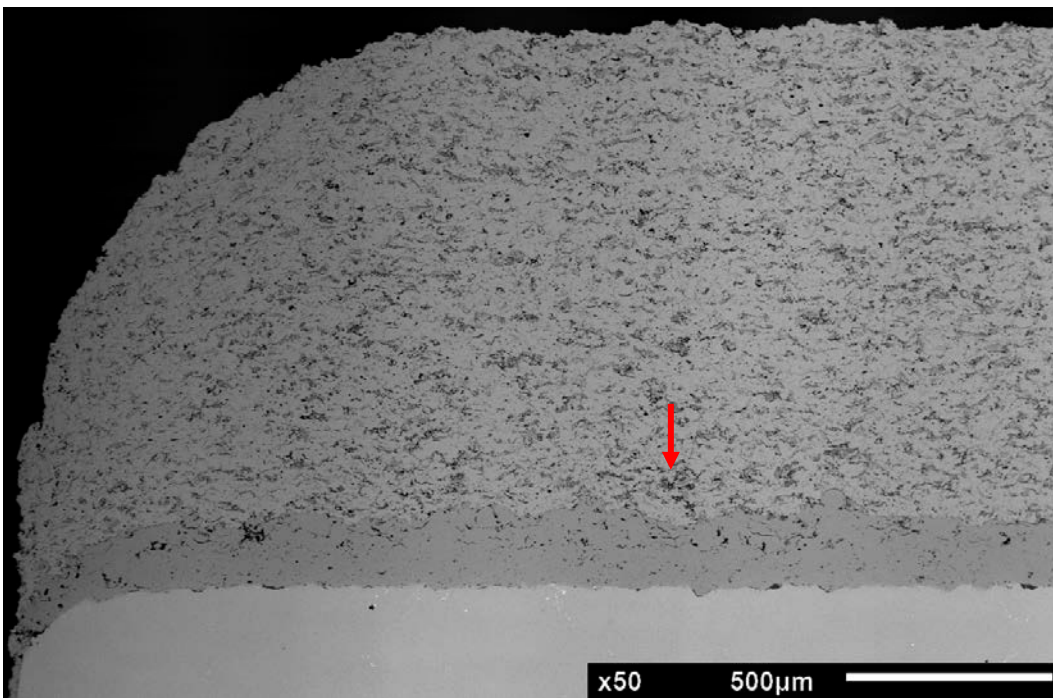


**Figure 58 – 1150 μm TBC in the as-processed condition. Red arrow indicates pull-out in the topcoat as a result of metallographic preparation.**

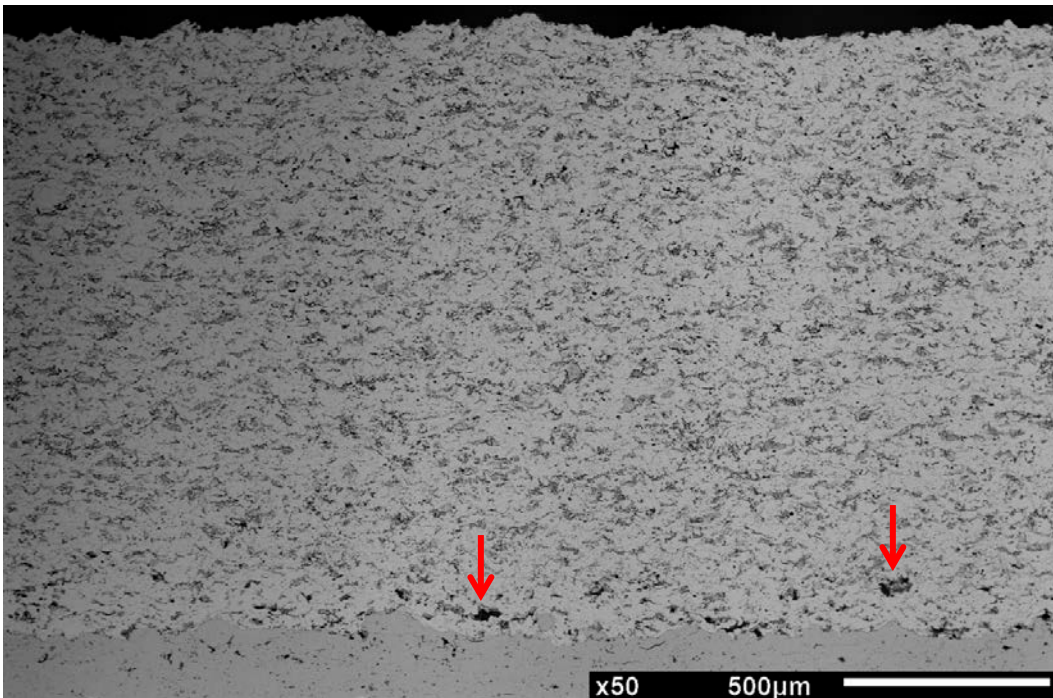


**Figure 59 – 1425  $\mu\text{m}$  TBC in the as-processed condition. Red arrows indicate pull-out in the topcoat as a result of metallographic preparation.**

The red arrows in Figure 58 and Figure 59 indicate areas in the topcoat where the YSZ has pulled-out. These defects are a result of the epoxy not penetrating the topcoat the entire way down to the bond coat interface to preserve the fragile microstructure during grinding and polishing. This was not a problem with the thinner topcoat specimens since the epoxy could easily penetrate the pores so as to preserve the entire topcoat. Besides these artifacts, all of the coatings appeared similar with regards to porosity and the amount of over-spray at the edges.

**4.1.2.3 Experimental Results** The results for the furnace cycle testing are shown in Figure 60.

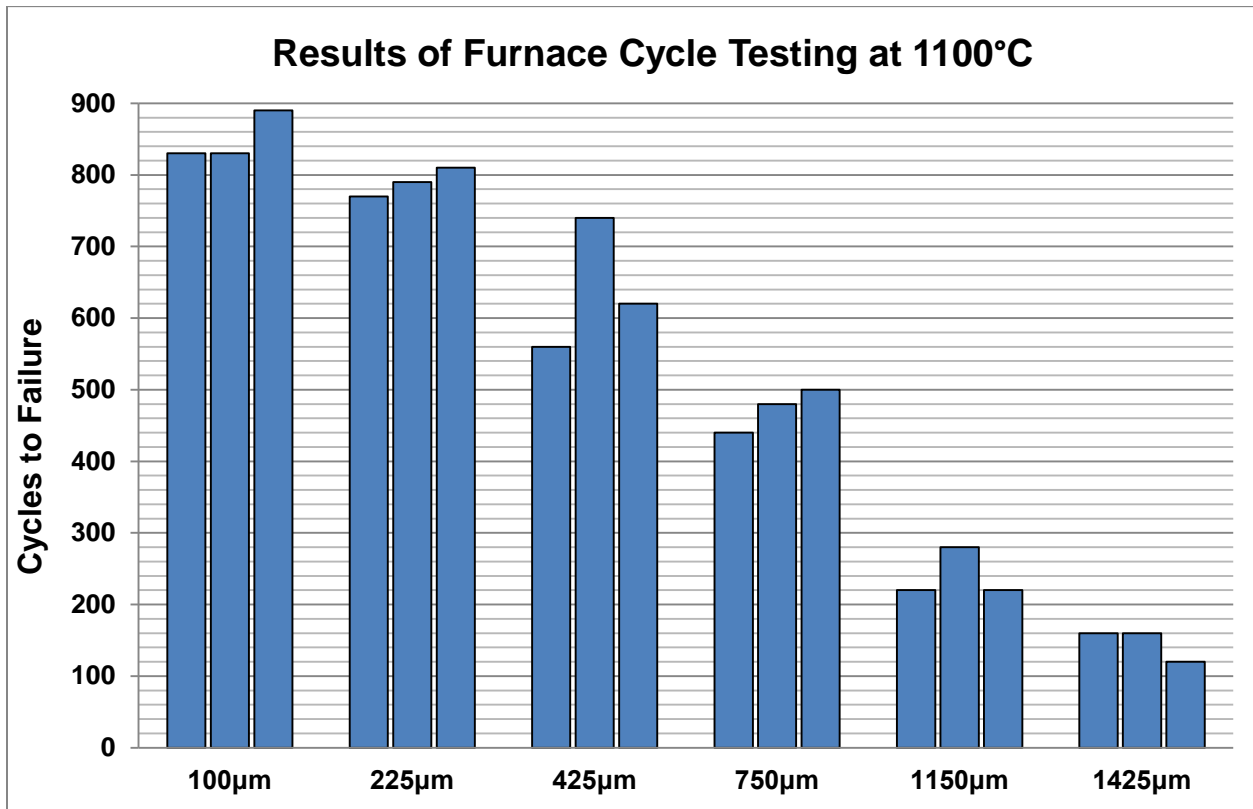
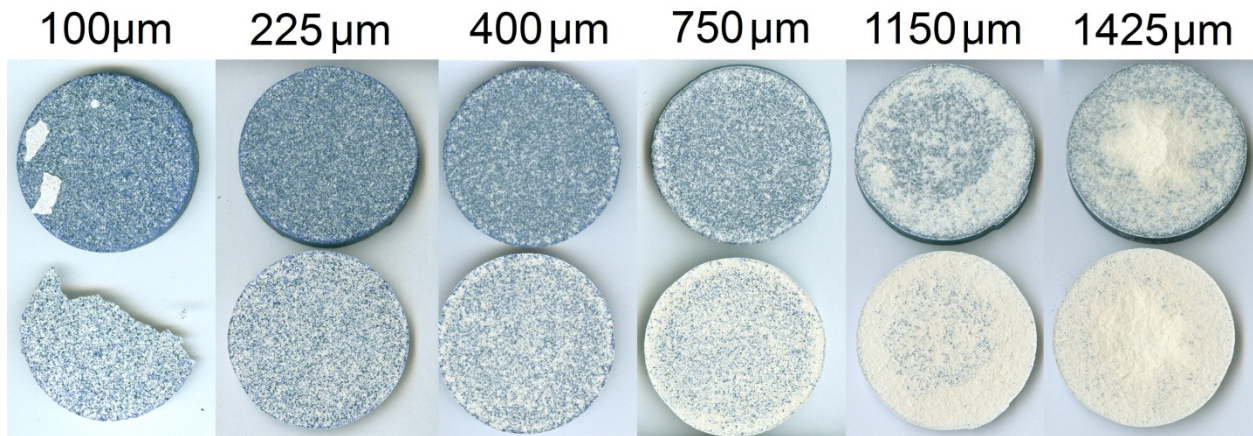


Figure 60 - FCT results for TBCs with varying topcoat thicknesses. All specimens had the same substrate (PWA 1484) and bond coat type (dual layer NiCoCrAlY).

The reproducibility within each coating thickness was relatively good indicated by the tight group of the bars in Figure 60. The 425µm coating had the largest spread in lifetime with a standard deviation of  $\pm 80$  cycles.

The representative fracture surfaces of each of the 6 different thicknesses are shown in Figure 61 which are high-resolution images taken with a flatbed scanner. The bluish color is

from the  $\text{NiAl}_2\text{O}_4$  spinel oxide that forms in the transient period [39] and the white material is YSZ left on the fracture surface.



**Figure 61 - High resolution images of the fracture surfaces of each of the 6 different thickness coatings. The upper circles are the substrate-bond coat portion of the TBC and the lower circles are the undersides of the corresponding topcoats that spalled off.**

Moving from left to right (thin to thick topcoat), the amount of YSZ on the fracture surface increases indicating the spallation crack is primarily propagating through the topcoat in the thicker TBCs. This observation is consistent with previous work [2] where 375, 750 and 1150  $\mu\text{m}$  topcoats on IN 718 were furnace cycle tested at the same temperature and produced similar results. Specifically, the 1150 $\mu\text{m}$  coating on IN718 produced a fracture surface almost identical to the 1425 $\mu\text{m}$  TBC in Figure 61.

Cross-sectional images of failed TBCs, some having suffered complete topcoat spallation and others only having suffered a technical failure, are shown in Figure 62 through Figure 67. These are back-scattered SEM images taken at the same magnification.

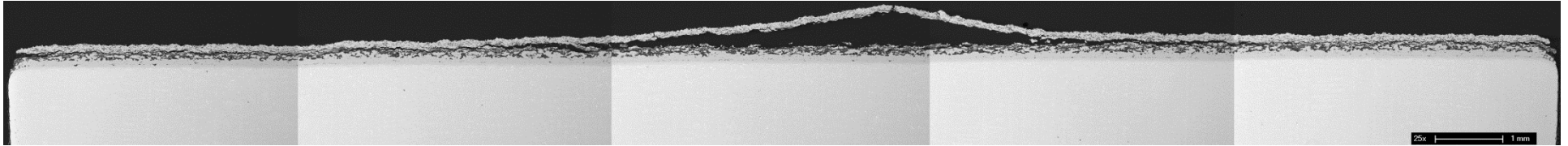


**Figure 62 - 100µm TBC with 830 cycles to failure. The topcoat is still intact however at least 30% had become delaminated which was termed to be a technical failure.**

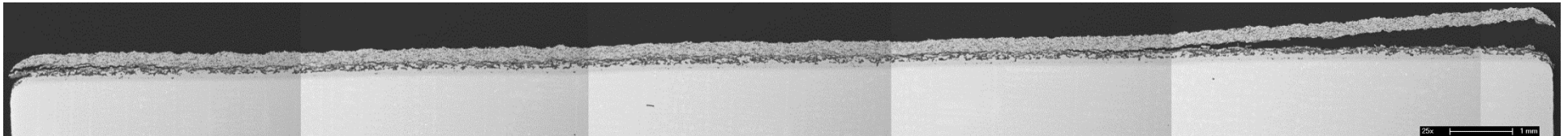


**Figure 63 - 225 µm TBC with 810 cycles at failure. The topcoat is still intact however at least 30% had become delaminated which was determined to qualify as a technical failure.**

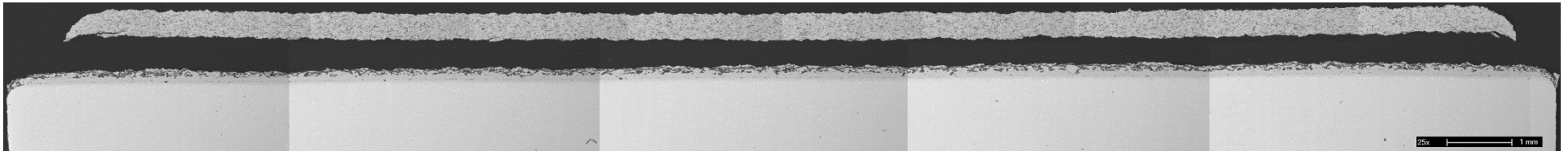


**Figure 64 - 425 µm TBC with 560 cycles at failure. Note, the topcoat and the substrate were cross-sectioned at different positions which accounts for their apparent differences in length.**

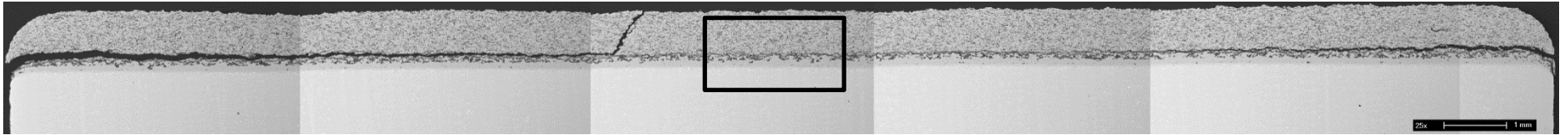


**Figure 65 - 750  $\mu\text{m}$  TBC with 440 cycles at failure. The topcoat is still intact however at least 30% had become delaminated which was determined to qualify as a technical failure.**

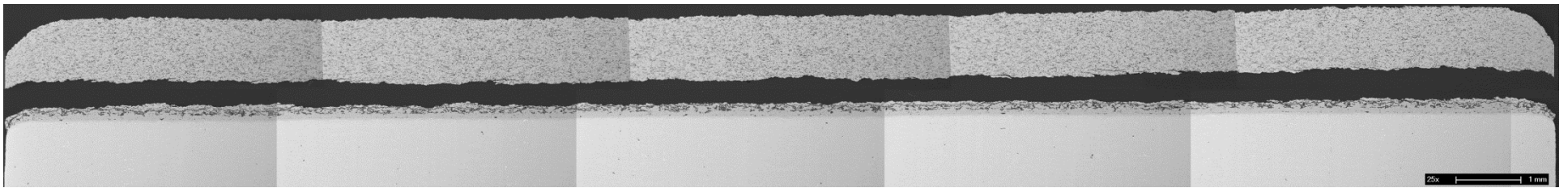


**Figure 66 - 1150  $\mu\text{m}$  TBC with 280 cycles at failure.**

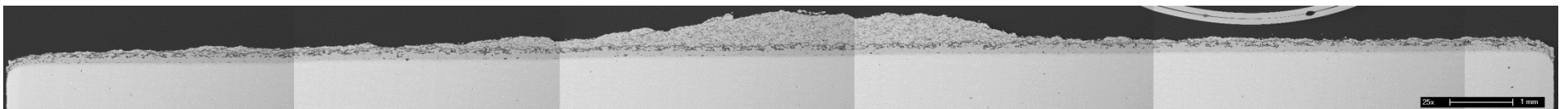


**Figure 67 - 1425  $\mu\text{m}$  TBC with 160 cycles at failure. The spalled topcoat is not present however there is a significant amount of YSZ present at the surface.**

For the TBCs that are still partially intact (Figure 63 and Figure 65), the cracking appears to be moving from the free edge and propagating towards the center of the specimen. While the 100  $\mu\text{m}$  topcoat in Figure 62 appears to have buckled up and away from the TGO, areas not shown in this cross-sectional image reveal this coating also experienced the same edge cracking as the 225 and 425  $\mu\text{m}$  topcoats exhibited. However, as Figure 62 depicts, buckling of the topcoat was also observed. This TBC was the only topcoat which exhibited this type of buckling failure.

The 1425 $\mu\text{m}$  coating and, to some extent, the 1150  $\mu\text{m}$  and 750  $\mu\text{m}$  coatings all experienced cracking within the topcoat layer. In the case of the 1425 $\mu\text{m}$  coatings, there was heavy diagonal cracking up into the topcoat which is depicted in Figure 68.

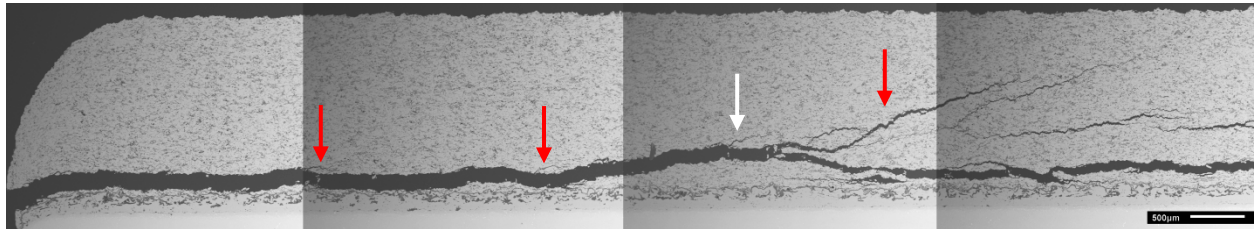


**Figure 68 - 1425 $\mu\text{m}$  coating which failed at 160 cycles. Note both the horizontal and diagonal cracking within the topcoat. The red arrows point out diagonal cracks which have formed but not propagated to the extent of the other diagonal cracks.**

While the 1150  $\mu\text{m}$  and the 750  $\mu\text{m}$  coatings exhibited some diagonal cracking, shown in Figure 69 and Figure 70, the horizontal cracking ultimately led to the spallation of the YSZ topcoat. This conclusion is based on the lack of extensive diagonal cracking (relative to that seen in the 1425 $\mu\text{m}$  coating) in the topcoats of these specimens.

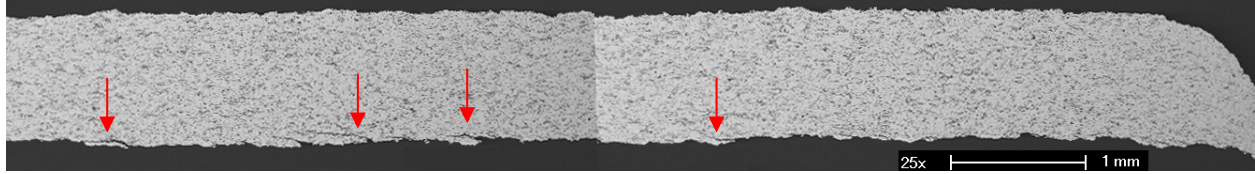


**Figure 69 - 1150µm topcoat after spalling off with 280 cycles. The red arrows highlight diagonal cracking that occurred near the topcoat-TGO interface.**

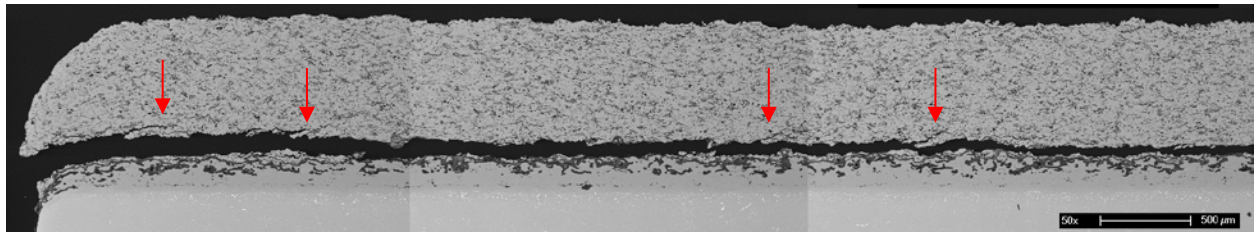


**Figure 70 – Enlarged composited micrograph of 750µm coating with 440 cycles at failure previously shown in Figure 65. Red arrows highlight diagonal cracks which formed in the topcoat.**

Moving down in topcoat thickness, the diagonal cracking was only observed near the free-edges of the thinner topcoat specimens. This cracking is likely caused by both the stress singularity that exists at the free edge of a multi-layered coating system subjected to biaxial thermal stresses and by the curvature of the bond coat – topcoat interface at this free edge [22]. This curvature can clearly be seen in Figure 58.

The primary cracking observed in the thinner TBCs (<1150µm) occurred in the TGO-topcoat-bond coat interface region. The path of the crack cut through the YSZ topcoat and the TGO, so the fracture surfaces of these failed specimens had a mixture of YSZ and various thermally grown oxides which were predominantly  $\text{Al}_2\text{O}_3$  and nickel-aluminum spinel  $\text{NiAl}_2\text{O}_4$ . As mentioned earlier, large scale delamination in these thinner specimens seemed to start at the edges and propagates toward the center of the specimen. Some of the TBCs which suffered technical failures (i.e. 30% of the coating became detached) were able to be mounted in epoxy

and cross-sectioned before complete spallation of the topcoat occurred allowing for microstructural observation of the still partially intact coating. This was possible for the 750, 225 and 100  $\mu\text{m}$  coatings. The right side of the 750  $\mu\text{m}$  coating shown in Figure 65 was still attached to the substrate/bond coat, however, closer examination of the topcoat-TGO region, Figure 71, revealed cracking all along the length of this “intact” portion of the coating,.

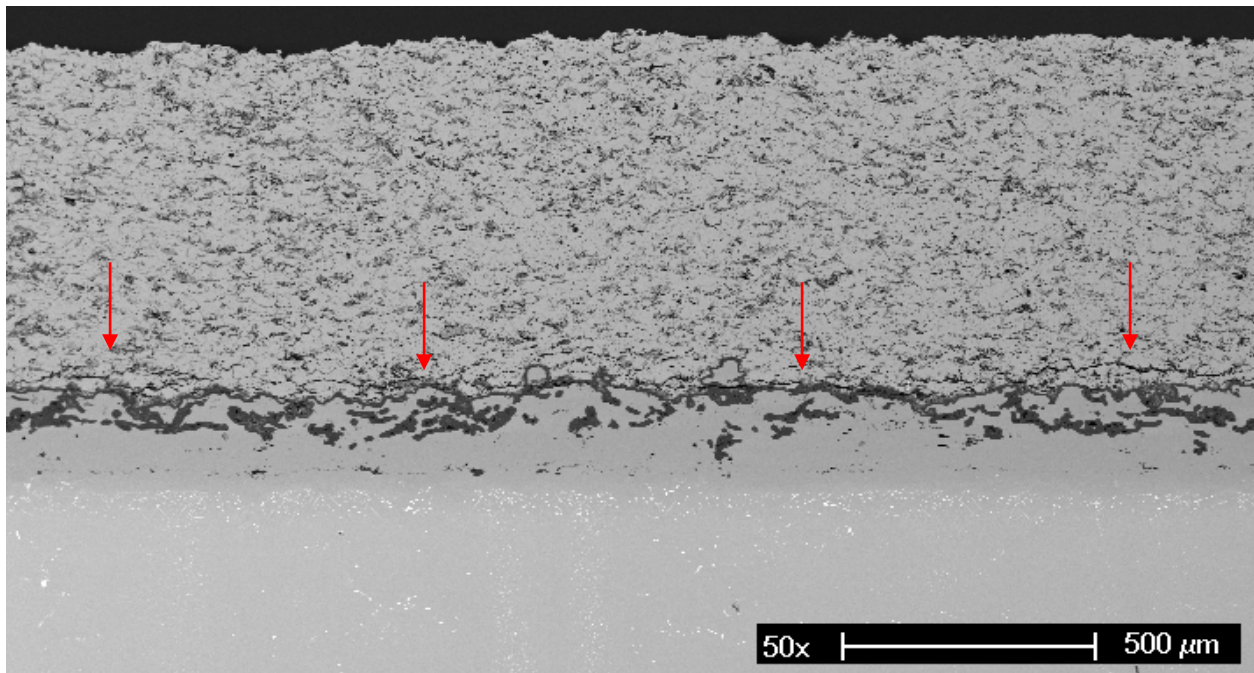


**Figure 71 – 750  $\mu\text{m}$  coating with 440 cycles until a technical failure occurred. This micrograph was taken in the interior of the specimen as indicated by the black box in Figure 65.**

Similarly, the 225  $\mu\text{m}$  coating shown in Figure 63 appeared almost entirely intact, with only the right side of the coating becoming delaminated. Closer examination of the ‘intact’ region also revealed extensive cracking depicted in Figure 72 by the red arrows.

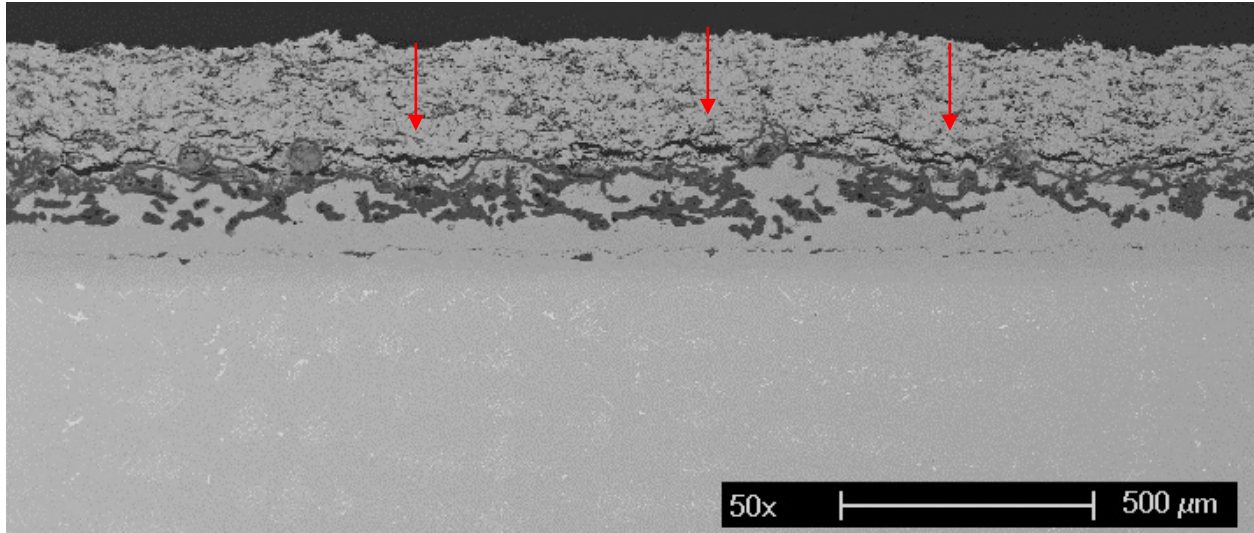


**Figure 72 – 225 μm coating with 810 cycles until technical failure.**

Based on these observations, both edge cracking and cracking within the bulk of the specimens seemed to be occurring. Furthermore, it is possible the spallation event was the end result of all of the individual pockets of cracks in the bulk (Figure 72) and at the edges linking together, however, this is speculation as a detailed picture of how these cracks formed, propagated and eventually caused failure was not available.

Regarding the oxidation of the bond coats, all the TBCs with the exception of the 100 and 225 μm specimens, at the time of failure, had TGOs primarily consisting of alumina along with isolated areas of nickel-aluminum spinel. Since all of the specimens had dual layer bond coats, the open porosity of the outer layer of the bond coats led to TGO formation at the pore surfaces and the subsequent faster depletion of the aluminum reservoirs in the bond coat (i.e. the  $\beta$ -phase). These oxidized pores can be seen in Figure 72. The overall extent of the oxidation appeared normal, in the sense that TBCs with longer lifetimes had thicker TGOs than those with fewer cycles. Oxide thickness measurements were not performed to confirm, however, it was not

expected the topcoat thickness would have any influence on the scaling kinetics and nothing during the characterization process indicated otherwise.

The 100 and 225 $\mu\text{m}$  coatings which had lifetimes close to and greater than 800 cycles had more severe bond coat oxidation at the time of failure. Portions of the outer layer of the dual layer bond coat had suffered chemical failure which was characterized by the prolific formation of base-metal oxides, which in the case of the NiCoCrAlY bond coats are NiO and CoO. Such oxides are shown in Figure 73. These oxides form because the aluminum content in these regions of the bond coat has dropped below the critical thermodynamic and/or kinetic level to maintain the alumina TGO thus resulting in the oxidation of the other metals present (Cr, Ni and Co).

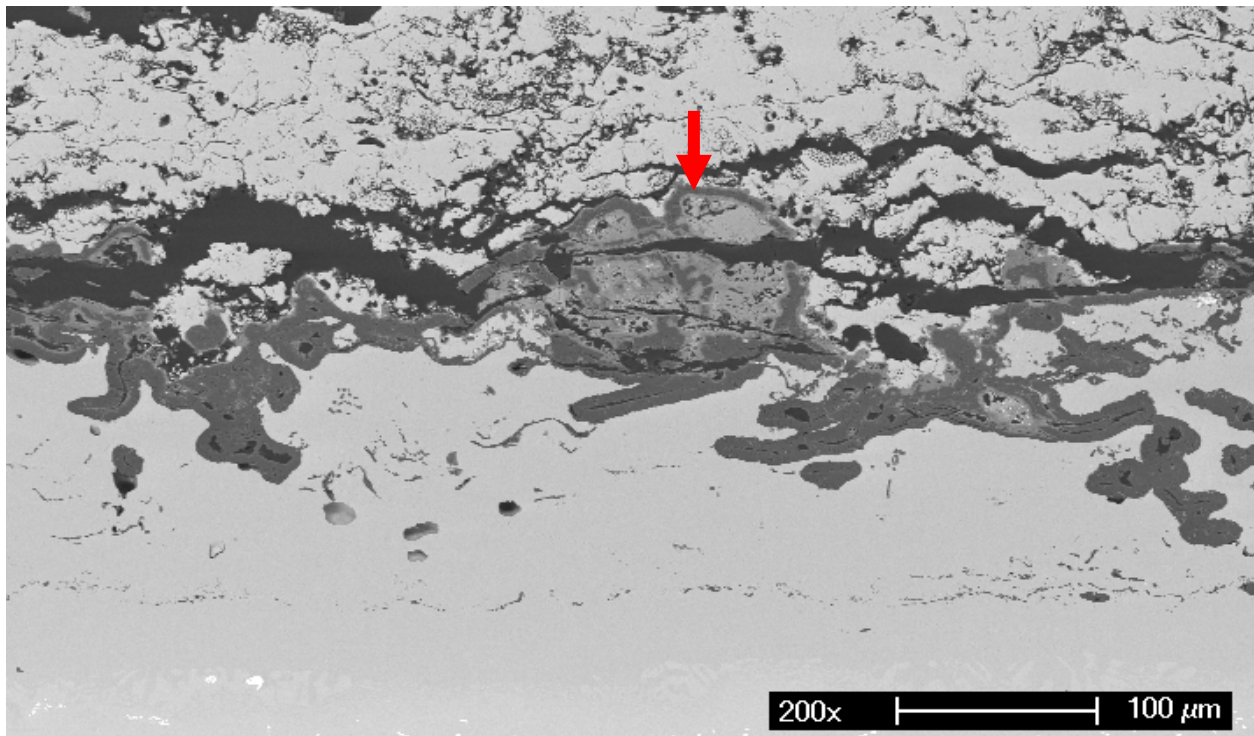


**Figure 73 - 100  $\mu\text{m}$  topcoat after 830 cycles at 1100°C. The white arrow points out areas in the outer portion of the dual layer bond coat that experienced chemical failure.**

**4.1.2.4 Discussion** Data from Figure 60 were used to construct an X-Y scatter plot to examine the lifetime-thickness relationship for FCT specimens. Figure 74 shows the number of cycles to failure and the corresponding thickness of each of the TBCs tested.

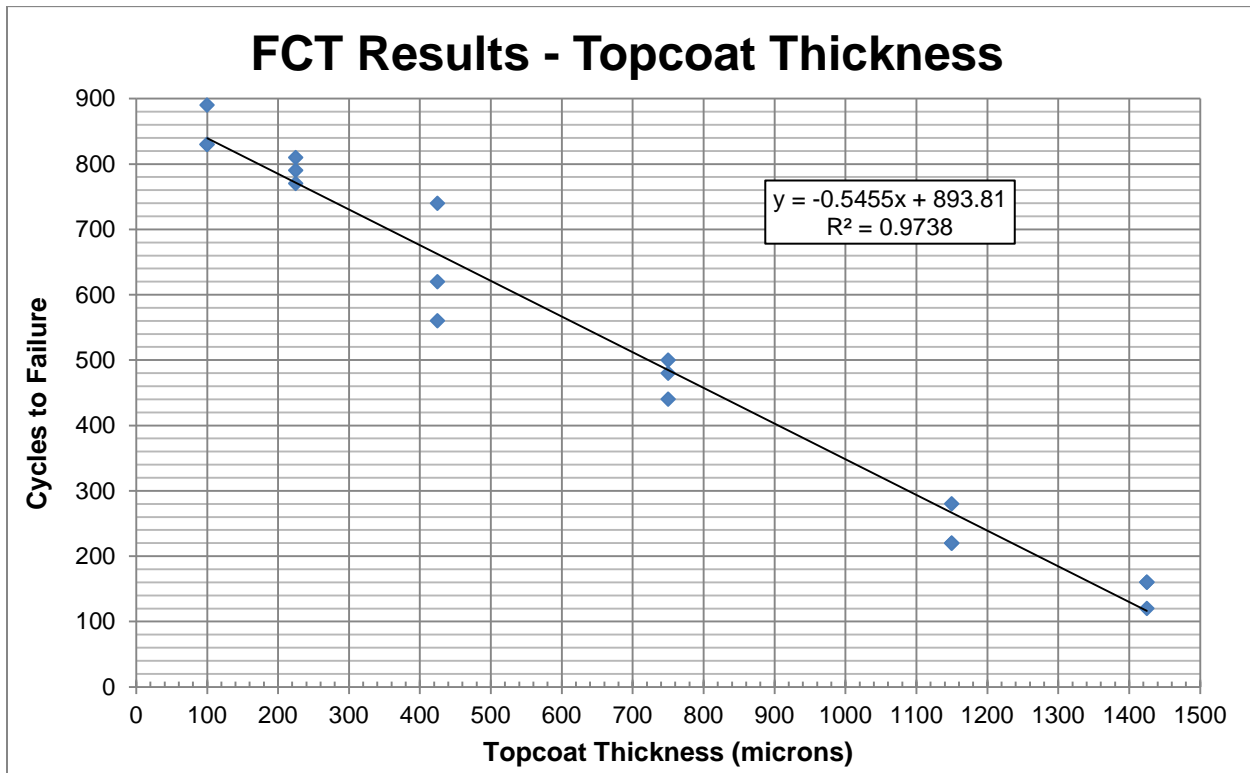


**Figure 74 - Plot of topcoat thickness vs. cycles to failure.**

The data was fit with both linear and parabolic trend lines. A parabolic trend was investigated because the stress intensity factor induced by the topcoat should increase with the square root of the thickness of the topcoat. Microsoft Excel offers a linear fit option but to fit the data with a parabolic trend line, the raw data had to first be manipulated by squaring either the cycles to failure or the thickness and then fitting this new plot with a linear trend line. A similar technique is used to measure the growth rate of oxide scales on metals and alloys where the mass

of an oxidized metal should increase with the square-root of time (assuming diffusion through the scale is the rate limiting step). The fit values of such lines are listed in Table 11.

**Table 11 - Data Type and Fit Parameter**

Input Data	Line Type	R <sup>2</sup>
Cycles to Failure - Thickness	Linear	0.9738
Cycles to Failure - (Thickness) <sup>2</sup>	Parabolic	0.9122
(Cycles to Failure) <sup>2</sup> - Thickness	Parabolic	0.9436

The data was fit best with the pure linear fit line (Cycles to Failure – Thickness) but the other fit lines had R-squared values close to one indicating the data trend was somewhat inconclusive since it could be described by several different trend lines. For the sake of analysis, the best fit line (Cycles to Failure – Thickness) is shown in Equation 9.

**Equation 9**

$$\# \text{ of Cycles to Failure} = 893.81 - 0.546 \times [\text{Topcoat Thickness } (\mu\text{m})]$$

Examination of the fit equation revealed two important points. First was the intersection of the fit line with the y-axis, which occurred at ~894 cycles and represents the lifetime of a TBC with a topcoat thickness of zero microns. Realistically speaking, this point has no practical purpose since a topcoat of zero thickness yields no thermal protection and so fundamentally contradicts the purpose of a thermal barrier coating. On a conceptual level though, this suggests that there is in fact an upper limit to the lifetime of a TBC and that further reduction in thickness does not extend the lifetime indefinitely. It is possible this upper lifetime represents the chemical lifetime of the TBC system. In other words, for this bond coat - superalloy – topcoat

combination, the oxidation of the bond coat alone is extensive enough after 894 cycles to cause even the thinnest of topcoats to fail.

Furthermore, while this max lifetime was extrapolated beyond the range of the data, decreasing the thickness beyond the last data point, 100 $\mu\text{m}$ , yields little or no thermal protection to the underlying layers of the TBC system. As an example, a 50 $\mu\text{m}$  APS topcoat exposed to hot expansion gases will only provide a temperature drop of  $\sim 15^\circ\text{C}$  to the bond coat (see Figure 10).

The second important point of this trend line is its intersection with the x-axis, which represents the maximum thickness at which a topcoat can be deposited before it will fail without even experiencing one thermal cycle. According to Equation 9, this thickness is  $\sim 1638\mu\text{m}$  (1.638mm) and following our previous example, this would provide a temperature drop of  $292^\circ\text{C}$  to the bond coat. Again, this point of intersection is being extrapolated beyond the range of our data and the idea of a TBC that fails before going into service is impractical, however this topcoat thickness represents the maximum thermal protection that can be achieved (for this topcoat microstructure and YSZ purity) even if only for one thermal cycle.

Before refocusing on the physical nature of the failure events for the TBCs, it should first be established that at the testing temperature of  $1100^\circ\text{C}$  it is assumed the sintering rate of the topcoats used in this study was almost negligible. This was verified in the previous section (2.2.2) where the sintering rate of the HP-LD coating at  $1200^\circ\text{C}$  was close to zero. Thus, at  $1100^\circ\text{C}$  the same behavior would be expected. At higher temperatures,  $1300^\circ\text{C}$ ,  $1400^\circ\text{C}$  and  $1500^\circ\text{C}$ , this statement would not be valid as significant densification rates have been observed [34]. Furthermore, any lateral or through-thickness shrinkage that may occur while at temperature, which could potentially introduce additional thermal stresses, will most likely be relieved by splat sliding and other forms of high temperature creep [23, 61]. Based on these

assumptions, topcoat sintering should not play a significant role in the failure of these TBCs or, at the very least, the sintering should not influence a thin topcoat any more than it should a thick topcoat at these temperatures.

Similarly, based on oxidation theory, the kinetics of oxide growth should not be influenced by the presence of an external coating, unless this coating can somehow reduce the oxygen flux to the surface. In this case, a thicker coating could potentially reduce the influx of oxygen to the surface as compared to a thinner coating and potentially slow the growth of the TGO, assuming O<sub>2</sub> supply to the surface was the rate limiting step. However, in the case of plasma sprayed YSZ, the combination of the porous microstructure and the abundance of oxygen vacancies in the lattice structure render the YSZ transparent to oxygen [12].

The microstructural observations indicated the failure characteristics of the TBCs depended upon the thickness of the topcoats. The very thick topcoats, 1425 & 1150  $\mu\text{m}$ , failed well within the topcoat YSZ material and after a comparatively short number of cycles. The final delamination crack started at the free edge and propagated solely within the YSZ towards the interior of the specimen. At times, it deviated upwards into the topcoat away from the bond coat interface which reduced the effective thickness of the topcoat that was still attached to the bond coat (Figure 68). This type of crack path deviation could indicate the crack was extending up into the topcoat as to reduce the effective thickness of the topcoat still attached to the bond coat. Thereby reducing the stress intensity at the crack tip and arresting crack growth. It would also explain why the small diagonal cracks (white arrow - Figure 68) stopped after traveling a short length up into the topcoat. The crack eventually reformed and continued to propagate inwards causing spallation. This cracking behavior along with the location of the failure suggests the stress intensity induced by the topcoat exceeded its fracture strength so the crack grew with each

thermal cycle. Although not observed, it would be expected there would be some sort of relationship between crack growth rate ( $da/dN$ ) and the thickness with this particular failure mechanism.

Moving down in topcoat thickness to 750, 425 and 225  $\mu\text{m}$  TBCs, the failure characteristics changed. Taking the 750  $\mu\text{m}$  TBC as an example, the failure occurred at the YSZ-TGO interface. The change in the location of the failure indicated topcoat's stress intensity factor did not exceed the fracture toughness of the YSZ. As Figure 65 depicts, edge cracks were the ultimate cause of the large scale delamination in this TBC but ahead of these cracks, significant damage had already taken place at the YSZ-TGO interface as depicted in Figure 75.

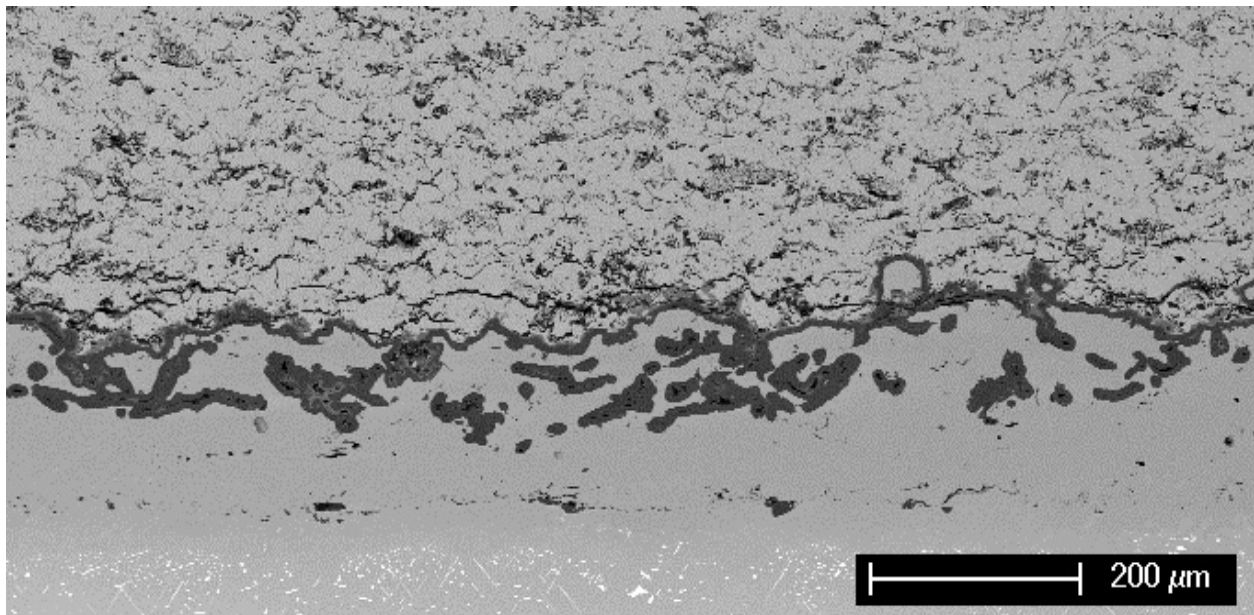


**Figure 75 - 750 $\mu\text{m}$  TBC after 440 cycles. This portion of the topcoat was still intact and far ahead of an edge crack.**

It appeared as though the edge crack was “consuming” an already damaged or weakened region of the interface. Such damage to the YSZ-TGO interface has been modeled by several

authors for APS TBC systems [3, 45, 62-65]. In these models, the thermal expansion mismatch stresses are the driving force for this damage. Before TGO formation, tensile out-of-plane stresses develop above peaks in the bond coat leading to crack formation. These cracks are unable to extend laterally because compressive stresses exist in the regions adjacent to the bond coat peaks (i.e. bond coat valleys). As the TGO begins to grow, the compressive out-of-plane stresses adjacent to the peaks begin to reverse allowing for the cracks at the peaks to extend laterally [45]. The bond coat roughness and the toughness of the topcoat influence the rate of this stress reversal process and the rate of crack extension. Furthermore, these models predict the cyclic damage is independent of topcoat thickness [3, 45, 66]. It would be expected that a denser YSZ topcoat or a smoother bond coat would accumulate damage differently potentially leading to a different topcoat thickness-TBC lifetime relationship.

This cyclic damage was also observed in a 425 $\mu\text{m}$  topcoat which was thermally cycled to 90% of its FCT lifetime, at which time the specimen was removed from the furnace, mounted in epoxy, cross-sectioned and observed in the SEM. After 510 cycles, there was visible edge cracking, Figure 76, and cracking within the interior of the specimen, Figure 77, yet the TBC was still intact.

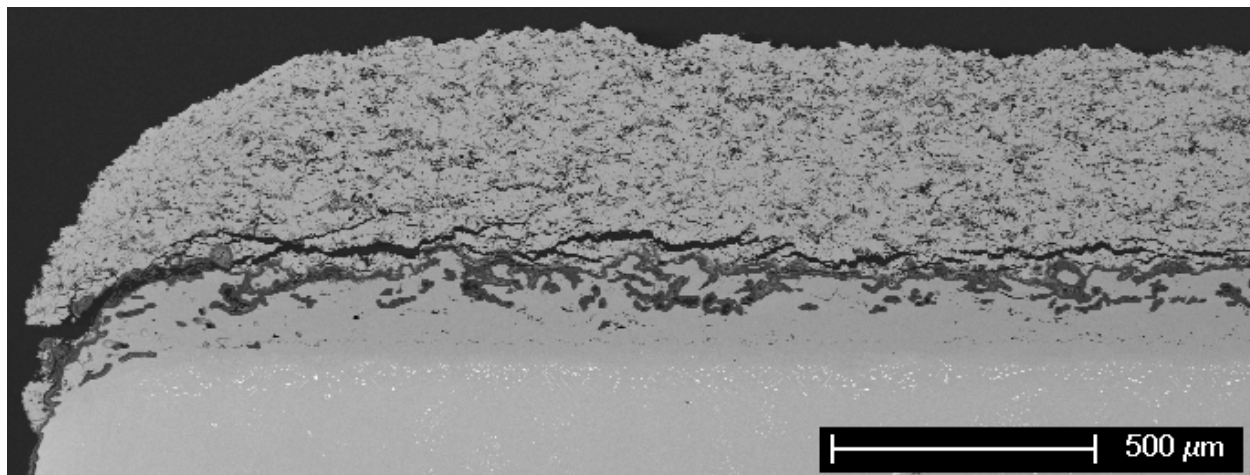


**Figure 76 – The edge of a 425 $\mu$ m topcoat after 510 cycles (91% lifetime).**

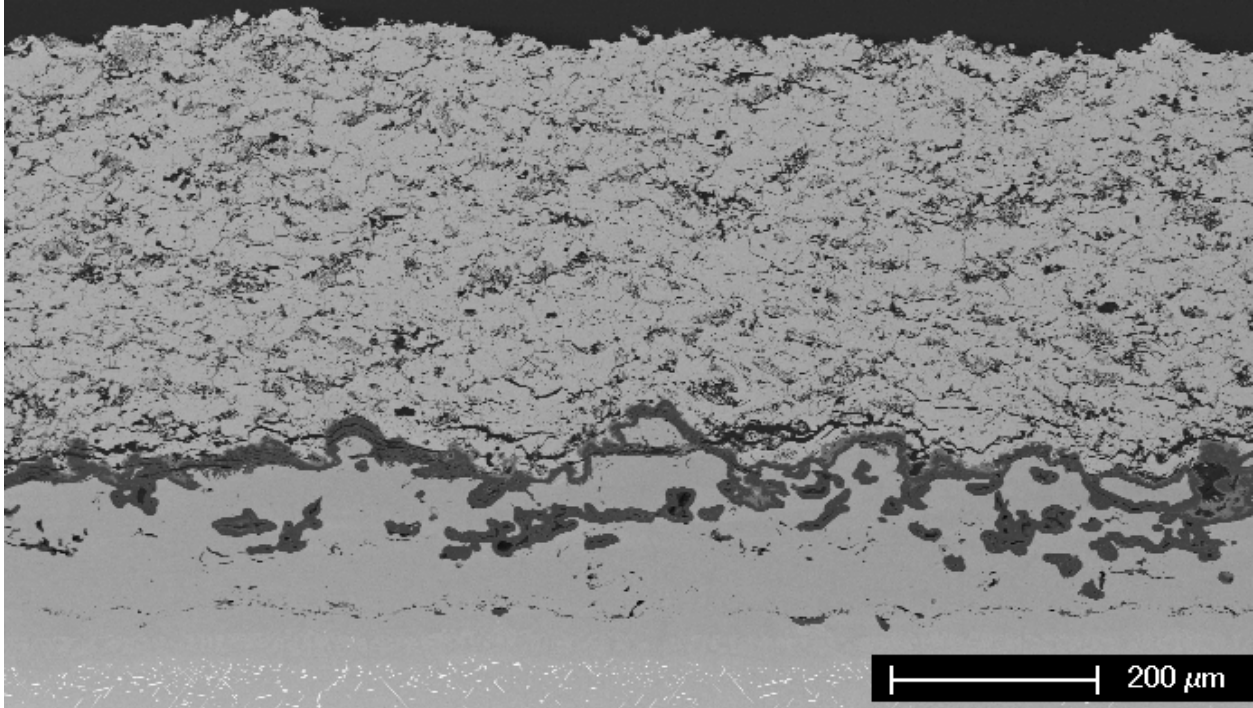


**Figure 77 – The interior of a 425 $\mu$ m topcoat after 510 cycles (91% lifetime).**

The entire interface appeared to be accumulating damage over the lifetime of the specimen, even though the topcoat remained attached. Eventually, edge cracks in the 750, 425 and 225  $\mu$ m TBCs extended causing complete topcoat spallation.

Based on these observations, the thickness dependence could factor into the TBC lifetime by dictating how much damage the TGO-YSZ interface can tolerate before edge delamination occurs. Essentially, the interfacial toughness of the topcoat-TGO interface would have a starting value based solely on the TBC system properties (i.e.  $\Gamma_{YSZ}$ ,  $\Gamma_{TGO-YSZ}$ ,  $E_{TBC}$ , surface roughness of the bond coat, etc...) and then decay a given amount with each thermal cycle. As discussed in Section 2.2.3, the stress intensity factor induced by the topcoat is dependent on the square-root of

the thickness of the topcoat. Once the strain energy release rate exceeded the interfacial toughness, crack growth would occur. After this, the growth of the crack could exhibit a fatigue crack growth mechanism.

This statement hinges on the assumption that the cyclic damage occurring at the TGO-YSZ layer is independent of topcoat thickness and instead only depends on the thermal stresses and other material properties. As mentioned previously, many of the current theories used to model this kind of cyclic damage do not include the topcoat thickness in their analyses and only consider the thermal stress thus supporting this first assumption. Similarly, a visual comparison of the 750  $\mu\text{m}$  TBC in Figure 75, which has 440 cycles, and the 425  $\mu\text{m}$  TBC in Figure 77, which has 510 cycles, does not suggest there is any profound difference in the amount of damage. If anything, the damage after 510 cycles is more severe than after 440 cycles.

For the thinnest TBC, 100  $\mu\text{m}$ , both edge delamination and buckling were observed (Figure 62). For buckling to occur Equation 10 must be satisfied [39]:

**Equation 10**

$$\sigma_b \geq \frac{1.22 E_{\text{topcoat}}}{1 - \nu_{\text{topcoat}}^2} \left( \frac{h_{\text{topcoat}}}{r_b} \right)^2$$

Where  $\sigma_b$  is the buckling stress,  $E_{\text{topcoat}}$  is the modulus of the topcoat,  $\nu_{\text{topcoat}}$  is Poisson's ratio of the topcoat,  $h_{\text{topcoat}}$  is the topcoat thickness and  $r_b$  is the radius of the delaminated region. The buckling stress is limited to the maximum CTE mismatch stress which is dictated by material properties and should be the same for all of the TBCs tested in this study. The only other adjustable parameter is the radius of the delaminated region. This critical radius can be solved for by using Equation 6 to calculate a typical value for the thermal stress with material

properties from Table 2, then plugging this value into Equation 10 and resolving for the buckling radius. Figure 78 is a graph of the critical delamination radius with topcoat thickness being the independent variable.

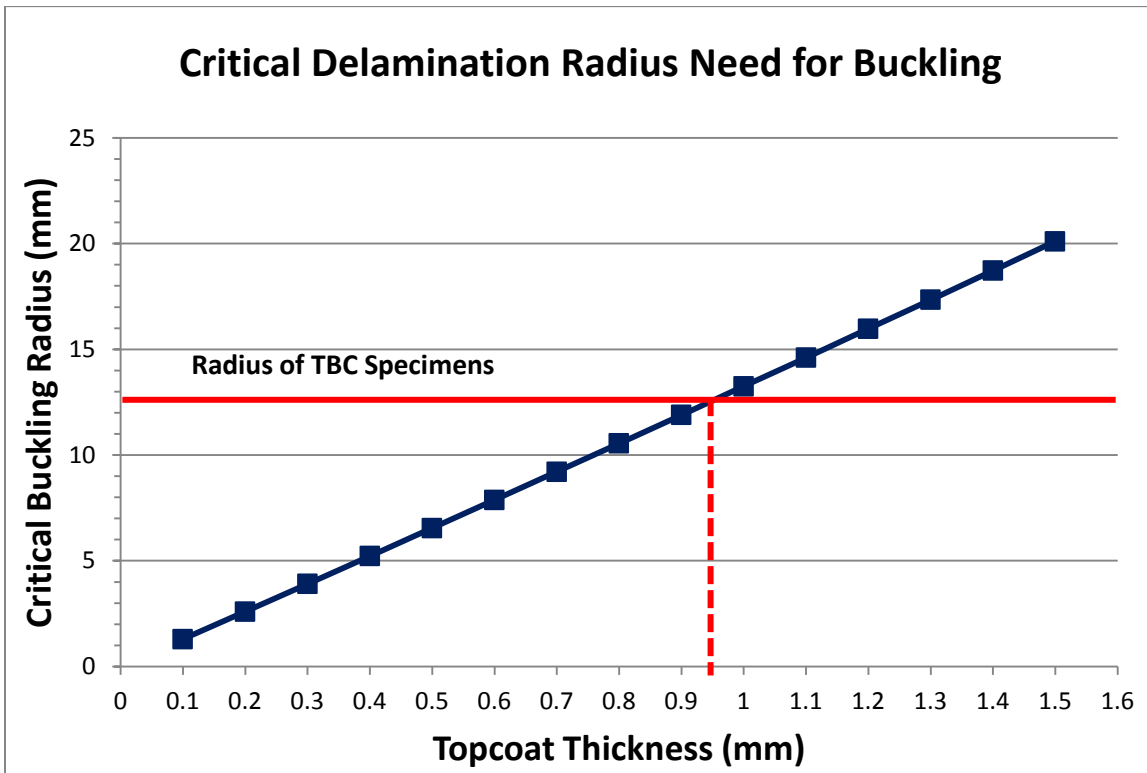


Figure 78 - Critical delamination radius needed for topcoat buckling.

For topcoats above ~0.95mm, buckling should be prohibited because the radius of the TBC specimens (12.5mm) is smaller than the critical radius needed for buckling. For the 750 and 425  $\mu\text{m}$  specimens, delamination of radii 10 and 6mm, respectively, are needed for buckling to occur. While these are physically achievable, buckling was not observed and instead edge delaminations dominated. Yu et al [67] determined that for thin films under a residual stress, an edge flaw of size  $h$  or  $2h$ , where  $h$  is the thickness of the coating, was needed to induce edge delamination whereas, in general, a delamination radius of  $10-20h$  was needed to induce

buckling [67, 68]. Thus it would seem reasonable that edge delamination could play a more dominant role than buckling since the crack lengths needed are much smaller.

Based on Figure 78, buckling could more so be a possibility for the 225 and 100  $\mu\text{m}$  TBCs since only  $\sim 3\text{mm}$  and  $\sim 1.5\text{mm}$  delaminations are needed to permit buckling. However, buckling was not observed in the 225  $\mu\text{m}$  TBC but only in the 100 $\mu\text{m}$  specimen. Possible reasons being that not enough small cracks, such as those seen in Figure 72, combined to form a delamination large enough for buckling, or that the edge driven delamination occurred before a large enough delamination could occur. The roughness of the TGO-YSZ interface and the discontinuous cracking could also hinder the crack coalescence thereby preventing buckling.

Based on all of these observations, it appears different failure mechanisms are present which are dependent on the thickness of the coating.

**4.1.2.5 Conclusions** TBCs with topcoats ranging in thickness from 100  $\mu\text{m}$  to 1425  $\mu\text{m}$  were thermally cycled at 1100°C for one hour cycles. The topcoat thickness and FCT lifetime relationship was best fit with a linear trend line, however, parabolic trend lines also fit the data quite well indicating the exact nature of the fit was somewhat inconclusive. The thickest topcoats (1425 & 1150  $\mu\text{m}$ ) failed by cracking within the topcoat layer which was attributed to the strain energy release rate of the topcoat exceeding the fracture strength of the YSZ topcoat. Moving down in thickness, the 750, 425 and 225 $\mu\text{m}$  TBCs did not fail within the topcoat suggesting the stress intensity factor induced by these topcoats were less than the fracture toughness of the YSZ. Instead, these TBCs failed due to cyclic-induced, bond coat oxidation damage at the YSZ-TGO interface. It was proposed the toughness of the interface had a high initial value which then, during cycling, steadily degraded until the stress intensity factor of the topcoat exceed the declining toughness. At this point, edge-delamination type failure occurred. Buckle failure was

suppressed in the thick TBCs ( $>1150\mu\text{m}$ ) because the buckling criteria required interfacial delaminations of sizes that were greater than the size of the TBC specimens in order to induce buckling. The thinner TBCs ( $< 1150 \mu\text{m}$ ) failed by edge delaminations with the exception of the  $100 \mu\text{m}$  TBC which did exhibit some buckling. Suppression of the buckling was attributed to roughness of the bond coat interface and irregular cracking which occurred during thermal cycling.

Regarding the numerical results (i.e. FCT data), there would be no extension in TBC lifetime achieved by reducing the thickness of the topcoat beyond  $100 \mu\text{m}$ . Further reductions would yield minimal increases in lifetime (+50 cycles) and could open the possibility of topcoat buckling becoming the dominant failure mechanism since the critical delamination radius needed for buckling also decreases with decreasing topcoat thickness. At the other end of the thickness spectrum, topcoats exceeding a thickness of  $1638\mu\text{m}$  would be predicted to fail after the first cycle.

Finally, it should be stressed the results of these FCT testing are very system dependent. Properties such as bond coat roughness, topcoat density, CTE of the superalloy and testing temperature will influence the strain energy release rate of the topcoat, the thermal stresses and the TGO-topcoat damage mechanisms. This in turn could change the topcoat thickness-FCT lifetime relationship. Superalloys with extremely high CTEs (larger thermal stresses and more strain energy) could potentially see an extension in the range of topcoat thicknesses that exhibit failure within the topcoat (see Section 4.3.2). Very dense topcoats (less strain tolerant and reduced toughness) could also extend the range of thicknesses which fail within the topcoat or potentially cause the damage mechanism at the TGO-topcoat interface to progress faster which could then flatten the slope of the fit line in Figure 74. Likewise, a very smooth bond coat could

reduce this fit line to almost zero (Section 4.2) potentially negating any topcoat thickness effect. Thus, when comparing APS TBC systems, a detailed description of the system parameters must be considered in order to predict how the TBC will behave.

### **4.1.3 Topcoat Microstructure**

**4.1.3.1 Overview** Investigating the influence of topcoat microstructure involved two approaches. The first approach was designed to minimize the variables associated with the TBC manufacturing process. This approach was designated as the “Design Approach.” Here, a set of TBCs were prepared in one processing batch where a single batch entails all specimens which had superalloy substrates cut from the same stock, all the bond coats were deposited in one coating run with a common powder lot and all superalloy/bond coat couples were heat treated in the same furnace at the same time. This method minimizes processing variables which may be introduced during the preparation process. Topcoats were then deposited on the bond coat/superalloy couples in separate runs where different powders, torches and spray parameters were used to produce distinct microstructures. The microstructures investigated included a low density topcoat (LD), a dense vertically fissured topcoat (DVF) and a combination LD-DVF topcoat (Dual TBC). These microstructures were chosen because the LD and DVF topcoats offer low thermal conductivity and high strain tolerance, respectively, which alone are desirable topcoat properties. However, the low thermal conductivity of the LD topcoat comes at the expense of strain tolerance and coating strength and the strain tolerance of the DVF topcoat comes at the expense of the thermal conductivity. Therefore the dual TBC was chosen in an attempt to capture the best of both, the low thermal conductivity to provide insulation and the

strain tolerance near the bond coat interface to alleviate thermal stresses during service. These TBCs were then tested head-to-head and the results were compared.

The second approach to investigating the influence of topcoat microstructure involved sorting through a collection of previously tested TBC specimens, which were prepared in different batches over a period of four years, and picking out “common” TBCs to compare their performances. This second approach was more so an “observation,” rather than a designed set of experiments since the individual specimens were created at different times and for different purposes. For this reason, these experiments are designated as the “Observation Approach.” All of the TBCs chosen for comparison nominally had the same superalloy substrate, bond coat and YSZ material but the topcoats ended up having different densities/porosities. Furthermore, the FCT results of these tests suggest lifetime is very sensitive to topcoat density.

#### **4.1.3.2 Design Approach**

**4.1.3.2.1 Experimental Overview** All the TBCs tested had the same substrate, PWA 1484, and bond coat, dual layer NiCoCrAlY bond coat, the compositions of which are given in Table 4. The bond coats were argon-shrouded plasma sprayed onto the substrate discs (2.5cm in diameter and 3mm thick) and then the entire batch of specimens was vacuum heat treated at 1080°C for four hours. After heat treatment, the topcoats were deposited by air plasma spraying. The topcoat microstructures investigated included a low density topcoat (LD), a dense vertically fissured topcoat (DVF) and a combination LD-DVF topcoat (Dual TBC) where a 125 μm thick layer of the DVF topcoat was deposited on the bond coat and then an additional 1100 μm of LD topcoat was deposited on top of the DVF layer. The total thickness of the LD topcoat was 1100μm, the DVF was 1100μm and the dual TBC was 1225μm.

After deposition, the edges of the specimens were gently brushed to remove over-spray, which is YSZ that was inadvertently deposited on the sides of the disk coupons due to the geometry of the spray process. If not removed, this artifact can induce complex stresses at the free edge of the coating causing premature failure.

Seven specimens were prepared for each topcoat type. Three of the seven TBC specimens were furnace cycle tested (FCT) in a CM bottom loading furnace where one furnace cycle consisted of a 10 minute heating period to 1100°C, a 45 minute isothermal hold and a 10 minute forced-air cooling period down to approximately 60°C. Every 20 cycles, specimens were examined and visually checked for spallation, cracking and delamination. Most of the TBCs failed by complete topcoat spallation, however, some experienced cracking, chipping and buckling without complete topcoat spallation. To account for this, failure was defined as at least 30% delamination/spallation of the topcoat. Furthermore, the term ‘technical failure’ was used to classify TBCs which did not fail by complete topcoat spallation but still met the failure criteria. After failure, the fracture surfaces were imaged with a high resolution scanner. Following, the specimens were mounted in warm epoxy, sectioned with a high-speed precision saw and polished to a 0.04µm finish and examined in an SEM equipped with standardless EDS.

Another three specimens were JETS tested for 2000 cycles at which time the specimens were stopped and examined for damage. For details of this testing method see section 3.1. The seventh specimen of each group was set aside for the purpose of characterizing the starting microstructure. The starting microstructures are shown in Figure 79 through Figure 81.

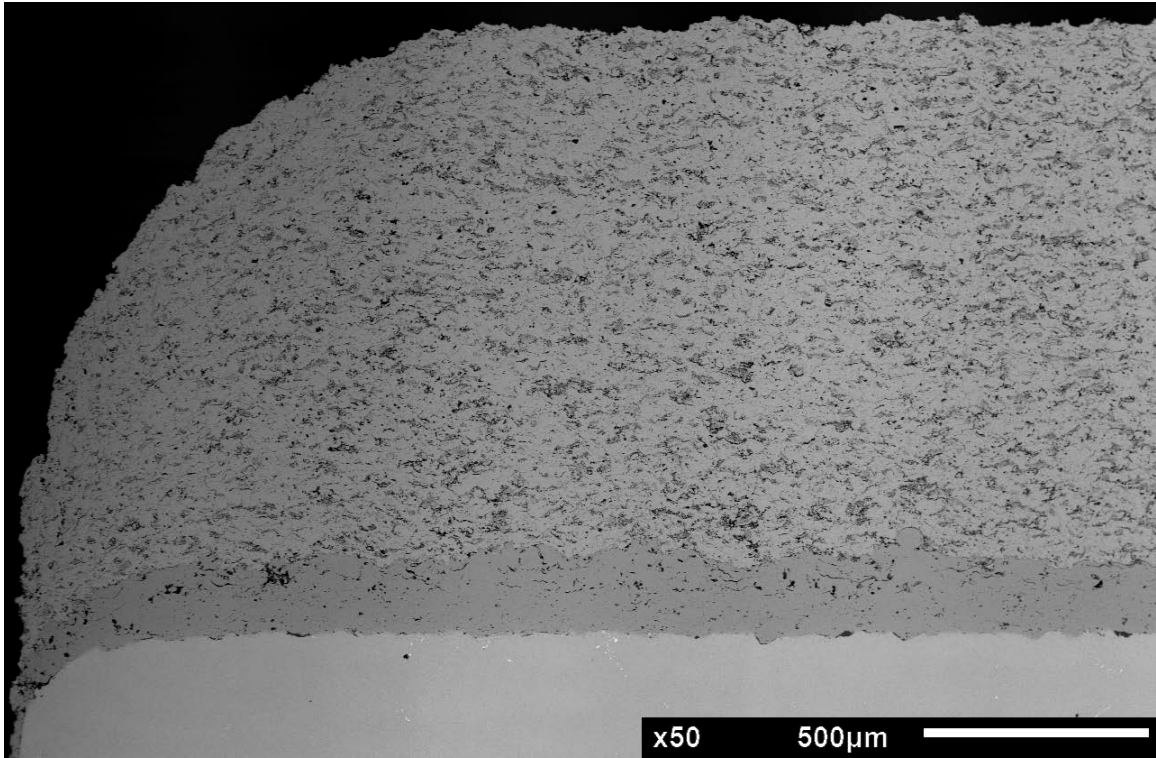


**Figure 79 – As-processed LD topcoat on DL bond coat on PWA 1484 substrate.**

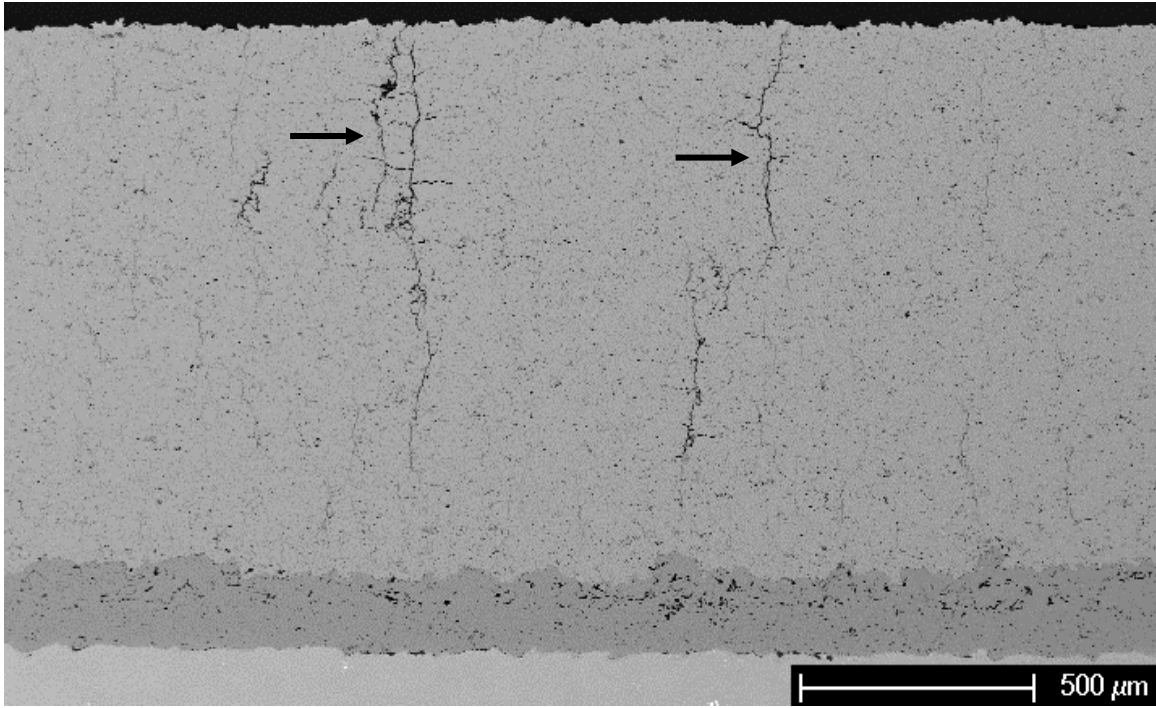


**Figure 80 - As-processed DVF topcoat on DL bond coat on PWA 1484 substrate. Black arrows indicate large vertical fissures.**

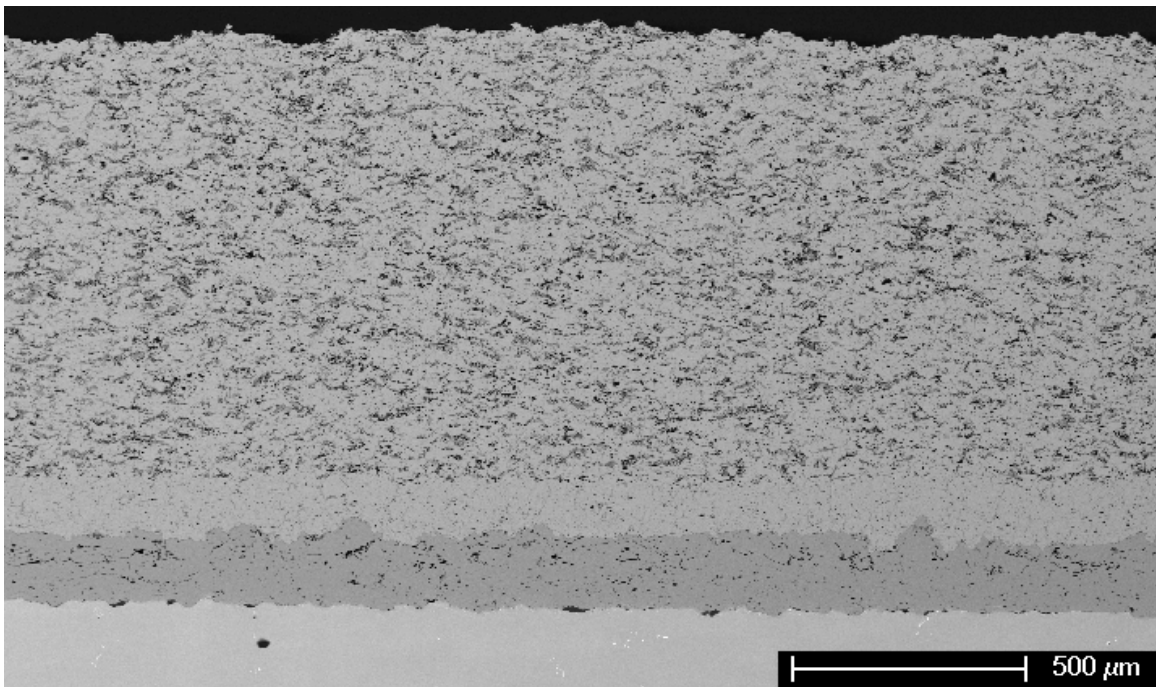


**Figure 81 - As-processed dual TBC on DL bond coat on PWA 1484 substrate.**

A higher magnification image of the interface between the LD and DVF layers of the dual TBC is shown in Figure 82.

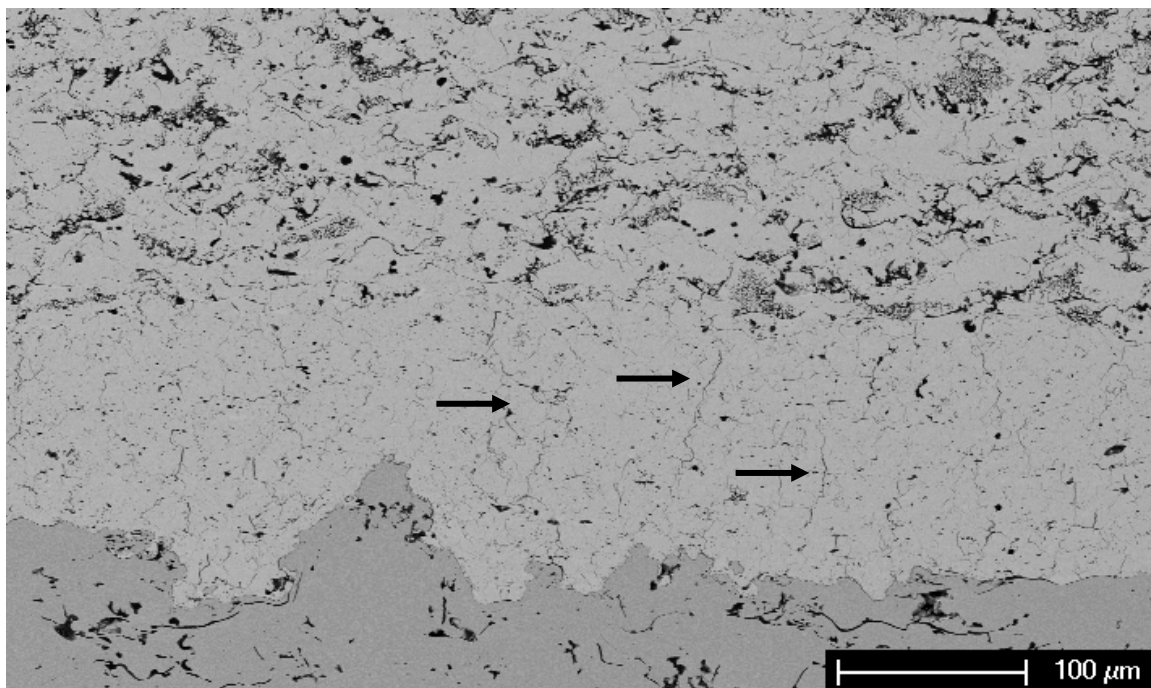


**Figure 82 - High magnification micrograph of interface between LD and DVF layers showing good adherence and no large delamination cracks between the layers.**

As the micrograph depicts, the adherence between the two layers was exceptional since no large separation cracks ( $<50\mu\text{m}$ ) were observed. Furthermore, from this micrograph, there is an obvious difference in the density and porosity between the two coatings. The DVF layer is dense and contains small vertical fissures throughout it (black arrows in Figure 82). The full DVF topcoat, Figure 80, also contains these small cracks, but it also contains large vertical fissures which extend anywhere from 50% to 100% of the  $1100\mu\text{m}$  thick topcoat (black arrows). The density of these large fissures was measured to be 11 fissures per centimeter of DVF

coating. The LD topcoat layers in Figure 82 and in Figure 79 contained large globular pores, inter-splat pores, and small micro-cracks. All of these pore types combine to yield a low density coating.

**4.1.3.2.2 Results: FCT Testing** The FCT results for the LD, DVF and dual TBC specimens are given in Figure 83.

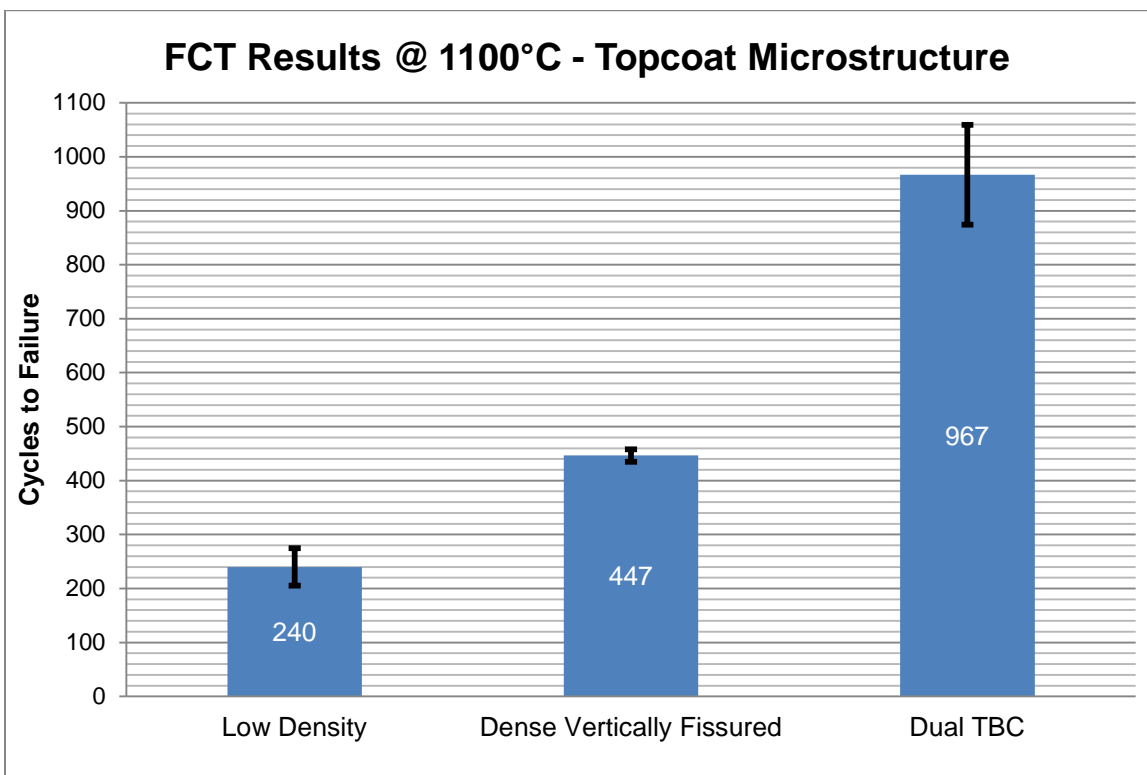
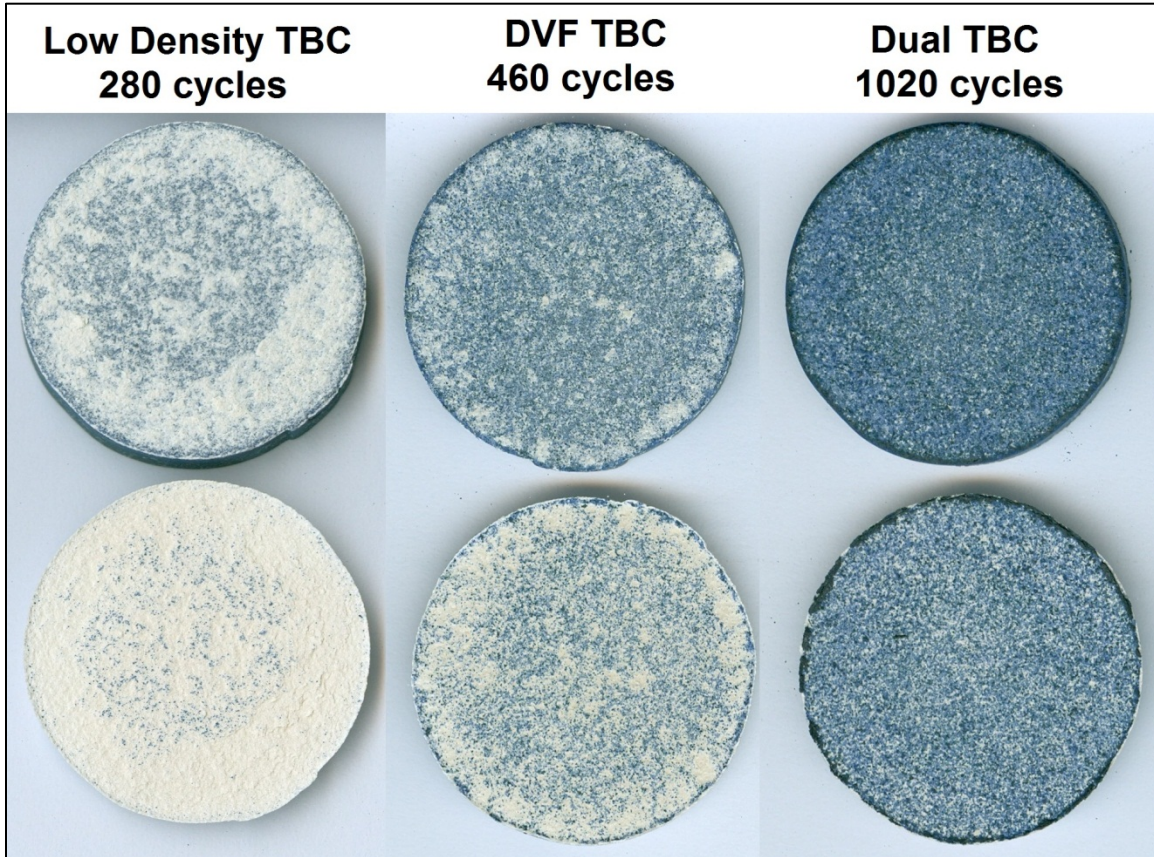


**Figure 83 – FCT results for the topcoat microstructure specimens.**

The reproducibility in the LD and DVF coatings was good as there was little scatter in the lifetime of the three specimens in each group (indicated by the small error bars), however, the dual TBC specimens had a much larger scatter in lifetime  $\pm 100$  cycles. Despite this, there was a statistically significant difference in the FCT lifetimes of the three topcoats. A factor of two

differentiated the LD and DVF TBC and another factor of two separated the DVF and the dual TBC specimens. These results indicate topcoat microstructure strongly influences FCT lifetime.

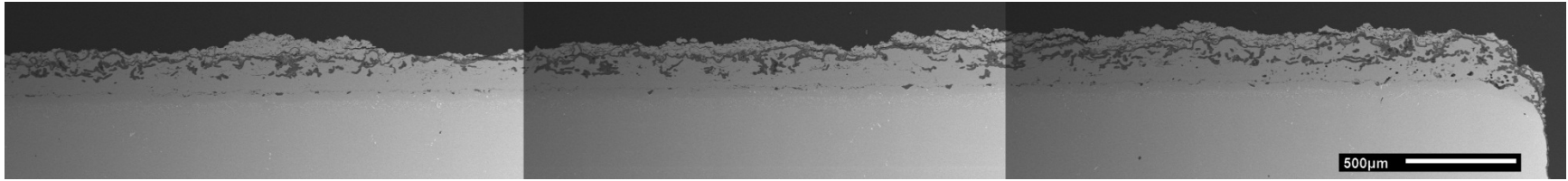
High resolution scanned images of the surfaces of the three groups are shown in Figure 84.



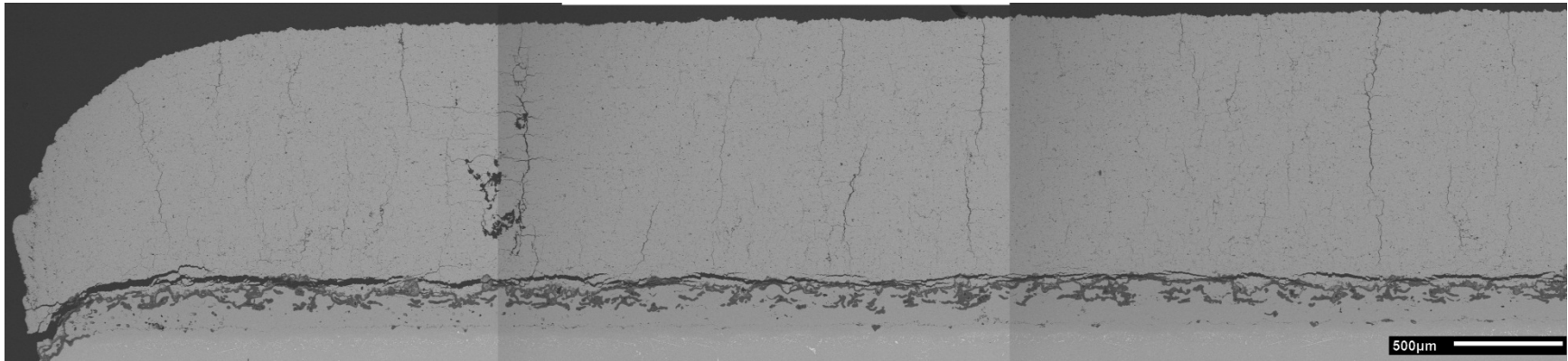
**Figure 84 - High resolution image of failed LD, DVF and dual TBC specimens.**

The LD specimen had heavy amounts of YSZ on the fracture surface while the DVF and the dual TBC had more TGO on their fracture surfaces. The surface of the dual TBC was covered with a dark blue oxide which is indicative of nickel aluminum spinel oxide. Furthermore, since the fracture surface of both the topcoat underside (lower right circle in Figure

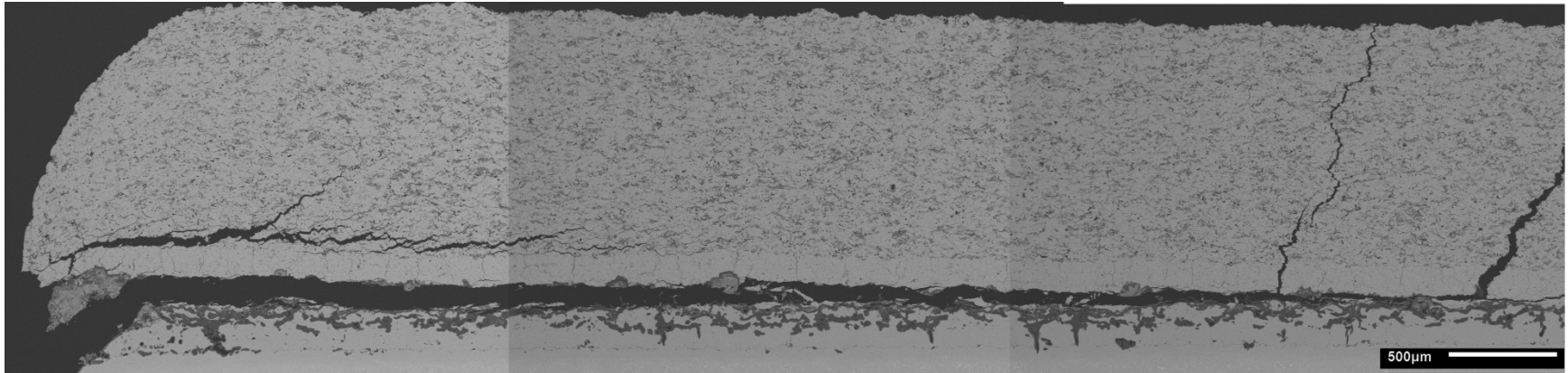
84) and the bond coat surface (upper right circle in Figure 84) were covered heavily with TGO, this indicated failure primarily occurred within the TGO and not at the interface between the two topcoat layers (i.e. between the LD and DVF layers). Cross-sections of the three specimens are shown in Figure 85 through Figure 87. The DVF and the dual TBC specimens in these figures were technical failures meaning while the topcoats are still intact, significant delamination has taken place in other regions of the specimens rendering their failures.



**Figure 85 - Failed LD specimen with 280 cycles at failure. Topcoat completely spalled off.**

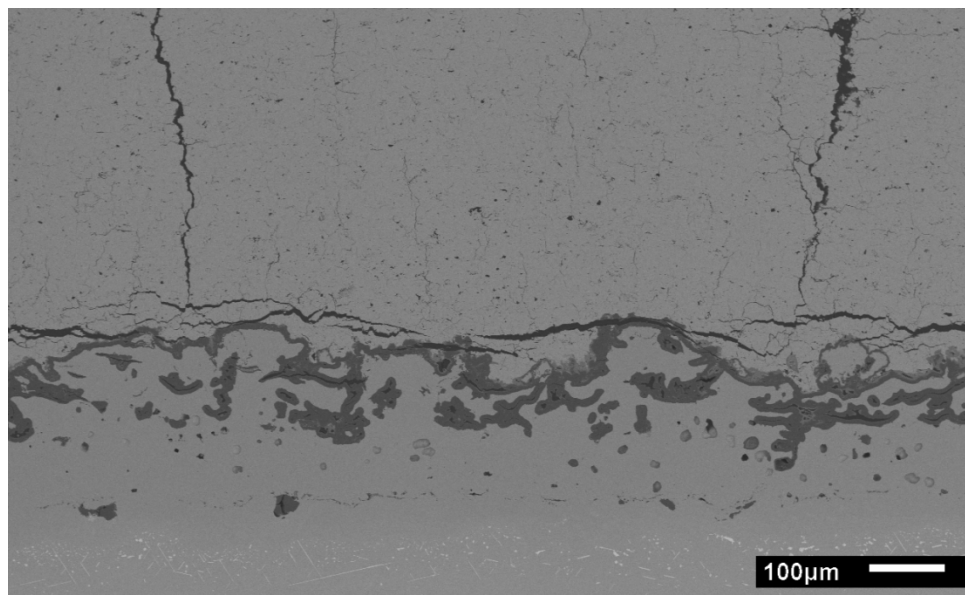


**Figure 86 - Failed DVF specimen with 440 cycles at failure.**



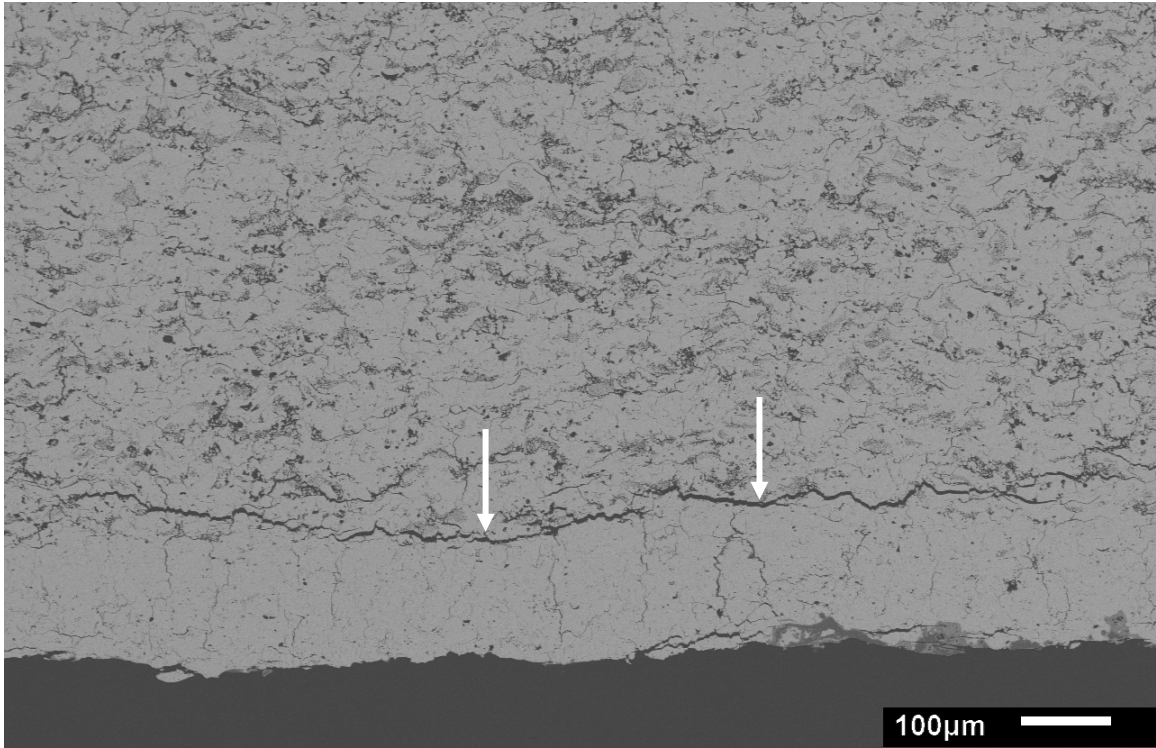
**Figure 87 - Failed dual TBC specimen with 1020 cycles at failure**

The final spallation crack in the LD specimen occurred within the topcoat, above the topcoat-TGO interface. Very little of the fracture took place in or around the TGO. As for the DVF specimen, cracking occurred along the topcoat/TGO interface. This observation alone indicates there was either a difference in the amount of stored strain energy or fracture resistance between the two coatings. Examining a higher magnification micrograph of the DVF TBC, Figure 88, the crack path went over the bond coat peaks and propagated through the YSZ valleys which is indicative of a bond coat oxidation induced failure.



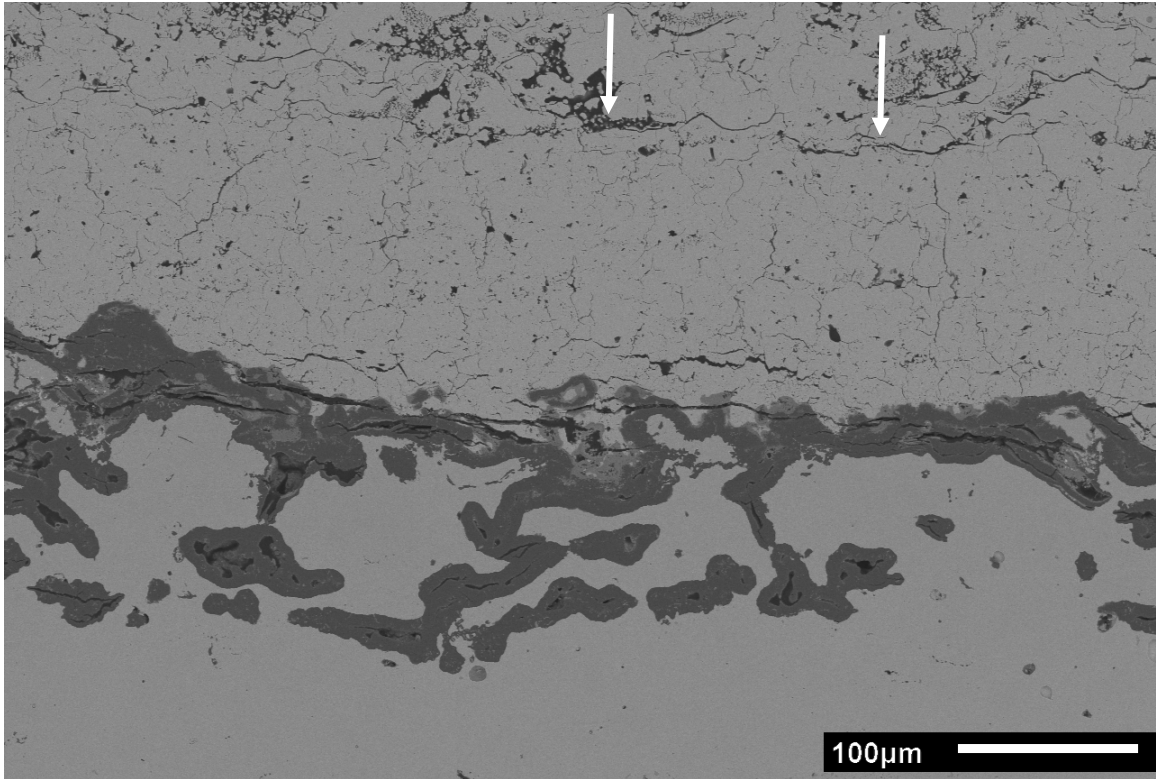
**Figure 88 - Failed DVF specimen with 440 cycles at failure.**

In the dual TBC, isolated separations between the two TBC layers was observed near the edges of the specimens as shown in Figure 87 and within the interior of the specimen as shown in Figure 89 and Figure 90.



**Figure 89 - Failed dual TBC specimen after 860 cycles. This is only a micrograph of the spalled topcoat.**

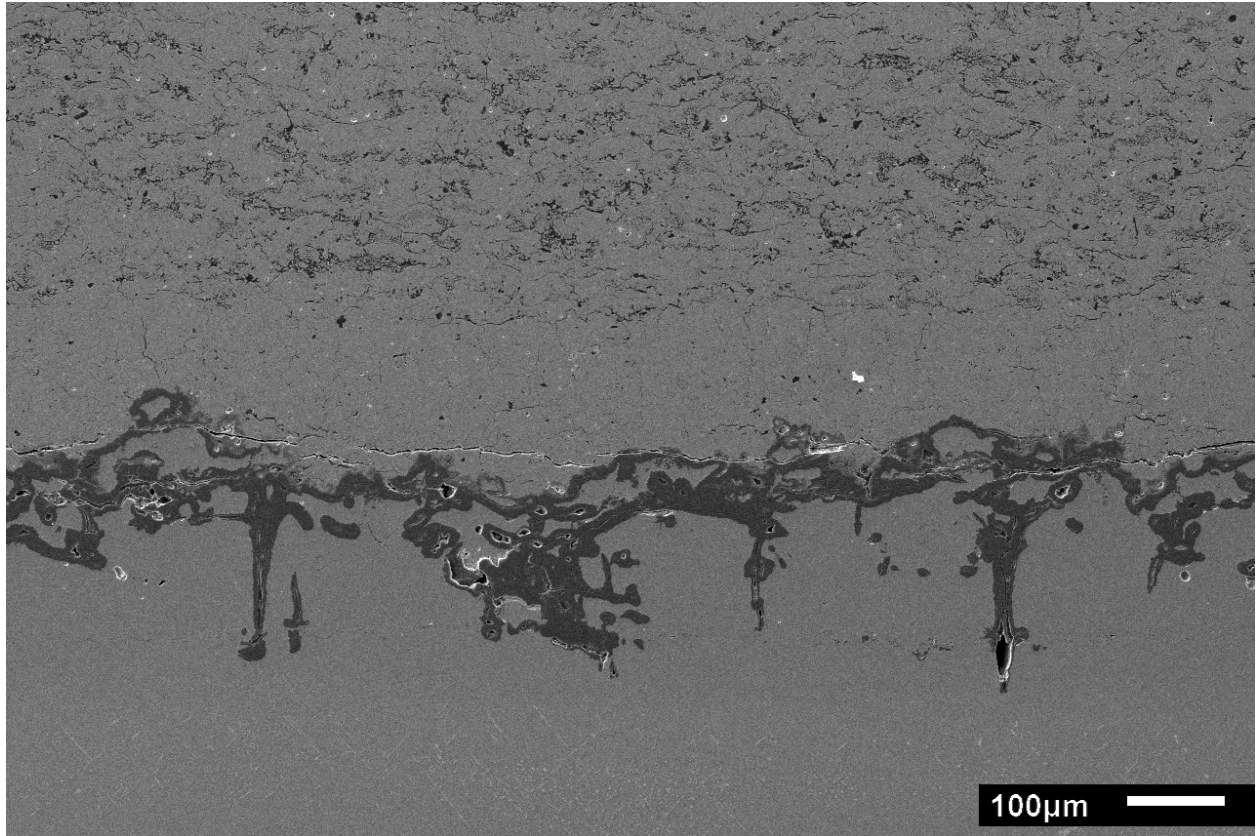
**Arrows indicate horizontal cracks present at the interface between the LD and DVF layers.**



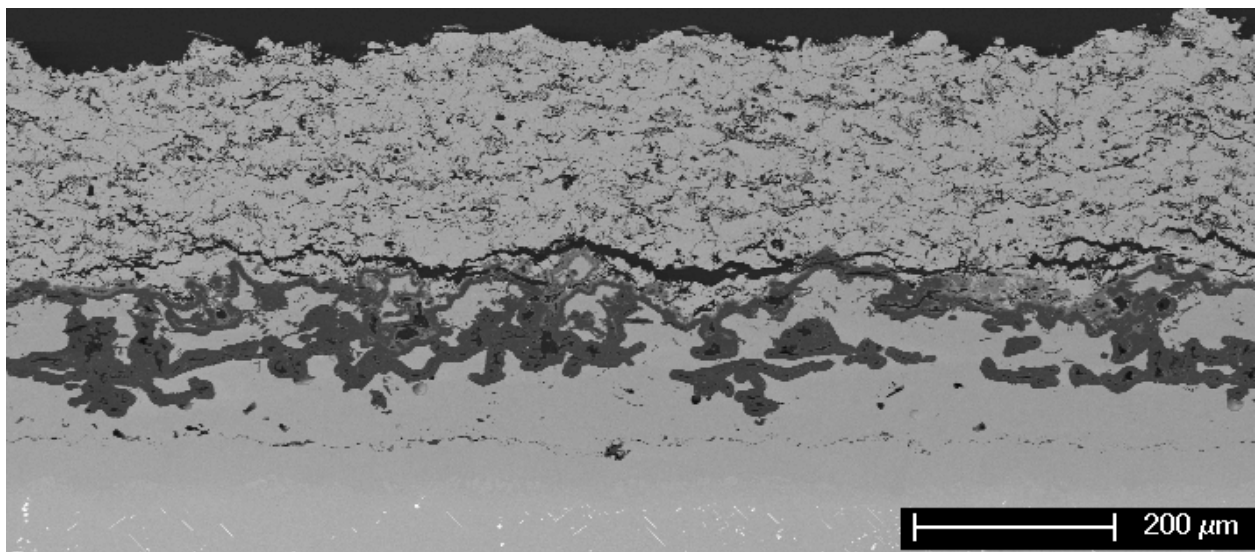
**Figure 90 – Dual TBC specimen which experienced a technical failure after 1020 cycles. Arrows indicate horizontal micro-cracks at the interface between the LD and DVF layers.**

Figure 89 indicated large cracks were found separating the two layers whereas Figure 90 depicts much smaller horizontal cracks between the two layers. The presence of these cracks could potentially reduce the thermal stresses experienced within the LD topcoat layer since contact is needed to translate stress from one layer to the next.

Closer examination of intact regions of the dual TBC, Figure 91, reveals minimal damage at the topcoat-TGO interface, especially since this specimen experienced 1020 cycles. For comparison purposes, a 225 μm LD topcoat with a dual layer bond coat on PWA 1484 with 810 cycles is shown in Figure 92.



**Figure 91 - Failed dual TBC with 1020 cycles at failure.**



**Figure 92 – 225  $\mu\text{m}$  topcoat after 810 cycles at 1100°C.**

Note the difference in the amount of cracking and damage between the two specimens around the topcoat-TGO region. This suggests the driving force for crack growth is different between the two specimens or that the toughnesses of the two topcoats are substantially different.

**4.1.3.2.3 Results: JETS Results** The three TBCs were JETS tested for 2000 cycles. Prior to testing, three specimens of each type were edge ground (i.e. edge curvature was removed by grinding on an abrasive wheel) so they could fit into the JETS testing rig. Next, using a traveling microscope, the length of edge cracks (horizontal separations between the topcoat and the bond coat) were measured and recorded for each specimen. The amount of edge cracking was quantified as the cumulative length of the cracks measured, divided by the total circumference of the specimens. Thus a specimen with 50 percent edge cracking means 50 percent of the edge of the topcoat is separated from the bond coat and 50 percent is still intact. None of the nine specimens contained edge cracks prior to testing. Once recorded, the specimens were loaded into the rig, cycled for 2000 heating and cooling cycles, and then removed to again measure the amount of edge cracking. The results of these measurements are detailed in Figure 93.

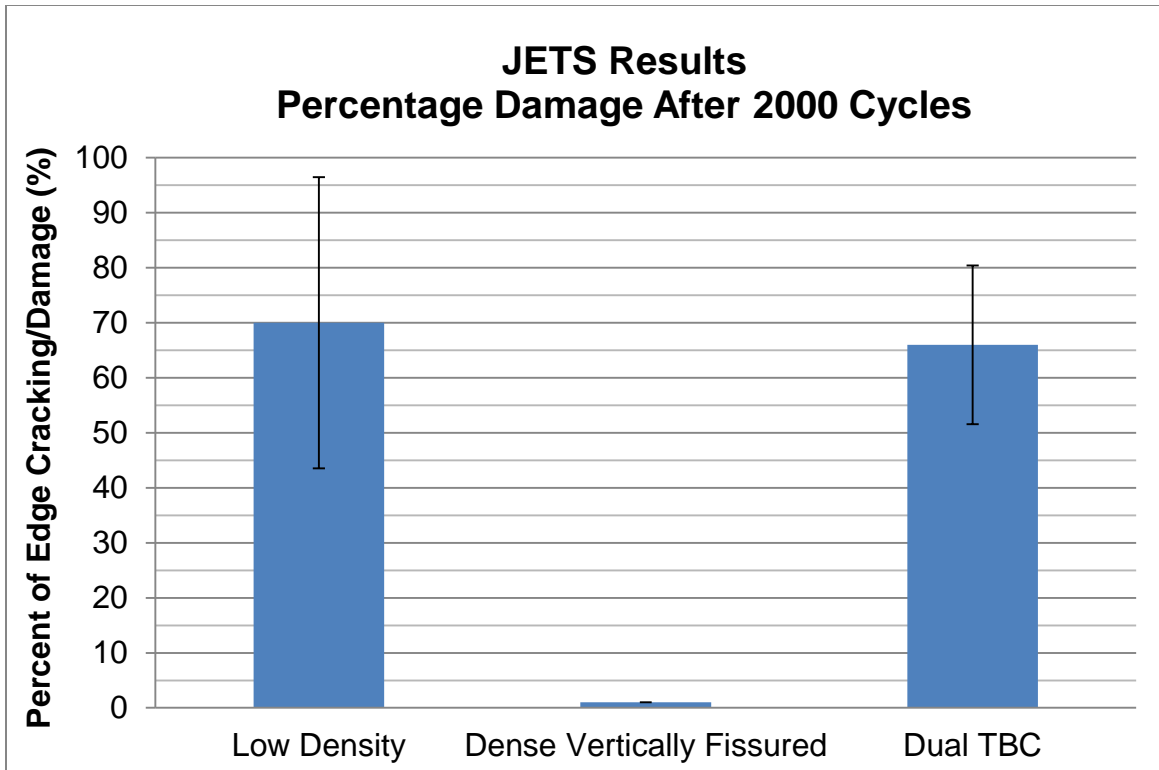


**Figure 93 - Percent edge cracking after 2000 cycles in the JETS apparatus.**

Remarkably, the DVC specimens did not record any increase in edge cracking whereas the dual TBC and the LD specimens experienced large amounts of cracking around the edges.

The LD topcoat experienced edge cracking (Figure 94), vertical cracking (Figure 95) and horizontal cracking near the bond coat/ topcoat interface.

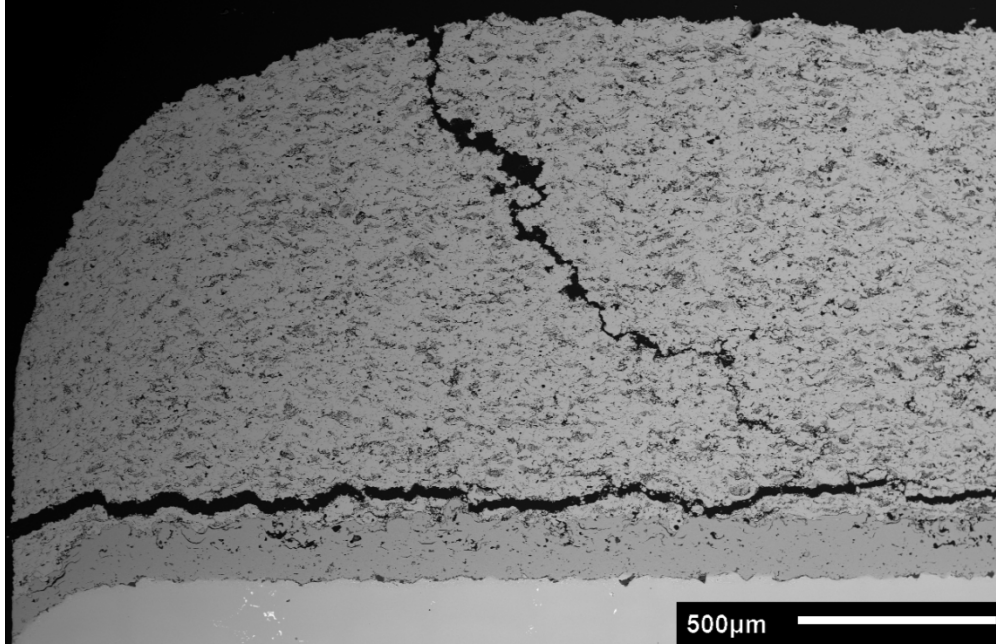


**Figure 94 - 1.1mm LD topcoat on PWA 1484 after 2000 JETS cycles.**

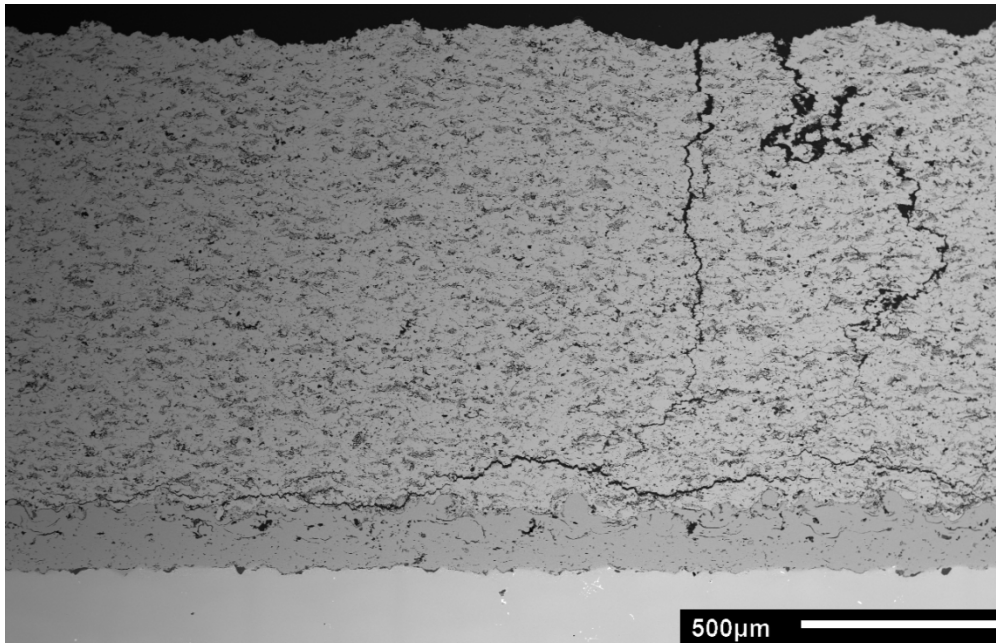


**Figure 95 - 1.1mm LD topcoat on PWA 1484 after 2000 JETS cycles. Micrograph was taken far from the edge of the specimen.**

The vertical cracks extended down from the outer surface and branched out horizontally as they approached the bond coat. Several of these vertical cracks were observed along the cross-section of the specimen.

The dual TBC exhibited similar cracking within the topcoat which is shown in Figure 96 and Figure 97.

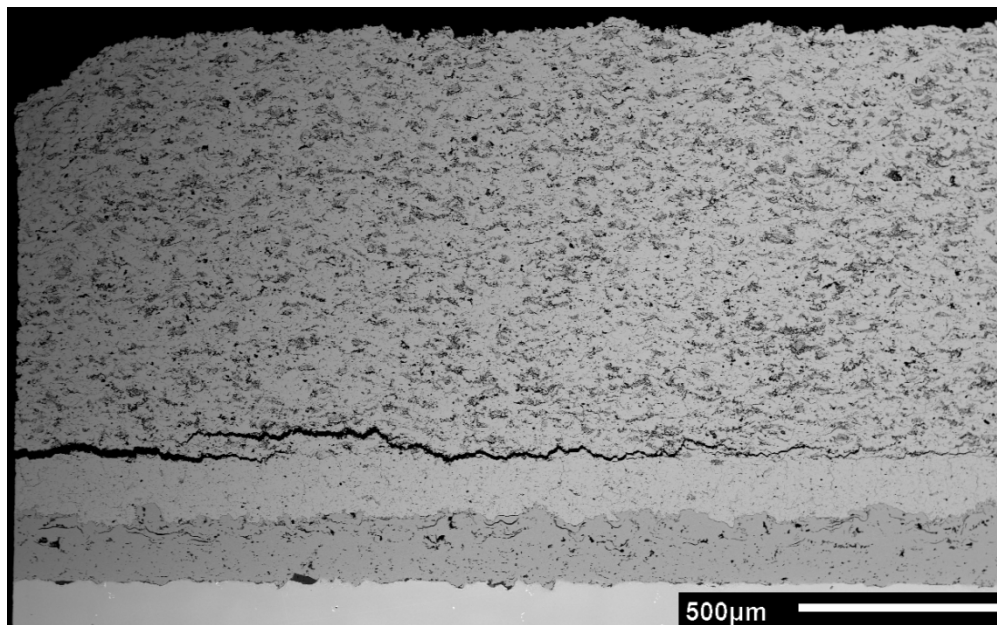


**Figure 96 - Dual TBC on PWA 1484 after 2000 JETS cycles.**

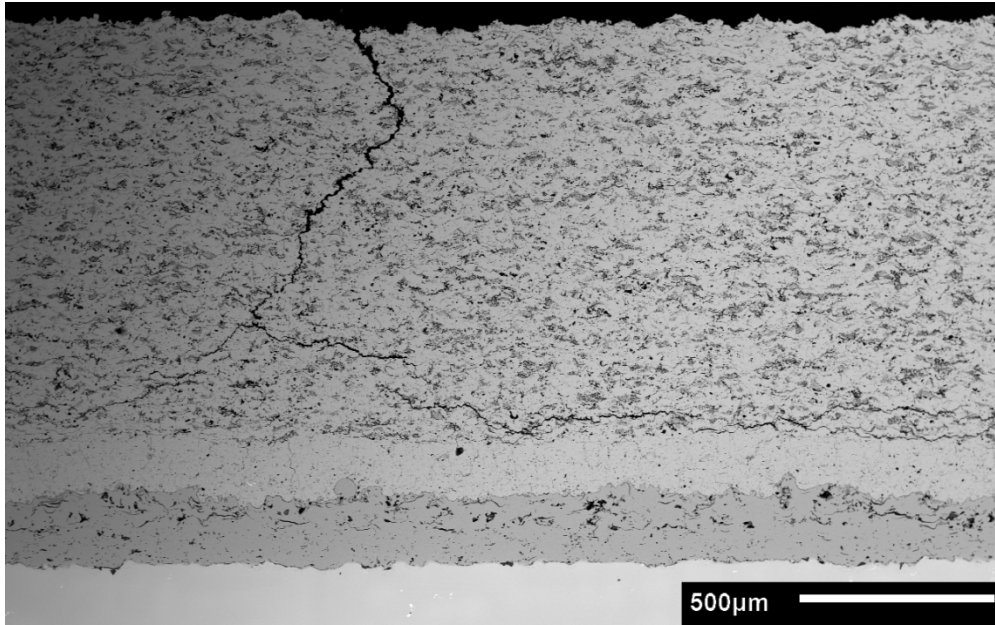


**Figure 97 - Dual TBC on PWA 1484 after 2000 JETS cycles. Micrograph was within the interior of the specimen away from the free edge.**

The same vertical cracking was observed as with the LD coating. This is somewhat expected since the LD microstructure is adjacent to the flame in both the LD and dual TBC specimens. The horizontal cracking, however, occurred between the LD and DVF layers and not at the DVF-bond coat interface. No cracking was observed within the DVF layer, aside from the already present vertical fissures.

The DVF TBCs experienced very minor edge cracking, Figure 98, and no large scale horizontal cracking near the bond coat interface.

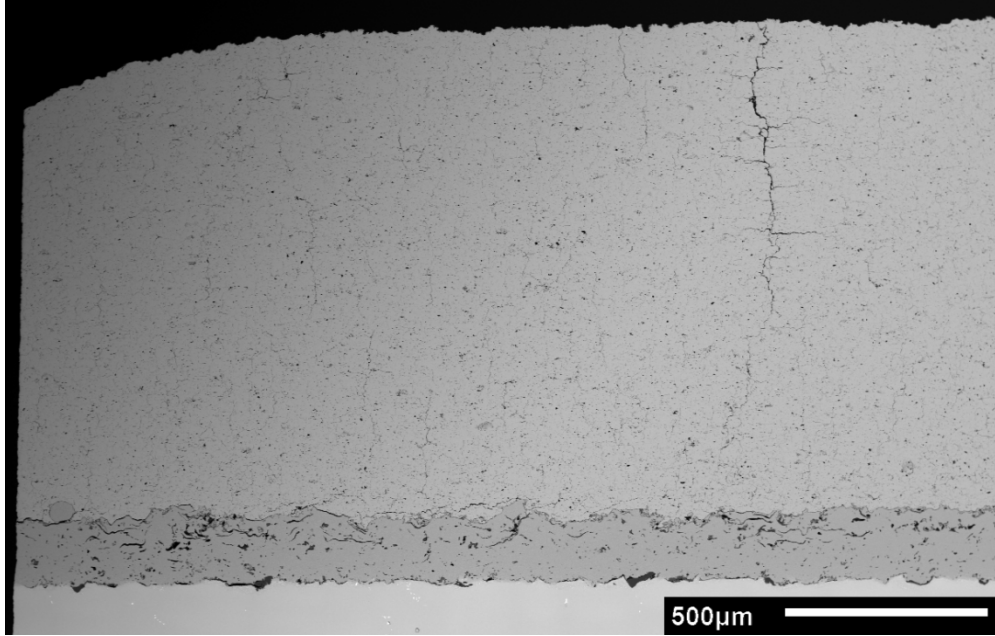


**Figure 98 - 1.1mm DVF topcoat on PWA 1484 after 2000 JETS cycles.**

The already present vertical fissures within the specimen did not appear to grow, extend, or branch out any more than they were in the as-processed state, Figure 99.

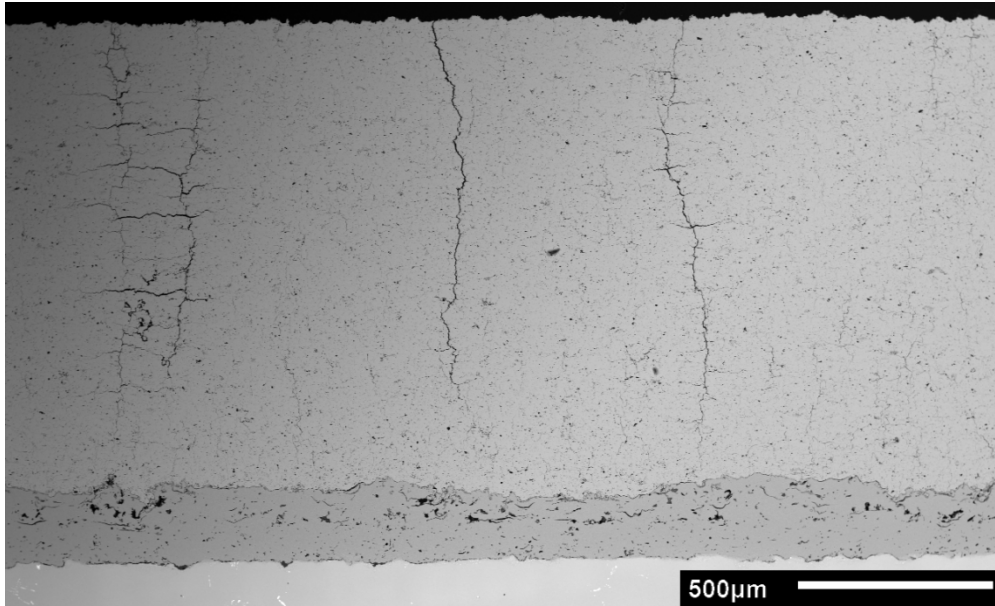


**Figure 99 - 1.1mm DVF topcoat on PWA 1484 after 2000 JETS cycles. Micrograph was taken far from the edge of the specimen.**

These specimens withstood the 2000 JETS cycles very well, likely because of the vertical fissures within the coating which relieved the stress buildup during heating.

**4.1.3.2.4 Discussion** The dual TBC performed the best in the FCT testing with the DVF TBCs having a factor of two shorter lifetime and the LD TBCs having a factor of four shorter lifetime. Failure of the LD TBCs occurred within the topcoat whereas the failure of the DVF TBCs occurred at the topcoat/TGO interface. The difference in the location of the failure indicates either the fracture resistance of the topcoats or the thermal stresses experienced during cycling differed between the two TBCs. Gou et al [22] have reported the vertical fissures in the DVF-type coatings reduced the thermal stresses by increasing the compliance of the topcoat. The cracks are able to open and close during thermal cycling which alleviates some of the thermal expansion mismatch strains between the topcoat and substrate. This in turn translates into smaller

residual compressive stresses and a decrease in the driving force (stored strain energy) for topcoat spallation. It is for this reason the DVF TBCs outperformed the LD TBCs.

The performance of the dual TBC in the FCT tests requires a more complex explanation. As with the DVF TBC, the DVF layer adjacent to the bond coat in the dual TBC provided some strain relief via a crack opening and closing mechanism during thermal cycling [22]. This mechanism likely extended the lifetime of the dual TBC beyond the lifetime of the LD TBC but does not fully explain the large difference in lifetime between the DVF TBCs and dual TBCs. In an attempt to explain this, the physical differences between the coatings must be examined. The DVF layer in the dual TBC is only 125 $\mu\text{m}$  thick whereas the DVF TBC is 1100 $\mu\text{m}$  thick, however, the dual TBC also has 1100  $\mu\text{m}$  of LD topcoat on top of the DVF layer. Cumulatively, the dual TBC is thicker but this does not necessarily mean the amount of stored strain energy in the topcoat is larger because the stored strain energy is also proportional to the residual stress of the topcoat. The vertical fissures in the coatings could reduce the stress in the DVF layer which would then, in the case of the dual TBC, be translated from the DVF layer into the low density layer. The transmission of stresses from one layer to the next could, however, be reduced by the presence of interfacial delaminations which were found in the failed dual layer TBCs (Figure 87, Figure 89 and Figure 90) and by interfacial sliding between the two layers. A literature survey on high and room temperature creep mechanisms of plasma sprayed coatings [23] revealed appreciable creep rates at both high and room temperatures. Moreover, at room temperature, sliding is enhanced in the presence of a smooth interface since diffusion aided creep mechanisms are not active. The surfaces of the DVF coatings, which are known to be smoother than surfaces of LD coatings [69], could therefore aid sliding in the case of the dual TBC. A combination of these mechanisms, delamination and sliding, could essentially decouple the LD layer from the

DVF layer in a way such that the 125  $\mu\text{m}$  layer would perform as though the LD is not present. There must remain some level of contact and adherence such that the entire LD layer does not completely delaminate yet enough sliding or separation to relieve some of the thermal stresses. Furthermore, the LD layer could also prevent the 125  $\mu\text{m}$  layer from buckling, which thinner TBCs are much more susceptible to since the critical buckling stress is proportional to the square of the coating thickness [39].

In the JETS tests, the DVF TBC performed the best and the LD and dual TBCs performed much worse. Explanation of this behavior is best explained by first examining the JETS testing conditions. As a reminder, in this test, the specimens experience a thermal gradient since they only receive heat flux on the TBC surface and receive no backside (superalloy) heating. During the front-side heating, they are rotated under an oxy-propylene torch for 20 seconds, where a peak surface temperature of 1400°C is reached. During this time, the flame induces a rapid transient temperature gradient within the topcoat where the outer surface is heated to a much higher temperature than the bond coat surface. As the coating rapidly heats, it expands in a manner proportional to its temperature change meaning the outer region of the topcoat expands more than the cooler inner region. This strain gradient then induces a tensile stress within the surface region of the coating. If a crack were to form or already be present at the surface, the induced tensile stress would provide the energy for growth. Once the crack grows the stresses would be relieved and crack growth would stop. However, upon the next heating and cooling cycle the thermal load would be reapplied spurring further crack growth. This type of thermal cycling fatigue crack growth was modeled by Zhu and Miller [70] and is very analogous to a crack wedging process. The cracking patterns observed in the LD and dual TBCs, Figure 95 and Figure 97, are consistent with this cracking model where cracks first form at the surface and

propagate down into the coating. Furthermore, the LD microstructure appears to be unable to resist this mode I type of crack growth.

In the dual TBC, the vertical cracking did not enter the DVF layer and instead branched out horizontally above this layer, Figure 97. The change in density and modulus when moving from the LD to the DVF microstructure is likely the explanation for this cracking behavior. Essentially, the DVF layer in the dual TBC felt and responded like the bond coat did in the full LD topcoat specimens so that when a crack extended down from the outer surface, the crack began to branch out horizontally before it encountered the DVF layer.

The exceptional performance of the DVF TBC can be attributed to the already present vertical cracks, both micro and macro. During cycling, these periodically spaced cracks were able to open and close during heating and cooling to relieve the thermal stresses.

### **4.1.3.3 Observational Approach**

**4.1.3.3.1 Experimental Overview** As mentioned in the overview section, the TBCs discussed here were prepared in three batches over the last four years. Because of the large time span from the first group to the last group, limited microstructural characterization was available to compare the starting microstructures and FCT results of all of these specimens. This is because the specimens were prepared, tested and characterized with specific purposes in mind (i.e. to examine substrate – bond coat interdiffusion or influence of bond coat roughness) and done so over a four year timespan. It was not until the proverbial dust had settled that the differences in TBC lifetimes were noticed. For these reasons, limited characterization will be shown for this portion of the chapter. The coating details of each batch of specimens are given below.

In the first batch, 375  $\mu\text{m}$  and 1100  $\mu\text{m}$  TBCs were prepared on René N5 (N5) substrates. The bond coats were dual layer argon-shrouded plasma sprayed and the topcoats were air plasma sprayed (APS) with high purity YSZ powder with a target density of 85% the theoretical density of 8YSZ. The nominal compositions of these alloys are detailed in Table 4. The density of the topcoats was measured by oil infiltration techniques and determined to be 85% the theoretical density (T.D.) of 7YSZ.

In the second batch, 375  $\mu\text{m}$  and 1100  $\mu\text{m}$  TBCs were again prepared on N5 substrates. The same nominal bond coat and topcoat materials were used in this batch as the previous one and same 85% T.D. was targeted for the density. After deposition the density of these topcoats, which were not measured but instead estimated using a regression equation proprietary to PST (where spray parameters such as torch current, powder feed rate, carrier gas flow rate are entered into an equation) was determined to be 89%T.D of 7YSZ.

In the third and final batch of specimens, 375  $\mu\text{m}$  and 1100  $\mu\text{m}$  TBCs were prepared on Pratt and Whitney Alloy 1484 (PWA1484) and 375  $\mu\text{m}$  TBCs were also prepared on N5 substrates. The FCT lifetimes of the 375  $\mu\text{m}$  TBCs on the two superalloys were almost identical thus it seems reasonable to assume a 1100  $\mu\text{m}$  TBCs on PWA 1484 would perform the same as a 1100  $\mu\text{m}$  TBC on N5. The same nominal bond coat and topcoat materials were used in this batch as the previous two and same 85% T.D. was targeted for the density. After deposition the density of these TBCs, which was measured by oil infiltration, was determined to be 82%T.D.

The TBCs were all thermally cycled in a bottom loading furnace with one cycle consisting of a 10 minute ramp to 1100°C followed by a 45 minute isothermal hold at 1100°C and then a 10 minute forced-air cooling rapid cooling step down to ~60°C.

#### 4.1.3.3.2 Results: FCT Testing

Figure 100 contains the cumulative results for the

FCT testing which spanned three generations of specimens.

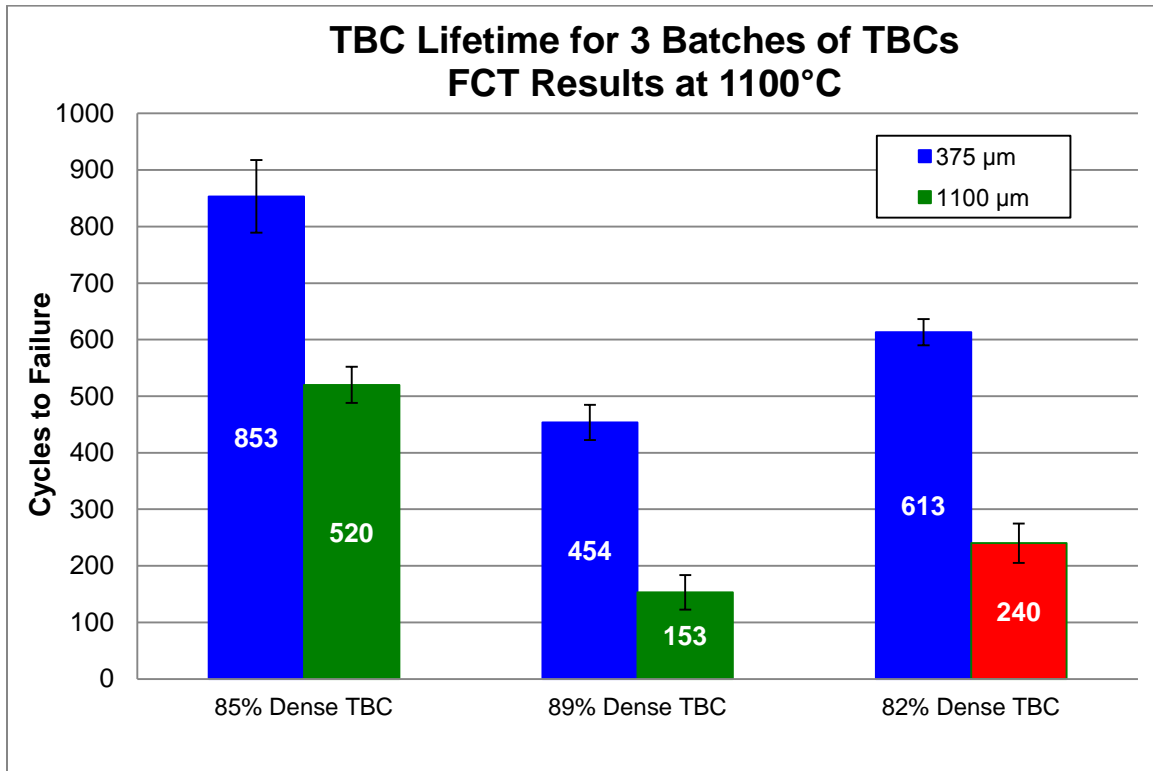


**Figure 100 - FCT lifetimes of TBCs from 3 different batches of specimens. All specimens had N5 substrates and dual layer bond coats with the exception of the red bar which had a PWA 1484 substrate.**

Based on these results alone, and assuming all other coating variables were held constant (i.e. bond coat roughness, substrate/bond coat/topcoat composition, topcoat thickness etc...) these data indicate topcoat density strongly influenced TBC lifetime. The best performance came with the 85% dense topcoat, followed by the 82% and then the 89% dense. The influence of density dependence was observed for both the 375 and 1100μm topcoats with the effect being more pronounced in the thicker TBCs (green and red bars Figure 100). Specifically, when moving from the 89% dense topcoat to the 85% dense, there is a factor of 3.4 difference in the lifetime

for the 1100 $\mu\text{m}$  topcoats and only a factor of 1.9 for the 375 $\mu\text{m}$  topcoats. There also appears to be a peak density of around 85% where going above or below this value decreases the lifetime of the specimen.

Cross sections of the failed 1100  $\mu\text{m}$  are shown in Figure 101 through Figure 103.

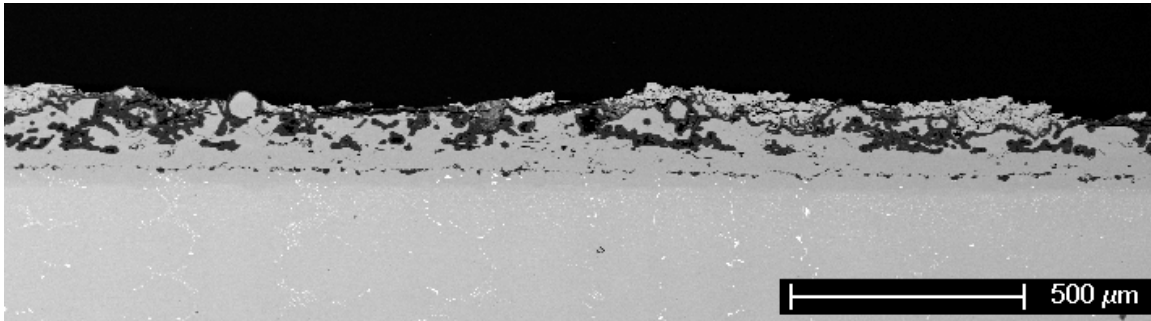


**Figure 101 - Generation II 85% dense 1100  $\mu\text{m}$  topcoat on a dual layer bond coat and N5 substrate with 560 cycles at failure.**

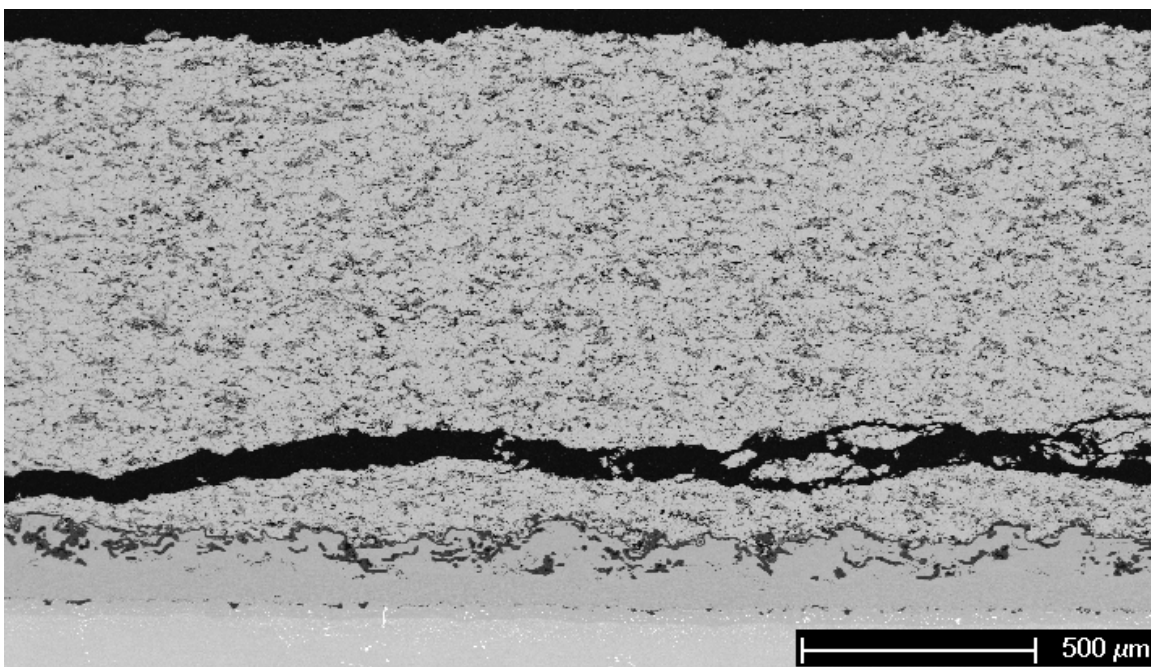


**Figure 102 - Generation III 89% dense 1100  $\mu\text{m}$  topcoat on a dual layer bond coat and N5 substrate with 120 cycles at failure.**

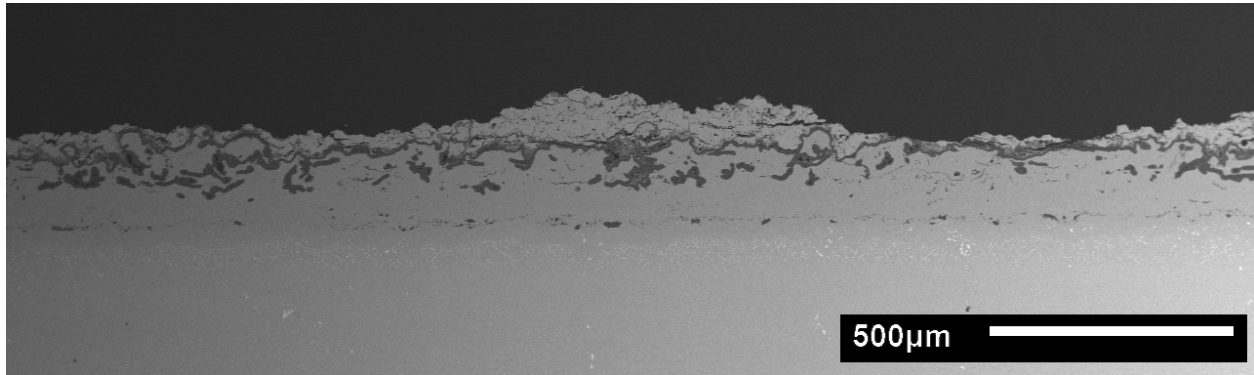


**Figure 103 - Generation IV 82% dense 1100  $\mu\text{m}$  topcoat on a dual layer bond coat and PWA 1484 substrate with 280 cycles at failure.**

The 89% and the 82% both failed within the topcoat layer whereas the 85% dense coating failed at the topcoat/TGO interface. This fracture behavior indicates the fracture resistances of the topcoats were substantially different. The 85% dense topcoat was able to resist crack growth within the topcoat and failed only after considerable bond coat oxidation induced damage had occurred at the topcoat/TGO interface. The 89% dense topcoat on the other hand, was much less resistant to cracking within the topcoat. This TBC did not experience enough cycles for bond coat oxidation to be a contributing factor and instead failed after crack propagation occurred in the topcoat. The 82% dense coating followed the behavior of the 89% dense coating however, the amount of YSZ left on the fracture surface was much less than the 89% dense coating.

The 375  $\mu\text{m}$  topcoats all failed at the topcoat/bond coat interface. Their fracture surfaces did not appear to be very different. The only noticeable difference was the extent of bond coat oxidation (i.e. TGO thickness, spinel formation and  $\beta$ -phase depletion), which was a result of the TBCs experiencing different numbers of cycles before failure.

**4.1.3.3.3 Discussion** In the last section it was assumed all other starting parameters such as the bond coat roughness, substrate composition, and topcoat composition were the same from one batch to the next. While this was not explicitly verified (i.e. material compositions were not analyzed and roughness measurements were not performed) there is certain evidence in the type of failure which would suggest certain parameters were not the same. Bond coat roughness, which will be discussed in the next chapter, can have a strong influence on the lifetime. If a bond coat is too smooth, the TBC lifetime will be short and the fracture surfaces will be covered with more TGO, some exposed bond coat and less YSZ. Upon failure a rough bond coat will be covered by a more even mixture of YSZ and TGO with no exposed bond coat. Given this behavior, the fracture surfaces of the three 375 $\mu$ m topcoats did not appear very different. All of them, regardless the number of cycles to failure, had a mixture of YSZ and TGO indicating the roughnesses were similar, if not the same.

Compositional differences in the bond coats and substrates could cause differences in the oxidation behavior which in turn could yield different TBC lifetimes. This possibility is not likely for two reasons. First, all topcoat and bond coat powders are held to industrial standards, where they must lie within a set compositional window. If there were any significant differences in composition or even powder size distribution, the powders would have been rejected. Second, the 89% dense 1100  $\mu$ m TBCs which failed after 120 cycles would have had little time for the compositional differences to manifest themselves in the form of TGO growth. Assuming the mechanical properties were unaffected, it is unlikely minor compositional fluctuations would have caused such large differences in lifetime.

Given these supporting arguments, it seems the density of the TBCs was the main variable between the three batches and was responsible for the difference in TBC lifetime. A

literature survey revealed thermal cycling lifetime of TBCs is very sensitive to topcoat density/porosity [15, 24, 71]. More specifically, not only is the amount of porosity important but also the pore size distribution. In a quantitative way the pore size distribution describes the amount of globular pores (large), intra-splat cracks (cracks within an individual splat)(small), inter-splat cracks (cracks extending through multiple splats), vertical segmentation cracks and inter-splat voids (small). These features combine to control the elastic modulus and thermal conductivity of the bulk coating which in turn control the cyclic durability [13, 15, 16, 23, 24]. Furthermore, certain pores types control a given property more than others. For example, segmentation cracks and vertical inter-splat cracks do little to reduce the thermal conductivity of a coating since they are oriented parallel to the heat flow direction, however, these cracks have a profound influence on the elastic modulus of the coating and provide large scale strain tolerance [16]. Essentially, not all pores are equal. This statement highlights the main point which is – that alone, a numerical value for the porosity of a topcoat does not provide all the information needed to predict how a TBC will perform. Additional microstructural information detailing the pore size distribution is also required to better understand how a TBC will perform and the physical properties it will have.

This being said, by itself, the porosity content is not totally useless but far from it. There are general rules of thumb which can be followed based solely on the porosity content. For example, a coating with an extremely high porosity (low density) will tend to have a small elastic modulus. A low modulus can be associated with poor wear performance and poor crack growth resistance. On the other hand, a low porosity coating (high density) can be too stiff and unable to arrest a growing crack because of its minimal elastic compliance. The coatings from each of the three batches seem to follow these rules of thumb. The 82% dense coatings were probably too

porous allowing for cracks to extend across the topcoat/TGO interface too easily. Likewise, the 89% dense coating was too dense and suffered from both a lack of compliance and low toughness. The 85% dense coating had a better balance of toughness and compliance which extended its lifetime beyond the other two coatings. Again, these are generalities. Specific correlations between the pores types and the coating performance could not be made due to the lack of experimental design. Instead the main idea to take from this is ultimately, porosity generally can give an approximate indication of how a coating will perform, but it does not tell the whole story.

**4.1.3.4 Conclusions** In the design approach, three topcoat microstructures were tested: low density (LD), dense vertically fissured (DVF) and a dual TBC which had a thin DVF layer adjacent to the bond coat and thicker LD layer on top. All topcoats were close to the same thickness. The dual TBC had the best performance in the FCT testing. Its performance was attributed to the compliance provided by the DVF layer, interfacial cracking and to some degree, interfacial sliding, between the DVF and LD layers. As a testament to the dual TBC's performance, it outperformed a 100  $\mu\text{m}$  LD TBC, which is a substantial feat, especially when taking into consideration the dual TBC is 1200  $\mu\text{m}$  thick. However in the JETS test, the LD and dual TBC performed poorly. The LD layers of these TBCs were susceptible to thermal fatigue crack growth where cracks formed at the free surface and propagated in towards the bond coat. The DVF TBC performed very well in the JETS test as they did not experience any additional cracking as a result of the thermal cycling which was attributed to the already present vertical segmentation cracks.

In the observational approach, "identical" TBCs from three batches of specimens were FCT tested. It was later determined that the topcoats of these specimens had different densities.

TBCs with 85% dense topcoats performed the best, followed by 82% dense and then 89% dense. Density fluctuation impacted the FCT lifetime of thick TBCs (1100  $\mu\text{m}$ ) more so than with thin TBCs (375  $\mu\text{m}$ ). Further information was uncovered with a literature survey which indicated topcoat density/porosity is not the only important property. More information about pore size distribution and pore type is needed to fully explain the different lifetimes of the three coatings. As a rule of thumb though, topcoats which are too dense or too porous tend to perform poorly.

## **4.2 BOND COAT VARIABLES**

### **4.2.1 Chapter Overview**

Experiments in this section had two aims. The first aim was to develop an understanding of how the bond coat roughness influences the lifetime of TBCs both in the sense of establishing a roughness-TBC lifetime relationship but also to develop a mechanistic understanding of how the failure progresses. Information gained could then be used to develop future coatings with better TBC performance.

The second aim of these experiments was to develop an economical bond coat deposition procedure that also maximizes TBC lifetime. Some of the argon-shrouded plasma sprayed bond coats currently used in industry are sprayed using a two-step deposition process. The current two-step process involves using two bond coat powders of different sizes but with identical compositions. The first layer in the bond coat (directly deposited on the substrate superalloy) is sprayed with a fine sized powder which produces a smooth dense coating. Afterwards, a second layer is sprayed on top of the first with the coarse powder which leaves a rough surface finish

containing numerous surface connected pores. The purpose of this two-step deposition process is to first seal the superalloy with a dense bond coat layer which thereby providing the superalloy with chemical protection and then to roughen the surface with the second step which gives the necessary roughness needed for a strong bond between the topcoat and bond coat. Considerable cost savings could be achieved by reducing this down to a one step deposition process however the path to this optimal one-step coating procedure remains unclear.

These two objectives were investigated by implementing a simple one-step deposition process which again used two separate powder sizes but blended them together in set ratios. By controlling the particle size distribution of the powder lots, the final roughness of the bond coat surface could be controlled. However roughness was not the only bond coat parameter altered by blending powders. Open porosity (pores connected to the free surface) was an additional variable linked to the powder blend ratio which was caused by incomplete coating buildup.

Comparisons were made between the two-step bond coat and the one-step blended bond coats. Particular focus was placed on how well all the bond coats provided chemical/oxidation protection during thermal cycling tests. Two thermal cycling tests were used, the furnace cycle testing (FCT) and the jet engine thermal shock (JETS) testing both of which are described in the section 3.1.

#### **4.2.2 Experimental Overview**

All of the TBC specimens consisted of a disk shaped superalloy substrate, with a bond coat deposited on only one of the surfaces on top of which a ceramic topcoat was then deposited. The superalloy substrate disks had an approximate diameter of 2.5cm and a thickness of 3mm. Two substrate alloys used were PWA 1484 and René N5 both of which are single crystal nickel-based

alumina-forming superalloys (at least at 1100°C). The topcoats were air plasma sprayed high purity, low density YSZ coatings with a density, measured according to ASTM-B328-94, of  $82.0 \pm 0.6\%$  the theoretical density of 7YSZ. The nominal compositions of these materials are given in Table 4.

There were four different bond coats investigated in this work. All of bond coats had the same nominal composition but their surface finishes were different. To achieve this, a single lot of bond coat powder was run through a sieve, separated into fine and coarse powder sizes where after the two powder types were either deposited separately or blended together and then deposited. The coarse powder was referred to as LN14 and the fine was referred to as LN11. The bond coats, two phase  $\beta/\gamma$ -NiCoCrAlY bond coats, were deposited by argon-shrouded plasma spraying to a total target thickness of 175-200 $\mu\text{m}$ . The four blend ratios (by weight) were: 100% LN11 (100:0), 75%LN11 - 25%LN14 (75:25), 50%LN11 - 50%LN14 (50:50) and the fourth ratio was a dual layer (0:100) bond coat which had a 100 $\mu\text{m}$  of 100% LN11 layer and 100 $\mu\text{m}$  100% LN14 layer on top (200 $\mu\text{m}$  total). After the bond coats were deposited on the superalloy substrates, they were vacuum heat treated at 1080°C for 4 hours.

Prior to topcoat deposition the surface roughnesses of the bond coats were measured with a Talysurf Surtronic 3+ contact profilometer with a 5  $\mu\text{m}$ -tip radius. In all of the measurements, a traverse distance of 4.2mm and a cut-off length of 0.8mm were used. Twenty passes were performed on each bond coat type and then an average roughness (Ra) and standard deviation were calculated from the collected data.

In attempts to further characterize the surface, a secondary roughness measurement technique was used which utilized cross-sectional SEM micrographs of the as-deposited TBCs (i.e. after topcoat deposition). First, 24 high resolution back-scattered SEM images were

collected of each specimen at a specific magnification and working distance (Figure 104a). The bond coat-topcoat interface was then manually traced with a white line to establish the location of the surface of the bond coat (Figure 104b). Then the image was converted into a binary image (black and white) where only the interface was present as white pixels (Figure 104c). Finally, this binary photo was loaded into Matlab where simple calculations were performed to compute an average roughness,  $R_a$ , and an average maximum height,  $R_z$ , of the profile.

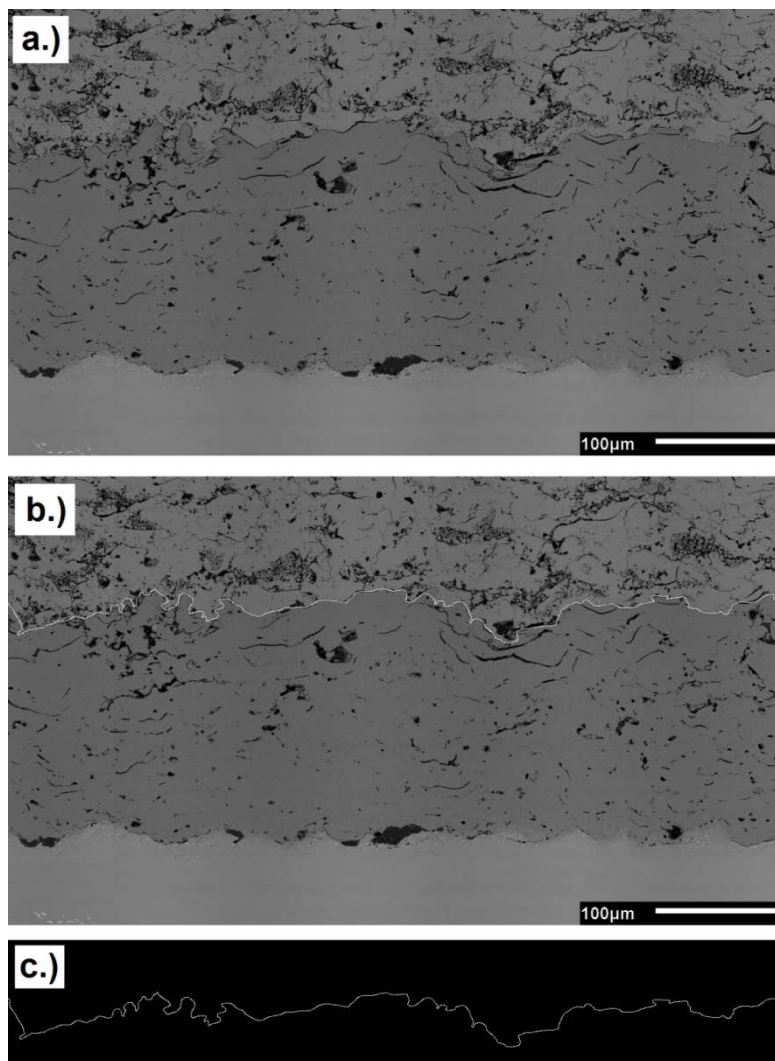


**Figure 104 - Dual layer bond coat in the as-processed state. Original micrograph (a), surface of bond coat outlined in white (b) and converted binary image with remaining white bond coat surface trace (c).**

Specimens were both FCT and JETS tested. The breakdown of the number of specimens for each type of thermal testing is shown in Table 12. Using estimated FCT lifetimes, two TBC specimens were cycled out to ~35% and ~80% of their overall lifetime with the purpose of examining how the failure progresses over the lifetime of the TBC. JETS testing was also performed on a group of the specimens on PWA 1484. The four bond coat types, 100:0, 75:25, 50:50 and 100:100 will be referred to from here on as SL, 75:25, 50:50 and DL, respectively.

**Table 12 - Number of TBCs tested for each type of thermal exposure.**

Substrate	Bond Coat Blend	Bond Coat Nomenclature	FCT (to failure)	30% FCT Lifetime	75% FCT Lifetime	JETS (2000 cycles)
PWA 1484	100:0	SL	1	1	1	-
	75:25	75:25	1	1	1	3
	50:50	50:50	1	1 (45%)	1	3
	100:100	DL	3	1 (45%)	1	3
René N5	100:0	SL	3	-	-	-
	75:25	75:25	3	-	-	-
	50:50	50:50	3	-	-	-
	100:100*	DL	3	-	-	-

The FCT was performed in a CM bottom loading furnace where one furnace cycle consisted of a 10 minute heating period to 1100°C, a 45 minute isothermal hold and a 10 minute forced-air cooling period down to ~60°C. Every 20 cycles, specimens were examined and visually checked for spallation, cracking and delamination. Most of the TBCs failed by complete topcoat spallation, however, some experienced cracking, chipping and buckling without

complete topcoat spallation. To account for this, failure was defined as at least 30% delamination of the topcoat. Furthermore, the term ‘technical failure’ was used to classify TBCs which did not fail by complete topcoat spallation but still met the failure criteria. The JETS testing was carried out to 2000 cycles at which the specimens were stopped and examined for damage. For details of this testing method see section 3.1.

### 4.2.3 Experimental Results

**4.2.3.1 Surface Characterization** Figure 105 displays the average surface roughness measurements of the four bond coats for both the cross-sectional and profilometer measurement methods.

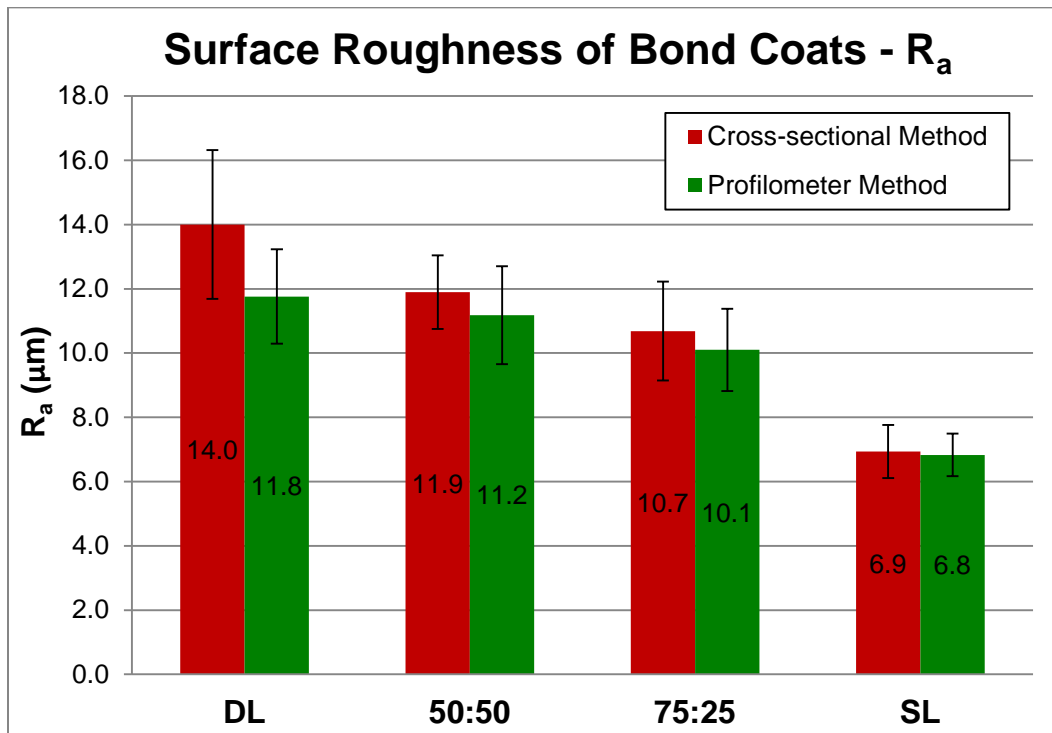


Figure 105 - Average roughness of the 4 bond coat types.

Examination of the profilometer measurements (green bars), indicated the average roughness, which is the average distance the surface varies from a central line, varied by a factor of two. Based on these measurements, there is a clear difference between the DL and SL bond coats, however, the spread between the 50:50 and the 75:25 was much smaller with significant overlap when taking the standard deviations into consideration. Next, examination of the cross-sectional technique (red bars), indicated a clear distinction between DL and the SL bond coats but the spread between the 50:50 and 75:25 is much smaller, although larger than with the profilometer method. Both measurement techniques indicate as the amount of LN14 (coarse) bond coat powder is increased from 0% in SL, to 25% in 75:25, to 50% in 50:50 and 100% in DL, the resultant surfaces are rougher.

In general, there was good agreement between the two measurement methods as there was considerable overlap in the measurement results in all four cases. The roughness measurements from the cross-sectional technique always tended to be larger than for the profilometer technique. This is not surprising since the profilometer method cannot pickup surface features such as sharp valleys which the diamond tip cannot access or points of inflection, such as a cave or horizontal indentation. Since all of these features can be resolved in cross-sectional microscopy, this measurement technique can resolve them. The microscopy technique is very time consuming and a destructive measurement method since the specimen must be mounted, cut and polished. As stated previously though, it does have its benefits.

A second cross-sectional surface measurement (i.e. mathematical calculation), known as the average maximum profile height parameter,  $R_z$ , was performed on these specimens. This parameter measures the average maximum peak to valley height differential over a given length

of the surface. Schematically this is shown in Figure 106 and the results from these measurements are presented in Figure 107.

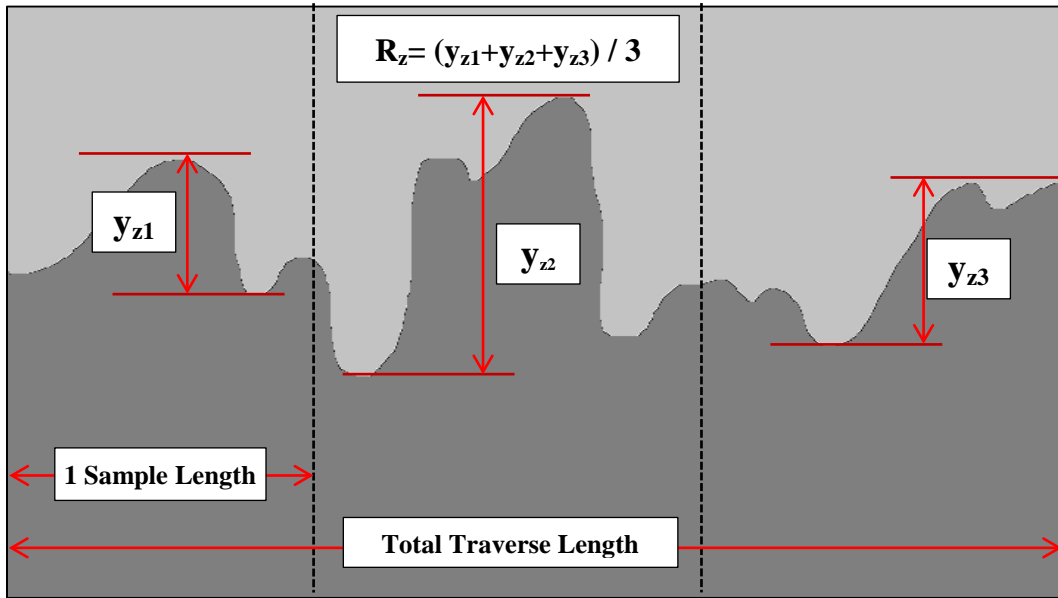


Figure 106 - Schematic of  $R_z$  measurement.

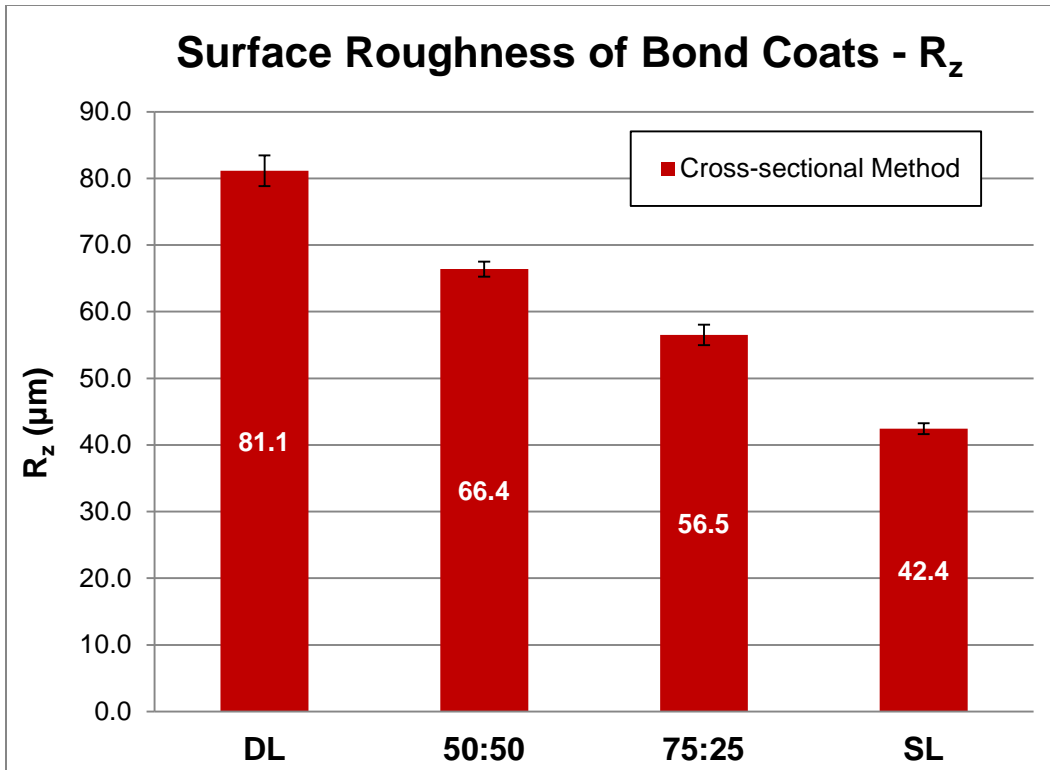
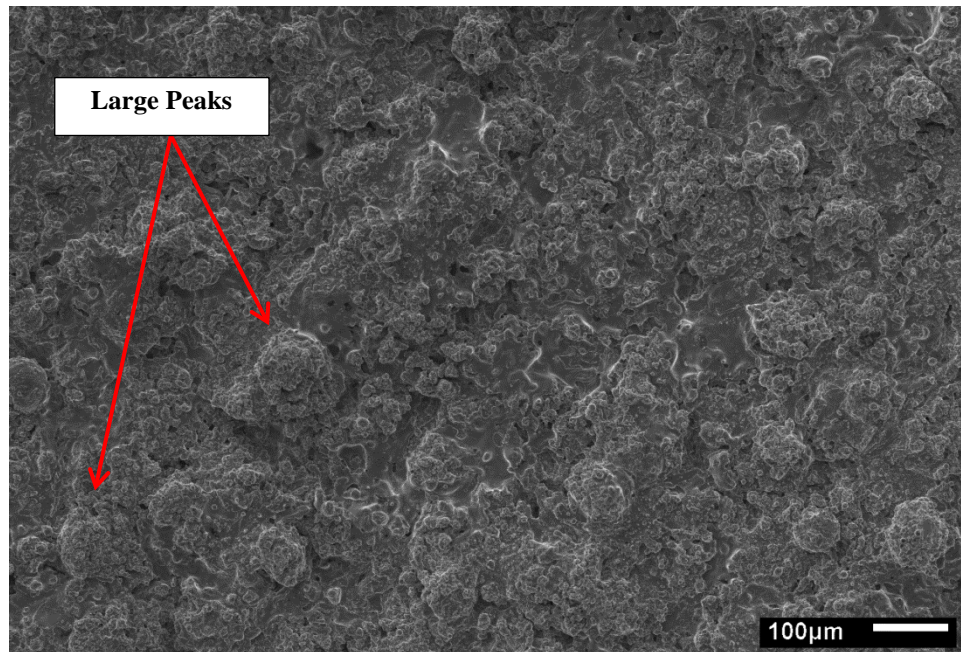


Figure 107 - Average maximum height of the bond coat surface profiles.

This surface characterization parameter again indicates as the amount of LN14 in the bond coat increases (SL < 75:25 < 50:50 < DL) so does the roughness. Furthermore, with this characterization parameter, there is a statistically significant difference between the 75:50 and the 50:50 bond coats which the average roughness parameter was unable to resolve. In the science of surface characterization this is a common problem, where one characterization parameter cannot differentiate between two surfaces whereas another parameter can.

When interpreting these measurement results, it would be expected that the surface of the DL bond coat would have numerous large peaks and valleys whereas the SL bond coat would have a relatively smooth surface and the 50:50 and 75:25 bond coats would fall somewhere in between those two extremes. Figure 108 through Figure 111 show secondary electron micrographs of the surfaces of these bond coats. This particular SEM imaging mode reveals, to

some degree, the surface topography, so features such as peaks and valleys can be resolved. Some of these features are indicated in the figures.



**Figure 108 - A secondary electron image of the surface of a DL bond coat.**

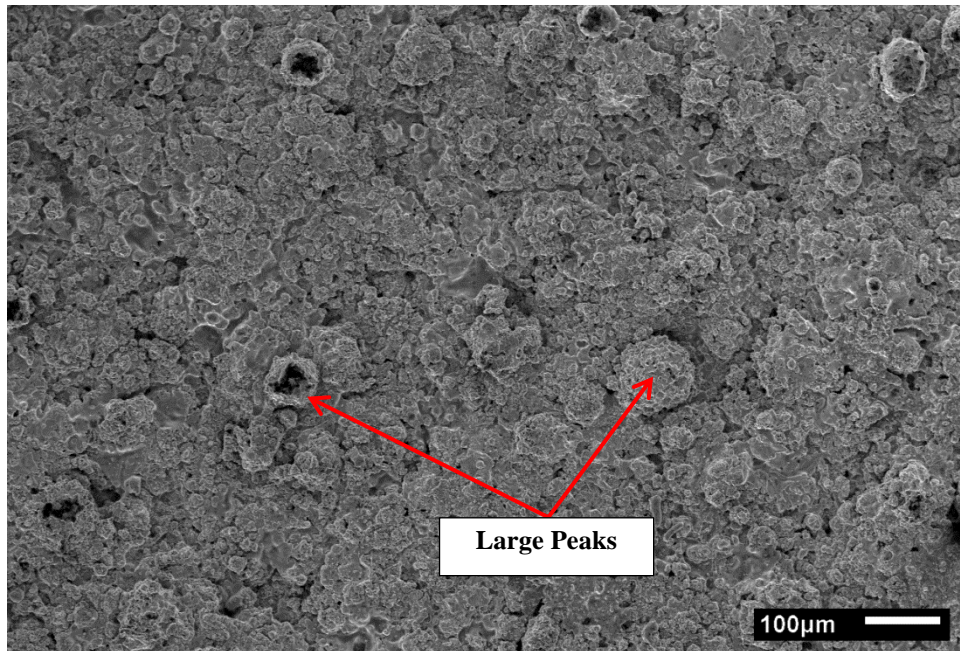


Figure 109 - A secondary electron image of the surface of a 50:50 bond coat.

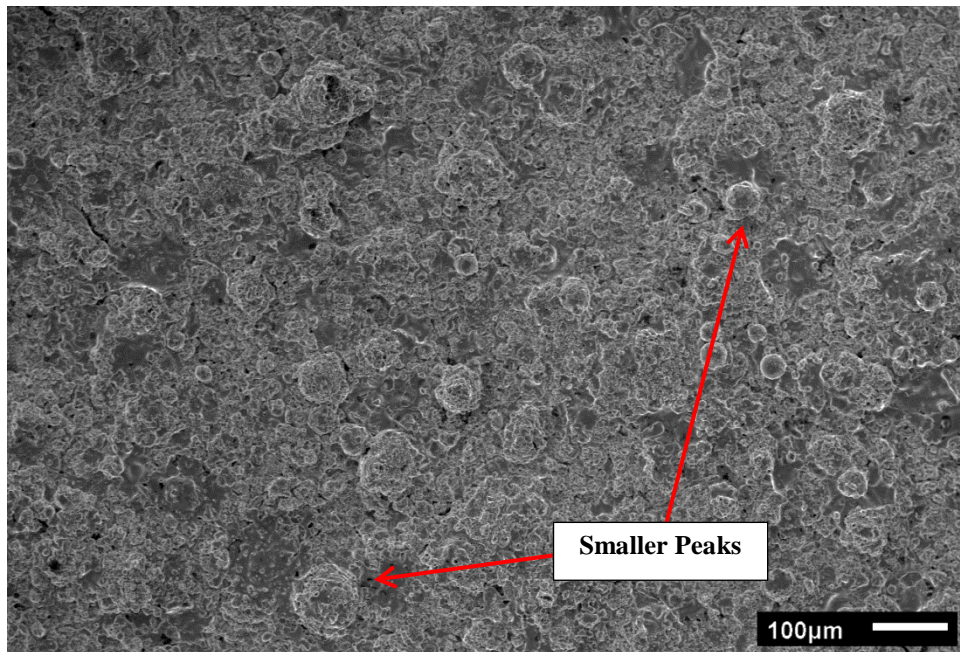
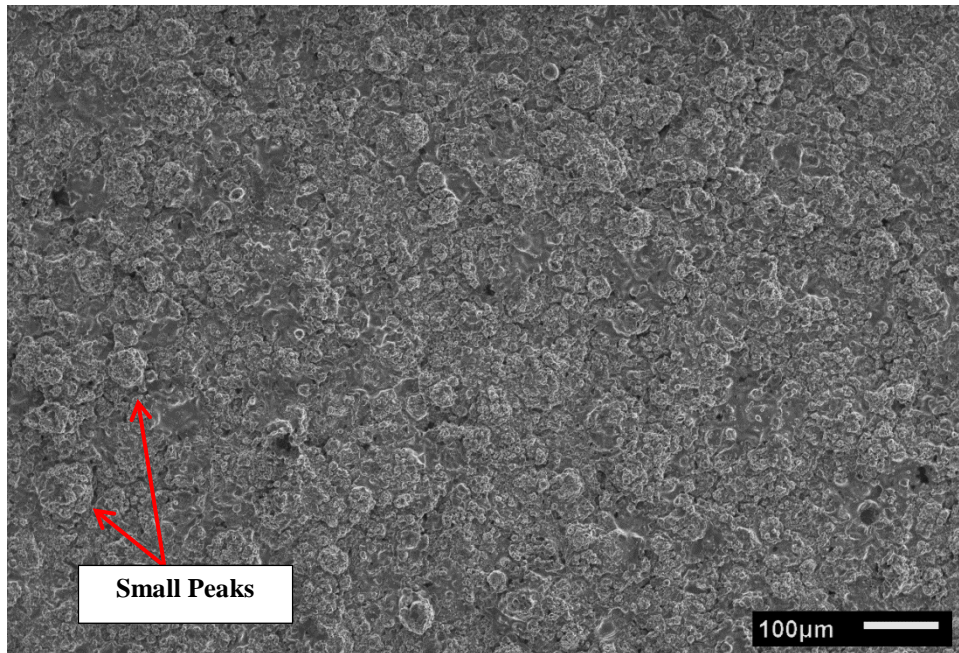


Figure 110 - A secondary electron image of the surface of a 75:25 bond coat.



**Figure 111 - A secondary electron image of the surface of a SL bond coat.**

The first general observation from these surface micrographs is the size of the features on the surfaces decrease as the amount of LN14 in the bond coat decreases. The large peaks ( $75 > \mu\text{m}$ ) in Figure 108, which are likely single LN14 particles, are not present in the SL bond coat micrograph. Some of these larger features are present in the 50:50 and 75:25 coatings but their size and frequency are smaller. Visually, the 50:50 bond coat appears more jagged than the DL bond coat which is likely caused by the smaller LN11 particles forming small agglomerations during spraying. The hills and peaks on the DL bond coat surface appear larger than on the 50:50 surface as well. The 75:25 bond coat appears similar to the SL bond coat, but with the addition of a few medium sized ( $75\text{-}25\mu\text{m}$ ) particles scattered over the surface. The SL bond coat does appear rough, but the amplitude of the roughness (i.e.  $R_a$ ) is much smaller than the other coatings. Cross-sectional micrographs of these specimens are shown in Figure 112

through Figure 115. The interfaces between the bond coat and YSZ topcoat and the bond coat and superalloy have been highlighted by white lines to enhance the visibility. The white arrows indicate large round particles which are likely individual LN14 particles, which are scattered throughout the outer layer of the DL bond coat and throughout the entire 50:50 and 75:25 bond coats. The red arrows indicate surface asperities which correspond to the peaks highlighted in Figure 108 through Figure 111.

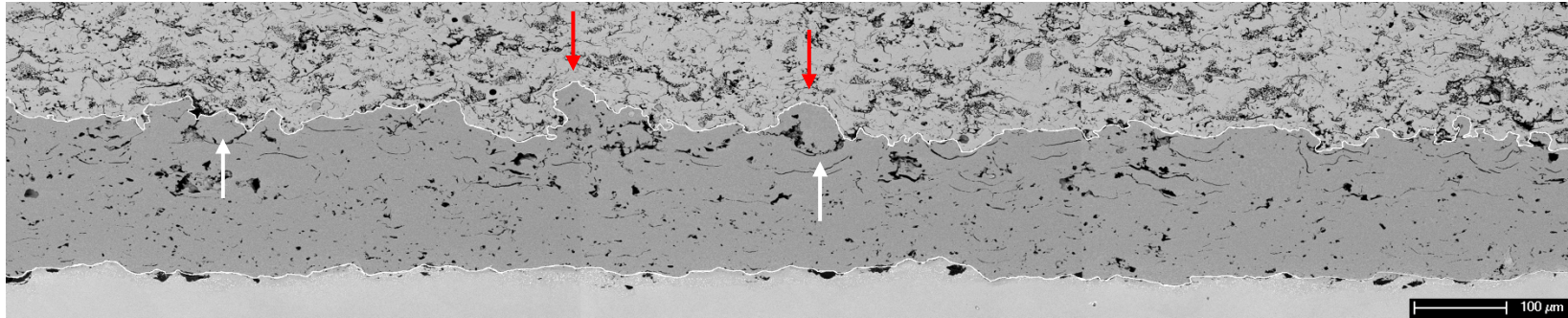


**Figure 112 - Cross sectional micrograph of a DL bond coat in the as-processed condition. A white outline has been added to enhance the visibility of the bond coat/topcoat interface. White arrows point to large round particles which are likely individual LN14 particles and the red arrows point out the large peaks which correspond to the highlighted peaks in Figure 108.**

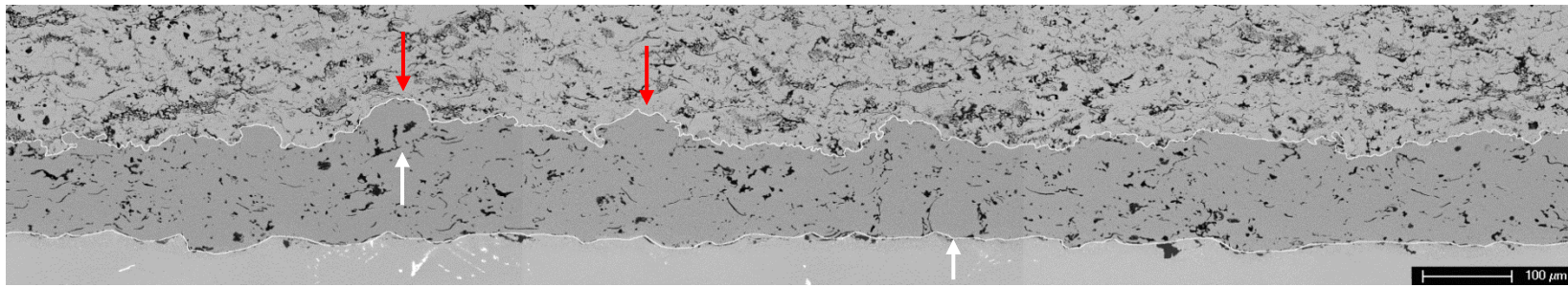


**Figure 113 - Cross sectional micrograph of a 50:50 bond coat in the as-processed condition. A white outline has been added to enhance the visibility of the bond coat/topcoat interface. White arrows point to large round particles which are likely individual LN14 particles and the red arrows point out the large peaks which correspond to the highlighted peaks in Figure 109.**

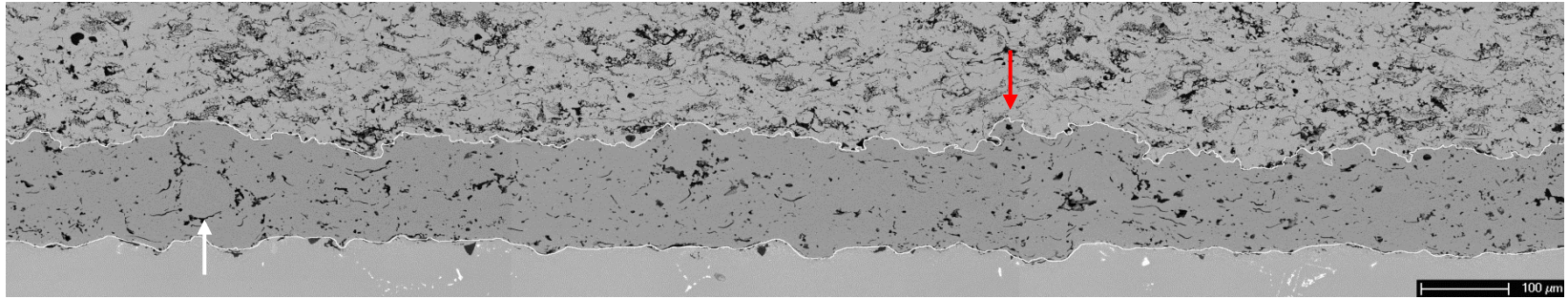


**Figure 114 - Cross sectional micrograph of a 75:25 bond coat in the as-processed condition. A white outline has been added to enhance the visibility of the bond coat/topcoat interface. White arrows point to large round particles which are likely individual LN14 particles and the red arrows point out the large peaks which correspond to the highlighted peaks in Figure 110.**

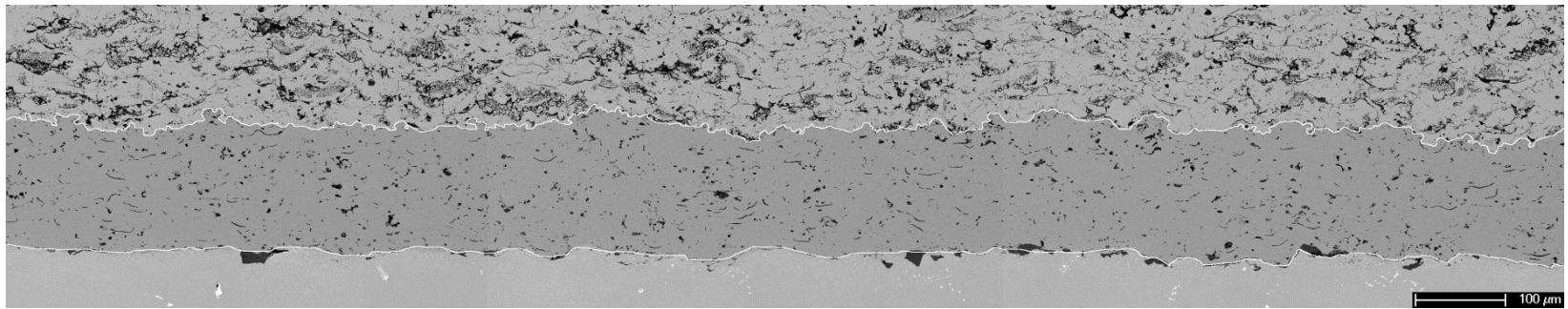


**Figure 115 - Cross sectional micrograph of a SL bond coat in the as-processed condition. A white outline has been added to enhance the visibility of the bond coat/topcoat interface .**

In the DL bond coat, the surface asperities have a higher frequency and larger amplitude (red arrows in Figure 112) than those on the 50:50 and 75:25 bond coats which is likely the reason for such a large difference in the  $R_z$  values ( $\Delta R_z \approx 15\text{-}20\mu\text{m}$ ). The SL bond coat clearly lacks these large peaks and valleys but there is still a significant level of roughness.

In each of these bond coats there is visible porosity, where the pores appear as black voids in the backscattered images. It is impossible to tell whether the pores are surface connected or isolated just by looking at the as-processed micrographs because the pore architecture is three dimensional in nature and these images are only two dimensional. The importance between the two pore types is that - the surface connected pores will oxidize (as opposed to the isolated pores not oxidizing) thereby effectively increasing the rate of aluminum depletion during thermal exposure. Differentiation between the pore types will become clear in the thermally exposed specimens.

Based on all the data and micrographs collected, it is reasonable to conclude the four bond coats have sufficiently different surface finishes, differentiated both by visual comparisons and by physical measurements. The DL bond coat has the highest roughness and contains large ( $>75\mu\text{m}$ ) peaks and valleys. The 50:50 bond coat still contains some large peaks but the frequency is not nearly as high as the DL bond coat. The 75:25 bond coat follows this trend of smoothing out as the LN14 (coarse) content of the bond coat decreases. However, with only 25%, there are still some medium ( $75\text{-}25\mu\text{m}$ ) peaks in the 75:25 coating. Finally, with the SL bond coat, the surface is relatively smooth and lacks any large asperities on the surface.

**4.2.3.2 FCT Results** Figure 116 shows the FCT testing results for the bond coat modification specimens. The red bars are TBCs with PWA 1484 substrates and the blue bars are TBCs with René N5 substrates.

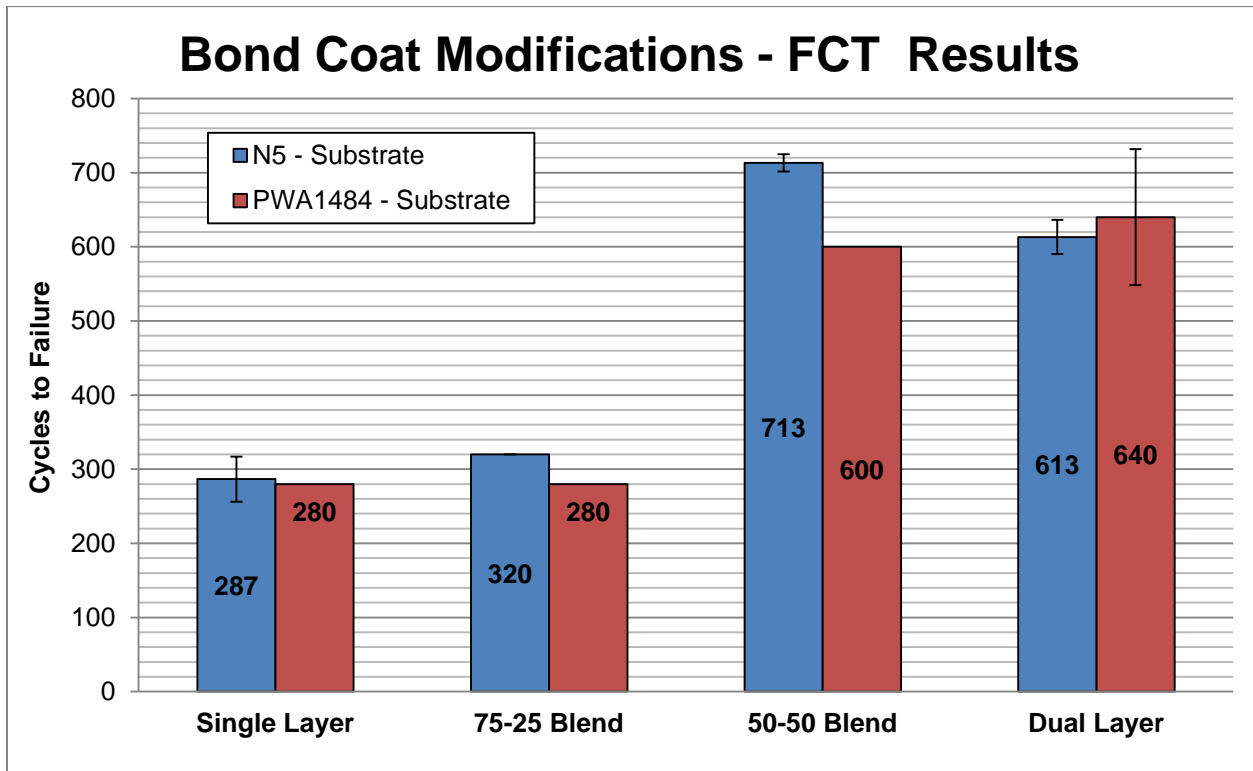


**Figure 116 - FCT results for the bond coat modification specimens tested at 1100°C.**

As a reminder, the blue bars represent the average lifetime of three specimens whereas the red bars, with the exception of the DL bond coat, only represent the lifetime of one specimen (as the other two specimens were used in the percent lifetime tests discussed in the next section). For the René N5 specimens, the reproducibility was exceptional within each specimen group which is depicted by the small or non-existent standard deviation bars atop each column. The PWA 1484 specimens had lifetimes close to the René N5 specimens which is not unexpected since these two alloys are very close in composition, oxidation performance (at 1100°C) and

other thermo-mechanical properties. The largest difference in lifetime occurred between the 50:50 specimens however it should be noted only one 50:50 specimen on PWA 1484 was tested meaning there is little statistical significance supporting this observed difference.

Refocusing solely on the René N5 specimens, the SL and the 75:25 specimens had nearly identical performances in the FCT testing both with lifetimes at or around 300 cycles. The 50:50 and DL specimens roughly had a factor of two longer lives than the previously mentioned specimens with the 50:50 specimens having a slightly longer lifetime than the DL specimen (100 cycles). The fracture surfaces of failed FCT specimens of each bond coat type are shown in Figure 117.

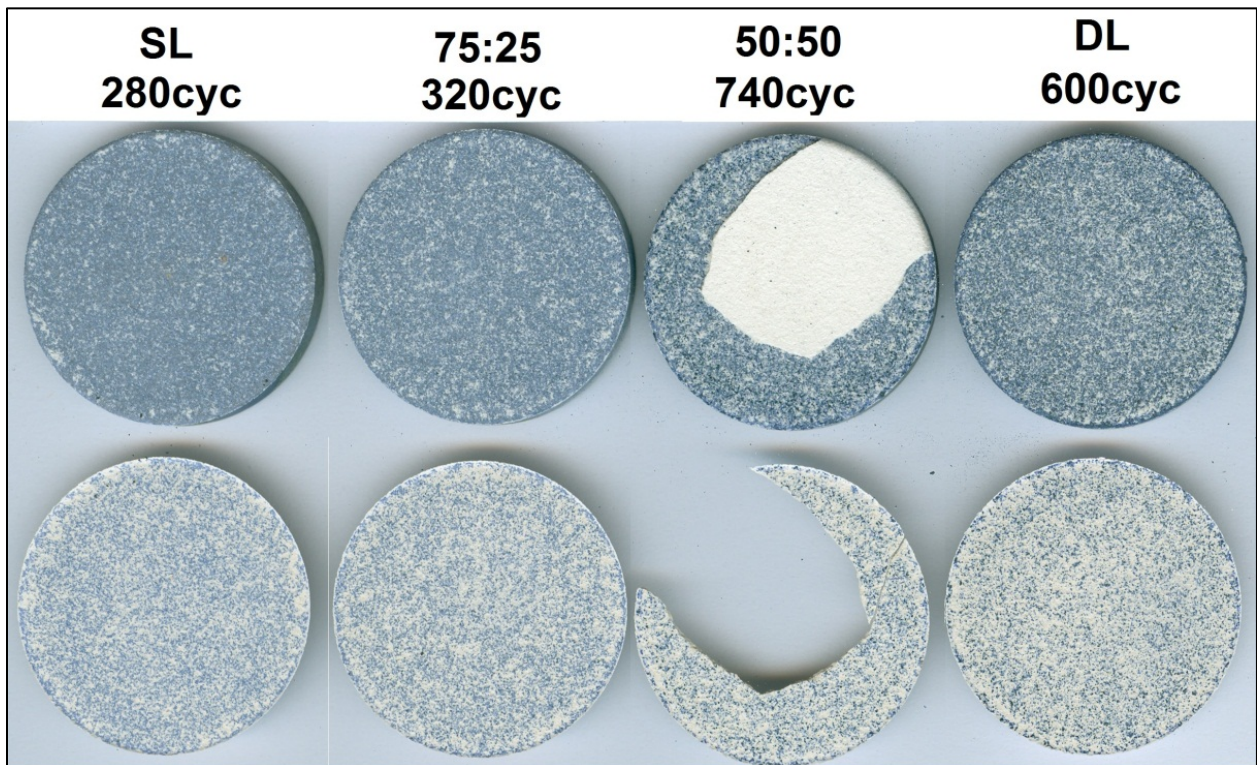


**Figure 117 - High resolution images of fracture surfaces. Top specimen is the bond coat surface and the bottom specimen is the spalled topcoat surface. The white material is YSZ and the blue is the TGO.**

The surfaces of the SL and 75:25 specimens contained more TGO (blue speckles in Figure 117) than the 50:50 and DL bond coats which had more YSZ (white speckles). Moreover, TGO covered both the fracture surface of the bond coat (top of Figure 117) and the fracture surface of the topcoat (bottom of Figure 117) for the SL and 75:25 specimens. Based on this observation (that both the fracture surface of the bond coat and the fracture surface of the topcoat are heavily covered by the TGO) it is apparent the spallation crack primarily propagated through the TGO (since TGO covers both fracture surfaces). This is in contrast to the DL and 50:50 specimens where the cracking moved in and out of the YSZ and TGO leaving each of the fracture surfaces covered with a mix of YSZ and TGO. This is more clearly seen in the cross-sectional micrographs, Figure 118 through Figure 121.

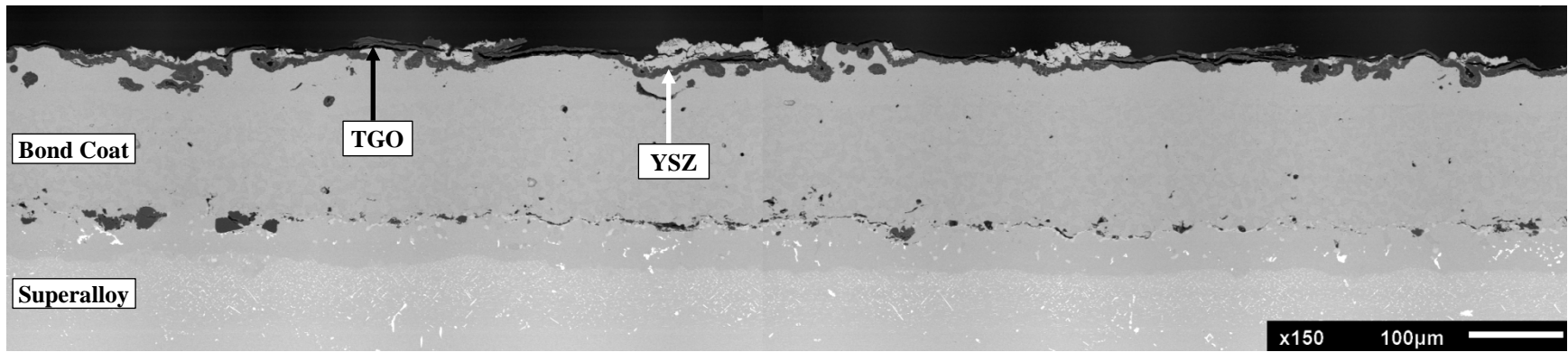


Figure 118 - Failed SL bond coat TBC on N5 after 320 cycles.

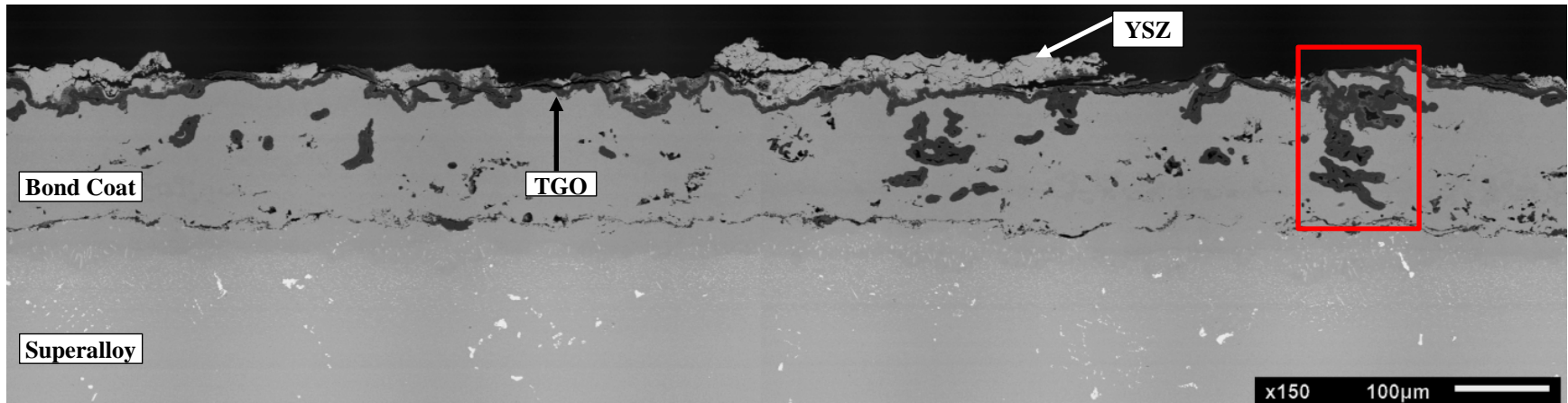


Figure 119 – Failed 75:25 bond coat TBC on N5 after 320 cycles.

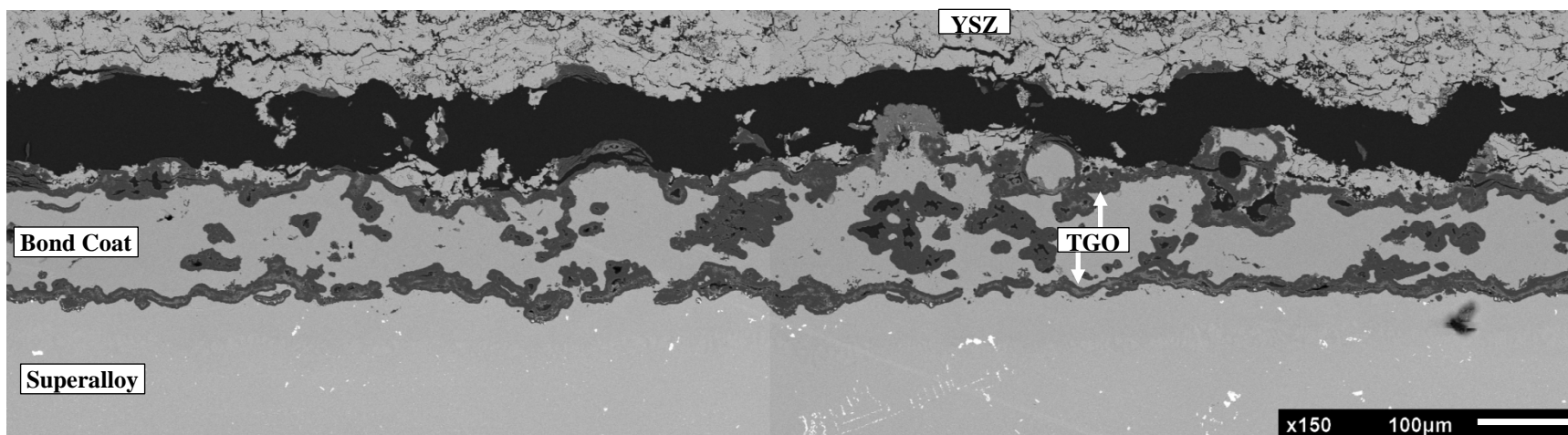


Figure 120 – Failed 50:50 bond coat TBC on N5 after 720 cycles.

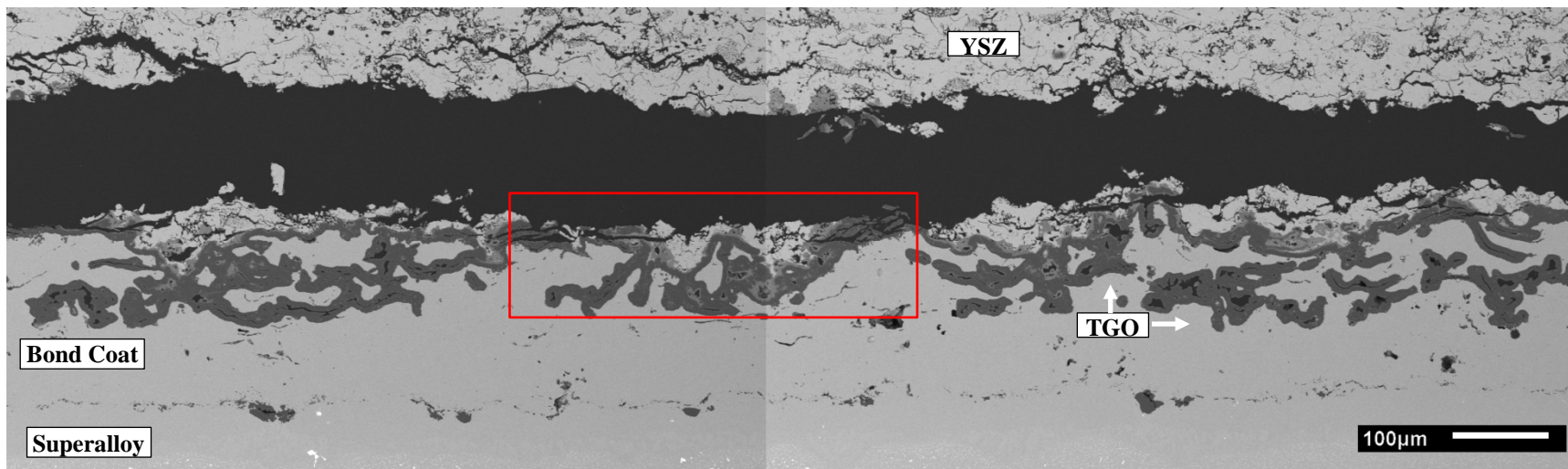
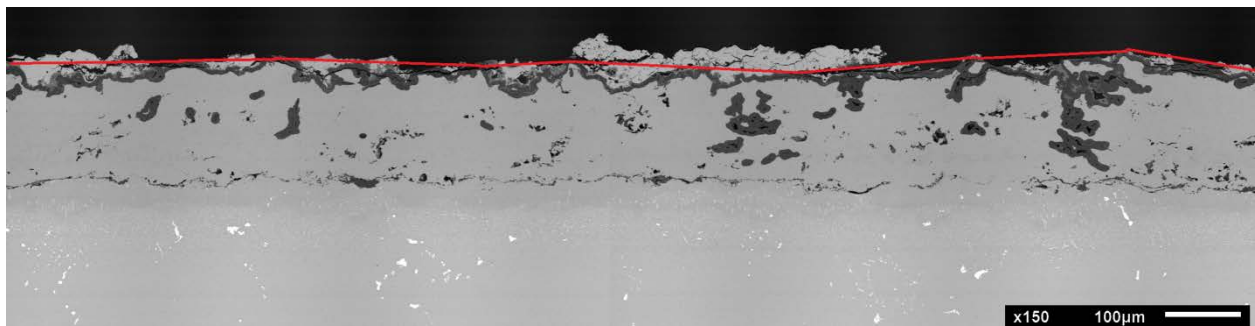


Figure 121 – Failed DL bond coat TBC on N5 after 600 cycles.

When examining these cross-sections, the relative roughness of the fracture surfaces varies from specimen to specimen. In the case of the 50:50 and DL bond coats, the fracture surfaces are quite rough. The spallation crack did not exactly follow the bond coat-TGO interface, instead, it deviated into the YSZ layer when it encountered extremely rough regions and turned back into the TGO in smoother regions which is highlighted by a red box in Figure 121. In the case of the SL and 75:25 bond coats, the fracture surface was much smoother where the crack seems to have encountered few obstacles blocking its path of propagation. Furthermore, the relative size of these obstacles is quite small compared to the large asperities in the 50:50 and DL specimens.

A general observation when examining these cross-sections was that – the crack which lead to spallation of the topcoats seemed to follow a straight line which connected all the highest peaks along the bond coat surface. To clarify this point, a red line has been added to the cross-sections of the 75:25 and DL bond coats which are shown in Figure 122 and Figure 123. The red line touches all of the peaks in the bond coats and extends over and above the valleys.



**Figure 122 - Failed 75:25 bond coat TBC on N5 after 320 cycles. The red line connects the peaks along the bond coat surface.**

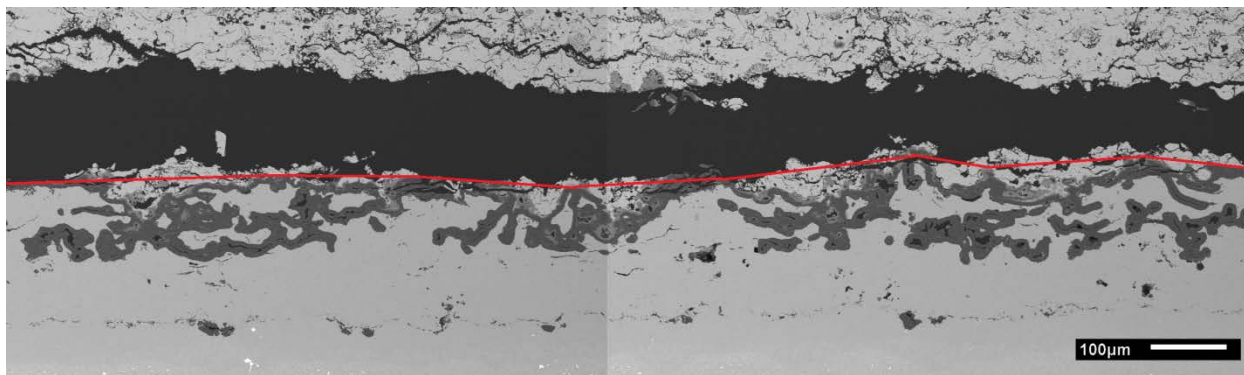


**Figure 123 - Failed DL bond coat TBC on N5 after 600 cycles. The red line connects the peaks along the bond coat surface.**

In the case of the DL specimen (and 50:50), the crack climbed over large peaks and propagated through patches of YSZ located over valleys in the bond coat. In the cases of the 75:25 and SL bond coats, the peaks and valleys still existed, however their relative size and frequencies were smaller. The relative size of these valleys and peaks are reflected in the  $R_z$  measurements ( $R_{zDL} > R_{z50:50} > R_{z75:25} > R_{zSL}$ ) performed in the previous section.

A drawback of the powder blending method alluded to in the previous section, was the issue with open porosity. The as-processed specimens contained two types of pores, open and closed pores. Porosity stems from the individual droplets not fitting together perfectly and leaving gaps and crevices in the coating. Based on cross-sectional analysis of the as-processed specimens, it was difficult to differentiate between the two types since pores are three dimensional in nature. However, after high temperature exposure the open pores have oxidized making them easier to identify. As a reminder, the bond coat, in addition to providing a bonding layer for the topcoat, is also designed to provide oxidation protection to the substrate. To do this, the bond coat composition is tailored to promote the selective oxidation of aluminum, which, when oxidized should form a dense and adherent alumina TGO on the exterior surface. This

layer then protects the underlying superalloy (and the remainder of the bond coat). For a given volume of bond coat material, the rate of aluminum depletion ( $\text{g}/\text{cm}^3\text{-sec}$ ) scales directly with the amount of surface area exposed to the oxygen containing environment. Therefore, if the surface area is doubled so too will the rate of aluminum consumption. For this reason, the surface connected pores (i.e. additional surface area) are detrimental to the coating lifetime for once the aluminum content in the bond coat reaches a critical level (Equation 3) other less stable oxides will begin to form. The transition from exclusive alumina growth to non-alumina growth is referred to as a “chemical failure” of the bond coat.

Taking this into consideration, micrographs of the four bond coat types were collected to examine the protectiveness of each coating. The images were taken at the point of TBC failure, so not all specimens have the same number of cycles. The SL bond coat is shown in Figure 124.

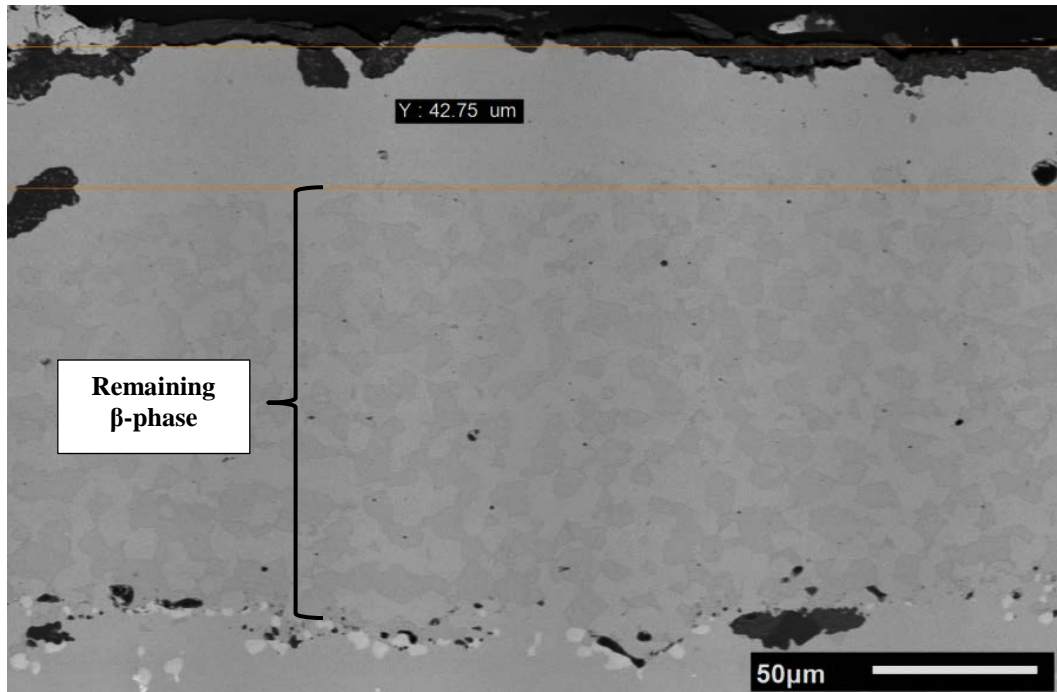
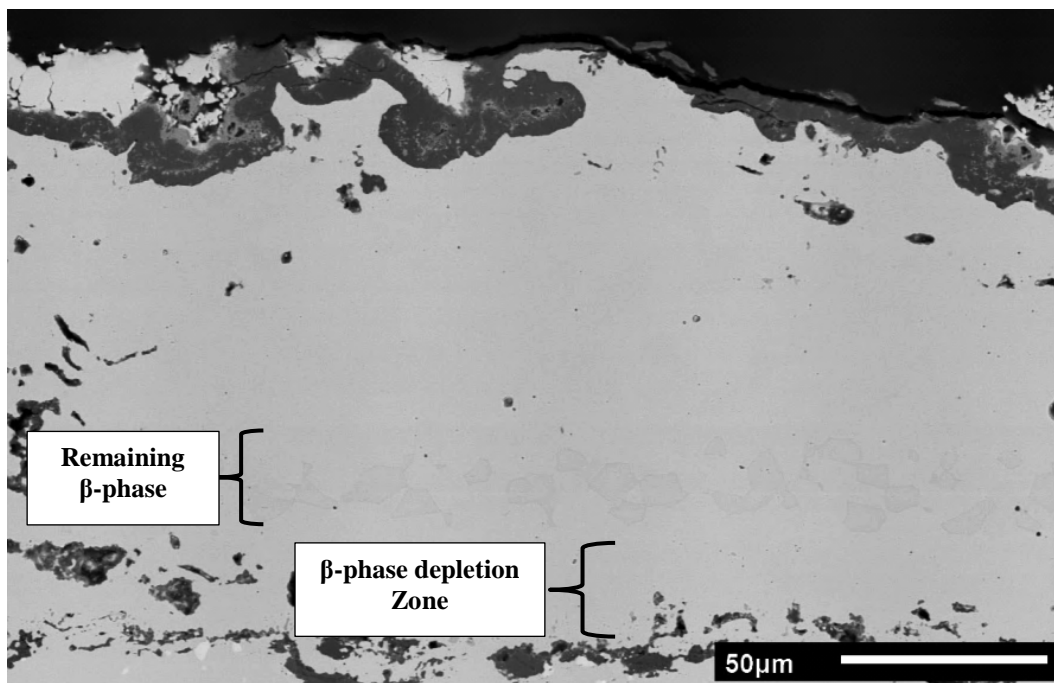


Figure 124 - SL bond coat after 320 cycles. Note 80%+ of the aluminum rich  $\beta$ -phase is still remains.

The SL bond coat was very protective and contained very few surface connected pores. After 320 cycles over 80% of the aluminum-rich  $\beta$ -phase was still present. There was minimal aluminum loss into the substrate through interdiffusion as there is no visible  $\beta$ -depletion zone adjacent to the substrate. Bond coat – superalloy interdiffusion is the subject of the next chapter to which the reader is referred for further interdiffusion discussion. The 75:25 bond coat is shown in Figure 125 and before in Figure 119.



**Figure 125 - 75:25 bond coat after 320 cycles. Note the limited amount of aluminum-rich  $\beta$ -phase remaining and the presence of a  $\beta$ -phase depletion zone adjacent to the bond coat / superalloy interface .**

There is some  $\beta$ -phase left, however, much less than with the SL bond coat. Likewise, there are more open pores than in the SL coating. In some regions (Figure 119 ‘red box’) the surface connected pores extended the entire way down to the bond coat/superalloy interface.

Despite having the same number of cycles as the SL specimen, there appears to be a significant depletion zone extending up from the superalloy substrate which is the result of interdiffusion. As to why there is  $\beta$ -phase dissolution at the bond coat/superalloy interface in this specimen and not in the SL specimen (despite having the same number of cycles) remains unclear. It is possible the depletion zone emanating from the aluminum loss to the TGO is having an influence on the depletion zone between the bond coat and substrate even though they are occurring at opposite sides of the bond coat. In the case of the 75:25 coating, this interaction could potentially be augmented by the presence of deep surface connected pores which effectively reduce the thickness of the bond coat thereby increasing the interaction zone between the two depletion mechanisms.

The 50:50 bond coat specimen which failed after 720 cycles is shown in Figure 126.

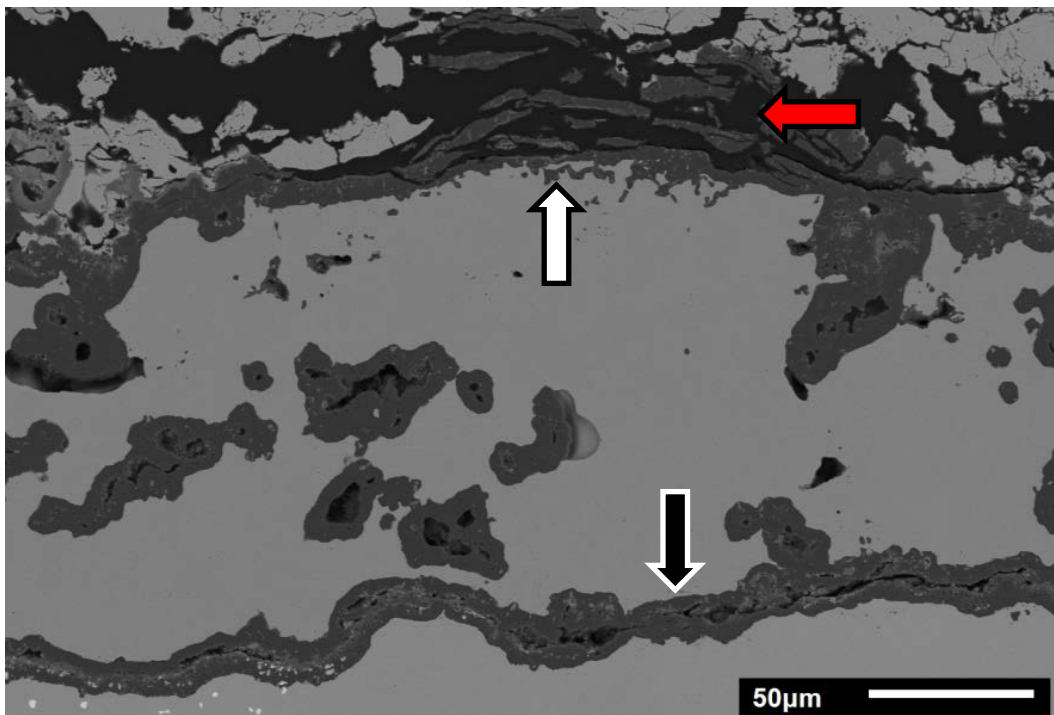


**Figure 126 - Failed 50:50 bond coat TBC on N5 after 720 cycles. Note the oxide layer at both the bond coat surface (white arrow) and at the superalloy-bond coat interface (black arrow).**

In this specimen, the bond coat did not seal off the superalloy at all. Both the outer (white arrow) and inner surfaces (black arrow) of the bond coat oxidized as did the surface of the superalloy along with the open pores. Repeated cracking and reformation of the TGO was observed (red arrow) which was likely caused by the thermal cycling [72]. Furthermore, the dark oxide fingers (at the tip of the white arrow) appear to be growing inward instead of laterally, indicating the kinetic criteria needed to reform an external alumina scale are not being met. Standardless energy dispersive spectroscopy (EDS) measurements in bond coat regions just below these fingers record the aluminum content to be less than 1at%Al which is below the critical level needed to reform a continuous oxide scale [40] and further confirms this hypothesis.

The DL bond coat specimen which failed after 620 cycles is shown in Figure 127.

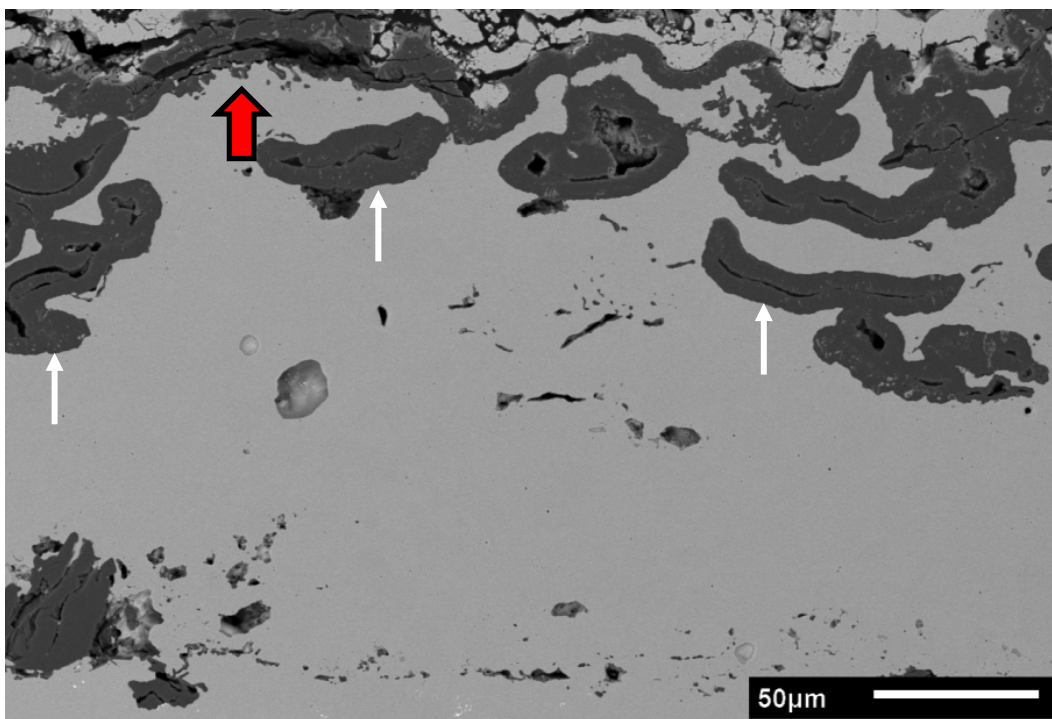


**Figure 127 - Failed DL bond coat TBC on N5 after 620 cycles. Note the surface connected pores which have oxidized (white arrows).**

As with the 50:50 bond coat, the outer layer of the dual layer bond coat completely oxidized. However, since this bond coat had a dense inner layer, the superalloy did not experience direct oxidation. In select regions (red arrow) the outer portion of the bond coat formed the inward growing alumina fingers indicating the aluminum content in these regions of the bond is dropping below the critical level needed to reform the protective oxide.

Taking the FCT data and the microstructural observations into consideration, the bond coats can be ranked in terms of FCT performance and oxidation protection. FCT ranking, in only the case of the René N5 specimens, was straightforward as the TBC lifetimes were very reproducible thus giving confidence in the observed values. Only one of each of the PWA 1484 specimens was tested so they will not be ranked. The FCT ranking for the N5 specimens goes as follows: the 50:50 performed the best with an average lifetime of 713 cycles, followed by the DL bond coat with 613 cycles, then the 75:25 bond coat with 320 cycles and the SL bond coat with 287 cycles.

The oxidation performance/protection of each of the bond coats is more of a qualitative than a quantitative ranking. Since a primary role of the bond coat is to protect the superalloy the 50:50 bond coat was clearly the worst performer as this coating did not prevent substrate oxidation. The remaining three bond coats were able to protect the superalloy to some degree so the next criterion of ranking was based on their oxidation performance, more specifically the rate of  $\beta$ -phase dissolution at the expense of oxide formation (i.e. aluminum consumption). Based on this scale, the SL bond coat had the best, by far, overall oxidation performance. The DL and 75:25 had similar rates of aluminum depletion so they fit in somewhere between the 50:50 bond coat (worst) and the SL bond coat (best).

Given these results, it is surprising the bond coat with the worst oxidation performance (50:50) had the best FCT lifetime. Generally because of the long isothermal hold times in FCT tests, this testing method tends to exploit any oxidation inadequacies a TBC system may contain. Thus it would be expected the TBC system with the worst oxidation would yield the worst performance if FCT testing were used. However, this was not apparent in these tests indicating there is another parameter of the TBC system that superseded the oxidation requirement. In the next section the four bond coat specimens were cycled to a percent of their lifetimes and cross-sectioned to gain insight on how the failure progresses in attempts to explain the FCT observations.

**4.2.3.3 Percent Lifetime** A total of 9 specimens, three of each bond coat type, on PWA1484 were used in this testing. The details of these experiments are given in Table 13. One of the three specimens was FCT tested until failure (100% Lifetime). The remaining two specimens were cycled to either 510 and 200 cycles (DL and 50:50) or 200 and 140 cycles (75:25 and SL).

**Table 13 - Percent Lifetime Testing Summary**

	DL on PWA 1484	50:50 on PWA 1484	75:25 on PWA 1484	SL on PWA 1484
100% Lifetime =	640 cycles	600 cycles	280 cycles	280 cycles
510 cycles =	80%	85%	-	-
200 cycles =	31%	33%	71%	71%
140 cycles =	-	-	50%	50%

The specimens were FCT tested then vacuum mounted in warm epoxy, cross-sectioned with a high speed precision saw, polished to a 0.04 $\mu$ m finish and imaged with a SEM equipped with EDS. Figure 128 shows a SL bond coat after 140 cycles.

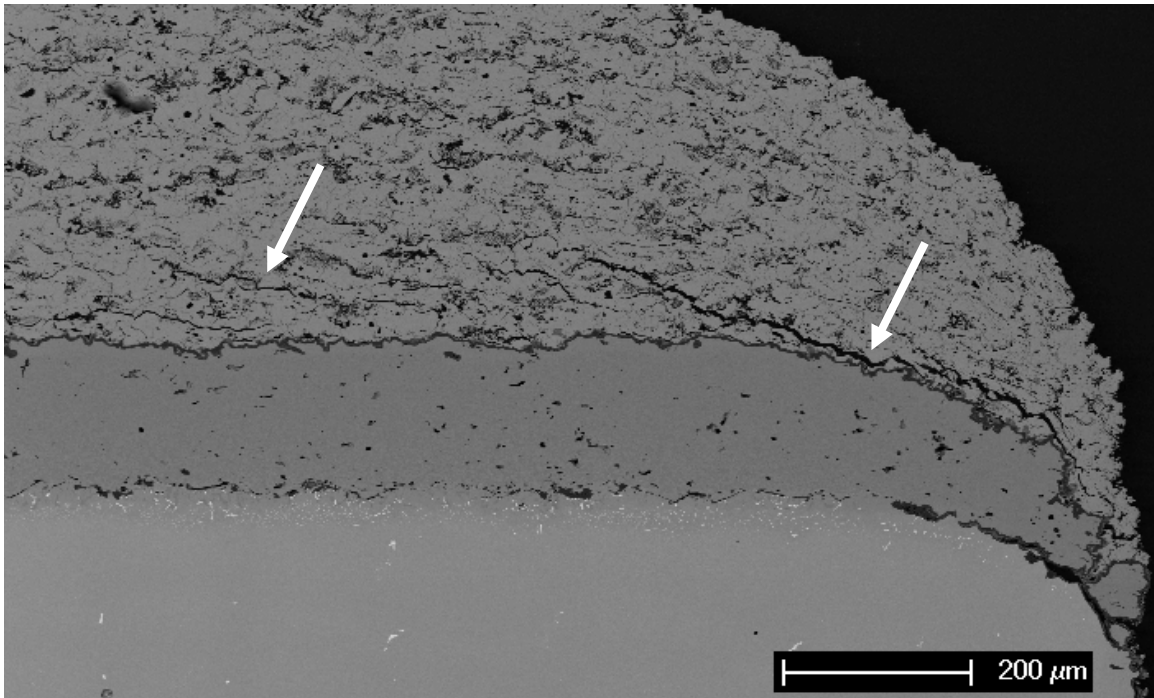


**Figure 128 - SL bond coat on PWA 1484 with 140 cycles (~50% Lifetime).**

This micrograph was taken at the edge of the specimen where cracks were found extending from the free edge into the coating. Cracking was also observed in the interior of the specimen, shown in Figure 129, (away from the free edge) however this cracking was very minimal.

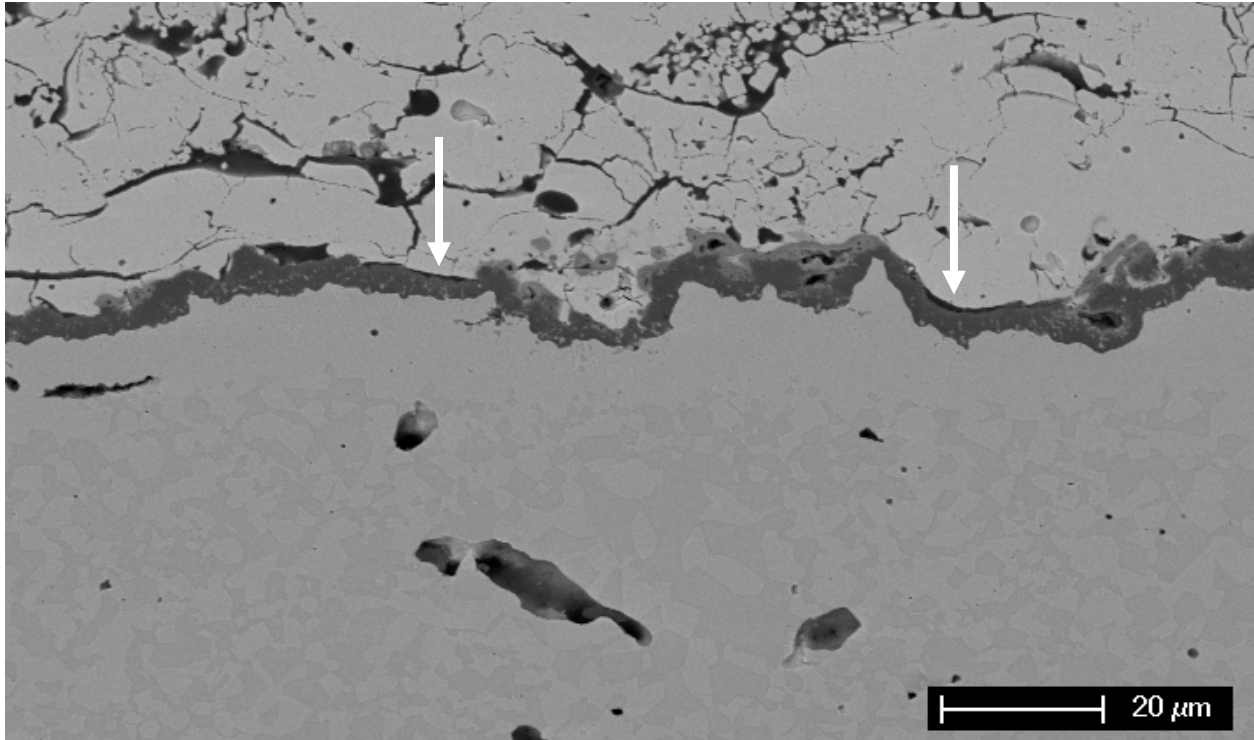


**Figure 129 - SL bond coat on PWA 1484 with 140 cycles. White arrows point out cracks at interface between TGO and YSZ.**

After 200 cycles the cracking in the SL bond coat was much more severe. The amount of edge cracking did not increase much as seen in Figure 130 however the cracking in the interior of the specimen increased, which is shown in Figure 131.

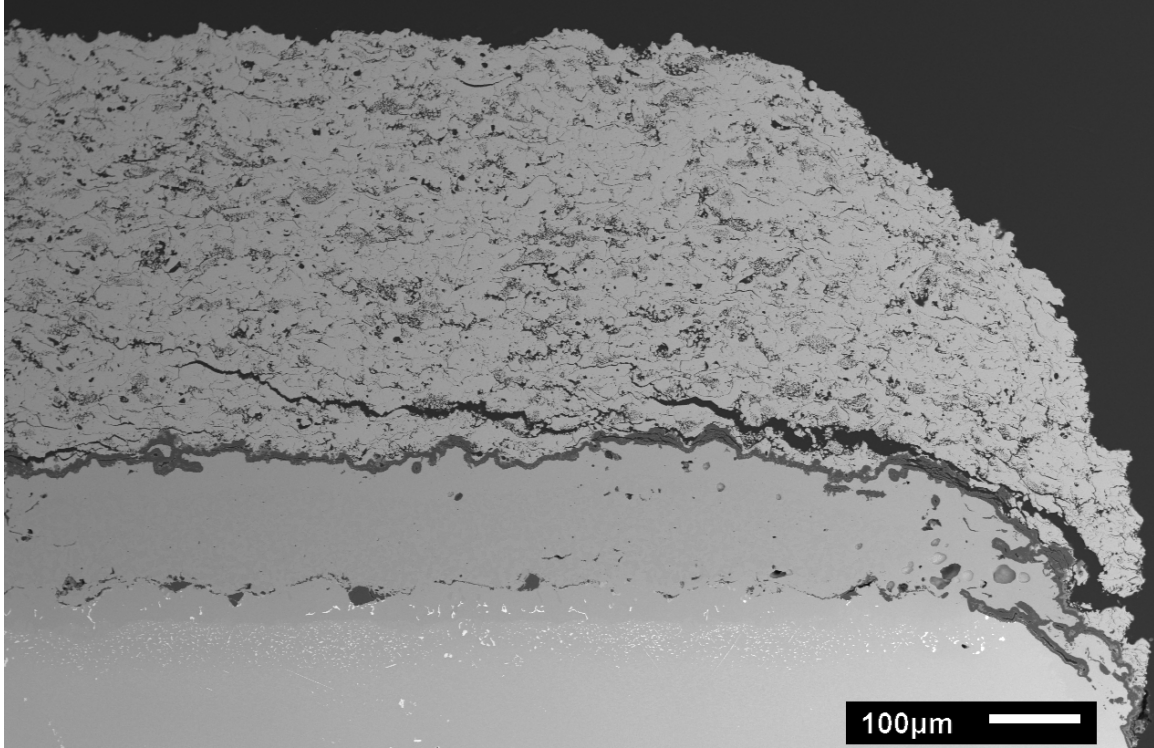


**Figure 130 - SL bond coat on PWA 1484 with 200 cycles.**

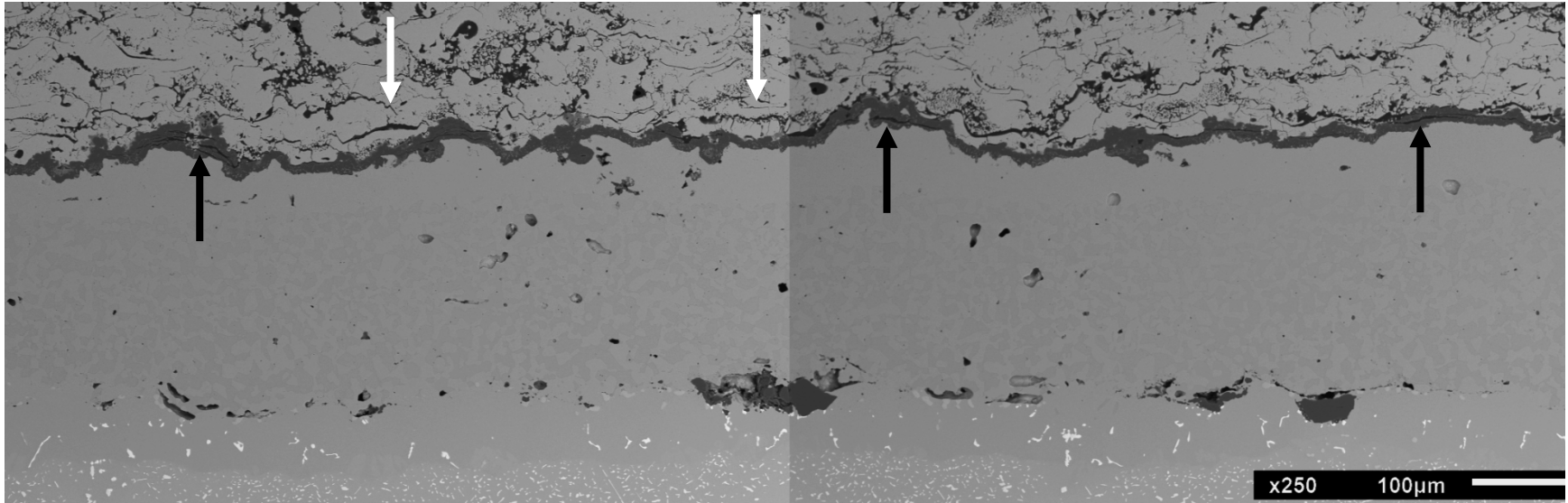
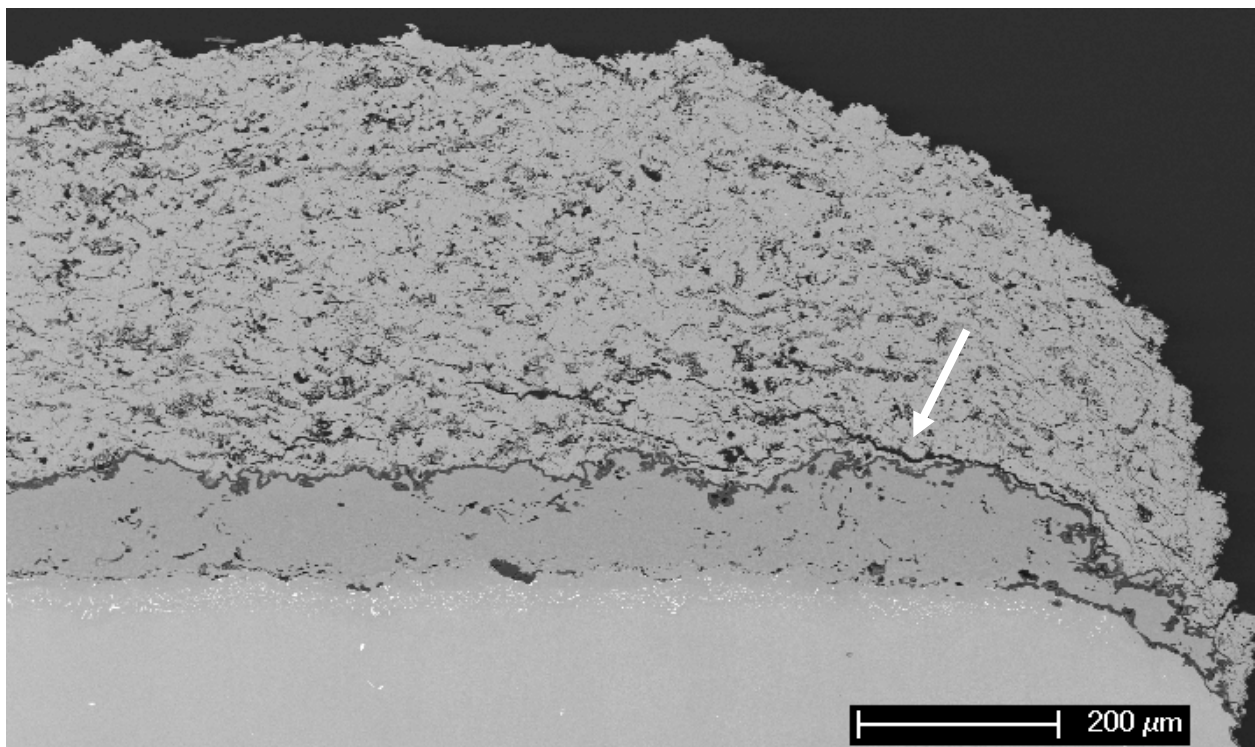


Figure 131 - SL bond coat on PWA 1484 with 200 cycles.

Heavy cracking occurred both in the TGO (black arrows) and in the YSZ (white arrows). The YSZ cracking seemed to occur over valleys/depressions in the bond coat while cracking in the TGO appeared to occur at peaks in the bond coat. This form of TGO cracking could be better described as a form of small scale buckling aided by the curvature of the bond coat and driven by the thermal misfit stresses between the bond coat and alumina TGO [73].

The 75:25 bond coat behaved much like the SL bond coat. It too experienced edge cracking after 140 cycles, Figure 132, but the amount of edge cracking did not seem to increase once it reached 200 cycles, Figure 133.



**Figure 132 - 75:25 bond coat on PWA 1484 with 140 cycles (50% lifetime).**

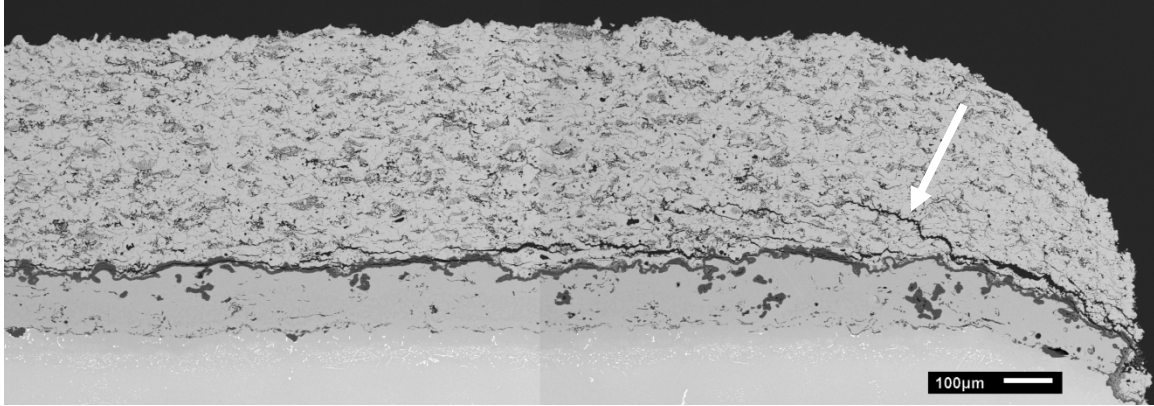


**Figure 133 - 75:25 bond coat with 200 cycles (71% lifetime).**

After 140 cycles, the 75:25 bond coat had noticeable amounts of cracking within the interior of the specimen shown in Figure 134.

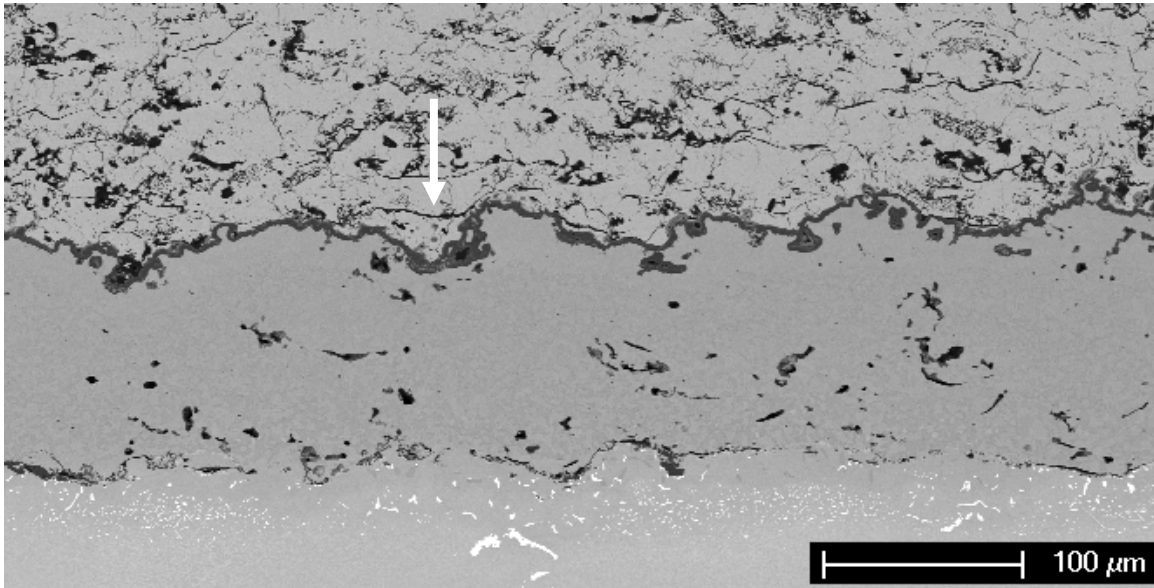


**Figure 134 - 75:25 bond coat with 140 cycles (50% lifetime).**

After 200 cycles the cracking had significantly progressed throughout the interior of the specimen. Again small scale buckling of the TGO was observed above the peaks in the bond coat

along with cracking in the YSZ above valleys. The only noticeable difference between the SL and 75:25 bond coats was the 75:25 bond coat had isolated regions with very high roughnesses. Such a region is shown in Figure 135 (red arrow).

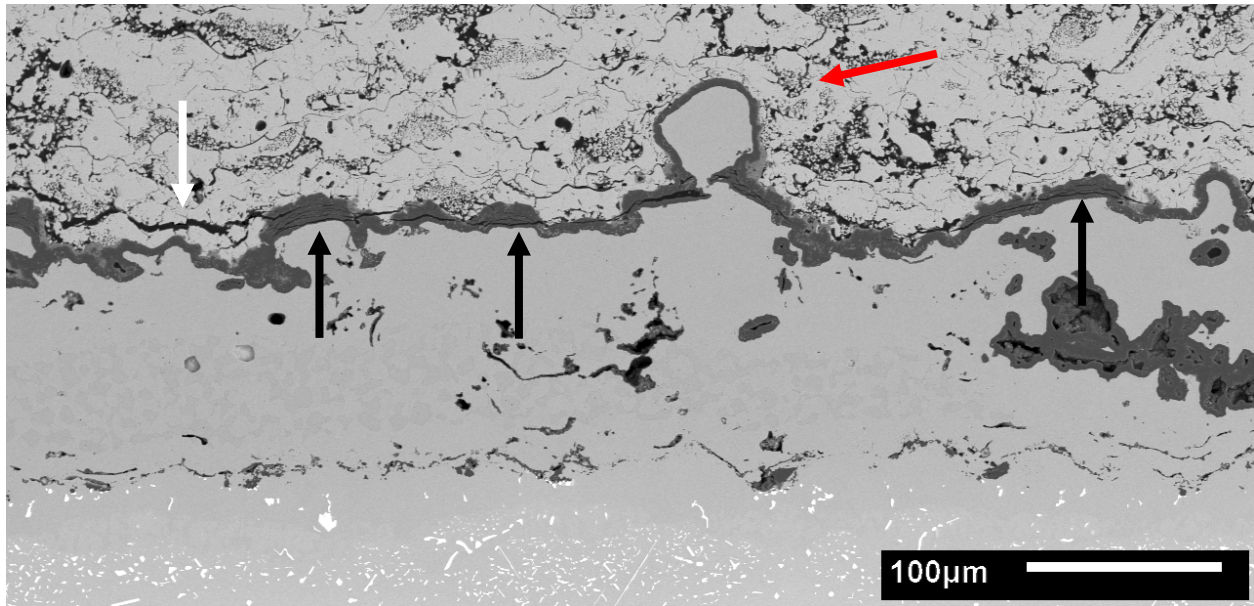


**Figure 135 - 75:25 bond coat with 200 cycles (71% lifetime).**

Interestingly, the large peak in the center of this micrograph, likely an LN14 particle, does not have cracking along its outer edge. Instead cracks from both sides of the particle appear to be propagating into its base where it is attached to the bulk of the bond coat. The two cracks seem to be cutting away at its base, attempting to coalesce. Essentially, this bond coat particle appears to be a barrier preventing the cracks on each side from coalescing. Such a feature could provide strength to the interface by either forcing cracks to propagate through them or around them.

Moving to the 50:50 bond coat, after 200 cycles this bond coat also exhibited edge cracking (Figure 136) and moderate cracking within the interior of the coating Figure 137.

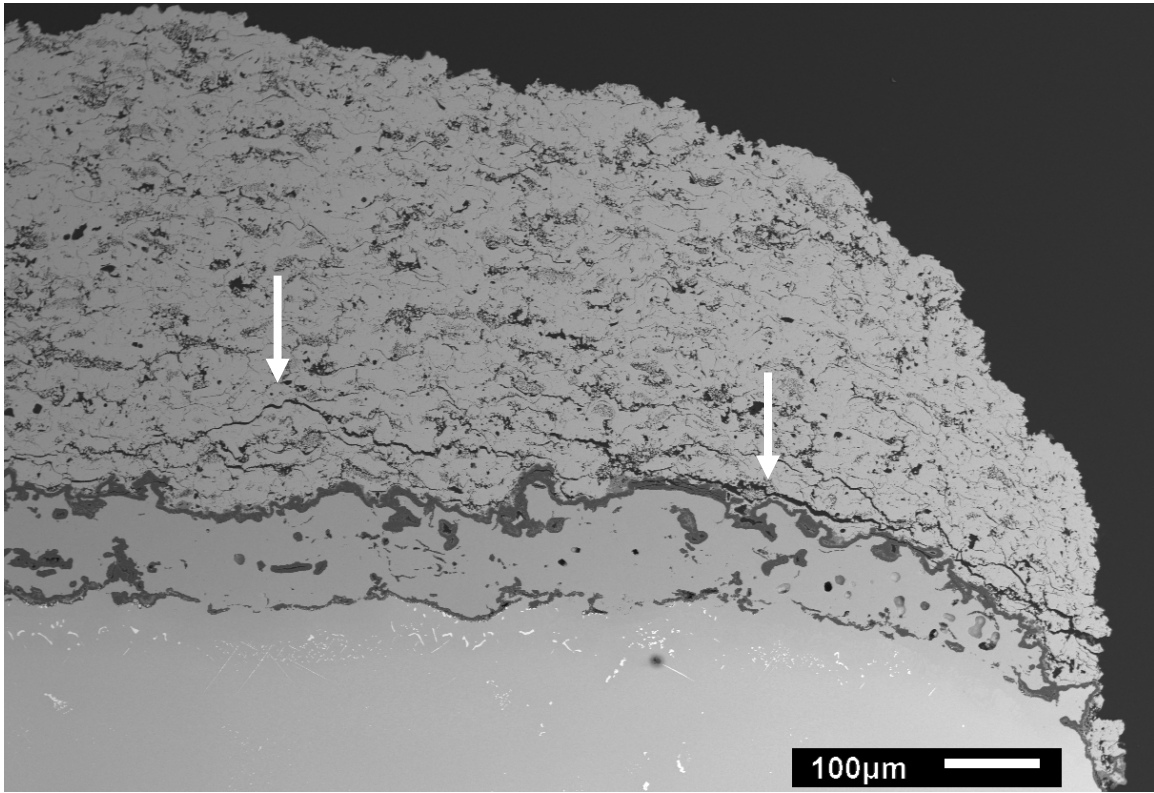


**Figure 136 - 50:50 bond coat with 200 cycles (33% lifetime).**

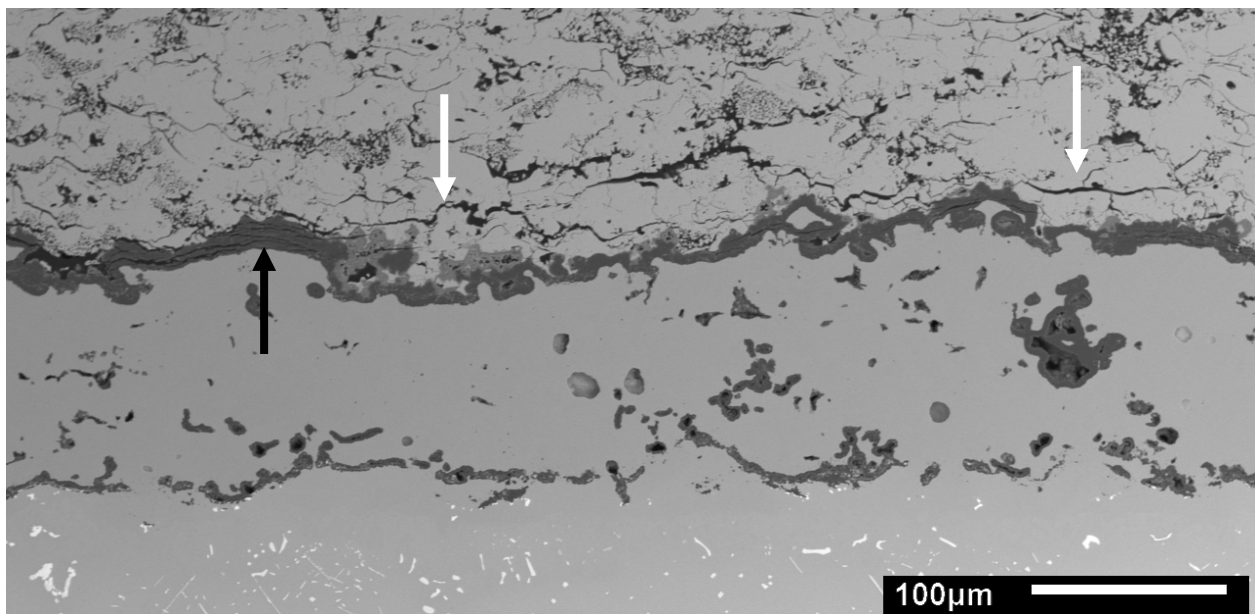


**Figure 137 - 50:50 bond coat with 200 cycles (33% lifetime).**

While extensive damage has occurred to the TGO/YSZ interface, the TBC is only at 33% of its lifetime. The amount of damage here is comparable to that of the 75:25 specimen after 200 cycles, where 200 cycles is 71% of the 75:25 coating's lifetime. The main microstructural difference between the two is the 50:50 bond coat had more of the large surface asperities spread over its surface, two of which are shown in Figure 138.

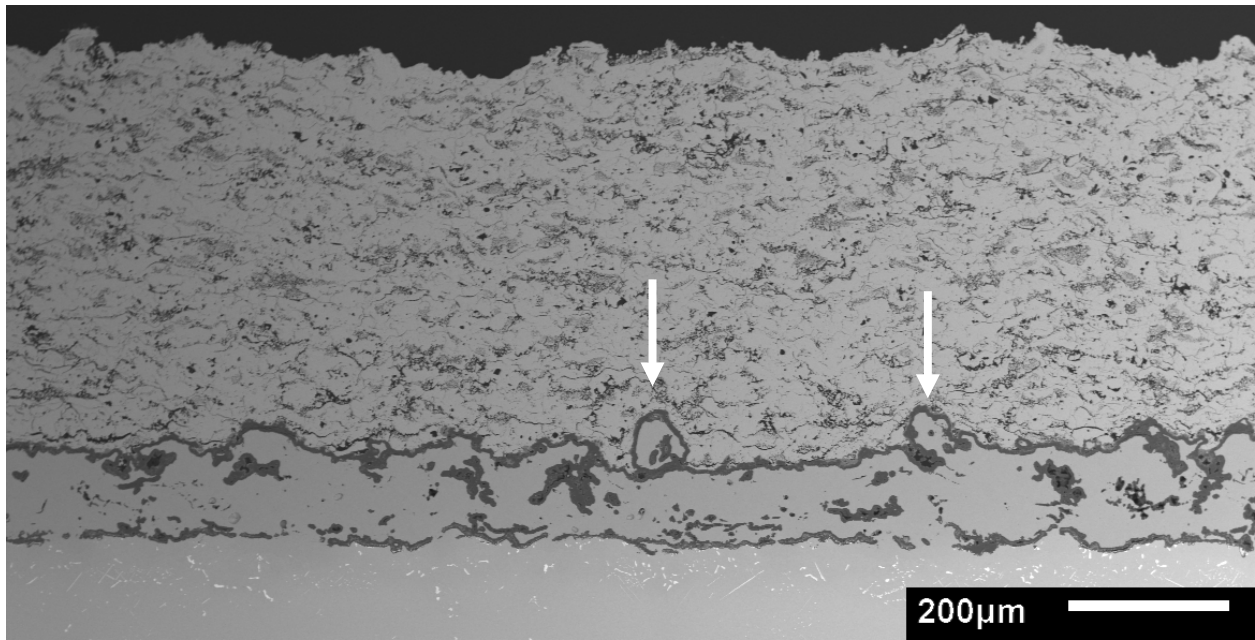


**Figure 138 - 50:50 bond coat with 200 cycles (33% lifetime).**

After 510 cycles, the scale and topcoat had severe damage. Large cracks extending in from the edges were visible (Figure 139) as were large delaminations within the bulk of the coating (Figure 140).

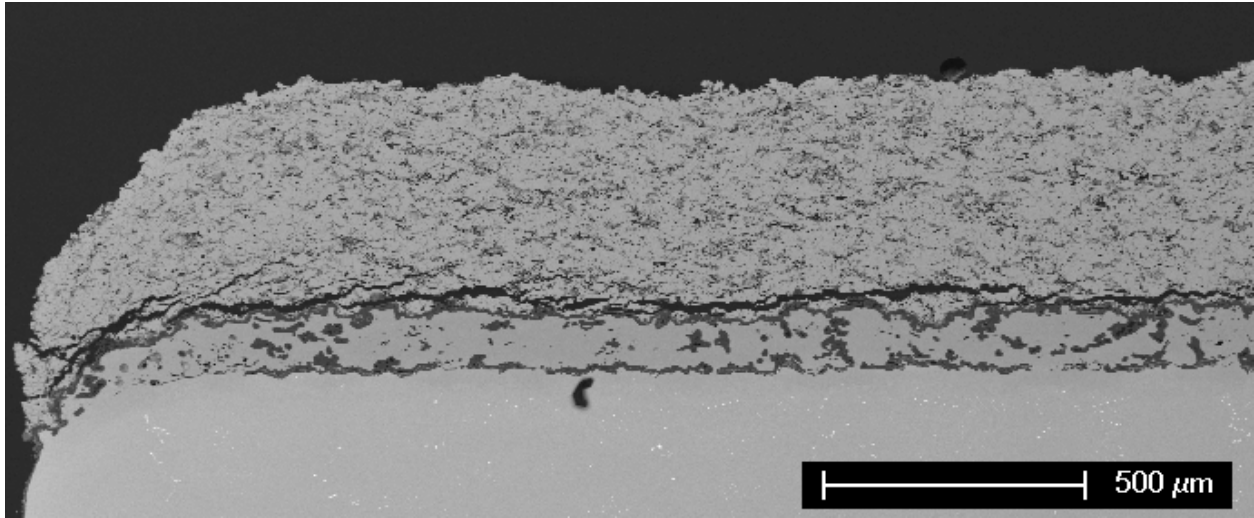


**Figure 139 - 50:50 bond coat with 510 cycles (85% lifetime).**

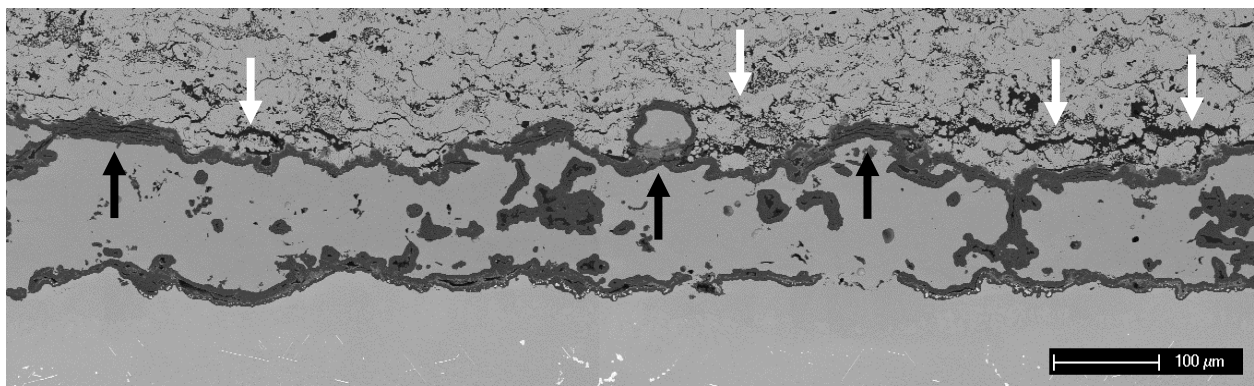


**Figure 140 - 50:50 bond coat with 510 cycles (85% lifetime).**

Ahead of the edge crack front (i.e. to the left of the crack shown in Figure 139) are smaller individual cracks similar to those in Figure 140. The large edge crack appears to be “consuming” or following the path of the smaller cracks, which have formed prior to the start of this edge delamination. In certain regions, such as that in Figure 141, the small individual cracks are approaching a large peak (black arrow) from the right and left (white arrows) and are being deflected up into the YSZ. This type of microstructural feature again appears to be deterring the two cracks from coalescing.

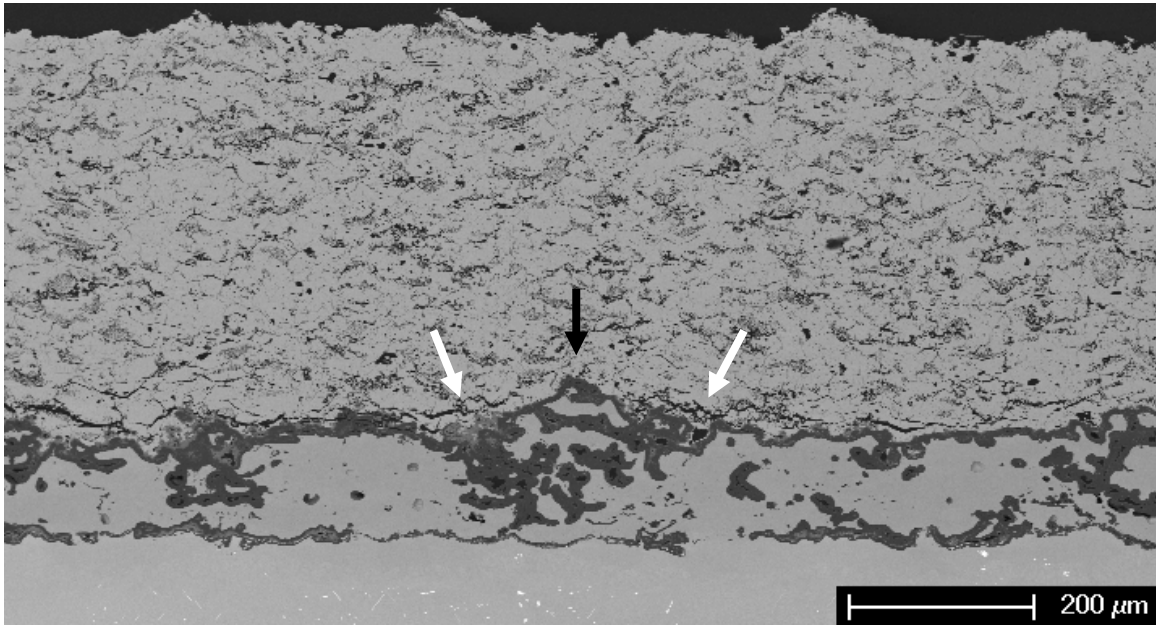


**Figure 141 – 50:50 bond coat with 510 cycles (85% lifetime).**

As with the 50:50 bond coat, after 200 cycles the DL bond coat had minimal cracking at the edges, Figure 142, and in the interior of the specimen, Figure 143.

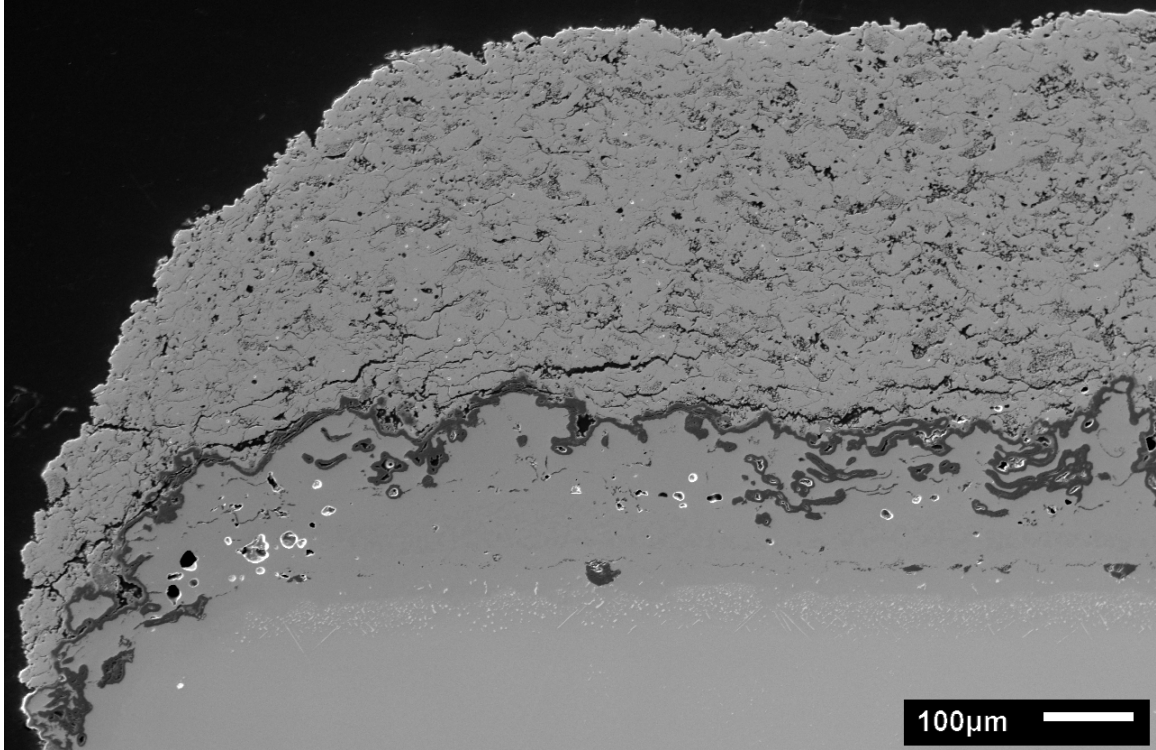


Figure 142 - DL bond coat with 200 cycles (35% lifetime).

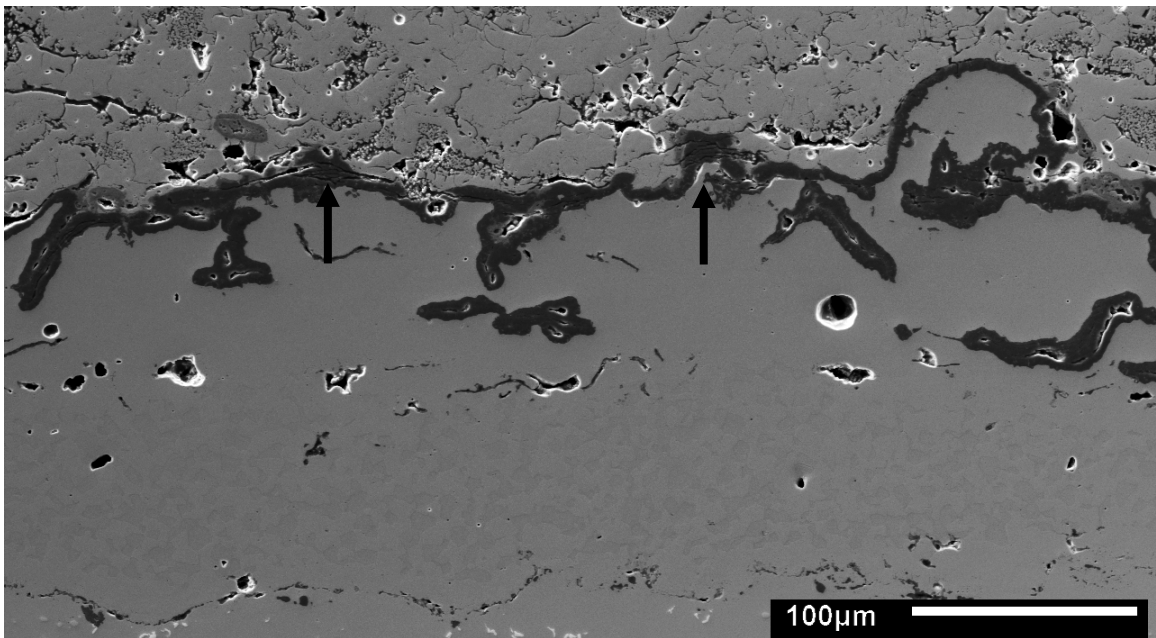
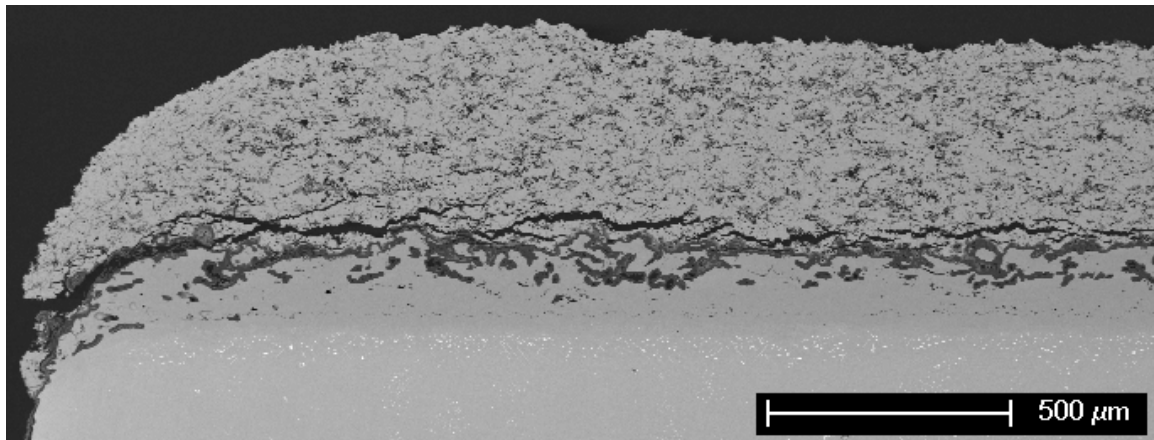
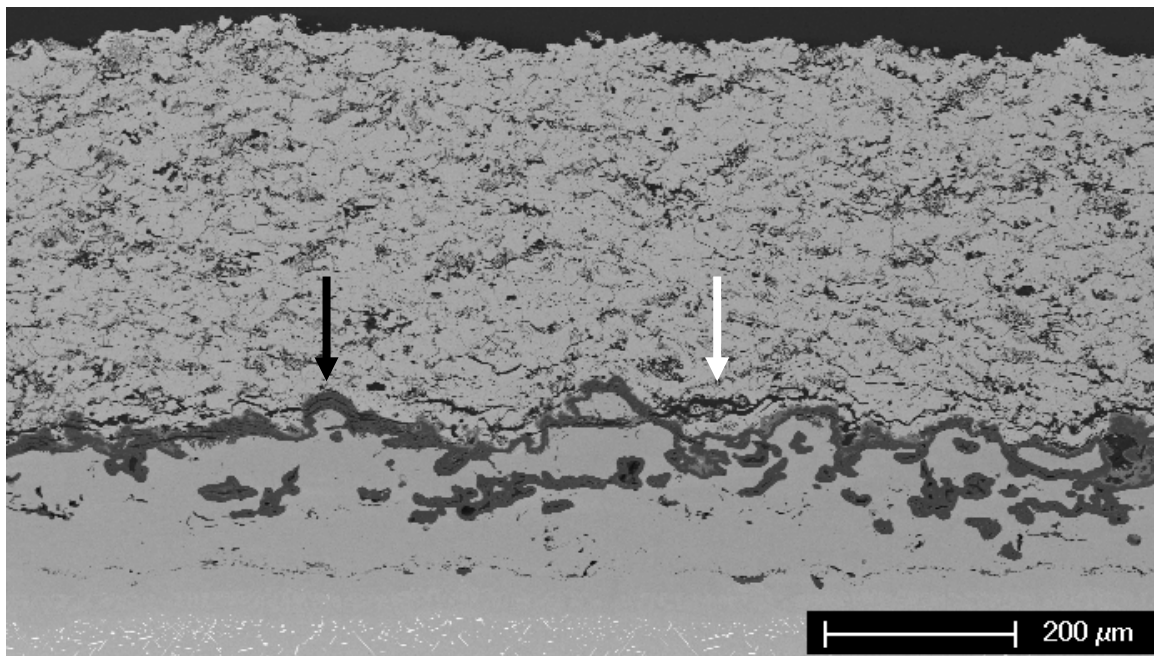


Figure 143 - DL bond coat with 200 cycles (35% lifetime).

After 510 cycles, which represents 80% of the coatings lifetime, the topcoat was almost completely delaminated, Figure 144. Heavy cracking in the TGO and within the YSZ was also prevalent, Figure 145. Overall, the DL coating appeared similar to the 50:50 coating after 510 cycles. It is thus not surprising they performed similarly in the FCT testing.



**Figure 144 - DL bond coat with 510 cycles (91% lifetime).**



**Figure 145 - DL bond coat with 510 cycles (91% lifetime).**

Table 14 summarizes the microstructural observations gained by examining all of the percent lifetime specimens.

**Table 14 - Characterization summary of Percent Lifetime Tests**

Microstructural Characterization Summary of Percent Lifetime Specimens				
	DL on PWA 1484	50:50 on PWA 1484	75:25 on PWA 1484	SL on PWA 1484
510 Cycles	- Topcoat almost completely delaminated - Large edge delamination - Severe TGO cracking at bond coat peaks - Severe YSZ cracking above bond coat valleys	- Topcoat almost completely delaminated - Large edge delamination - Severe TGO cracking at bond coat peaks - Severe YSZ cracking above bond coat valleys	-	-
200 cycles	- Minimal edge cracking - Minimal TGO cracking at bond coat peaks - Minimal YSZ cracking above bond coat valleys - 10 $\mu$ m $\beta$ -phase depletion zone <sup>1</sup>	- Minimal edge cracking - Medium TGO cracking at bond coat peaks - Medium YSZ cracking above bond coat valleys - No $\beta$ -phase left in bond coat <sup>1</sup>	- Medium edge cracking - Severe TGO cracking at bond coat peaks - Severe YSZ cracking above bond coat valleys - 10 $\mu$ m $\beta$ -phase depletion zone <sup>1</sup>	- Medium edge crack - Severe TGO cracking at bond coat peaks - Severe YSZ cracking above bond coat valleys - No $\beta$ -phase depletion zone <sup>1</sup>
140 cycles	-	-	- Medium edge cracking - Minimal TGO cracking at bond coat peaks - Medium YSZ cracking above bond coat valleys - No $\beta$ -phase depletion zone <sup>1</sup>	- Minimal edge cracking - Minimal TGO cracking at bond coat peaks - Minimal YSZ cracking above bond coat valleys - No $\beta$ -phase depletion zone <sup>1</sup>
$\beta$ -phase depletion zone is a result of aluminum diffusion (i.e. $\beta$ -phase dissolution) down into the superalloy which creates a zone at the base of the bond coat devoid of the $\beta$ -phase. This was measured from the bond coat – superalloy interface to the nearest $\beta$ -grain in the bond coat.				

**4.2.3.4 JETS Results** JETS testing was only performed on the DL, 50:50 and 75:25 bond coat specimens. Prior to testing the specimens were edge ground so they could be placed into the JETS testing rig. After grinding the specimens should have a flat edge (i.e. no radius of curvature to the bond coat, substrate or YSZ) however the grinding process actually induced minor edge

chipping and cracking. The pretest cracking was as follows: DL – 40%, 50:50 – 48% and 75:25 – 42%.

After they were measured, they were loaded into the rig and run for 2000 cycles with the flame adjusted to yield a topcoat surface temperature of 1250°C. Once they reached 2000 cycles, they were removed and measured again for edge cracking. Their post-test cracking levels were identical to their pretest levels. This is not a surprising result considering the JETS test is primarily used to test the durability of topcoats and has minimal effect on the bond coat type because of the short dwell times under the flame [74]. Since all of the specimens have the same topcoat it seems reasonable to find they performed similarly in the JETS test. Figure 146 through Figure 148 show the tested specimens of each bond coat type. Note the large edge cracks and chips which were induced during grinding.

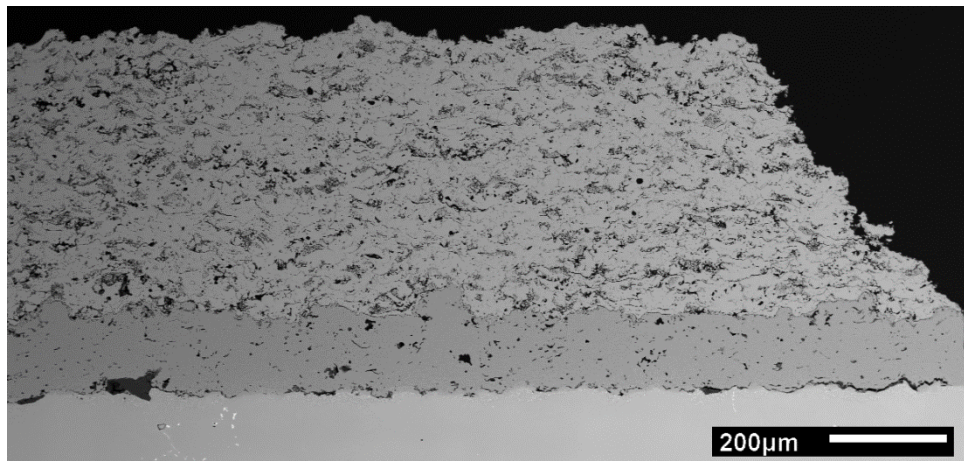


**Figure 146 - 75:25 bond coat on PWA 1484 with 2000 JETS cycles.**

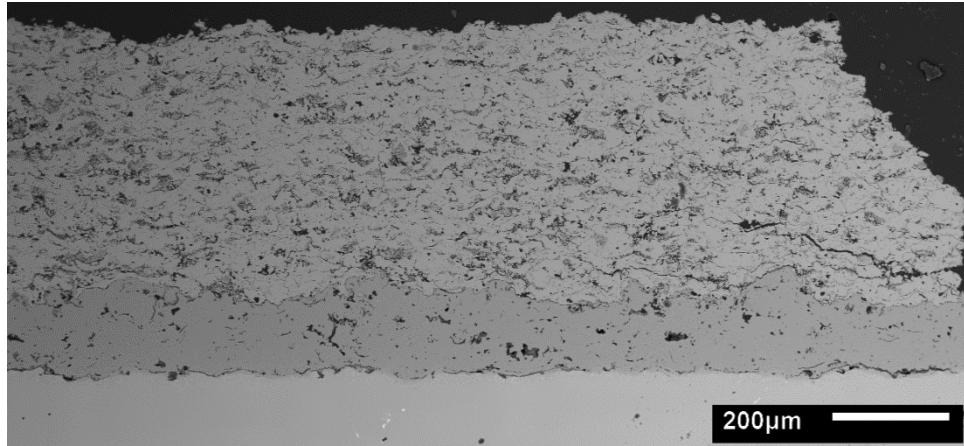


**Figure 147 - 50:50 bond coat on PWA 1484 with 2000 JETS cycles.**

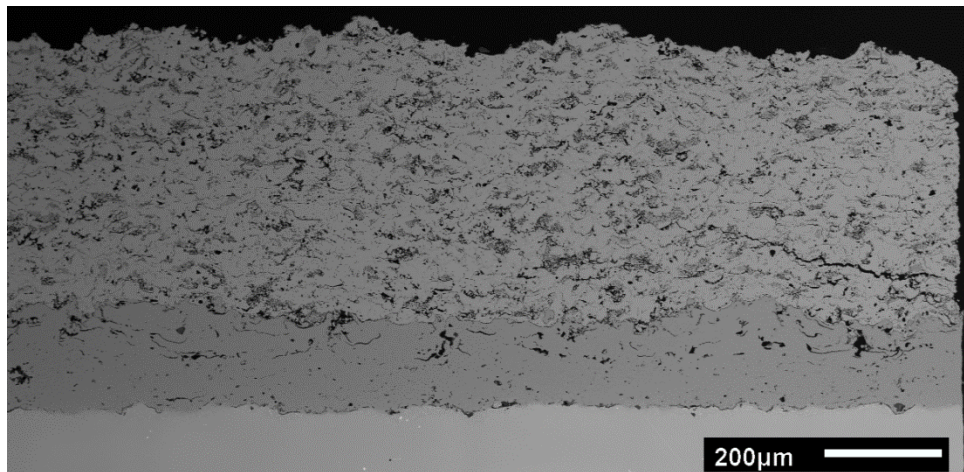


**Figure 148 - DL bond coat on PWA 1484 with 2000 JETS cycles.**

#### **4.2.4 Discussion**

Starting with the surface characterization, it was concluded all four of the bond coat types had significantly different surfaces. The SL bond coat was relatively smooth ( $R_a=6.9 \mu\text{m}$ ,  $R_z=42.4 \mu\text{m}$ ) and contained little open porosity. Small ( $< 25 \mu\text{m}$ ) protrusions and undulations populated the surface of this coating, but by far it was the smoothest of the four types. The 75:25 bond coat had a higher roughness ( $R_a=10.7 \mu\text{m}$ ,  $R_z=56.5 \mu\text{m}$ ) and contained small ( $< 25 \mu\text{m}$ ) and medium

(75- 25  $\mu\text{m}$ ) sized peaks and undulations. In cross-section the 75:25 coating appeared similar to the SL bond coat with the difference being more open porosity and the presence of occasional large surface asperities such as that shown in Figure 135. The 50:50 bond coat was rougher than the 75:25 coating ( $R_a=11.9 \mu\text{m}$ ,  $R_z=66.4 \mu\text{m}$ ) and the surface was populated with medium and large ( $>75\mu\text{m}$ ) peaks. The frequency (i.e. surface density) of the large bond coat asperities was higher than that in the 75:25 bond coat. This yielded a larger average  $R_z$  value and, because there were so many peaks spaced closer together, this also led to the formation of artificial valleys in between the large particles which was another major difference between the 75:25 and 50:50 bond coats. This coating also contained significant amounts of open pores which lead to its poor oxidation performance. Finally, the DL bond coat had the highest roughness ( $R_a=14.0 \mu\text{m}$ ,  $R_z=81.4 \mu\text{m}$ ) of all the coatings. The surface contained a high frequency of large and medium surface peaks and valleys. The outer layer of this coating was very porous and as a result experienced heavy oxidation during high temperature exposure. The dense inner layer of this coating however provided the oxidation protection to the substrate.

In the FCT test, the average lifetime of the René N5 specimens was as follows: SL – 287 cycles, 75:25 – 320 cycles, 50:50 – 713 cycles and DL – 613 cycles. While the 50:50 coating had the longest FCT lifetime, it also had the worst oxidation performance. It did little to provide oxidation protection to the superalloy, whereas the SL bond coat, which had the worst FCT lifetime, provided the best oxidation protection to the superalloy. This fact alone indicates other TBC system parameters are as important, if not more important, than bond coat oxidation behavior. Similarly, the 75:25 and the DL bond coats had similar oxidation behavior but entirely different performance in the FCT tests. Fracture surfaces of the SL and 75:25 coats revealed cracking occurred primarily within the TGO as both the under surface of the topcoat and the top

surface of the bond coat (i.e. the mating surfaces) were covered with alumina. Small patches of YSZ were present but surface coverage was dominated by the TGO, more so in the case of the SL bond coat (Figure 118) than in the case of the 75:25 bond coat (Figure 119). The DL and 50:50 specimens had fracture surfaces with a mix of YSZ and TGO. In cross-section, it was revealed the YSZ patches were actually bond coat valleys that contained YSZ, where the delamination crack extended above the valley (Figure 121).

In order to obtain more understanding on how the failure progressed, specimens were FCT cycled out to percentages of their lifetimes following which they were cross-sectioned and analyzed. All four specimens were examined after 200 cycles, at which this represented roughly 70% of the lifetime of the SL and 75:25 bond coats and 30% of the lifetime of the 50:50 and DL bond coats. The SL and 75:25 specimens had heavy cracking within the TGO (Figure 131 and Figure 135 respectively) which was believed to be small scale buckling which occurred around round peaks in the bond coat. Cracking within the YSZ was also observed over valleys in the bond coat. The 50:50 also had significant amounts of TGO buckling and cracking within the YSZ above the bond coat valleys (Figure 137) as did the DL specimen after 200 cycles (Figure 143). At this point all of the coatings had significant levels of damage and appeared to be close to failure; however the 50:50 and DL coatings were only at 30% of their lifetimes. This suggests these type of bond coats are able to sustain larger amounts of small scale TGO damage without succumbing to TBC spallation.

Based on the observed cracking behavior the following mechanisms are suggested to have caused the difference in the failure lifetimes and failure behaviors. All of the specimens sustained widespread small scale buckling of the TGO after 200 cycles. Unlike the 50:50 and DL specimens, the SL and 75:25 bond coats were relatively smooth. They (75:25 and SL) both had

smooth level surfaces with small ( $<25\mu\text{m}$ ) peaks and very few valleys as shown in Figure 118. They both had large patches of relatively flat defect-free bond coat surfaces. If a crack in the TGO were to form near one of these regions there would be nothing to stop it from propagating the entire length of the smooth regions. Sources of these cracks could be the larger bond coat peaks such as those in Figure 131 (far-right black arrow). Once enough of these cracks form, the interface between the TGO and the YSZ becomes so weak that large scale delamination becomes possible. Furthermore, because failure occurs in the TGO, both fracture surfaces (topcoat and bond coat) would be covered with TGO which is entirely consistent with the observations. Based on this understanding, the slightly longer lifetime of the 75:25 bond coat, as compared to the SL bond coat, could be rationalized by taking into consideration the large, yet infrequent, surface asperities (Figure 135) scattered across the surface of the 75:25 bond coat. These large features could again act as barriers delaying the coalescence of these individual TGO cracks. Continuing with this reasoning, the 50:50 and DL bond coats have rough irregular surface morphologies, so even if small scale buckling of the TGO occurs, the cracks would only propagate a short distance before either reaching a free surface of some type or a propagation barrier such as another bond coat peak or a YSZ valley. A highly porous topcoat, such as the topcoats used in this study, have small elastic moduli and high toughness as compared to an alumina TGO and are able to arrest small cracks. A denser YSZ topcoat, however, may be unable to arrest such a crack [45] leading to shorter lifetimes for TBC with dense topcoats.

Failure of the DL and 50:50 bond coats requires a different explanation, as although there was heavy cracking within the TGO (Figure 145 and Figure 141 respectively); their fracture surfaces were primarily covered with YSZ whereas the 75:25 and SL bond coats were more so TGO. This type of cracking within the topcoat has been modeled by several authors [62, 65, 75]

and seems appropriate given the experimental results. The model by Vassen et al. [65] begins by constructing a topcoat/bond coat geometry as shown in Figure 149. This is obviously an idealized model as the bond coat interfaces in this study are much more complex.

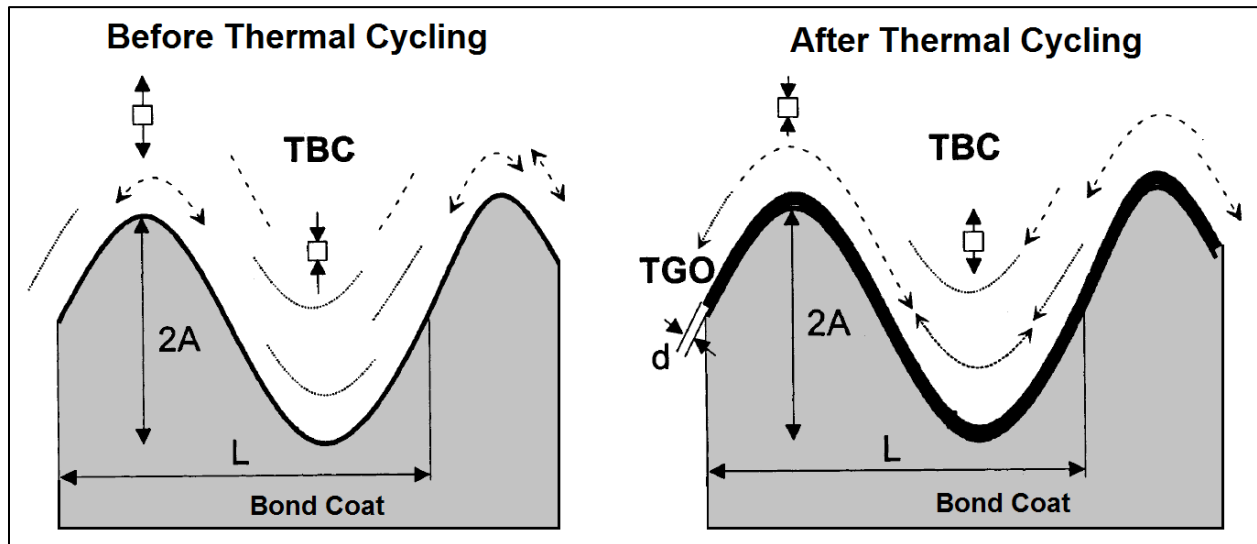


Figure 149 - Bond coat and accompanying stresses before and after thermal exposure. Figure was taken from [65].

Prior to growth of a TGO, during thermal cycling, the difference in thermal expansion coefficients (CTE) of the YSZ and bond coat induce tensile stresses above the peaks of the bond coat and compressive stresses above the valleys (left side of Figure 149). The tensile stresses can lead to the formation of cracks in the topcoat above the peaks. It is also accepted that microcracks already exist in the topcoat due to its porous defect filled microstructure. These cracks are unable to propagate though because they are bound by compressive regions on either side of the peak. However, when an alumina TGO begins to grow, because its CTE is smaller than that of the YSZ, a stress reversal begins to occur causing the tensile stresses above the peaks to become compressive and the compressive stresses in the valleys to become tensile. Over time,

this allows the cracks to bridge the valleys. It is then assumed that as these cracks bridge the valleys, they link up and cause large scale buckling or delamination. Based on this model the resultant fracture surface should be primarily covered with YSZ, which is consistent with the fracture surfaces of the DL and 50:50 bond coats. This model also predicts that as the amplitude of the bond coat peaks increases (i.e. roughness of the surface), the time needed until stress reversal also increases meaning a rougher bond coat should have a longer lifetime. While this aspect is consistent with the PWA 1484 specimens where the DL bond coat ( $R_a = 14.0 \mu\text{m}$ ) had a longer lifetime than the 50:50 bond coat ( $R_a = 11.9 \mu\text{m}$ ), it is not consistent with the René N5 specimens because the DL bond coats had shorter lifetimes than the 50:50 bond coats. Deviations from the predicted outcomes of this model could be due to a multitude of oversights or oversimplifications built into the model such as an ability to account for surface irregularities, inhomogeneous TGO growth or small scale TGO buckling, all of which could influence the stress behavior. However, there could also be experimental error associated with the definition of TBC lifetime used in this study. Specifically, while the 50:50 and DL specimens on N5 had 713 and 613 cycles to failure respectively, after 510 cycles (Figure 145 and Figure 140) both TBCs had severe cracking along the edges and within the interior of the specimens. Even though the TBC was ‘intact’ and had not ‘failed’, it could be argued the modeled crack bridging from peak to peak had already been completed but that some other ‘force’ helped keep the topcoat intact for an additional 100-200 cycles. Such ‘forces’ could be irregular bond coat peaks gripping the topcoat (Figure 140) or crack sliding frictional forces preventing the propagation of the large delamination cracks [68]. This being said, in the end, the location of the cracking observed in the 50:50 and DL bond coats is consistent with the cracking growth theories proposed by the model.

#### 4.2.5 Conclusions Summary

Through this set of experiments, it was concluded the four types of bond coats, three made from single set deposition procedures (SL, 75:25 and 50:50) and one from a two-step procedure (DL), had appreciably different surface profiles. The 50:50 specimens had the longest FCT lifetime (on Rene N5 substrates) however they also had the worst oxidation performance whereas the SL bond coat was the exact opposite. This observation suggests bond coat roughness can have a greater impact on the FCT lifetime than can the oxidation performance of the bond coat, at least for these particular TBCs. The exceptional performance of the DL and 50:50 bond coats was attributed to cyclic damage taking place in the YSZ just above the TGO (and in the TGO) which is more fracture resistant than the TGO assuming the topcoat is porous and tough. Furthermore, the large surface asperities in these two coatings also extended the lifetime by preventing crack coalescence and crack propagation. When cracks encountered the large particles, they were forced to either extend through them or over them, which presumably required more thermal cycles. The SL and 75:25 specimens were too smooth and susceptible to extensive TGO cracking which ultimately lead to their short failure lives. The slightly longer lifetime of the 75:25 specimens over the SL specimen was also attributed to large bond coat asperities randomly populating the surface which hindered the growth of cracks. This type of crack barrier or crack deflection surface feature could provide the answer for future bond coats.

While the single-processing-step 50:50 bond coat had the longest lifetime, it was neither the best option nor a practical one. Third, fourth and fifth generation superalloys have poor oxidation resistance and depend on the bond coat for this. Since the 50:50 bond coat could not provide this protection, it cannot be considered a solution. The dual layer therefore was the best option because it provided the best average performance. It is possible there exists some other

ratio of coarse to fine powders that may effectively seal the superalloy and provide topcoat adherence, however it was not produced here.

## **4.3 SUBSTRATE INFLUENCES**

### **4.3.1 Overview**

Two approaches to establish the influence of the substrate superalloy on TBC lifetime were investigated; the first was the mechanical influence and the second was the compositional influence.

The mechanical approach focused on identifying the influences of the physical properties (CTE, elastic modulus) on the mismatch stresses in the coatings and how this contributes to TBC failure. This was carried out experimental by thermally cycling TBC systems with multiple superalloy substrates and comparing their performance. Details of these experiments are detailed in later sections.

The compositional approach focused on identifying the significance of the interdiffusion between the bond coat and the superalloy and what influence this may have had on the oxidation performance of the bond coat. This was accomplished by argon-shrouded plasma spraying one composition bond coat onto five separate superalloy materials. These bond coat- superalloy couples were then thermally cycled and periodically imaged and characterized to track the compositional changes of the TGO and within the bond coat. The particulars of these experiments are also detailed in later sections.

Finally, after discussing these two influences, an explanation will be given as to how they interact and both contribute to failure.

## **4.3.2 Mechanical Effects**

**4.3.2.1 Experimental Overview** The experimental results for the influence of substrate CTE on TBC lifetime have also been discussed in previous work [2]. The experimental procedures and results will be summarized for the reader's convenience.

The superalloy substrates used to investigate the influence of substrate CTE on the lifetime of TBCs were: Inconel 718 (IN718), Haynes 188 (HA188) and René N5 (N5). The bond coats were dual layer argon-shrouded plasma sprayed NiCoCrAlY coatings and the topcoats were air plasma sprayed with high purity YSZ powder with a target theoretical density of 85% of 8wt% YSZ.

The dual layer bond coats were produced in two deposition processes, hence the name dual layer. First, a fine sized NiCoCrAlY powder was argon-shrouded plasma sprayed onto the substrates producing a thin dense layer of bond coat material. Then a second larger sized powder, of identical composition, was deposited on top of the dense layer producing a rough surface finish which also contained a significant number of surface connected pores. Dual layer bond coats are utilized in APS TBC applications to provide a rough surface finish for a strong mechanical attachment of the TBC to the bond coat. The total thickness of the bond coat was 150  $\mu\text{m}$ .

Two different thicknesses of topcoats were prepared on each of the three substrate superalloys, which were 375  $\mu\text{m}$  and 1100  $\mu\text{m}$ . The nominal compositions of these alloys and

materials are detailed in Table 4. The density of the topcoats was measured by oil infiltration techniques to be 85% T.D.

The TBCs were thermally cycled in a bottom loading furnace with one cycle consisting of a 10 minute ramp to 1100°C followed by a 45 minute isothermal hold at 1100°C and then a 10 minute forced-air rapid cooling step down to ~60°C. Testing was continued until 50% or more of the topcoat was cracked and/or visually separated or spalled from the substrate.

**4.3.2.2 Mechanical Results and Discussion** Previous work indicated the substrate superalloy strongly influenced the lifetime of high-purity low-density YSZ TBCs as did the thickness of the topcoat layer [2]. Figure 150 shows the lifetimes of the thick (green bars) and thin (blue bars) TBCs on the three superalloys.

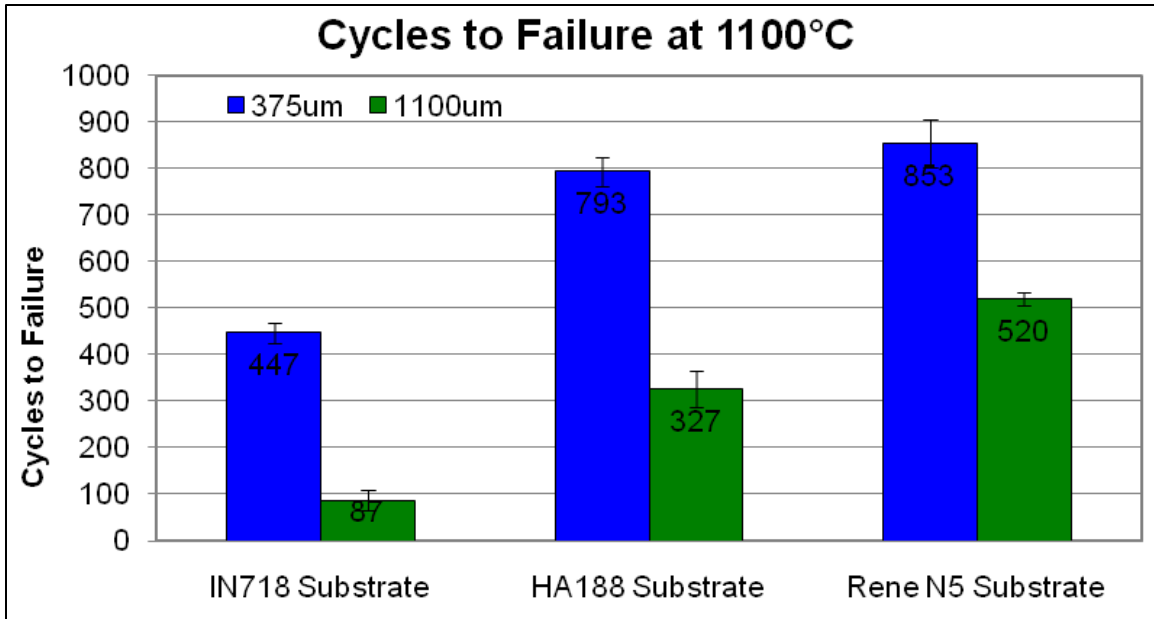


**Figure 150 - The number of cycles to failure for low density, high purity APS TBCs of two topcoat thicknesses on Inconel 718, Haynes 188 and Rene´ N5 substrates. All substrates had dual layer NiCoCrAlY bond coats.**

**Each bar is the average of three specimens with the error bars showing the standard deviations [2].**

Failure of the 1100 µm TBCs occurred after a relatively small number of cycles as compared to the 375 µm TBCs. For the thick TBCs on IN718, failure occurred after 87 cycles at which point cross-sectional microscopy revealed little bond coat oxidation had taken place. Furthermore, failure occurred well above (>200 µm) the topcoat/bond coat interface indicating bond coat oxidation was not a major contributing factor to failure. If it had been, the expected fracture path would have been along the bond coat/TGO/topcoat interface and it was not. It is also presumed the other two superalloys would have had similar levels of bond coat oxidation after 87 cycles further supporting the argument that bond coat oxidation was not the primary cause for the short lifetime of the IN718 TBC. It should be pointed out, however that no experimental work was completed to confirm this at the time these TBCs were originally tested.

Complementary experiments were completed in this body of work which will be discussed in the next section.

Suspecting the CTE of the superalloys was influencing the lifetimes, all three substrates in addition to MarM 509 (MM509) and Inconel 738 (IN738) were sent to Thermophysical Properties Research Laboratory (TPRL) in West Lafayette, Indiana where their CTEs were measured. The CTE measurement data are presented in Figure 151 as a function of temperature.

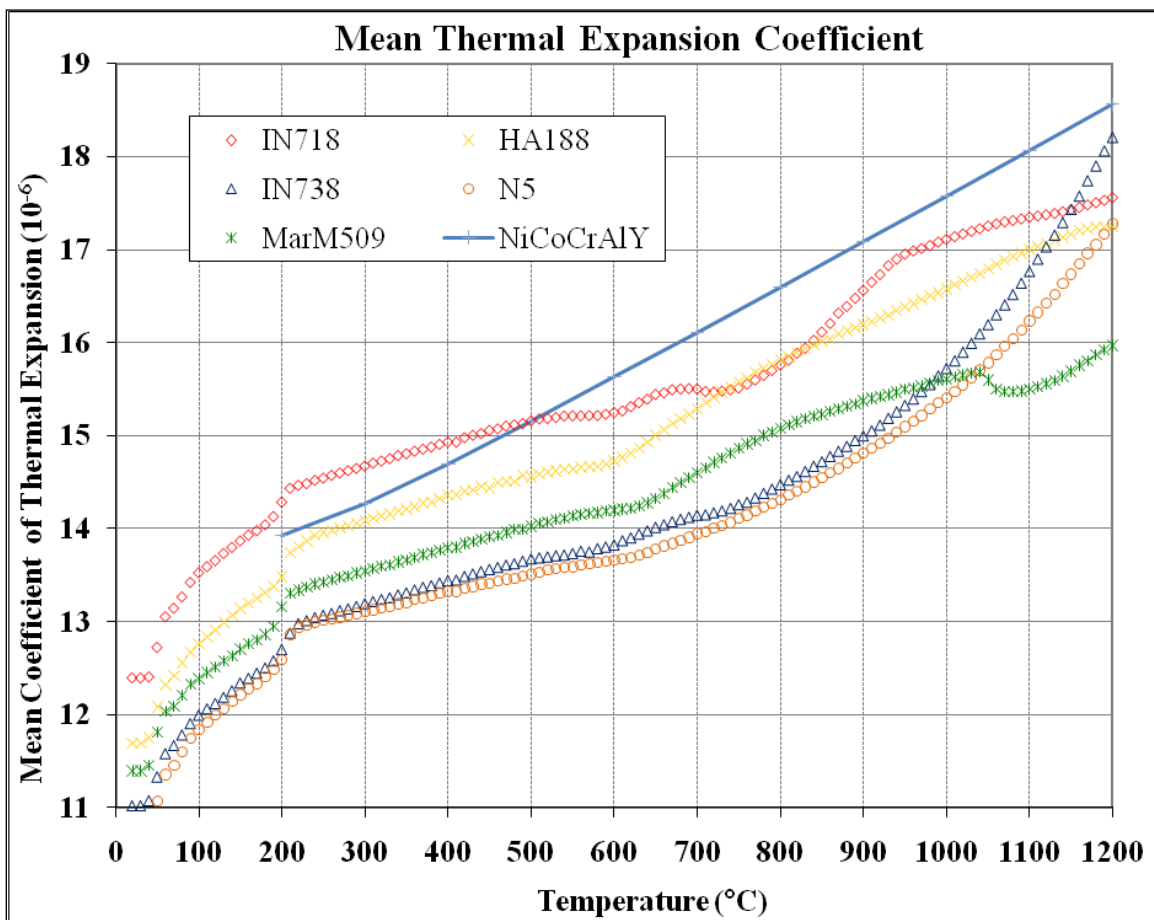


Figure 151 - Mean CTE of the alloys used in this study.

At 1100°C, the CTE of IN718 was largest followed by HA188 and then N5. Relating this data back to Equation 6 and Equation 7, the stored strain energy in the topcoat is proportional to

the square of the CTE mismatch between the topcoat and superalloy substrate. Therefore it would follow the stored strain energy in the IN718 topcoat was the highest followed by HA188 and then N5. If then, other mechanical properties of the system, the elastic modulus and the fracture toughness of the topcoat, are assumed to be the same in the three alloy systems, the plausible explanation for the short lifetime of the IN718 TBC is the high CTE of the IN718 substrate. The high CTE mismatch increases the amount of stored elastic strain energy in the topcoat to the point where the fracture toughness is exceeded resulting in crack growth and spallation of the topcoat [2, 34].

Moving to the thinner topcoat specimens, the 375  $\mu\text{m}$  TBCs had significantly longer lifetimes than the 1100  $\mu\text{m}$  specimens and appeared to experience bond coat oxidation related failure. This type of failure is characterized by fracture along the bond coat/TGO/topcoat interface and only occurs after extensive bond coat oxidation has taken place. An example of such a failure is depicted in Figure 152.

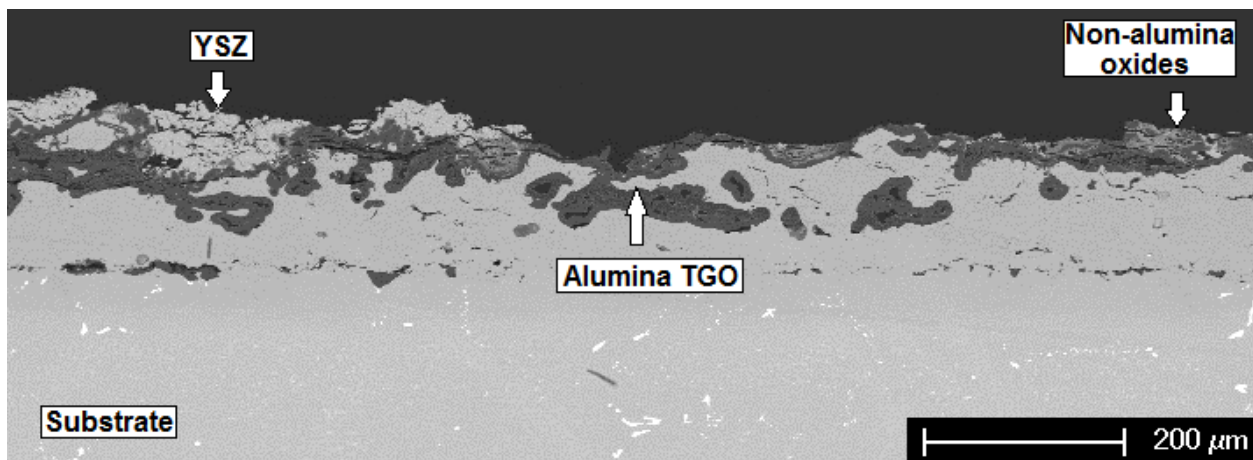


Figure 152 - Failed 375  $\mu\text{m}$  TBC on N5 after 920 cycles.

However, at the time of the testing, the exact influence of the substrate on the lifetimes of the 375  $\mu\text{m}$  TBCs was not fully understood. A literature survey identified several potential influences of the substrate material on TBC lifetime [48, 49, 76, 77]. The two main cases involved minor substrate elements, such as sulfur, yttrium, or hafnium, diffusing into the bond coat from the substrate and the second involved scale-forming elements in the bond coat, such as aluminum, diffusing down into the substrate. The former influences the scaling kinetics and TGO adhesion whereas the later influences the ability of the bond coat to continually form a protective TGO. The compositional influence of the substrate will be discussed in the subsequent section.

### **4.3.3 Compositional Effects**

**4.3.3.1 Experimental Overview** Five disc shaped superalloys were used to examine the effect of superalloy substrate on the oxidation characteristics of the bond coat: Inconel 718 (IN718), Inconel 738 (IN738), René N5 (N5), Haynes 188 (HA188) and Mar M 509 (MM509). This group of superalloys was selected to represent the wide variety of superalloys used in industry today ranging from disc materials and combustor materials to blade alloys. The discs were 25mm in diameter and 3mm thick. In some cases the specimens were cut into quarters to provide more specimens for cycling. The specimens were coated on one side with a dual layer NiCoCrAlY bond coat at Praxair Surface Technologies (Indianapolis, IN) by argon-shrouded plasma spraying. After deposition, the bond coats were given a four hour heat treatment at 1080°C. This produced a microstructure consisting of two phases,  $\beta$ -NiAl phase ( $B_2$  structure)

and a solid solution  $\gamma$ -Ni phase ( $A_1$  structure). The nominal compositions of the materials used are listed in Table 4 and the starting microstructure of the bond coat is shown in Figure 153.

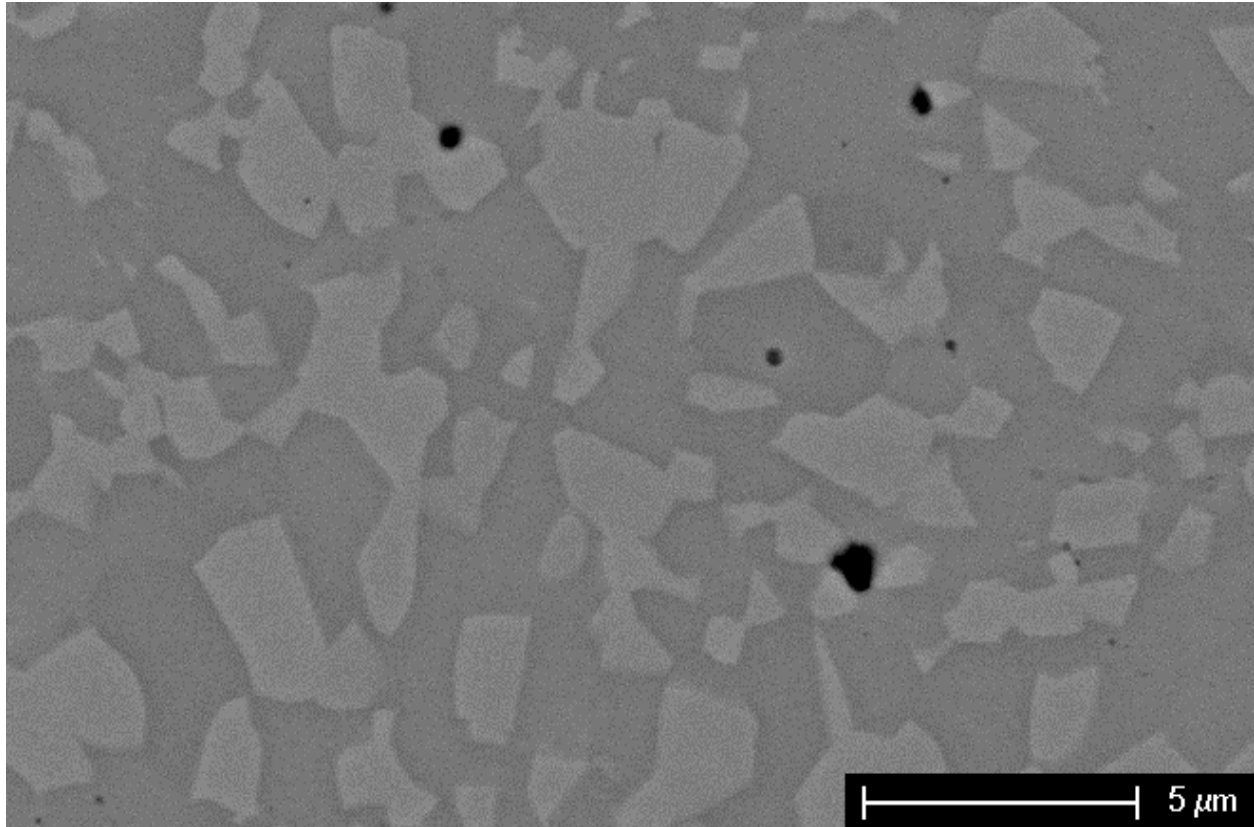


**Figure 153 - Starting microstructure of  $\beta$ - $\gamma$  NiCoCrAlY bond coat. Dark grey phase is the  $\beta$ -phase and the lighter regions are  $\gamma$ -phase. The black regions are pores within the bond coat.**

The specimens were thermally cycled in a bottom loading furnace that heated the specimens to 1100°C in 10 minutes, held them at this temperature for 45 minutes and then cooled them to 45°C in 10 minutes using forced air cooling. The specimen testing details, including bond coat type and number of cycles are listed in Table 15.

**Table 15 - Number of cycles the bond coat only specimens were cycled to and examined.**

Substrate	Bond Coat Type	Cycles Specimens Were Examined
Inconel 718	Dual Layer	0, 60, 180, 300 and 500*
Inconel 738	Dual Layer	0, 60, 180, 300 and 500*
René N5	Dual Layer	0, 60, 400, 500 and 1000*
Haynes 188	Dual Layer	0, 60, 400, 500 and 1000*
Mar M 509	Dual Layer	0, 60, 180, 300 and 500*
* Asterisks indicate full-sized specimens (25mm discs) while all others were one quarter specimens		

Five specimens were tested for each substrate/bond coat combination. The test duration for the IN718, IN738 and MarM509 specimens was limited to 500 cycles because the uncoated portions of the substrates were experiencing rapid degradation at this temperature. It should be noted that in typical applications, IN718 and MM509 do not experience temperatures higher than 600-700°C so the rapid degradation at 1100°C is not surprising. Exposure of these alloys to such high temperatures is justified for several reasons. First, these two alloys, along with the other three (IN 738, Haynes 188 and René N5), cover a wide range of CTEs which is one variable which is targeted in this study as it has already shown an influence on the TBC lifetime [2]. Second, the five alloys chosen provide a wide variation in the potential for interdiffusion with the bond coat which is representative of the various superalloys in service today. Finally, many new 3rd, 4th, and 5th generation superalloys would also experience rapid degradation if left uncoated at these elevated temperatures [19] thus IN718 and MM509 are representative of these alloys with respect to high temperature degradation.

Specimens were imaged every 20-40 cycles using a high resolution scanner (4800dpi with 96-bit color depth) to monitor surface degradation. After the specimens reached their prescribed number of thermal cycles, their surfaces were examined with a scanning electron microscope (SEM) and with glancing angle surface x-ray diffraction (XRD) was performed using an incidence angle of  $1.0^\circ$ . Cross-sectional microscopy was also performed again using a SEM equipped with a EDS capabilities.

Aluminum depletion in the bond coat was estimated by measuring the extent of the depletion of the aluminum-rich  $\beta$ -phase.  $\beta$ -phase depletion occurs in the bond coat, which has a two phase  $\beta(\text{Ni,Co})(\text{Al,Cr}) - \gamma(\text{Ni,Co})$  structure, when aluminum is consumed by either interdiffusion with the substrate or by growth of an alumina TGO. The  $\beta$ -phase essentially acts as the reservoir of aluminum, so depletion can be quantified by the rate of dissolution of this phase. To do this, three SEM micrographs were taken of each specimen at 250X magnification. Then, in the case of depletion due to substrate interdiffusion, the distance between the bond coat-substrate interface and the nearest  $\beta$ -phase grain was measured in ten separate areas on each micrograph giving a total of 30 measurements which were then averaged together. The same procedure was used to measure  $\beta$ -phase depletion due to TGO formation. This, however, was more complicated because the bond coats did not have a smooth continuous surface. These dual layer bond coats contained numerous surface connected pores which made locating the true external surface (which is necessary for the measurement) difficult and consequently introduced additional error into the measurements.

**4.3.3.2 Compositional Results and Discussion: Aluminum Depletion** The solid lines in Figure 154 show the results for the  $\beta$ -phase depletion due to substrate interdiffusion and the dashed lines show the depletion from TGO growth as a function of exposure time at 1100°C.

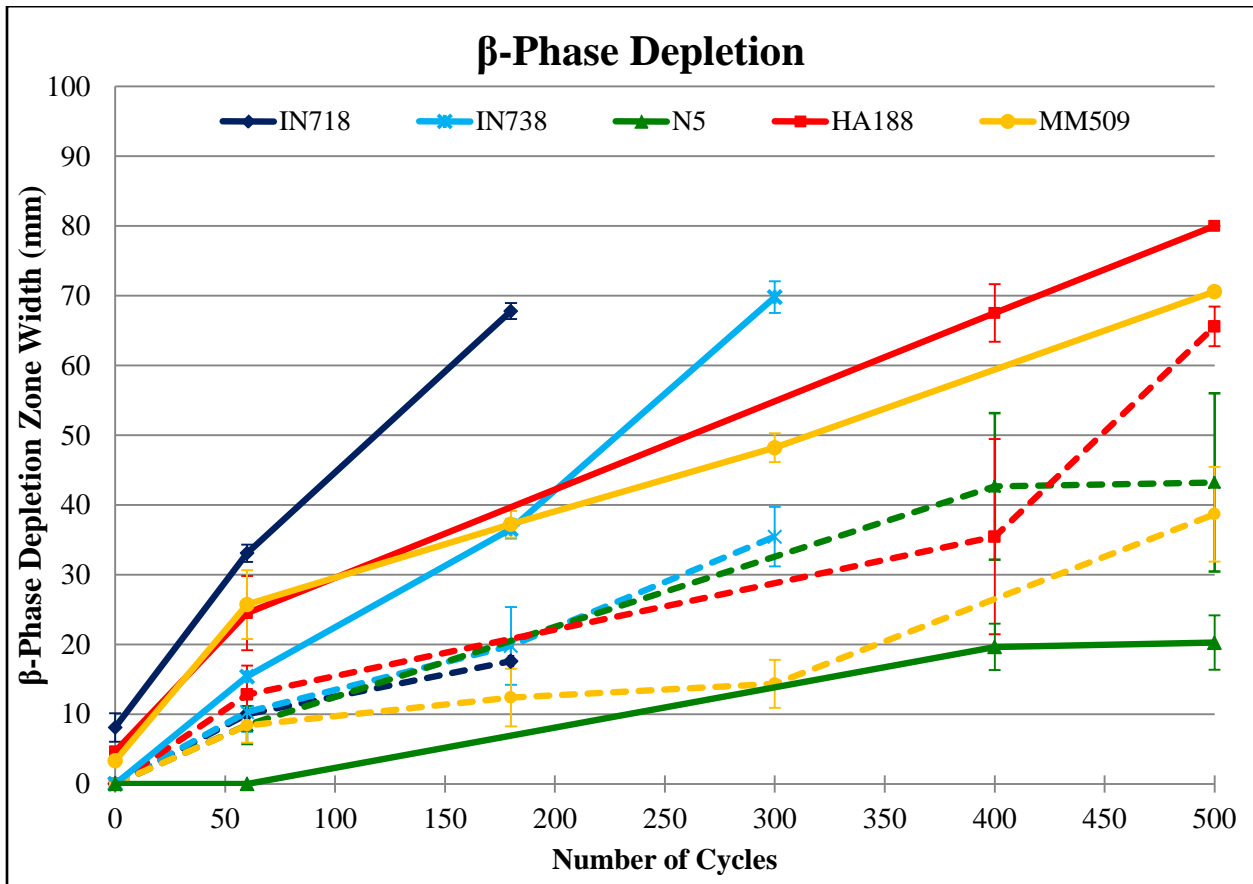


Figure 154 - Depth of  $\beta$ -phase depletion zone as a function of thermal cycles. Solid lines represent depletion due to interdiffusion and the dashed lines represent depletion due to TGO formation.

The rate of aluminum depletion due to substrate interdiffusion was highest in IN718 followed by IN738 then HA188 and MM509, which had similar rates, and finally by N5 with the slowest rate.

To understand this behavior, it is first important to examine the starting conditions of these diffusion couples and then identify the parameters controlling the flux of aluminum between the bond coat and the superalloy. In each of these diffusion couples, a two phase NiCoCrAlY bond coat ( $\beta$ - $\gamma$ ) is coupled to either a  $\gamma$ -phase nickel-based superalloy (IN718), a  $\gamma$ -phase cobalt-based superalloy (HA188 and MM509), or to a  $\gamma$ - $\gamma'$  nickel-based superalloy (IN738 and N5). The second starting condition to take note of is the aluminum concentrations in the superalloys. Both HA188 and MM509 have no aluminum and IN718, IN738 and N5 nominally have 1, 7.8 and 13.4at%, respectively.

The kinetic and thermodynamic parameters controlling the flux of aluminum between the bond coat and the superalloy are numerous, especially when taking into account the complex compositions of these alloys (Table 4). However this complexity can be reduced by assuming these alloys behave like ternary alloys of either Ni-Cr-Al or Co-Cr-Al compositions. Fick's 1st law for the flux of aluminum in a ternary alloy then becomes Equation 11.

$$J_{Al} = -D_{AlAl}^{Ni,Co} \frac{\partial C_{Al}}{\partial X} - D_{AlCr}^{Ni,Co} \frac{\partial C_{Cr}}{\partial X}$$

**Equation 11**

Where D is the diffusivity, C is the concentration and X is the distance in the diffusion direction. With regard to the diffusivity term, the superscript identifies the host/solvent material (i.e. base alloy element), the first subscript specifies the diffusing element (aluminum) and the second subscript specifies the gradient field the diffusing element is responding to. The main diffusion term, or direct term which in this case is  $D_{AlAl}$ , is the diffusivity of aluminum due to an aluminum concentration gradient and the cross diffusion term, or indirect term which in this case

is  $D_{AlCr}$ , is the diffusivity of aluminum in a chromium gradient. Depending on the sign of the cross term, this contribution may be positive or negative whereas  $D_{AlAl}$  is always positive. Likewise, the direction of the flux of aluminum will be dependent on both the sign and magnitude of the concentration gradient of the aluminum and chromium. Finally, it should be pointed out the diffusivity is dependent on the host matrix (base alloying element) so this detail must not be overlooked.

Having established these basic parameters, the experimental results can be discussed. For the superalloys with little or no aluminum, IN718, HA188 and MM509, the rate of depletion was faster with IN718 (nickel based) than with HA188 and MM509 (cobalt-based). A literature survey provided diffusion data for ternary Ni-Cr-Al and Co-Cr-Al alloys at 1100°C which is presented in Table 16.

**Table 16 - Diffusion coefficients for ternary Ni-Cr-Al and Co-Cr-Al alloys.**

Diffusion Coefficients at 1100°C		
	$D_{AlAl}$ (cm <sup>2</sup> /sec)	$D_{AlCr}$ (cm <sup>2</sup> /sec)
Co-11at%Cr-4at%Al [78]	0.50E-10	0.60E-11
Ni-11at%Cr-4at%Al [79, 80]	1.60E-10	4.00E-11

In both alloys, the main terms are about an order of magnitude larger than the cross terms indicating the primary driving force for aluminum diffusion is the aluminum concentration gradient and rules out any significant influence of chromium concentration gradients that may exist. Next, in the case where the chromium and aluminum concentrations are identical and the

only difference is the base alloying element, the main diffusion term is almost four times larger in the nickel based alloy than the cobalt based alloy.

Given these findings and that the aluminum concentration gradient between the bond coat and the three superalloys are essentially identical, the difference in the flux of aluminum depletion between the cobalt and nickel alloys must be due to the differences in the diffusivity of aluminum brought about by the different base alloying elements. There could also be further reductions in the diffusivity of aluminum in the two cobalt-based superalloys from solid solution interactions through the additions of tungsten.

Moving to the nickel-based alloys, the rate of depletion was largest in IN718 followed by IN738 and N5. Since they are all nickel-based alloys, the diffusion coefficients should be similar from one alloy to the next so the remaining terms in Equation 11 that could account for this flux behavior are the concentration gradient terms. It was previously stated the cross terms are an order of magnitude smaller than the main terms so again the chromium gradient contribution to the overall flux should be minimal. Following from this, the only remaining term is the aluminum concentration gradient that exists between the bond coat and the superalloy. This gradient is largest in IN718 followed by IN738 and then N5. This ordering agrees with the experimental results indicating the concentration gradient is the likely cause of the differences in aluminum flux in the nickel-based alloys.

The rate of depletion caused by TGO growth, dashed lines in Figure 154, did not seem to depend on the substrate material, especially after a short number of cycles (< 60 cycles), which is evident by the tight grouping of the dashed lines in the figure. This suggests that substrate elements, such as niobium or tantalum, which were found to have diffused into the bond coat, did not have a significant influence on the TGO growth rate and subsequently the rate of

phase depletion. At these early stages, the aluminum depletion due to TGO growth was independent of substrate material.

When comparing aluminum depletion due to interdiffusion and TGO growth, interdiffusion dominated in the cases of IN718, IN738, MM09 and HA188. In fact, the substrate interdiffusion was far more detrimental to the overall aluminum depletion than the growth of the TGO. In the case of René N5 the difference between the rates of the two mechanisms was far less significant which is attributed to the higher aluminum concentration in N5 than in the other superalloys.

**4.3.3.3 Compositional Results and Discussion: Oxide Formation** Figure 155 contains high resolution scanned images of the specimens after 0, 60, 180, 300, 420 and 500 cycles.

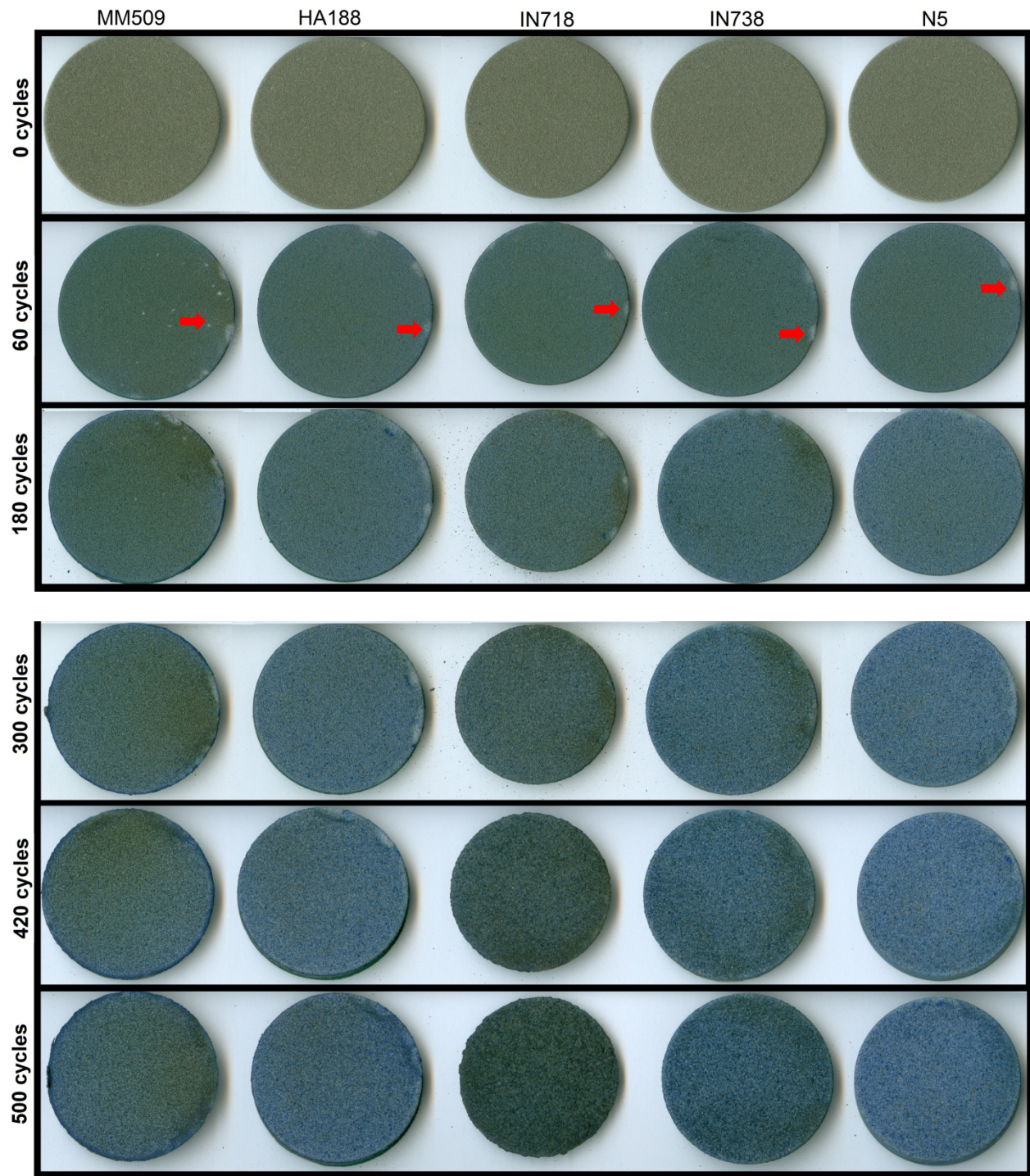
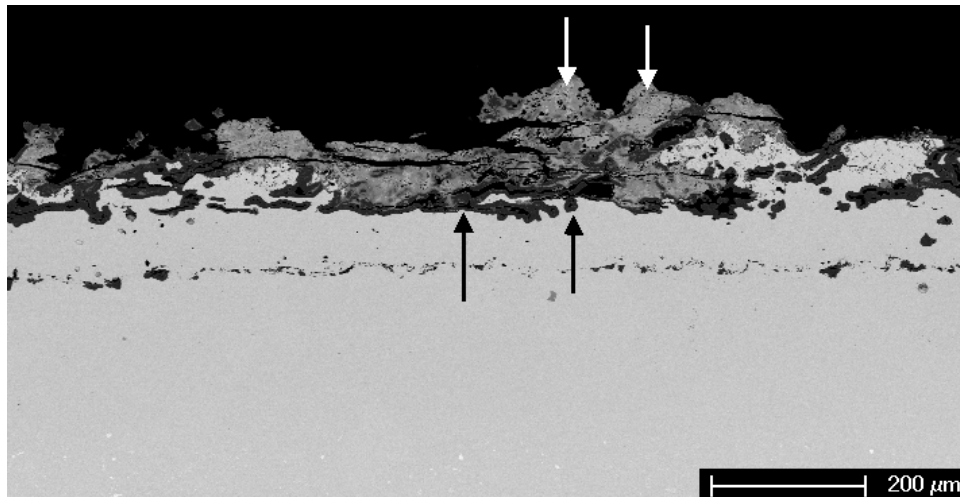


Figure 155 - High resolution images of the surfaces of the specimens for various number of cycles. Red arrows point out some of the marks left by the ceramic trays the specimens are placed in during thermal cycling.

The white marks that appear on the specimens (red arrows in Figure 155) are marks left by the ceramic trays which supported the specimens during the thermal cycling in the bottom loading furnace.

After 60 cycles the specimens appeared identical. Both surface and cross-sectional microscopy confirmed this as well as a visual inspection of the surfaces in Figure 155. The TGO consisted of  $\alpha$ -alumina with small isolated areas of nickel, chromium, and aluminum mixed oxides. These non-alumina oxides are most likely transient oxides formed during the first few thermal cycles. Based on these observations, the early stages of oxidation are independent of substrate material.

After 500 cycles, significant changes occurred in the oxide scale on the IN718 specimen. Visually, the specimen's size has reduced slightly due to scale spallation and the color has changed to a dark green with black spots. Surface EDS (standardless) indicated the presence of nickel and chromium rich oxides along with the alumina. A cross-sectional image of this specimen is shown in Figure 156.



**Figure 156 - Cross-section of IN718 specimen after 500 cycles. White arrows indicate oxides rich in Ni, Co, Cr, Nb, and Fe and the black arrows point out  $\text{Al}_2\text{O}_3$ .**

The dark regions in the TGO, indicated by the black arrows, are alumina and the light-appearing oxides, indicated by the white arrows, were rich in nickel, chromium, and cobalt with traces of niobium and iron. Based on the structure of the dual layer bond coat and the location and composition of the oxide scale after 500 cycles, it appears the base metal in the outer layer of the bond coat has completely oxidized, forming a layer of Ni, Cr, and Co rich oxides. Standardless EDS measurements made during SEM characterization revealed the composition of the bond coat material below the outer oxidized layer was almost completely depleted of aluminum.

For the IN718 specimens, it is proposed that the combination of rapid depletion of aluminum due to substrate interdiffusion, oxidation of the porous outer region of the bond coat and cracking and healing occurring in the undulating TGO during thermal cycling all caused the bond coat aluminum content to drop below the minimum concentration needed to maintain an alumina scale. This then resulted in the oxidation of the base metal in the bond coat. This series of events is often referred to as chemical failure of the bond coat, or the point at which an

alumina scale can no longer form resulting in the formation of less protective oxides [40]. Furthermore, since it is likely the chemical failure was influenced/enhanced by the mechanical damage to the TGO during thermal cycling, the more accurate term of mechanically-induced chemical failure is the better fitting nomenclature [40]. Based on the timeline of all of the observations, it appears the IN718 specimens experienced chemical failure somewhere between 300 and 500 cycles. Comparing this with the lifetime of the 375  $\mu\text{m}$  TBCs on IN718, 420 cycles (taken from Figure 150), reveals the two events occurred at nearly the same number of cycles. This supports the literature sources that link the formation of these non-protective oxides to the failure of the TBCs [33, 38, 40, 44].

After 500 cycles, the testing of IN738 and MM509 specimens were stopped because the substrate oxidation was too severe due to excessive scale spallation during the thermal cycling. Cross-sections of the IN738 revealed isolated breakdown of the bond coat where, in certain regions, the base elements in the bond coat were oxidizing while other regions of the bond coat still had enough aluminum to sustain and re-heal an alumina TGO. The bond coat on the MM509 substrate was not in chemical failure. Instead the surface was still primarily alumina and the aluminum content was at an acceptable level. Had it not been for the severe substrate oxidation, this bond coat would have been able to continue thermal cycling.

The bond coats on HA188 and N5 also visually showed significant changes after 500 cycles. XRD and cross-sectional microscopy revealed the TGO was primarily alumina but with isolated areas of nickel, chromium and aluminum spinel oxides. Extensive cracking in the alumina TGO was also observed in both specimens.

After 1000 cycles the HA188 specimen, Figure 157, visually appeared similar to the IN718 bond coat after 500 cycles.

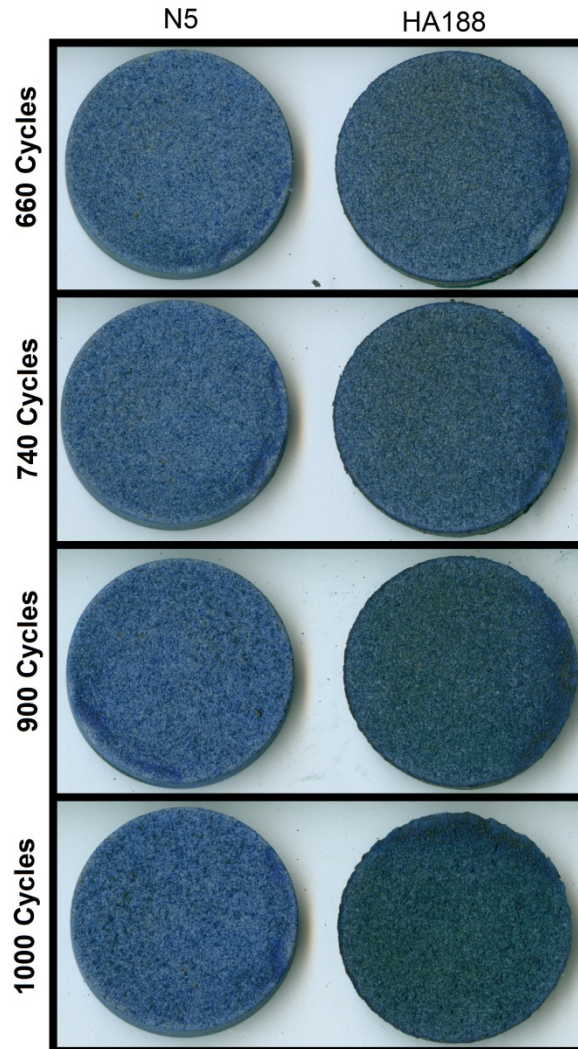


**Figure 157 - High resolution scanned images of HA188 and N5 specimens after a set number of cycles.**

The surface EDS (standardless) indicated the presence of nickel, chromium, cobalt, and aluminum rich oxides. As with the IN718 specimen, the outer layer of the dual layer bond coat on HA188, seen in Figure 158, is almost completely depleted of aluminum with approximately 1wt%Al remaining (determined by standardless EDS analysis during SEM observation), and Ni, Cr, and Co rich oxides were present throughout the TGO (white arrows).

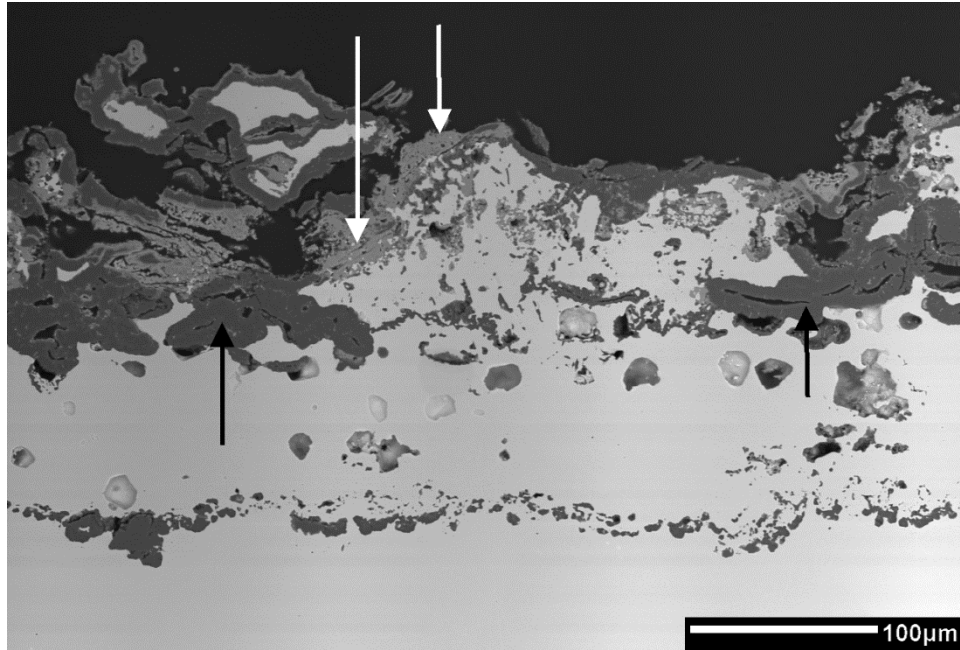


**Figure 158 - HA188 specimen with 1000 cycles. White arrows indicate non-aluminum oxides and the black arrows point to the aluminum oxides.**

The presence of these oxides and the low aluminum content in the bond coat indicate mechanically induced chemical failure has occurred or is in the process of occurring. Comparing the time to chemical failure with the lifetime of the 375  $\mu\text{m}$  TBC on HA188, 793 cycles, there is again generally good agreement between the two events. This further supports the relationship between the formation of non-alumina oxides and TBC failure being linked [33, 38, 40, 44].

After 1000 cycles, the dual layer bond coat on N5 still had an alumina TGO, however, there were numerous isolated regions in the outer region of the bond coat that contained Ni, Cr, Co spinel oxides which are highlighted by white arrows in Figure 159.

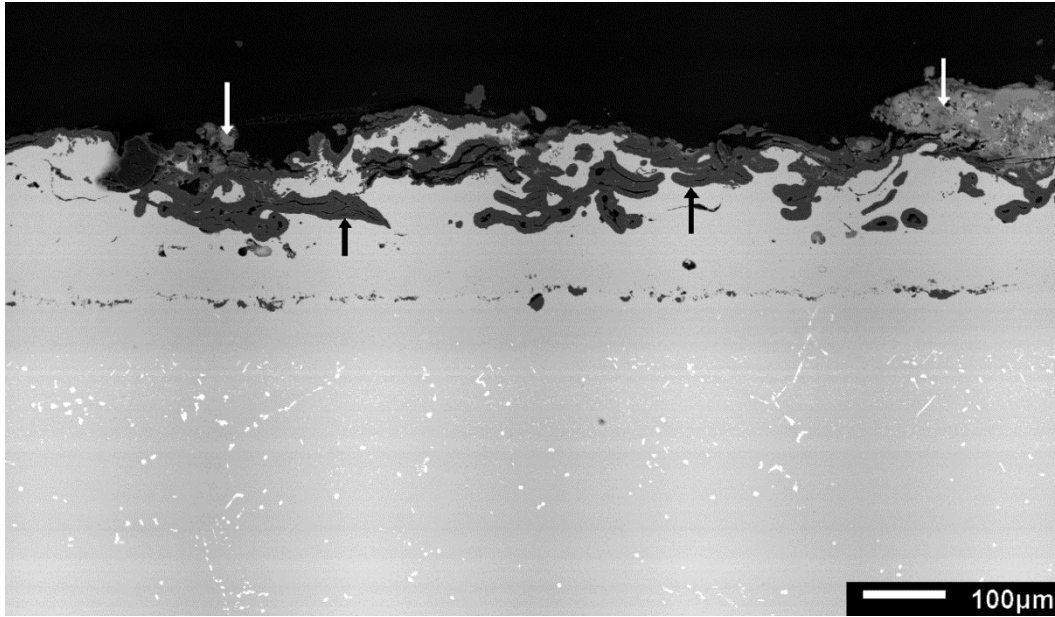


**Figure 159 - N5 specimen after 1000 cycles. White arrows indicate non-aluminum oxides and the black arrows indicate aluminum oxide.**

Below these spinel regions in the dense portion of the bond coat, the aluminum content was between 3.0-6.0at%. This amount of aluminum is close to the amount required to reform an alumina TGO if scale cracking/spallation occurs and well above the required amount needed to sustain the growth of an established adherent alumina scale [40].

It is proposed these isolated regions of spinel oxide are a byproduct/drawback of the dual layer bond coat structure. More specifically, during high temperature exposure, the surface connected pores in the outer layer oxidize and form a TGO as does the external surface of the bond coat. Thus the bond coat material in the outer region is depleted of aluminum by scale formation on the pore surfaces and the external surface. Normally the aluminum content in the outer region is replenished by the bulk of the coating however as the pores oxidize and consume aluminum, the supply to the external surface gradually decreases. Over time, these outer regions become isolated from the bulk of the coating (white arrows in Figure 159). Once isolated, it is a

matter of time (i.e. thermal cycles) until chemical failure, whether it be intrinsic or mechanically induced, occurs. These isolated regions are analogous to the “diffusion cell” concept introduced by Evans et al [40] for the case of air plasma bond coats and argon-shrouded plasma sprayed bond coats. In their model, regions of the bond coat become isolated from the bulk of the coating due to oxidation of the molten bond coat particles during deposition. This produces isolated diffusion cells throughout the coating. During subsequent oxidation, the aluminum content in these cells decreases as the TGO grows. Since these cells are cut off from the bulk of the coating, the aluminum content decreases without replenishment from the bulk. Eventually, due to kinetic and thermodynamic limitations, alumina is no longer the stable oxide and other less protective oxides form [40].

This scenario is unlike the cases for HA188 and IN718 because the bond coat on the N5 specimen still contained 3.0-6.0at% aluminum. So instead of complete chemical failure of the bond coat, as it was with the IN718 and HA188 specimens, only isolated chemical failure occurred with the N5 specimen.

When the time to isolated chemical failure is compared to the time to failure of the TBCs on N5 with dual layer bond coats, 850 cycles, there is again generally good agreement between the two events. This indicates that localized chemical failure is sufficient to contribute to TBC failure. Likewise, these findings suggest the dual layer bond coats, even when paired with an alumina forming substrate alloy, will have an upper limit to lifetime which is brought about by rapid aluminum depletion in the outer portion of the coating.

#### 4.3.4 Substrate Effect Summary

This body of work in combination with previous work [2] experimentally showed superalloy substrate selection influences the lifetime of both thick and thin TBCs. With thick TBCs (1100  $\mu\text{m}$ ), CTE mismatch between the substrate and the topcoat proved to be a key factor in the lifetime of the TBCs especially in the case of TBCs on IN718 which had the largest CTE of all the alloys tested. These TBCs failed only after an average of 87 cycles. The results from complementary composition effect experiments, which focused on the compositional roles of the substrate-bond coat interactions, supported the assumption that after 60 to 80 cycles the bond coat oxidation was the same for all specimens, regardless of the substrate material. This effectively supported the experimental finding that CTE mismatch between the substrate and the topcoat can play a primary role in the TBC lifetime.

For thin and thick TBCs on low-CTE superalloys, where failure occurred at the topcoat/TGO/bond coat interface, compositional effects of the substrate were dominant. The primary influence of the substrate alloy was the rate at which aluminum in the bond coat diffused into the substrate. In all alloy systems, except for N5, the amount of aluminum lost due to interdiffusion with the substrate was far more than that lost to growth of the TGO. The rate of interdiffusion was dependent on both the base alloying element and on the aluminum concentration gradient between the bond coat and the substrate. Larger aluminum losses were observed for nickel-based superalloys than for cobalt-based alloys (in the presence of similar aluminum concentration gradients) which was a result of a larger aluminum diffusivity in nickel-based alloys than in cobalt based alloys. For the nickel based alloys, the rate of depletion was also heavily dependent upon the aluminum content of the substrate, where lower substrate contents were associated with larger fluxes of aluminum into the substrate.

In the end, a combination of substrate interdiffusion, TGO formation and cracking and healing of the TGO during thermal cycling led to the chemical failure of the bond coats, whether it was an isolated or complete form of chemical failure. Chemical failure of the bond coat was characterized by the prolific formation of non-aluminum oxides which are brittle, have faster growth kinetics and are outward growing oxides. All of these attributes are detrimental to the toughness of the bond coat/TGO/topcoat interface and therefore to the lifetime of TBC systems. The time until complete chemical failure of the bond coat could be extended by pairing the bond coats with an aluminum containing or a cobalt-based superalloy, however isolated chemical failure, brought about by the porous nature of these bond coats, seems to be an inherent drawback of the dual layer bond coat. Based on these observations, it seems all TBCs with this type of bond coat have an upper limit to their lifetime which is dictated by the time until some form of chemical failure can occur.

## 5.0 CONCLUDING REMARKS

Throughout the course of this study, a variety of TBC system variables were investigated. Some of the research was focused on how a particular variable influenced the lifetime of a TBC (bond coat roughness, topcoat thickness, substrate CTE, topcoat porosity, topcoat microstructure) while other research focused on better understanding one aspect of the TBC system and how it developed during testing (YSZ purity – sintering behavior, substrate – bond coat interactions). As a result of so many variables being investigated, it became apparent some of them had a more pronounced influence on the lifetime than others.

Bond coat roughness was one of those variables which had a relatively strong influence on the lifetime of TBCs. The large asperities on the surfaces of the DL and 50:50 bond coats hindered the growth and coalescence of cracks which then prolonged the life of the TBC. Additionally, in the rough bond coat specimens, the final delamination crack extended through both the TGO and the low-density YSZ whereas in the smoother bond coats, fracture occurred almost entirely in the TGO. The low-density YSZ, being more compliant than the TGO, was able to slow crack extension and prolong the lifetime of the rough bond coat TBCs. In this case, the compliance of the low-density YSZ was vital to the TBC's lifetime. Had the topcoat been denser, less compliant, or even too porous, then the added benefits of the fracture taking place in the topcoat may have been negated. This sensitivity of TBC lifetime to topcoat density was demonstrated in Section 4.1.3.1 where TBCs with different starting densities had different

lifetimes despite having similar bond coats, substrates and topcoat thicknesses. A density of 85% the theoretical density of 7YSZ offered the longest FCT lifetime while increasing or decreasing the density beyond this value resulted in shorter FCT lifetimes. The reason being, a denser topcoat is too rigid and lacks the compliance needed to accommodate thermal stresses whereas a less dense topcoat has insufficient strength and stiffness to resist crack growth [15].

The interaction between these two parameters (roughness and topcoat density) highlights an important point. Under non-optimized conditions, the topcoat density and bond coat roughness may separately have only modest influences on TBC lifetime. Take as an example a set of hypothetical TBCs all of which have the same substrate material, N5, and the same bond coat type, a smooth, single-layer NiCoCrAlY bond coat. Applying either a low-density (85%), high density (89%) or ultra-low-density (82%) topcoat to this system with the purpose of trying to produce the longest lifetime would be futile because all three would likely fail for the same reason – because the bond coat was too smooth. Here, the non-optimized parameter, bond coat roughness, limited the overall performance of the system and essentially masked the potential influence of the other system parameters.

Topcoat density had a similar interaction with the effect of topcoat thickness. Of the wide range of topcoat thicknesses tested in this body of work, the thickest TBCs failed within the topcoat because the strain energy release rate was larger than the interfacial toughness of the topcoat material. Thinner topcoats, having a smaller energy release rate than the YSZ toughness, failed at the TGO-topcoat interface after a larger number of cycles and due to bond coat oxidation related damage. Here, the interfacial toughness of the topcoat separated the two failure types. Considering this, a topcoat with an ideal amount of porosity, compliance and toughness may be able to suppress the first mechanism (topcoat failure) thereby extending the lifetime of

the coating. In fact, this type of topcoat could even be deposited in larger thicknesses without suffering the first type of failure. Conversely, a topcoat which is too dense could fail by the first mechanism even at smaller thicknesses. This behavior was observed in the two 1100  $\mu\text{m}$  topcoats on N5 (Figure 100) where the 85% dense TBC failed due to bond coat oxidation (second mechanism) after 520 cycles and the 89% dense TBC (too dense) failed within the topcoat (first mechanism) after 123 cycles.

For the array of topcoat thicknesses specimens investigated in this study, had the topcoat density been optimized from 82% dense to 85% dense, the thickness effect could have been more pronounced than it already was. This could have potentially changed the slope of the fit line in Figure 74 (Thickness-TBC Lifetime graph) and changed the threshold thickness which separated the two types of failures (i.e. topcoat failure or TGO-topcoat interfacial failure). Likewise, swapping out the low-density YSZ for the DVF topcoat material could have also changed this relationship since the DVF coatings are more compliant than the low-density coatings.

Following the same logic but now considering the interplay between topcoat thickness and superalloy CTE, had the superalloy been designed to have a smaller CTE, then the thermal stresses present in the topcoat could have been reduced thereby minimizing the strain energy release rate. This in turn could influence the thickness threshold separating the two failure types along with the general thickness-lifetime relationship as it did with the 1100 $\mu\text{m}$  85% dense topcoats on Inconel 718, Haynes 188 and N5 (Figure 150). In this case, the superalloy with the largest CTE, IN718, failed within the topcoat whereas the other two, which had low CTEs, failed due to bond coat oxidation. While this approach is not very practical (being that superalloy design is primarily concerned with high temperature strength) it does demonstrate the importance

of the interactions between systems parameters and their subsequent influence on the TBC failure mechanisms.

Other influences of the substrate superalloy on the lifetime of TBCs, besides CTE effects, were the compositional effects. The loss of bond coat aluminum due to interdiffusion with the substrate was found to be just as detrimental as the loss of aluminum due to TGO growth. The interdiffusive flux of aluminum was reduced when the dual layer bond coats were paired with either cobalt-based superalloys ( $D_{CoAl} < D_{NiAl}$ ) or nickel-based superalloys containing aluminum (reduced  $dC_{Al}/dX$ ). However, even when the interdiffusion was minimized (as was the case for the N5-bond coat couples), the oxidation resistance of the dual layer bond coat was limited by its porous outer layer which suffered isolated chemical failure despite having enough aluminum in the bulk of the bond coat to sustain and/or reform an alumina TGO. So here, a non-optimized parameter, bond coat morphology, limited the potential influence of another system parameter, substrate composition.

Again, with the bond coat roughness, the 50:50 bond coat specimens were observed to have the longest FCT lifetimes despite providing minimal chemical protection to the superalloys and having the worst oxidation performance (i.e. fastest aluminum depletion rate). In contrast, the SL bond coat specimens provided the best chemical protection to the superalloy and they exhibited the best oxidation behavior (i.e. slowest aluminum consumption rate) yet they had the worst FCT lifetimes. These findings appear to suggest bond coat oxidation performance had less of an influence on TBC lifetime than did bond coat roughness. However, this only may partially be valid because the surface roughness was not optimized for the SL bond coat. Thus the bond coat roughness may have skewed the impact of bond coat oxidation performance on TBC lifetime.

The densification rates of free-standing topcoats exhibited a dependency on the purity of the YSZ powder. Ultra-pure YSZ topcoats had negligible densification rates at 1200°C whereas coatings with higher silica and/or alumina contents (>0.1wt%) exhibited an increase in the density after 100 hours. At 1300°C, all of topcoats densified but the high purity coatings still densified less than the impure coatings. The starting microstructure also seemed to have an influence on the sintering rate where the HP-DVF coating experienced more densification than the HP-LD coating despite having similar, though not identical, impurity contents. Regardless of purity level, microstructural changes occurred in all of the coatings during the thermal exposures. Micro-cracks closed, pores grew and delamination cracks bridged in all four of the coatings, but to different extents. While the direct impact of YSZ purity on TBC lifetime is difficult to judge, some speculation can be made regarding their thermophysical properties. Based on the observed microstructural changes, the conventional purity coatings likely would have exhibited a large increase in the thermal conductivity and elastic modulus. In the FCT tests, the thermal conductivity has minimal influence on coating performance because the test is isothermal, however, an increase in the stiffness of the coating could be detrimental to the lifetime of the TBCs, especially the thick TBCs, which tended to fail within the topcoat.

Lastly, it should be emphasized a majority of the variables discussed in this work have been optimized for the purpose of FCT testing at 1100°C. It is possible a change in temperature or thermal exposure type could yield different optimum TBC system parameters. In other words, a variable optimized for FCT testing at 1100°C may not perform as well in another testing condition. An example of this was the difference in the FCT and JETS performance of the dual TBC. In FCT testing, the dual TBC exhibited the best overall performance of any TBC tested to date, but in the JETS testing, this same TBC exhibited poor performance.

Finally, it should be emphasized that certain TBC system variables such as bond coat roughness, topcoat density and topcoat microstructure influenced the lifetime more than others. Furthermore, strong interactions between the variables were also observed indicating the system is more complex than – one variable, one effect. Instead, the variables are intertwined. When one is altered, others can be affected.

## 6.0 SUGGESTED FUTURE WORK

Numerous variables were investigated in the body of this work however there were a few that require more investigating. The porosity/density of the topcoat was observed to have a profound influence on the lifetime of the TBCs which was believed to be a result of the toughness being different for the coatings. There is a possibility that other factors such as coating residual stress or At the very least, it would be beneficial to determine if there was an optimum density that maximized both the FCT and JETS lifetime.

Numerous variables were investigated in the body of this work however there were a few that require more investigating.

The porosity/density of the topcoat was observed to have a profound influence on the lifetime of the TBCs which was believed to be a result of the toughness being different for the coatings. There is a possibility other factors such as coating residual stress, statistical variations in bond coat roughness or inconsistencies in the testing procedures which could have factored into these results. Thus, it would be beneficial to determine if there was an optimum density that maximized both the FCT and JETS lifetime by systematically preparing and testing TBCs with different starting densities spanning a wide range of values with small enough increments to yield a high enough resolution. Experimentally speaking, it would also be beneficial to minimize the variables by preparing all of the specimens in one batch and testing them at the same time.

Furthermore, multiple thicknesses of topcoats could be prepared in attempts to test for cross effects between the two variables (density and thickness)

It would also be scientifically beneficial to attempt to characterize the microstructure of the coatings not only with density measurements (oil infiltration) but with a more robust measurement method such as image analysis or mercury porosimetry in attempt to characterize what type of porosity is present. Each of these methods has its drawbacks however they yield more information than just a bulk density value. Analogous studies have been performed studying the microstructure – thermal conductivity relationship of topcoats [13, 14, 81]. The key to these studies is the characterization of the microstructure and the close control over the spraying parameters during the deposition process.

In addition to TBC specimens, sintering tests with free-standing topcoats could be used provide information on the stability of these topcoats as they are exposed to high temperatures. As indicated in Section 4.1.1.3.1, the starting microstructure seemed to influence the sintering rate of these coatings.

## BIBLIOGRAPHY

1. Feuerstein, A., J. Knapp, T. Taylor, A. Ashary, A. Bolcavage and N. Hitchman, *Technical and Economical Aspects of Current Thermal Barrier Coating Systems for Gas Turbine Engines by Thermal Spray and EBPVD: A Review*. Journal of Thermal Spray Technology, 2007. **17**(2): p. 199-213.
2. Helminiak, M.A., *Factors Affecting the Lifetime of Thick Air Plasma Sprayed Thermal Barrier Coatings*, in *Mechanical Engineering and Materials Science 2010*, University of Pittsburgh: Pittsburgh. p. 140.
3. Traeger, F., Ahrens, M., Vaßen, R. and Stöver, D., *A life time model for ceramic thermal barrier coatings*. Materials Science and Engineering A, 2003. **358**(1-2): p. 255-265.
4. Vaidyanathan, K., E.H. Jordan, and M. Gell, *Surface geometry and strain energy effects in the failure of a (Ni, Pt)Al/EB-PVD thermal barrier coating*. Acta Materialia, 2004. **52**(5): p. 1107-1115.
5. Birks, N., G.H. Meier, and F.S. Pettit, *Introduction to the high-temperature oxidation of metals*. Second Edition ed2006, New York: Cambridge University Press.
6. Young, D.J., *High Temperature Oxidation and Corrosion of Metals*. 1st ed2008: Elsevier. 574.
7. Kawagishi, K., et al., *The oxidation properties of fourth generation single-crystal nickel-based superalloys*. JOM, 2006. **58**(1): p. 43-46.
8. Pint, B.A., J.R. DiStefano, and I.G. Wright, *Oxidation resistance: One barrier to moving beyond Ni-base superalloys*. Materials Science and Engineering: A, 2006. **415**(1-2): p. 255-263.
9. Wagner, C., *Theoretical Analysis of the Diffusion Processes Determining the Oxidation Rate of Alloys*. Journal of The Electrochemical Society, 1952. **99**(10): p. 369-380.
10. Wagner, C., *Reaktionstypen bei der Oxydation von Legierungen*. Zeitschrift für Elektrochemie, Berichte der Bunsengesellschaft für physikalische Chemie, 1959. **63**(7): p. 772-782.

11. Echsler, H., Renusch, D. and Schutze, M., *Bond coat oxidation and its significance for life expectancy of thermal barrier coating systems*. *Materials Science and Technology*, 2004. **20**: p. 307-318.
12. Fox, A.C. and T.W. Clyne, *Oxygen transport by gas permeation through the zirconia layer in plasma sprayed thermal barrier coatings*. *Surface and Coatings Technology*, 2004. **184**(2-3): p. 311-321.
13. Chi, W., S. Sampath, and H. Wang, *Microstructure–Thermal Conductivity Relationships for Plasma-Sprayed Yttria-Stabilized Zirconia Coatings*. *Journal of the American Ceramic Society*, 2008. **91**(8): p. 2636-2645.
14. Friis, M., C. Persson, and J. Wigren, *Influence of particle in-flight characteristics on the microstructure of atmospheric plasma sprayed yttria stabilized ZrO<sub>2</sub>*. *Surface and Coatings Technology*, 2001. **141**(2–3): p. 115-127.
15. Vaßen, R., F. Traeger, and D. Stöver, *Correlation between spraying conditions and microcrack density and their influence on thermal cycling life of thermal barrier coatings*. *Journal of Thermal Spray Technology*, 2004. **13**(3): p. 396-404.
16. Golosnoy, I., A. Cipitria, and T. Clyne, *Heat Transfer Through Plasma-Sprayed Thermal Barrier Coatings in Gas Turbines: A Review of Recent Work*. *Journal of Thermal Spray Technology*, 2009. **18**(5): p. 809-821.
17. McPherson, R., *A review of microstructure and properties of plasma sprayed ceramic coatings*. *Surface and Coatings Technology*, 1989. **39–40, Part 1**(0): p. 173-181.
18. Taylor, T.A., *U. S. Patent 5,073,433*, 1991.
19. Incropera, F.P. and D.P. DeWitt, *Fundamentals of Heat and Mass Transfer*. 5th ed 2002, New York: John Wiley & Sons. 981.
20. Ahmaniemi, S., et al., *Modified thick thermal barrier coatings: microstructural characterization*. *Journal of the European Ceramic Society*, 2004. **24**(8): p. 2247-2258.
21. Taylor, T.A., *Thermal properties and microstructure of two thermal barrier coatings*. *Surface and Coatings Technology*, 1992. **54–55, Part 1**(0): p. 53-57.
22. Guo, H.B., R. Vaßen, and D. Stöver, *Thermophysical properties and thermal cycling behavior of plasma sprayed thick thermal barrier coatings*. *Surface and Coatings Technology*, 2005. **192**(1): p. 48-56.
23. Ahrens, M., R. Vassen, D. Stover, S. Lampenscherf, *Sintering and creep processes in plasma-sprayed thermal barrier coatings*. *Journal of Thermal Spray Technology*, 2004. **13**(3): p. 432-442.

24. Choi, S.R., D. Zhu, and R.A. Miller, *Effect of Sintering on Mechanical Properties of Plasma-Sprayed Zirconia-Based Thermal Barrier Coatings*. Journal of the American Ceramic Society, 2005. **88**(10): p. 2859-2867.
25. Eaton, H.E., Novak, R. C., *Sintering studies of plasma-sprayed zirconia*. Surface and Coatings Technology, 1987. **32**(1-4): p. 227-236.
26. Goedjen, J.G., W.J. Brindley and R.A. Miller. *Sintering of Plasma-Sprayed Sol Gel Zirconia-Yttria as a Function of Silica Content*. in *8th National Thermal Spray Conference*. 1995. Houston, Texas: ASM International.
27. Miller, R.A., W.J. Brindley, J.G. Goedjen, R. Tiwari and D. Mess. *The Effect of Silica on the Cyclic Life of a Zirconia-Yttria Thermal Barrier Coating*. in *7th National Thermal Spray Conference*. 1994. Boston, MA: ASM International.
28. Paul, S., Cipitria, A., Golosnoy, I. O., Xie, L., Dorfman, M. R. and Clyne, T. W., *Effects of Impurity Content on the Sintering Characteristics of Plasma-Sprayed Zirconia*. Journal of Thermal Spray Technology, 2007. **16**(5): p. 798-803.
29. Tekeli, S., M. Erdogan, and B. Aktas, *Microstructural evolution in 8 mol% Y<sub>2</sub>O<sub>3</sub>-stabilized cubic zirconia (8YSCZ) with SiO<sub>2</sub> addition*. Materials Science and Engineering A, 2004. **386**(1-2): p. 1-9.
30. Vaßen, R., Czech, N., Malléner, W., Stamm, W. and Stöver, D., *Influence of impurity content and porosity of plasma-sprayed yttria-stabilized zirconia layers on the sintering behaviour*. Surface and Coatings Technology, 2001. **141**(2-3): p. 135-140.
31. Tsipas, S.A., *Effect of dopants on the phase stability of zirconia-based plasma sprayed thermal barrier coatings*. Journal of the European Ceramic Society, 2010. **30**(1): p. 61-72.
32. Timoshenko, S., *Analysis of Bi-Metal Thermostats*. J. Opt. Soc. Am., 1925. **11**(3): p. 233-255.
33. Schlichting, K.W., N. P. Padture, E. H. Jordan and M. Gell, *Failure Modes in Plasma Sprayed Thermal Barrier Coatings*. Materials Science and Engineering A, 2003. **342**(1-2).
34. Helminiak, M.A., et al., *The behavior of high-purity, low-density air plasma sprayed thermal barrier coatings*. Surface and Coatings Technology, 2009. **204**(6-7): p. 793-796.
35. Guo, H.B., R. Vaßen, and D. Stöver, *Atmospheric plasma sprayed thick thermal barrier coatings with high segmentation crack density*. Surface and Coatings Technology, 2004. **186**(3): p. 353-363.
36. Yanar, N., F. Pettit, and G. Meier, *Failure characteristics during cyclic oxidation of yttria stabilized zirconia thermal barrier coatings deposited via electron beam physical vapor deposition on platinum aluminide and on NiCoCrAlY bond coats with processing*

- modifications for improved performances. Metallurgical and Materials Transactions A*, 2006. **37**(5): p. 1563-1580.
37. Taylor, T.A. *Review of Thermally Sprayed Thermal Barrier Coating*. in *AMS International Surface Engineering Congress*. 2004. Orlando, FL.
  38. Rabiei, A. and A.G. Evans, *Failure mechanisms associated with the thermally grown oxide in plasma-sprayed thermal barrier coatings*. *Acta Materialia*, 2000. **48**(15): p. 3963-3976.
  39. Smialek, J.L., *Improved oxidation life of segmented plasma sprayed 8YSZ thermal barrier coatings*. *Journal of Thermal Spray Technology*, 2004. **13**(1): p. 66-75.
  40. Evans, H.E. and M.P. Taylor, *Diffusion Cells and Chemical Failure of MCrAlY Bond Coats in Thermal-Barrier Coating Systems*. *Oxidation of Metals*, 2001. **55**(1): p. 17-34.
  41. Di Ferdinando, M., Fossati, A., Lavacchi, A., Bardi, U., Borgioli, F., Borri, C., Giolli, C., Scrivani, A., *Isothermal oxidation resistance comparison between air plasma sprayed, vacuum plasma sprayed and high velocity oxygen fuel sprayed CoNiCrAlY bond coats*. *Surface and Coatings Technology*, 2010. **204**(15): p. 2499-2503.
  42. Gil, A., Shemet, V., Vassen, R., Subanovic, M., Toscano, J., Naumenko, D., Singheiser, L. and Quadackers, W. J., *Effect of surface condition on the oxidation behaviour of MCrAlY coatings*. *Surface and Coatings Technology*, 2006. **201**(7): p. 3824-3828.
  43. Meier-Jackson, E.M., et al., *Effect of surface preparation on the durability of NiCoCrAlY coatings for oxidation protection and bond coats for thermal barrier coatings*. *Materials and Corrosion*, 2008. **59**(6): p. 494-500.
  44. Li, Y., Li, C.J., Zhang, Q., Yang, G.J. and Li, C.X., *Influence of TGO Composition on the Thermal Shock Lifetime of Thermal Barrier Coatings with Cold-sprayed MCrAlY Bond Coat*. *Journal of Thermal Spray Technology*, 2010. **19**(1): p. 168-177.
  45. Naumenko, D., Shemet, V., Singheiser, L. and Quadackers, W., *Failure mechanisms of thermal barrier coatings on MCrAlY-type bondcoats associated with the formation of the thermally grown oxide*. *Journal of Materials Science*, 2009. **44**(7): p. 1687-1703.
  46. Ogawa, K., Ito, K., Shoji, T., Seo, D., Tezuka, H. and Kato, H., *Effects of Ce and Si additions to CoNiCrAlY bond coat materials on oxidation behavior and crack propagation of thermal barrier coatings*. *Journal of Thermal Spray Technology*, 2006. **15**(4): p. 640-651.
  47. Tang, F. and J.M. Schoenung, *Local accumulation of thermally grown oxide in plasma-sprayed thermal barrier coatings with rough top-coat/bond-coat interfaces*. *Scripta Materialia*, 2005. **52**(9): p. 905-909.

48. Pint, B.A., Wright, I. G., Lee, W. Y., Zhang, Y., Prüßner, K. and Alexander, K. B., *Substrate and bond coat compositions: factors affecting alumina scale adhesion*. Materials Science and Engineering A, 1998. **245**(2): p. 201-211.
49. Rensch, D., M. Schorr, and M. Schütze, *The role that bond coat depletion of aluminum has on the lifetime of APS-TBC under oxidizing conditions*. Materials and Corrosion, 2008. **59**(7): p. 547-555.
50. Barrett, C.A., R.V. Miner, and D.R. Hull, *The effects of Cr, Al, Ti, Mo, W, Ta, and Cb on the cyclic oxidation behavior of cast Ni-base superalloys at 1100 and 1150°C*. Oxidation of Metals, 1983. **20**(5): p. 255-278.
51. Miller, R.A. and C.E. Lowell, *Failure mechanisms of thermal barrier coatings exposed to elevated temperatures*. Thin Solid Films, 1982. **95**(3): p. 265-273.
52. Stecura, S., *Two-Layer Thermal-Barrier Systems for Ni-Al-Mo Alloy and Effects of Alloy Thermal Expansion on System Life*. American Ceramic Society Bulletin, 1982. **61**(2): p. 256-262.
53. Wu, B.C., Chang, E., Chang, S.F. and Tu D. , *Degradation Mechanisms of ZrO<sub>2</sub>-8 wt% Y<sub>2</sub>O<sub>3</sub>/Ni-22Cr-10Al-1Y Thermal Barrier Coatings*. Journal of the American Ceramic Society, 1989. **72**(2): p. 212-218.
54. Krogstad, J.A., Krämer, S, Lipkin, D. M., Johnson, C. A., Mitchell, D. R. G., Cairney, J. M. and Levi, C. G., *Phase Stability of t'-Zirconia-Based Thermal Barrier Coatings: Mechanistic Insights*. Journal of the American Ceramic Society, 2011. **94**: p. s168-s177.
55. Heuer, A.H. and M. Rühle, *Overview no. 45: On the nucleation of the martensitic transformation in zirconia (ZrO<sub>2</sub>)*. Acta Metallurgica, 1985. **33**(12): p. 2101-2112.
56. Brandon, J.R. and R. Taylor, *Phase stability of zirconia-based thermal barrier coatings part I. Zirconia-yttria alloys*. Surface and Coatings Technology, 1991. **46**(1): p. 75-90.
57. Chevalier, J., et al., *The Tetragonal-Monoclinic Transformation in Zirconia: Lessons Learned and Future Trends*. Journal of the American Ceramic Society, 2009. **92**(9): p. 1901-1920.
58. Kilo, M., Borchardt, G., Lesage, B., Kaïtasov, O., Weber, S. and Scherrer, S., *Cation transport in yttria stabilized cubic zirconia: 96Zr tracer diffusion in (ZrxY1-x)O2-x/2 single crystals with 0.15 ≤ x ≤ 0.48*. Journal of the European Ceramic Society, 2000. **20**(12): p. 2069-2077.
59. Ashby, M.F., *A first report on sintering diagrams*. Acta Metallurgica, 1974. **22**(3): p. 275-289.
60. VanValzah, J.R. and H.E. Eaton, *Cooling rate effects on the tetragonal to monoclinic phase transformation in aged plasma-sprayed yttria partially stabilized zirconia*. Surface and Coatings Technology, 1991. **46**(3): p. 289-300.

61. Cipitria, A., I.O. Golosnoy, and T.W. Clyne, *A sintering model for plasma-sprayed zirconia thermal barrier coatings. Part II: Coatings bonded to a rigid substrate*. Acta Materialia, 2009. **57**(4): p. 993-1003.
62. Ahrens, M., R. Vaßen, and D. Stöver, *Stress distributions in plasma-sprayed thermal barrier coatings as a function of interface roughness and oxide scale thickness*. Surface and Coatings Technology, 2002. **161**(1): p. 26-35.
63. Evans, A.G., D. R. Mumm, J. W. Hutchinson, G. H. Meier and F. S. Pettit, *Mechanisms Controlling the Durability of Thermal Barrier Coatings*. Progress in Materials Research, 2001. **46**(5).
64. Haynes, J.A., M.K. Ferber, and W.D. Porter, *Thermal cycling behavior of plasma-sprayed thermal barrier coatings with various MCrAlX bond coats*. Journal of Thermal Spray Technology, 2000. **9**(1): p. 38-48.
65. Vaßen, R., G. Kerkhoff, and D. Stöver, *Development of a micromechanical life prediction model for plasma sprayed thermal barrier coatings*. Materials Science and Engineering: A, 2001. **303**(1–2): p. 100-109.
66. Echsler, H., et al., *Cracking in and around the thermally grown oxide in thermal barrier coatings: A comparison of isothermal and cyclic oxidation*. Journal of Materials Science, 2006. **41**(4): p. 1047-1058.
67. Yu, H.H., M.Y. He, and J.W. Hutchinson, *Edge effects in thin film delamination*. Acta Materialia, 2001. **49**(1): p. 93-107.
68. Balint, D., Hutchinson, J.W., *Mode II edge delamination of compressed thin films*. J. Appl. Mech., 2001. **68**: p. 725-730.
69. Li, L. and T.A. Taylor, *Surface Finish of Plasma Sprayed - Dense Vertically Cracked Thermal Barrier Coatings*, M. Helminiak, Editor 2013.
70. Zhu, D. and R.A. Miller, *Investigation of thermal fatigue behavior of thermal barrier coating systems*. Surface and Coatings Technology, 1997. **94–95**(0): p. 94-101.
71. Siebert, B., et al., *Changes in porosity and Young's Modulus due to sintering of plasma sprayed thermal barrier coatings*. Journal of Materials Processing Technology, 1999. **92–93**(0): p. 217-223.
72. Pint, B. and K. More, *Characterization of alumina interfaces in TBC systems*. Journal of Materials Science, 2009. **44**(7): p. 1676-1686.
73. Haynes, J., Ferber, M., Porter, W. and Rigney, E., *Characterization of Alumina Scales Formed During Isothermal and Cyclic Oxidation of Plasma-Sprayed TBC Systems at 1150°C*. Oxidation of Metals, 1999. **52**(1): p. 31-76.

74. Bolcavage, A., et al. *Thermal Shock Testing of TBC/Bondcoat Systems*. in *Heat Treat/Surface Engineering Conference*. 2003. Indianapolis, IN: ASM.
75. Freborg, A.M., et al., *Modeling oxidation induced stresses in thermal barrier coatings*. *Materials Science and Engineering: A*, 1998. **245**(2): p. 182-190.
76. Pint, B.A., J.A. Haynes, and T.M. Besmann, *Effect of Hf and Y alloy additions on aluminide coating performance*. *Surface and Coatings Technology*, 2010. **204**(20): p. 3287-3293.
77. Wu, R.T., Kawagishi, K., Harada, H. and Reed, R. C., *The retention of thermal barrier coating systems on single-crystal superalloys: Effects of substrate composition*. *Acta Materialia*, 2008. **56**(14): p. 3622-3629.
78. Roper, G.W. and D.P. Whittle, *Interdiffusion in ternary Co-Cr-Al alloys*. *Metal Science*, 1980. **14**(1): p. 21-28.
79. Nesbitt, J. and R. Heckel, *Interdiffusion in Ni-Rich, Ni-Cr-Al alloys at 1100 and 1200 °C: Part I. Diffusion paths and microstructures*. *Metallurgical and Materials Transactions A*, 1987. **18**(12): p. 2061-2073.
80. Nesbitt, J. and R. Heckel, *Interdiffusion in Ni-rich, Ni-Cr-Al alloys at 1100 and 1200 °C: Part II. Diffusion coefficients and predicted concentration profiles*. *Metallurgical and Materials Transactions A*, 1987. **18**(12): p. 2075-2086.
81. Tan, Y., et al., *Optimizing Compliance and Thermal Conductivity of Plasma Sprayed Thermal Barrier Coatings via Controlled Powders and Processing Strategies*. *Journal of Thermal Spray Technology*, 2012. **21**(5): p. 950-962.